

Anthropometric and Genetic Determinants of Cardiac Morphology and Function

Submitted to Imperial College London

for the degree of Doctor of Philosophy

by

Antonio de Marvao

MB ChB (Hons) MRCP (UK)

Cardiovascular Magnetic Resonance Imaging and Genetics

MRC Clinical Sciences Centre

Imperial College London

April 2015

1 Abstract

Background

Cardiac structure and function result from complex interactions between genetic and environmental factors. Population-based studies have relied on 2-dimensional cardiovascular magnetic resonance as the gold-standard for phenotyping. However, this technique provides limited global metrics and is insensitive to regional or asymmetric changes in left ventricular (LV) morphology.

High-resolution 3-dimensional cardiac magnetic resonance (3D-CMR) with computational quantitative phenotyping, might improve on traditional CMR by enabling the creation of detailed 3D statistical models of the variation in cardiac phenotypes for use in studies of genetic and/or environmental effects on cardiac form or function.

Purpose

To determine whether 3D-CMR is applicable at scale, and provides methodological and statistical advantages over conventional imaging for large-scale population studies and to apply 3D-CMR to anthropometric and genetic studies of the heart.

Methods

1530 volunteers (54.8% females, 74.7% Caucasian, mean age 41.3 ± 13.0 years) without self-reported cardiovascular disease were recruited prospectively to the Digital Heart Project. Using a cardiac atlas-based software, these images were computationally processed and quantitatively analysed. Parameters such as myocardial shape, curvature, wall thickness, relative wall thickness, end-systolic wall stress, fractional wall thickening and ventricular volumes were extracted at over 46,000 points in the model. The relationships between these parameters and systolic blood pressure (SBP), fat mass, lean mass and genetic variations

were analysed using 3D regression models adjusted for body surface area, gender, race, age and multiple testing.

Targeted resequencing of titin (TTN), the largest human gene and the commonest genetic cause of dilated cardiomyopathy, was performed in 928 subjects while common variants (~700.000) were genotyped in 1346 subjects.

Results

Automatically segmented 3D images were more accurate than 2D images at defining cardiac surfaces, resulting in fewer subjects being required to detect a statistically significant 1 mm difference in wall thickness. 3D-CMR enabled the detection of a strong and distinct regionality of the effects of SBP, body composition and genetic variation on the heart. It shows that the precursors of the hypertensive heart phenotype can be traced to healthy normotensives and that different ratios of body composition are associated with particular gender-specific patterns of cardiac remodelling. In 17 asymptomatic subjects with genetic variations associated with dilated cardiomyopathy, early stages of ventricular impairment and wall thinning were identified, which were not apparent by 2D imaging.

Conclusions

3D-CMR combined with computational modelling provides high-resolution insight into the earliest stages of heart disease. These methods show promise for population-based studies of the anthropometric, environmental and genetic determinants of LV form and function in health and disease.

2 Table of Contents

1	Abstract	2
2	Table of Contents	4
3	Declaration of Originality	8
4	Copyright Declaration.....	8
5	Acknowledgments.....	9
6	List of Figures and Tables.....	10
7	Publications, Presentations and Prizes arising from this work	14
	7.1 Peer reviewed papers	14
	7.2 Abstracts and Poster Presentations	16
	7.3 Oral Presentations	18
	7.4 Prizes.....	18
8	Glossary of terms and abbreviations.....	19
9	Introduction.....	22
	9.1 Left Ventricular Anatomy	24
	9.2 Left Ventricular Histology	28
	9.3 Left Ventricular Physiology.....	31
	9.4 Blood Pressure	34
	9.5 Aortic Pulse Wave velocity	36
	9.6 Inherited Cardiac Conditions	38
	9.6.1 Hypertrophic Cardiomyopathy.....	39
	9.6.2 Dilated Cardiomyopathy	40
	9.7 Genetics, genotyping and sequencing.....	45

9.7.1	DNA Sequencing Strategies.....	48
9.7.2	Study designs used in genetic studies	50
9.8	Cardiovascular Magnetic Resonance	54
9.8.1	History, principles and techniques of Magnetic Resonance Imaging	54
9.8.2	Cardiac Magnetic Resonance	61
9.8.3	Cardiac Magnetic Resonance in research.....	72
9.8.4	2D-CMR Imaging and Analysis.....	73
9.8.5	Atlas-Based Segmentation of CMR	79
9.9	Phenomics and genomics: towards personalised medicine	84
10	Aims of the thesis.....	86
11	Study methods and population characteristics assessed by 2D-CMR	87
11.1	Introduction	87
11.2	Methods.....	89
11.3	Results	94
11.4	Discussion	105
11.5	Conclusions	110
11.6	Acknowledgments.....	110
12	3D-CMR cardiac atlas and automated analysis methods.....	111
12.1	Introduction	111
12.2	General methods.....	114
12.3	3D cardiac atlas method	117
12.4	Automated segmentation method.....	118

12.5	3D-CMR derived phenotypes.....	125
12.6	Results	127
12.7	Discussion	135
12.8	Conclusions	138
12.9	Acknowledgments	139
12.10	Appendix	140
13	Blood pressure as a determinant of left ventricular morphology and function.....	142
13.1	Introduction	142
13.2	Methods	143
13.3	Results	147
13.4	Discussion	157
13.5	Conclusions	160
13.6	Acknowledgements	160
14	Body composition as a determinant of left ventricular morphology and function	161
14.1	Introduction	161
14.2	Methods	162
14.3	Results	163
14.4	Discussion	170
14.5	Conclusions	174
14.6	Acknowledgements	174
15	Truncating variants in titin as a determinant of cardiac morphology and function in a healthy population.....	175

15.1	Introduction	175
15.2	Methods	178
15.3	Results	183
15.4	Discussion	190
15.5	Conclusions	195
15.6	Acknowledgements	196
16	Future work - 3D genome-wide association study	197
16.1	Introduction	197
16.2	Preliminary methods	200
16.3	Preliminary 3D-GWAS experiments	202
16.4	Conclusions	204
16.5	Acknowledgments	204
17	Overview of thesis	205
18	References	210

3 Declaration of Originality

The work contained in this thesis is my own. There have been many contributions of others to the work described herein and their inputs are duly acknowledged in the respective chapters and otherwise appropriately referenced.

4 Copyright Declaration

The copyright of this thesis rests with the author and is made available under a Creative Commons Attribution Non-Commercial No Derivatives licence. Researchers are free to copy, distribute or transmit the thesis on the condition that they attribute it, that they do not use it for commercial purposes and that they do not alter, transform or build upon it. For any reuse or redistribution, researchers must make clear to others the licence terms of this work.

5 Acknowledgments

I am forever indebted to my supervisors Declan O'Regan and Stuart Cook for their support, encouragement, and guidance. I could not have had more available and helpful mentors.

To Tim Dawes for his clarity of thought, tireless work and willingness to share his immense knowledge of programming and statistics with me.

To Marina Quinlan for always being there with a supportive word and contagious laughter.

A large number of people contributed to this work with their advice, knowledge and practical help. To Tamara Diamond and Laura Monje Garcia that incredibly recruited all our volunteers. To Giuliana Durighel, Amy McGuinness and Catherine Holden for scanning them with such professionalism. Thanks to Pawel Tokarczuk for his witty teachings in physics. To Wenzhe Shi for being so amazingly smart, helpful and for developing the segmentation methods with Wenjia Bai and Daniel Rueckert. To the RBH Genetics and Genomics lab team for all their help with the genetic sequencing and bioinformatics support. I am particularly grateful to James Ware, Katie Francis, Angharad Roberts, Rachel Buchan, Sam Wilkinson and Roddy Walsh. To Hannah Meyer at the EBI for her friendly help with the GWAS project.

This work was supported by a Chain Florey Fellowship jointly funded by the Medical Research Council, the NIHR Biomedical Research Centre at Imperial College Healthcare NHS Trust and Imperial College London. Additional support came from the NIHR Cardiovascular Biomedical Research Unit at Royal Brompton & Harefield NHS Foundation Trust, the British Heart Foundation and the Fondation Leducq.

To the over 1800 volunteers that generously gave their time to be part of this study.

To Jessica Serrano for driving me mad and keeping me sane.

Lastly, to my mother for her unlimited and unconditional support and love.

6 List of Figures and Tables

Figure 9.1 – Left ventricular anatomy	26
Figure 9.2 – Diagram of a cardiac sarcomere	29
Figure 9.3 – The impact of TTNtv position on cardiac morphology and function.....	43
Table 1 – Framingham Heart Study CMR phenotype grouped by TTNtv presence.....	44
Figure 9.4 – Magnetic Resonance system components	60
Figure 9.5 – Two-dimensional balanced steady state free precession of the heart.....	65
Figure 9.6 – Aortic magnitude and velocity encoded acquisitions and pulse wave velocity measurement	68
Figure 9.7 – A 32-elements cardiac-coil	69
Figure 9.8 – Three-dimensional balanced steady state free precession sequence of the heart.....	71
Figure 9.9 – Two-dimensional balanced steady state free precession sequence of the heart	71
Figure 9.10 – Number of annual publications on cardiac magnetic resonance	72
Figure 9.11 – The American Heart Association 17 segment model	74
Figure 9.12 – Standard CMR volumetric analysis.....	75
Table 2 – Published normal ranges of myocardial mass and function by age and gender.....	77
Table 3 – Published normal CMR ranges and subject characteristics by gender.	78
Table 4 – Reproducibility of CMR measurements.....	95
Table 5 – Digital Heart Project subject characteristics and CMR parameters	96
Table 6 – Digital Heart Project CMR-derived cardiac measurements by age and gender.....	97
Table 7 – Digital Heart Project CMR-derived cardiac measurements by race	98
Table 8 – Summary of linear regression models for the whole cohort	99
Table 9 – Summary of linear regression models split by gender	101
Figure 11.1 – Scatterplot of indexed left ventricular mass against systolic blood pressure by Race.....	103

Figure 12.1 – One of the initial 20 cardiac atlases	117
Figure 12.2 – The PatchMatch automated cardiac segmentation method	118
Figure 12.3 – Flow chart for atlas construction	119
Figure 12.4 – Diagram of a left ventricular short axis image	120
Figure 12.5 – Rendering of the automated segmentation (white contours) and the manual label map	121
Figure 12.6 – Example of a failed automated segmentation	122
Figure 12.7 - Example of two failed automated segmentations	123
Figure 12.8 – Automated segmentation superimposed on a 3D-CMR image of one of the Digital Heart Project’s volunteers	124
Figure 12.9 – Curvature of a surface	126
Figure 12.10 – The Digital Heart Project cardiac atlas	128
Figure 12.11 – End-diastolic template from 1092 volunteers of the Digital Heart Project ..	128
Figure 12.12 – End-diastolic template from 1092 subjects of the Digital Heart Project with the corresponding 3D surface mesh	129
Figure 12.13 – The accuracy of cardiac segmentation measured with the Dice coefficient.	129
Figure 12.14 – Left ventricular long axis reconstructions of short-axis cine MR images	130
Figure 12.15 – Segmentations of the myocardium in a healthy volunteer	131
Figure 12.16 – Comparison of automated 3D-LVSA segmentations to their respective manually labelled cardiac atlas	132
Figure 12.17 - Comparison of automated 3D-LVSA segmentations to manual volumetry .	132
Figure 12.18 – The reduction in sample size required for 3D LVSA segmentations to detect a 1mm difference in left ventricular wall thickness	133
Figure 12.19 – Inter-study variability in wall thickness measurements	134

Figure 12.20 – Voxelwise comparisons between LV wall thickness on 2D and 3D LVSA myocardial segmentations.....	134
Figure 13.1 – 3D-CMR atlas-based automated method.....	145
Figure 13.2 – Density plot showing the distribution of blood pressure readings	148
Table 10 - Subject characteristics and CMR-derived cardiac measurements by SBP group	150
Figure 13.3 – Scatterplot of age against systolic blood pressure by gender	151
Figure 13.4 – Three dimensional R^2	152
Figure 13.5 – Three dimensional model of the regional changes in left ventricular geometry associated with systolic blood pressure	152
Figure 13.6 - Three dimensional regression models of the association between systolic blood pressure and left ventricular relative wall thickness	153
Figure 13.7 - Three dimensional regression models of the association between systolic blood pressure and left ventricular geometry.....	154
Figure 13.8 - Three dimensional regression models of the association between systolic blood pressure and fractional wall thickening across the cohort	155
Figure 13.9 - Three dimensional regression models of the association between systolic blood pressure and regional end-systolic wall stress	156
Table 11 – Linear regression models using body composition data.	164
Table 12 – Linear regression models using body composition data split by gender	166
Figure 14.1 – Three dimensional regression models of the association between fat mass and endocardial left ventricular geometry	168
Figure 14.2 - Three dimensional regression models of the association between relative wall thickness and body composition	169
Figure 15.1 – Schematic of the TTN meta-transcript with sarcomeric regions demarcated	183
Table 13 - Titin truncating variants identified in 18 out of 928 volunteers	184

Table 14 – Subject characteristics and CMR-derived cardiac measurements split by the presence (TTNtv) or absence (TTNtv negative) of titin truncating variants	185
Figure 15.2 – Box plot of cardiac parameters by gender in TTNtv positive and negative sub-cohorts.....	186
Table 15 – Linear modelling of the relationship between the TTN genotype and cardiac phenotypes.	187
Figure 15.3 – Three dimensional regression models of the association between TTNtv and left ventricular wall thickness.	188
Figure 15.4 – Three dimensional regression models of the association between TTNtv and relative ventricular wall thickness	188
Figure 15.5 – Three dimensional regression models of the association between TTNtv and epicardial and endocardial left ventricular geometry.....	189
Figure 16.1 – PEER	199
Figure 16.2 – Bayesian factor analysis	203
Figure 16.3 – Preliminary data of the Digital Heart Project genome-wide association study for 2D left ventricular mass	203

7 Publications, Presentations and Prizes arising from this work

7.1 Peer reviewed papers

de Marvao A, Dawes TJ, Shi W, Durighel G, Rueckert D, Cook SA, O'Regan DP.

Precursors of Hypertensive Heart Phenotype Develop in Healthy Adults: A High-Resolution 3D MRI Study. *JACC Cardiovascular imaging*. 2015;8:1260-9.

Wang H, Shi W, Bai W, **de Marvao A**, Dawes TJ, O'Regan DP, Edwards P, Cook SA, Rueckert D. Prediction of clinical information from cardiac MRI using manifold learning [accepted for publication in *Lecture Notes in Computer Science*]

Roberts AM, Ware JS, Herman DS, Schafer S, Baksi J, Bick AG, Buchan RJ, Walsh R, John S, Wilkinson S, Mazzarotto F, Felkin LE, Gong S, MacArthur JA, Cunningham F, Flannick J, Gabriel SB, Altshuler DM, Macdonald PS, Heinig M, Keogh AM, Hayward CS, Banner NR, Pennell DJ, O'Regan DP, San TR, **de Marvao A**, Dawes TJ, Gulati A, Birks EJ, Yacoub MH, Radke M, Gotthardt M, Wilson JG, O'Donnell CJ, Prasad SK, Barton PJ, Fatkin D, Hubner N, Seidman JG, Seidman CE, Cook SA. Integrated allelic, transcriptional, and phenomic dissection of the cardiac effects of titin truncations in health and disease. *Science translational medicine*. 2015;7(270):270ra6.

de Marvao A, Dawes TJ, Shi W, Minas C, Keenan NG, Diamond T, Durighel G, Montana G, Rueckert D, Cook SA, O'Regan DP. Population-based studies of myocardial

hypertrophy: high resolution cardiovascular magnetic resonance atlases improve statistical power. J Cardiovasc Magn Reson 2014;16:16.

Wang Z, Bhatia KK, Glocker B, **Marvao A**, Dawes T, Misawa K, Mori K, Rueckert D. Geodesic patch-based segmentation. Medical image computing and computer-assisted intervention : MICCAI International Conference on Medical Image Computing and Computer-Assisted Intervention 2014;17:666-73.

Shi W, Lombaert H, Bai W, Ledig C, Zhuang X, **Marvao A**, Dawes T, O'Regan D. Multi-atlas spectral PatchMatch: application to cardiac image segmentation. Medical image computing and computer-assisted intervention : MICCAI International Conference on Medical Image Computing and Computer-Assisted Intervention 2014;17:348-55.

Shi W, Caballero J, Ledig C, Zhuang X, Bai W, Bhatia K, **de Marvao AM**, Dawes T, O'Regan D, Rueckert D. Cardiac image super-resolution with global correspondence using multi-atlas patchmatch. Medical image computing and computer-assisted intervention : MICCAI International Conference on Medical Image Computing and Computer-Assisted Intervention 2013;16:9-16.

Corden B, Keenan NG, **de Marvao AS**, Dawes TJ, Decesare A, Diamond T, Durighel G, Hughes AD, Cook SA, O'Regan DP. Body fat is associated with reduced aortic stiffness until middle age. Hypertension 2013;61:1322-7.

7.2 Abstracts and Poster Presentations

Abstract and oral presentation – The Biology of Genomes 2015, May 2015: Meyer H, **de Marvao A**, Dawes T, Shi W, Diamond T, Rueckert D, Pettreto E, Bottolo L, O'Regan D, Cook S, Birney E. Understanding cardiac structure and function in humans using 4D imaging genetics.

Abstract and moderated poster presentation – 18th Annual Society for Cardiovascular Magnetic Resonance Scientific Sessions / EuroCMR Conference, February 2015: **de Marvao A**, Dawes T, Shi W, Durighel G, Rueckert D, Cook S, O'Regan D. Adverse changes in left ventricular structure begin at normotensive systolic blood pressures: a high resolution MRI study. Journal of Cardiovascular Magnetic Resonance. 2015;17(Suppl 1):M11.

Abstract – 18th Annual Society for Cardiovascular Magnetic Resonance Scientific Sessions / EuroCMR Conference, February 2015: Alenaini W, O'Regan D, de Marvao A, Dawes T, Shi W, Cook S. Three dimensional modelling of the effect of arterial pulse wave velocity and body size on left ventricular geometry. Journal of Cardiovascular Magnetic Resonance. 2015;17(Suppl 1):O44.

Poster presentation - The North-West Thames Foundation School Academic Symposium, July 2013: Gandhi A, Tokarczuk P, Dawes T, **De Marvao A**, Durighel G, Steenkamp K, Quinlan M, Buzaco R, Corden B, De Cesare A, Cook S, O'Regan D. Pulmonary Artery Pulse Wave Velocity: A New, Robust and Reproducible Assessment Method.

Abstract and Poster presentation - British Cardiovascular Society Conference, July 2013: **de Marvao A**, Dawes T, Keenan N, Minas C, Shi W, Durighel G, Diamond T, Cook S,

O'Regan D. Asymmetrical Septal Hypertrophy is associated with mean arterial blood pressure in healthy adults: data from high resolution 3D cardiac MRI. Heart 2013, 99: A136-A137

Abstract and Poster presentation - British Cardiovascular Society Conference, July 2013:

Dawes T, **de Marvao A**, Keenan N, O'Regan D. High Resolution 3D Cine Imaging: A novel approach for automated Right Ventricular Phenotyping. Heart 2013, 99: A56

Abstract and Poster presentation - British Cardiovascular Society Conference, July 2013:

Corden B, Keenan NG, **de Marvao A**, Dawes T, De Cesare A, Diamond T, Durighel G, Hughes AD, Cook SA, O'Regan DP. (2013) The effect of obesity on aortic stiffness is age dependent. Heart 2013, 99: A67

Poster Presentation - International Imaging Workshop, MRC Clinical Sciences Centre,

Imperial College London, March 2013: O'Regan D, **de Marvao A**, Dawes T, Keenan N, Shi W, Minas C, Durighel G, Diamond T, Montan G, Petretto E, Rueckert D, Cook S. Imaging-Genetics: Statistical modelling of genetic effects in the heart.

Abstract and Poster Presentation - 16th Annual SCMR Scientific Sessions, February 2013:

de Marvao A, Dawes T, Keenan N G, Bai W, Shi W, Durighel G, Diamond T, Monje-Garcia L, Cook S A, O'Regan D P. The UK GenScan study - population-based imaging genetics research using 3D Cardiac Magnetic Resonance, Journal of Cardiovascular Magnetic Resonance 2013, 15 (Suppl 1):E2

Abstract and Poster Presentation - 16th Annual SCMR Scientific Sessions, February 2013:

Corden B, Keenan N G, **de Marvao A**, Dawes T, De Cesare A, Diamond T, Durighel G, Hughes A D, Cook S A, O'Regan D P. Obesity has divergent effects on aortic

stiffness in young and old adults, Journal of Cardiovascular Magnetic Resonance 2013; 15(Suppl 1): P229.

7.3 Oral Presentations

Moderated poster – 18th Annual Society for Cardiovascular Magnetic Resonance Scientific Sessions / EuroCMR Conference, February 2015. Adverse changes in left ventricular structure begin at normotensive systolic blood pressures: a high resolution MRI study.

Invited Speaker – Hammersmith Hospital Staff Round, November 2014. Big data, big insights: Computational Modelling of Genetic Effects on the Heart.

Invited Speaker – Fabrics of Life – Designing with the Materials of Life: Big Data Workshop. MRC Clinical Sciences Centre, Bartlett School of Architecture and Central Saint Martins, February 2013. The Big Heart.

Invited Speaker - Chain-Florey Clinical Research Fellowship Workshop, MRC Clinical Sciences Centre, October 2013. Computational Modelling of Genetic Effects on the Heart.

7.4 Prizes

- Best Moderated Poster at 18th Annual Society for Cardiovascular Magnetic Resonance Scientific Sessions / EuroCMR Conference, February 2015
- Society for Cardiovascular Magnetic Resonance 2015 Scholarship, December 2014.

8 Glossary of terms and abbreviations

2D	two dimensional
3D	three dimensional
3D-CMR	three-dimensional cardiac magnetic resonance
Atlas	it refers to an image that was manually labelled and curated and provides prior knowledge to guide automated analysis of new CMR images
AV	atrioventricular
bp	base pairs – the length of a (double-stranded) DNA sequence is reported in base pairs. Standard prefixes are used to indicate larger units, such as kbp and Mbp
BP	blood pressure
BMI	body mass index
BSA	body surface area
b-SSFP	balanced Steady State Free Precession
CAP	Cardiac Atlas Project
CI	concentricity index (left ventricular mass / left ventricular end diastolic volume)
CMR	cardiac magnetic resonance
DCM	dilated cardiomyopathy – cardiomyopathy characterised by increased ventricular cavity size without increased wall thickness, often inherited
DNA	deoxyribonucleic acid
Dominant inheritance	pattern of inheritance in which one aberrant copy of a gene is sufficient for the disease or trait to develop
ECG	electrocardiogram
EDV / EDVI	end diastolic volume / indexed end diastolic volume
EF	ejection fraction
ESV / ESVI	end systolic volume / indexed end diastolic volume
Exon	protein-coding portion of a gene
FDR	false discovery rate

FHS	Framingham Heart Study
FWT	fractional wall thickening
Genotyping	the process of identifying genetic variation in an individual genome
GWAS	genome-wide association study
HCM	hypertrophic cardiomyopathy – cardiomyopathy characterised by increased ventricular wall thickness, without increased cavity size, usually inherited
ICC	inherited cardiac condition
K-space	‘raw data space’ where the digitised MRI signal data is stored
LV	left ventricular
LVH	left ventricular hypertrophy
LVM	left ventricular mass
MAF	mean allele frequency
MRI	magnetic resonance imaging
Mendelian	a Mendelian trait is one that is controlled by a single locus that is inherited according to Mendel's laws
MESA	Multi-Ethnic Study of Atherosclerosis study
NGS	next generation sequencing
NMR	nuclear magnetic resonance
NTP	nucleoside triphosphate
PCA	principal component analysis
Penetrance	proportion of individuals carrying a particular variant of a gene (allele or genotype) that also expresses an associated phenotype
Phenotype	observable characteristics or traits, such as morphologic, biochemical or physiological properties and behaviour. A phenotype results from the expression of an organism's genes as well as the influence of environmental factors and the interactions between the two
PSI	proportion spliced-in (an estimate of the percentage of TTN transcripts that incorporate this exon based on RNAseq data)
PWV	pulse wave velocity
Recessive inheritance	pattern of inheritance in which both copies of a gene must be aberrant in

	order for the disease or trait to develop
RF	radiofrequency
ROI	region of interest
RV	right ventricle
RWT	relative wall thickness
SBP	systolic blood pressure
SCD	sudden cardiac death
SENSE	SENSitivity Encoding - parallel imaging method for accelerating image acquisition
SNP	single nucleotide polymorphism
SNR	signal to noise ratio
SSM	statistical shape model
SV / SVI	stroke volume / index stroke volume
TE	echo time – time between excitation and echo
TR	repetition time – time between successive excitation pulses
TTN	Titin (gene or protein)
WES	whole exome sequencing
WGS	whole genome sequencing
WS	wall stress
WT	wall thickness

9 Introduction

The modern discipline of cardiology builds upon millennia of scientific discoveries and accrued knowledge (1). Even though medical historians tend to trace the speciality back to the pivotal work of William Harvey in the 17th century (2), the first documented notion of the cardiac system can be found in the Smith Egyptian papyrus believed to be a copy of a work written in 3000 BC (3). Certainly by 1500 BC, when the Eber papyrus was written, the role of the heart as the centre of the body's blood supply was understood (4). It has been this endless drive to improve and refine earlier contributions that led to the range of advanced diagnostic and therapeutic tools currently available to cardiologists. In recent years, this array of resources has vastly expanded due to the transformative changes ushered in by genetic sequencing technologies (5). Indeed, our understanding of the fundamental genetic and environmental underpinnings of cardiac morphology and physiology is limited, at least in part, by our inability to phenotype the heart at an equivalent resolution.

Leveraging all these technological advances, cardiovascular research must aim to further our knowledge of the elementary correlation between cardiac function and morphology, in health and in disease, for 'function without structure cannot exist and structure has no meaning unless it serves a functional purpose'(1).

The aim of this project was to define the anatomical and functional properties of the left ventricle associated with a variety of anthropometric and genetic variables. To achieve this, a novel high-throughput method, combining state-of-the-art cardiac imaging, with computational statistical analysis was developed, tested and validated in a large cohort of healthy volunteers. This work builds on the findings and achievements

of generations of clinicians and scientists and intends to provide greater insights into the biological pathways that determine cardiac morphology and function.

9.1 Left Ventricular Anatomy

Fairly accurate anatomical descriptions of the heart and the great vessels can be found as far back as the Smith and Ebers papyri, the Bible and the Talmud (6). Galen of Pergamon (129-201 AD) greatly contributed to medical progress by studying anatomy and physiology through experimentation and dissection. Erroneously, he believed that the circulatory system consisted of two separate one-way systems of distribution in which all the vessels connected to the heart were arteries and those connected to the liver were veins. Unfortunately, his work was so influential that it was considered to have been the result of divine inspiration and therefore infallible (7). It was not until the Renaissance, in the 15th and 16th centuries, that Galen's findings were challenged. This work culminated in William Harvey's definitive observations on the circulatory system in 1628. In his book titled *De Motu Cordis*, Harvey stated: 'It has been shown by reason and experiment that by the beat of the ventricles blood flows through the lungs and it is pumped to the whole body. There it passes through pores in the flesh into the veins through which it returns from the periphery...finally coming to the vena cava and right auricle...It must then be concluded that the blood in the animal body moves around in a circle continuously, and that the action or function of the heart is to accomplish this by pumping. This is the only reason for the motion and beat of the heart' (8).

The human heart is a muscular organ that lies inside the thoracic cavity, above the diaphragm and in a space between the lungs, called the mediastinum. Its posterior border is near the vertebral column and its anterior border near the sternum. The upper part of the heart, conventionally described as the base, lies beneath the second rib. The distal end of the heart, the apex, is normally in line with the fifth intercostal space. The heart is enclosed by a double-layered, fibrous sac, called the pericardium that separates it from the other structures

in the mediastinum. The heart wall is formed by three distinct layers: the epicardium (the inner layer of the pericardium constituted mostly of connective tissue and abundant adipose tissue), the myocardium (striated muscle with intervening connective tissue, blood vessels and nerves) and the endocardium (endothelium on the surface with underlying collagenous and elastic tissue, as well as the specialised Purkinje fibres). The heart is divided into right and left sides by an obliquely placed, longitudinal septum. Each side consists of an atrium, which receives blood from the veins, and a ventricle, which propels the blood into the arteries.

The normal left ventricle is a conical structure with its long axis in the thorax, from cardiac base to apex, directed leftward, anteriorly and inferiorly. It can be divided into three parts: the smooth inlet portion that contains the mitral valve apparatus, a smooth outlet portion leading to the aortic valve, and an apical portion characterised by a meshwork of thin muscle bundles called trabeculations (**Figure 9.1**). The medial wall of the left ventricle is the ventricular septum which curves and convexes into the right ventricle (RV). The remaining ventricular wall is referred to as the free wall of the left ventricle. When viewed from the anterior aspect of the body, most of the left ventricle hides behind the RV.

Arising from the middle to the apical third of the left ventricular (LV) wall are usually two groups of papillary muscles that attach to the mitral valve: the anterolateral and the posteromedial. Occasionally other papillary muscles are present, arising from the free wall or from near the leaflet of the mitral valve. Overall there is a wide variability in the anatomy of these muscles.

Blood flows in via the atrioventricular (AV) orifice lined by the mitral valve and flows out passing through the aortic valve into the aorta. The mitral valve has an area of 4 to 6 cm² and is formed by the anterior and the posterior leaflets. Each leaflet is divided into three regions

split by commissures. In the normal valve, all parts of the leaflets usually have cords connecting the free edge to the papillary muscle. The aortic valve consists of three half-moon-shaped cusps that are named through their association with the respective coronary ostia: left, right and posterior (non-coronary).

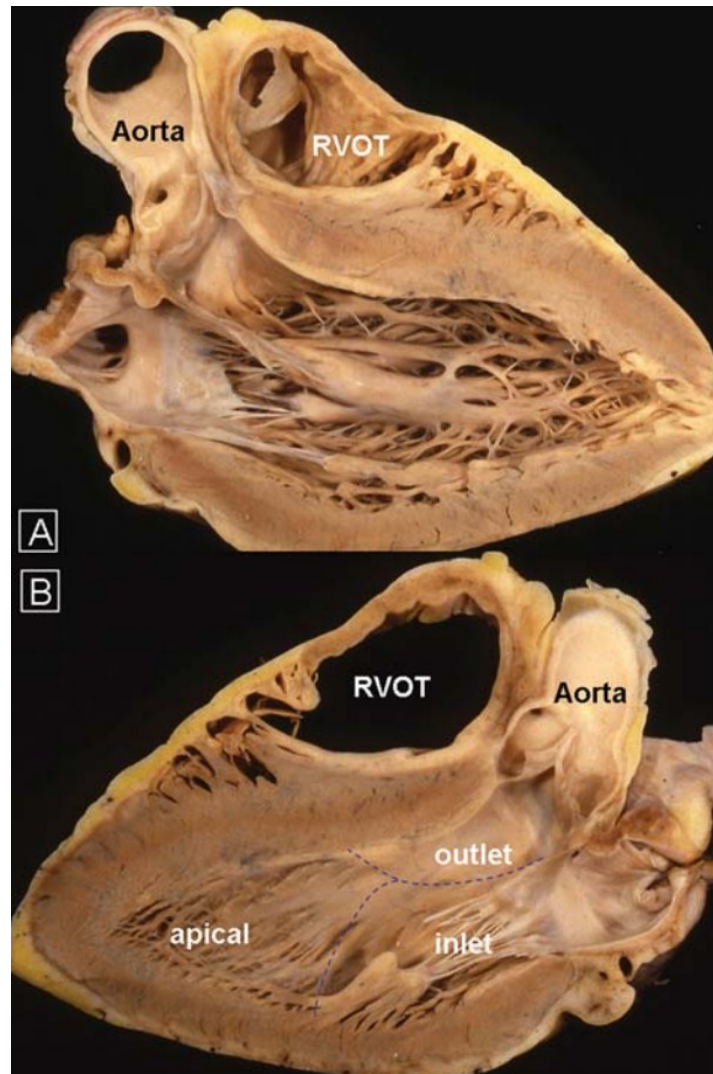


Figure 9.1 – Left ventricular anatomy. Two parts of the same heart sectioned longitudinally. The broken lines divide the left ventricle into its three portions. RVOT = right ventricular outflow tract. (Figure courtesy of Professor Siew Hen Ho)

In adults, the ventricular wall is thickest at the base and thins to only 1-2mm at the apex (9). Excluding trabeculations, the LV septal wall thickness is on average 7-12mm. The interventricular septum is triangular in shape, with the base of the triangle at the level of the

aortic valve. It is entirely muscular except for the small membranous septum, located superiorly and just below the right coronary and the posterior coronary cusps.

9.2 Left Ventricular Histology

The myocardium is comprised primarily of fibroblasts (the most populous cell type), endothelial cells and cardiomyocytes, which measure $\sim 30\mu\text{m}$ in diameter and $\sim 120\mu\text{m}$ in length. Each myocyte is connected to adjacent myocytes by specialised structures called intercalated disks. These intercalated disks enable the cardiomyocytes to form a complex, three-dimensional network and to work as single functional organ (or syncytium). Gap junctions within the intercalated disks permit the passage of ions between cells and that allows electrochemically coordinated contraction across the heart (10).

The LV wall is constituted by three interconnected layers of myocytes that have different spatial orientations: superficial (subepicardial), middle and deep (subendocardial). The myocytes in the superficial layer are arranged obliquely, in the middle strand circumferentially, while in the deep layer they follow a longitudinal plane (11).

The circumferential layer tends to be the thickest in the normal heart (53-59% of wall thickness) and increases with age (12). It is thickest near the base of the heart and tapers out towards the apex. In hypertension and heart failure the orientation of the fibres does not change although there is evidence of increase in the connective tissue content (13).

The sarcomere is the basic repeating contractile unit of muscle and is formed by an array of overlapping thin and thick filaments that give the cardiac muscle its striated appearance. Sarcomeres are defined as the segments between two neighbouring Z-disks. Z-disks are one of the most complex macromolecular structures in biology (14). Among hundreds of different proteins, the core of a Z-disc consists of actin filaments coming from adjacent sarcomeres which are crosslinked by α actinin molecules (15). The Z-disk allows the transmission of tension during myocyte contraction. At the middle of the sarcomere lies the M-line which is

formed by cross-connecting elements of the cytoskeleton and allows the uniform distribution of tension (16). The region of the sarcomere containing the Z-disk and the part of the thin filaments not overlapping the thick filaments is the I-band (for isotropic). The remaining region containing the M-line and the entire length of the thick filaments is the A-band (for anisotropic). H-band is the zone of the thick filaments that is not superimposed by the thin filaments (**Figure 9.2**).

The proteins of the cardiomyocyte can be broadly categorised as contractile, sarcomeric skeleton, membrane associated and proteins of the intercalated disk (17). The thin filaments are composed of actin and troponins C, T, and I. Sarcomere thick filament proteins include myosin heavy chain, myosin essential and regulatory light chains, myosin-binding protein-C and titin. The sarcomere is anchored through titin and actin interactions with Z disc proteins α -actinin, calsarcin-1, muscle LIM protein (MLP), telethonin (T-cap), and Z-band alternatively spliced PDZ-motif protein (ZASP) (**Figure 9.2**).

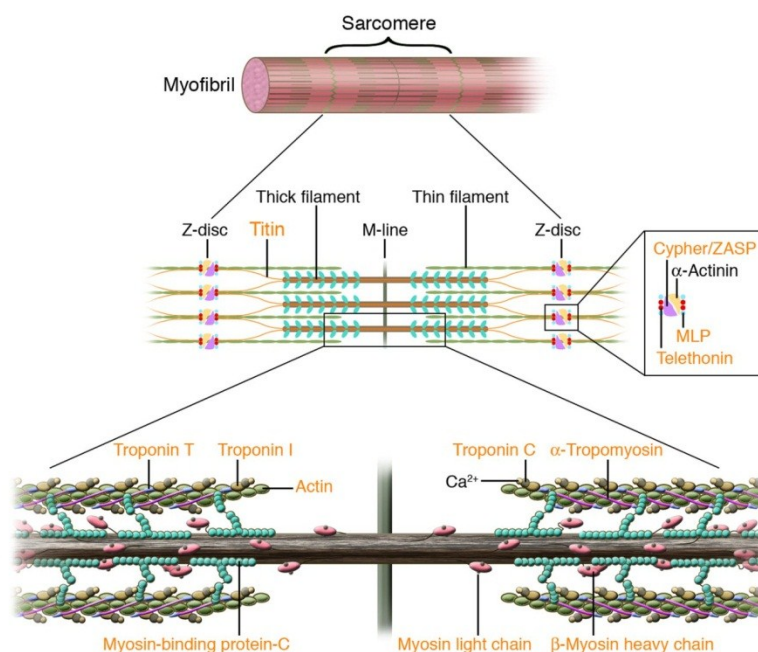


Figure 9.2 – Diagram of a cardiac sarcomere. Mutations in the proteins highlighted in orange might lead to hypertrophic or dilated cardiomyopathies. (From Morita H, et al. Genetic causes of human heart failure. The Journal of clinical investigation. 2005)

The fundamental functions of heart cells are the generation of contractile force by the sarcomere and its transmission to the extracellular matrix. Inadequate performance in either component prompts cardiac remodelling in the form of LV hypertrophy (increased wall thickness without ventricular cavity expansion) or dilation (normal or thinned walls with enlarged ventricular cavity) (18).

In hypertrophic cardiomyopathy (HCM, see section 9.6.1 below), the ventricular septum presents an asymmetric pattern of thickening (19). In particular there is an increase in the thickness of the longitudinal deep layer (20). Histologically, the middle circumferential layer is mostly destroyed at the junction between the ventricular septum and the right and left ventricular free walls and severely affected in the middle portion of the ventricular septum. The pathological process includes a combination of myocyte disarray and interstitial and focal fibrosis. In contrast, the LV free wall has a normal appearance of the midwall layer.

In dilated cardiomyopathy (DCM, see section 9.6.2 below), the cross connections between myocytes are lost resulting in slippage and realignment of adjacent bundles of myocytes. Cardiac remodelling is driven on a histologic level by myocyte hypertrophy and apoptosis, fibroblast proliferation and interstitial fibrosis (21). The end result is LV wall thinning.

9.3 Left Ventricular Physiology

Coordinated contraction of the cardiac muscle cells propels blood out of the atria into the ventricles and from the ventricles into the great vessels. The repetitive process of contraction and relaxation is referred to as the cardiac cycle. Pressure changes during the cycle are responsible for blood movement, as it travels from high pressure to low pressure areas. Systole is defined as the period from mitral valve closure to the aortic valve closure, when the LV ejects blood into the systemic arterial circulation. During diastole the ventricles relax and receive blood from the left atrium.

Due to the spiral architecture of the cardiac myofibers, in addition to systolic myocardial shortening and thickening, there is left ventricular rotation and twist. When viewed from the LV apex, the base rotates clockwise while the apex rotates counter clockwise (22).

Cardiac contraction is coordinated by specialised myocytes that form the conduction system of the heart. This system includes the sinoatrial (SA) node, the AV node, the AV bundle, right and left bundle branches and the Purkinje fibres. All these cells have the ability to produce spontaneous action potentials. Under normal conditions the electrical depolarisation of the heart begins at the SA node which is found in the right atrial wall near the orifice of the superior vena cava. The SA node generates action potentials at the rate of about 70 per minute. From the SA node, the action potential spreads throughout the atria, which initiates atrial contraction and active filling of the ventricles. The AV node is located at the boundary between the atria and ventricles and provides the only conducting path from the atria to the ventricles. If the AV node is not triggered with a higher pulse frequency originating from the SA node, it has an intrinsic frequency of about 50 per minute. From the AV node the action potential then travels down the AV bundle in the ventricular septum until it divides into left

and right bundle branches. From there the action potentials are carried by the Purkinje fibres to the ventricular myocytes. This is represented by the QRS complex of the electrocardiogram (ECG) and marks the start of ventricular systole. As pressure rises in the ventricle the mitral valve closes. When the cavity pressure rises above systemic diastolic pressure the aortic valve opens and blood is expelled into the aorta.

By definition, the volume of blood within a ventricle immediately before a contraction is known as the end-diastolic volume (EDV). Likewise, the volume of blood left in a ventricle at the end of contraction is end-systolic volume (ESV). Each time the heart beats, a volume of blood, known as the stroke volume (SV) is ejected to the aorta. The ability of the LV to empty can be quantified as the LV ejection fraction (EF). This is the ratio of stroke volume to end-diastolic volume: $EF (\%) = SV / EDV \times 100$. Cardiac output (CO) is calculated by multiplying the SV by the heart rate (HR): $CO = SV \times HR$.

Adenosine triphosphate (ATP), which transports chemical energy within cells for metabolism, is required in addition to calcium (Ca^{2+}) as a cofactor for the contraction of muscle cells during the process of excitation-contraction coupling (23). Ca^{2+} plays a key role in cardiac electrical activity and is the direct activator of the myocytes. In response to action potentials, Ca^{2+} enters the myocyte through depolarisation-activated Ca^{2+} -channels. This triggers the release of Ca^{2+} from the sarcoplasmic reticulum (Ca^{2+} -induced Ca^{2+} -release). At rest, actin and myosin are prevented from contacting each other by tropomyosin and the troponin complex (troponin C, I and T). When the Ca^{2+} concentration within the cell increases it binds to troponin C, which induces a conformational change of tropomyosin and allows the formation of strong cross bridges between actin and myosin. The myosin head acts as a lever, hydrolysis of ATP produces force and the relative movement of myosin along actin, shortens the sarcomere. Subsequent release from Troponin C and re-sequestration of calcium in the sarcoplasmic reticulum allows relaxation (24).

Myocytes are rich in mitochondria, which produce ATP at a rapid rate and are able to sustain the high energy requirements of cardiac muscle. Extensive capillary networks provide the muscle with adequate oxygen supply.

When faced with a rising haemodynamic stress, the heart responds through one of 3 mechanisms: increase cross bridge formation; increase in muscle mass or recruitment of neurohormonal mechanisms to increase contractility. Of these, only increase in LV mass plays a key long-term compensatory role (25). In an over-simplified model, pressure overload, such as the one seen in hypertension, leads to parallel addition of sarcomeres resulting in wall hypertrophy. Volume overload leads to myocyte lengthening by sarcomere replication in series, resulting in cavity dilatation and an eventual drop in the wall thickness to cavity size ratio.

Left ventricular mass (LVM) is a highly heritable complex trait (26) and an independent risk factor for all-cause mortality, heart failure and sudden cardiac death (SCD) (27). The estimates of heritability of LVM in the general population vary from 20 to 70% (26, 28-31) . Variability in LVM arises from complex interactions between causal and modifier genes, environmental factors and the regulators of transcription and translation, including epigenetic factors, microRNAs and protein modifiers (32).

The most highly significant and independent predictors of LVM, in both men and women are age, height, systolic blood pressure, body weight or body mass index (33, 34). Furthermore body weight changes have been found to be closely followed by reductions or increase in LV mass (35).

9.4 Blood Pressure

It was Stephen Hales in 1773 that first measured blood pressure (BP) by inserting fine glass tubes into the arteries of animals and measuring the height to which the column of blood rose (36). Although several devices were proposed over the years to measure BP non-invasively, it was in 1896 that Scipione Riva-Rocci developed the forerunner of the modern mercury sphygmomanometer (1). Harvey Cushing led the clinical implementation of this device for the measurement of systolic blood pressure during surgery. It was in 1905, and thanks to Nikolai Korotkoff's work on the characteristic sounds of blood flowing through arteries (37), that the modern technique of BP measurement was born and its widespread clinical use began.

Blood pressure is defined as the force that blood exerts against the inner walls of blood vessels. Most commonly it refers to the pressure measured within the aorta or in the arteries supplied by the aortic braches. The maximum pressure, achieved during ventricular systole, is referred to as the systolic blood pressure (SBP). During diastole the pressure in the arteries falls and this is the diastolic blood pressure (DBP). Arterial pressure is measured in millimetres of mercury (mmHg).

Hypertension is one of the most important preventable contributors to myocardial infarction, stroke, renal failure, and death (38). It is defined as SBP of 140 mmHg or above and a DBP equal or higher than 90 mmHg (39).

Although for most of the 20th century, the medical community believed that the risks associated with hypertension were due to the level of DBP, this paradigm shifted in 1971, when the Framingham Heart Study reported (40, 41). One of the mains findings of the study into the contribution of SBP and DBP to the risk of coronary heart disease, was that SBP was

more strongly associated with the complications of hypertension (42). From the Fifth Report of the Joint National Committee on Detection, Evaluation, and Treatment of High Blood Pressure (JNC 5) in 1993, onwards, SBP was used to define hypertension in guidelines (43). The Prospective Collaborative Study Group meta-analysis of 61 observational studies, included more than 1 million people and showed SBP to be a significantly better predictor of strokes and coronary heart disease than DBP (44). The JNC 7, in 2003, again confirmed SBP as the primary focus of risk stratification and treatment goals (45). In 2014, the JCN 8 guidelines continued to state that in patients over the age of 60 the most important cardiovascular risk factor is SBP (38). However, in subjects under 60, treating DBP to a level below 90mmHg was highlighted as the best approach to reduce cerebrovascular events, heart failure, and overall mortality. Despite this finding, the JCN 8 recommendations continue to support the treatment of SBP to a target under 140 mmHg.

Afterload can be defined as the tension or stress developed in the wall of the LV during systole. In other words, it is the load against which the heart must eject blood. In the absence of aortic valve stenosis, afterload is very similar to SBP. Left ventricular wall stress (WS) is directly related to ventricular chamber radius (R) and SBP, but inversely related to ventricular wall thickness (WT). Thus, raised SBP or dilatation of the ventricle causes an increase in wall stress, while thickening of the ventricular wall leads to a reduction. WS is calculated as: $\text{Wall stress} \propto \text{SBP} \times R/\text{WT}$. Hypertrophy is thought to be the process by which the LV adapts to rising SBP (46).

9.5 Aortic Pulse Wave velocity

Aortic pulse wave velocity (PWV) has been extensively used as a noninvasive measure of arterial stiffness and is strongly predictive of adverse cardiovascular outcomes and all-cause mortality both in the general population (47-51) and in specific aortic diseases (52-54). Importantly, aortic elastic function, as measured by PWV exerts its effects largely independently of other known cardiovascular risk factors (47, 48). This implies that there are other biological mechanisms of vascular risk that are, thus far, poorly understood.

Assessment of the vascular phenotype using PWV enables subclinical vascular disease to be quantified even before the onset of systemic hypertension (55, 56). This makes it a particularly interesting cardiovascular phenotype when investigating healthy subjects with normal blood pressure. Although the association between obesity and adult cardiovascular disease has been extensively studied, there are fewer data available on the effects of body composition and aging on the vascular status of healthy adults.

Traditionally, PWV was measured using a carotid-femoral technique (49). However, this approach is error prone as it incorporates disparate abdominal aorta, iliac and femoral vessel properties and uses a path length that is indirectly (and often inaccurately) measured (57). These limitations can be addressed by measuring aortic PWV from cardiovascular magnetic resonance (58). This is possible by analysing the transit time of blood flow curves between the ascending and descending aorta (Δt) and directly measuring the distance (Δd) between those two sections. PWV corresponds to the ratio of Δd to Δt (59). As is the case in other cardiovascular phenotypes, PWV is highly heritable with research in twins estimating it to be around 50% (60, 61). However, the exact genetic mechanisms underlying this are still

unknown. Genome wide association studies (GWAS) of PWV have detected a limited number of common genetic variants of very small effects sizes (62, 63).

9.6 Inherited Cardiac Conditions

Inherited cardiac conditions (ICCs) are a heterogeneous group of Mendelian disorders that involve the cardiovascular system. It includes arrhythmia syndromes, cardiomyopathies, arteriopathies, muscular dystrophies and disorders of lipid metabolism. As a group they affect around 340,000 individuals in the UK (64). ICCs are the commonest cause of sudden cardiac death (SCD) in the young and are also a major cause of death and disability across all age groups. Average annual risk of SCD is about 0.1% for long QT syndrome and under 1% in HCM (65), while in familial hypercholesterolaemia the annual average mortality is around 0.1-0.5% but affects young individuals (64). Genetic testing for cardiac channelopathies and cardiomyopathies has developed substantially over the last couple of decades and is starting to inform prognosis and impact management at the 'bedside' (66, 67). In the matter of only a few years, genetic testing in clinical practice has moved from targeting individual genes in patients with affected family members to more comprehensive disease panels. Further technological improvements have led to reduced costs and sequencing time and therefore it can be expected that whole exome or genome sequencing will be widely used in the coming years. These developments, allied with more sophisticated imaging and statistical analysis methods have greatly increased our understanding of the complexity and diversity of the underlying genetic substrate, the clinical phenotype, natural history, and therefore approaches to the treatment of ICCs.

The classification of cardiomyopathies has been updated frequently since, in 1980, the World Health Organisation (WHO) defined these conditions as 'heart muscle diseases of unknown cause' (68). A more contemporary definition from 2006 states: 'cardiomyopathies are a heterogeneous group of diseases of the myocardium associated with mechanical and/or

electrical dysfunction that usually (but not invariably) exhibit inappropriate ventricular hypertrophy or dilatation and are due to a variety of causes that frequently are genetic. Cardiomyopathies either are confined to the heart or are part of generalized systemic disorders, often leading to cardiovascular death or progressive heart failure–related disability’ (69).

9.6.1 Hypertrophic Cardiomyopathy

Donald Teare, in 1957, was probably the first to describe the pathological appearance of HCM in young adults, and its close association with SCD (70). In this paper, Teare described 8 cases of severe asymmetric septal hypertrophy with ‘bizarre and disorganized arrangement of muscle bundles associated with hypertrophy of individual muscle fibres and their nuclei’. In 7 out of the 8 cases these young adults died suddenly. Interestingly, Teare appears to suggest a genetic substrate to this condition by noting in an addendum, that the brother of one of the patients he reported on, also suffered from SCD and another sister was found to have clinical signs of HCM.

The first HCM-associated gene was discovered in 1990 (71) and since then our understanding of the genetic basis of this cardiomyopathy has grown exponentially. HCM affects around 1 in 500 individuals (72) and is defined as unexplained LV hypertrophy associated with non-dilated ventricular cavity in the absence of another cardiac or systemic disease that could produce the magnitude of hypertrophy evident in a given patient (69). The systemic conditions that can account for a degree of hypertrophy include amyloidosis and glycogen storage diseases. The most common differential diagnoses for HCM are hypertensive heart disease and the physiological remodelling in response to exercise (‘athlete’s heart’). For diagnosis of HCM, the traditional maximal ventricular WT cut-off is $\geq 15\text{mm}$. However,

recent guidelines highlight that any degree of WT is compatible with the diagnosis of HCM in the presence of disease causing genetic mutations within a family, the so-called genotype positive/phenotype negative individuals (72). The characteristic phenotypic diversity of HCM is attributable to the variety of disease-causing mutations and to the influence of modifier genes and environmental factors.

HCM is caused by autosomal dominant mutations in genes that encode sarcomere proteins or sarcomere-associated proteins. Mutations in genes encoding β -cardiac myosin heavy chain (MYH7), cardiac myosin-binding protein-C (MYBPC3), cardiac troponin T (TNNT2), cardiac troponin I (TNNI3), essential myosin light chain (MYL3), regulatory myosin light chain (MYL2), α -tropomyosin (TPM1), cardiac actin (ACTC), and titin (TTN) are found in 40-70% of HCM patients (71, 73-75). MYBPC3 and MYH7 mutations are the most frequent genetic causes of HCM.

9.6.2 Dilated Cardiomyopathy

DCM is a leading cause of heart failure and SCD and the most frequent indication for heart transplantation (76). The estimated prevalence of DCM is 1 in 250 (77) , although with recent guidelines recommending family screening and the widespread use of more sensitive diagnostic imaging such as CMR, the prevalence of DCM will certainly rise.

DCM is defined by the European Society of Cardiology as LV dilatation and impaired EF in the absence of abnormal loading conditions, such as hypertension or valve disease, or coronary artery disease (CAD), sufficient to cause the level of systolic impairment observed (78). Impaired systolic function was defined as an EF more than 2 standard deviations below the mean and dilatation as LV end-diastolic diameter of more than 2 standard deviations

above the mean of the predicted after correction for age, gender and body surface area (79, 80). Non-genetic causes of cardiac dilation and impairment include myocardial infarction, toxic insults (e.g. alcohol or certain chemotherapeutic drugs), metabolic imbalances (e.g. hypothyroidism) or infectious agents (e.g. *Trypanosoma cruzi* or HIV).

DCM has a strong genetic basis exhibiting variable penetrance and expressivity, and mainly autosomal dominant inheritance, although autosomal recessive, X-linked and mitochondrial inheritance all occur (81, 82). The considerable phenotypic variability displayed by individual mutations points towards the existence of other factors that influence clinical progression and outcome (83). Although these genetic, epigenetic, and environmental modifiers seem to play an important role they are not yet well characterized or understood. This makes the interpretation of protein-altering variation of uncertain significance particularly challenging at the population level.

In recent years, several approaches have expanded our understanding of the genetic basis of DCM, including family-based approaches such as linkage analysis and whole-exome sequencing (WES) (84-86), GWAS in large cohorts (87, 88) and broad gene-panel sequencing (50-90 genes) in DCM patients (89, 90). So far, more than 60 genes have been associated with DCM, including several also linked to other cardiomyopathies (76). These include: sarcomeric proteins (MYH7, TNNT2, TNNI3, TPM1, ACTC, and TTN), calcium cycling proteins (phospholamban and cardiac ryanodine receptor), cardiac ATP-sensitive potassium (KATP) channel, Z-disc proteins (MLP and telethonin), dystrophin-complex proteins (δ -sarcoglycan, β -sarcoglycan, and dystrophin), desmosome proteins (plakoglobin, desmoplakin, and plakophilin-2), lamin, desmin, cypher/ ZASP and metavinculin (18). DCM and heart failure that originate from sarcomere mutations are due to either a deficit of force production or a deficit of force transmission.

Truncating variants in TTN (TTNtv) have been reported to account for approximately 25% of familial and severe DCM (91), while all other DCM genes combined account for ~30% of cases, with individual genes typically contributing <1% (92).

DCM may manifest at any age, in either sex and in any ethnic origin although it is more common in males and in blacks and typically presents in adulthood (93-96).

9.6.2.1 Titin

Titin is the largest protein in the human body and plays a key role in the sarcomere. Each molecule is more than 1µm long and spans half the sarcomere, with the N-terminus embedded in the Z-disk and the C-terminus in the M-line. TTN filaments form a contiguous system within myofibrils and interact with multiple proteins: with α -actinin and telethonin (T-cap) at the Z-disc, with calpain3 and obscurin at the I-band, and with MYBPC3, calmodulin, and calpain3 at the M-line region.

At its N terminus, TTN is essential for myofibril assembly, stabilization and maintenance (97). The elastic I-band region behaves as a bidirectional spring, restoring sarcomeres to their resting length after systole and limiting their stretch in early diastole (98). The inextensible, thick filament binding A-band region is thought to be critical for biomechanical sensing and signalling. The M-band contains a kinase that may participate in strain-sensitive signalling and affect gene expression and cardiac remodelling in DCM (99).

Several isoforms ranging in size from 5,604 amino acids (novex-3) to 34,350 amino acids (the "canonical" full length sequence) are produced through extensive alternative splicing from the 364 exons of TTN. The major isoforms expressed in the adult myocardium are the long N2BA isoform, which contains the N2A and N2B unique segment, and the short

N2B isoform that contains the N2B unique segment only. Isoform shift toward a higher N2BA/N2B ratio is typically seen in DCM (100).

In our study of more than 5200 healthy and DCM subjects we found that TTNtv occur in ~2% of the general population (9 out of 308 healthy volunteers and in 47 out of 3603 community-based Framingham and Jackson Heart studies' volunteers), in 13% of ambulatory unselected DCM patients (49 out of 374), and in 20% of end-stage DCM patients (34 out of 155) (101). Nonsense, frameshift, and canonical splice site TTNtv, particularly those that truncate both principal isoforms of TTN and/or reside towards the C terminus (**Figure 9.3**), cause DCM with severely impaired LV function and life-threatening ventricular arrhythmias. TTNtv in the asymptomatic control subjects were more likely to affect minor TTN isoforms as compared with DCM cases, including novex-3, a low-abundance isoform that does not span the cardiac sarcomere.

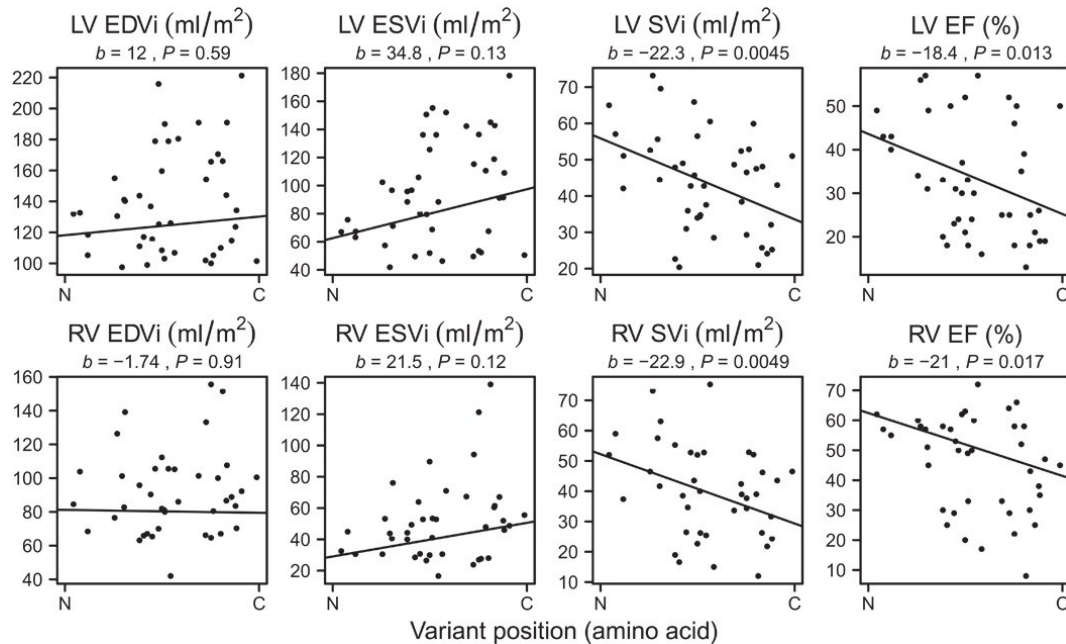


Figure 9.3 – The impact of TTNtv position on cardiac morphology and function. The relationships between TTNtv location and cardiac morphology and function assessed by CMR imaging in 43 unselected DCM patients with TTNtv. The TTNtv location (x axis) is plotted from the amino (N) to the carboxyl (C) end of the protein. Distal (C-terminal located in the M-band) TTNtv were associated with worse cardiac contractile performance,

specifically diminished indexed stroke volume and EF of both LV and RV as compared to proximal truncations. A regression line is shown for each variable. EDVi = indexed end-diastolic volume; ESVi = indexed end-systolic volume; SVi = indexed stroke volume, EF = ejection fraction. (Adapted from Roberts AM, et al. Integrated allelic, transcriptional, and phenomic dissection of the cardiac effects of titin truncations in health and disease. Science translational medicine. 2015)

Despite these advances in characterising the role of TTNtv in heart failure and DCM, relatively little is known about its expressivity and penetrance in populations without known disease. **Table 1** summarises the cardiac magnetic resonance derived LV parameters from a subgroup of the longitudinal, community-based, Framingham Heart Study cohort subdivided by the presence of TTNtv.

	TTNtv Negative (n=807)	TTNtv Positive (n=12)	P-value
LVEDV / BSA (ml/m ²)	66 ± 13	65 ± 16	0.35
LVESV / BSA (ml/m ²)	22 ± 8.4	21 ± 10.9	0.27
LVSF / BSA (ml/m ²)	44 ± 7.4	44 ± 9.0	0.56
LVEF (%)	67 ± 6.9	68 ± 9.8	0.2
LVSWT (mm)	7.9 ± 1.4	8.3 ± 1.4	0.39
LVIWT (mm)	6.8 ± 1.3	7.0 ± 1.2	0.65
LVM / BSA (g/m ²)	55 ± 12	56 ± 11	0.82

Table 1 – Framingham Heart Study CMR phenotype grouped by TTNtv presence. BSA = body surface area; LVEDV = left ventricular end diastolic volume; LVESV = left ventricular end systolic volume; LVEF = left ventricular ejection fraction; LVSF = Left ventricular septal wall thickness; LVIWT = Left ventricular inferior wall thickness; LVM = left ventricular mass. (Adapted from Roberts AM, et al. Integrated allelic, transcriptional, and phenomic dissection of the cardiac effects of titin truncations in health and disease. Science translational medicine. 2015)

9.7 Genetics, genotyping and sequencing

Although Gregor Mendel is considered the ‘father of genetics’ through his work on the patterns of inheritance of ‘units of information’ (or genes as they eventually became known) in plants 1865, it was Friederich Miescher in 1868/9 that first identified nucleic acids (102). In 1944, Oswald Avery, Colin MacLeod and Maclyn McCarty demonstrated that deoxyribonucleic acid (DNA), and not proteins, as was previously thought, serves the purpose of carrying genetic information (103). In 1953 James Watson and Francis Crick proposed the double-helix model of DNA structure (104) based on experimental data from Rosalind Franklin and Maurice Wilkins. Crick, Watson and Wilkins were awarded the 1962 Nobel Prize in Physiology or Medicine for what is regarded as one of the most significant scientific discoveries of the 20th century. Sequencing of the complete human genome started in 1990 and a working draft was completed and published in 2001 at a cost of US\$3billion (5).

The human genome is at the same time an extremely simple and phenomenally complex macromolecule. It is simple, in that it is formed by only 4 repeating nucleotides: adenine (A), cytosine (C), guanine (G) and thymine (T). It is complex because the single DNA molecule is 2 meters long and comprises roughly 3200000000 nucleotides, arranged in a seemingly random order, forming a three dimensional structure. The DNA molecule is formed by two polynucleotide strands winding around a helix axis in a right-handed spiral. The two polynucleotide chains run in opposite directions and are held together by weak thermodynamic forces: adenine forms 2 hydrogen bonds with thymine on the opposite strand while guanine forms 3 hydrogen bonds with cytosine on the opposite strand. Nucleotides are composed of a five-carbon sugar to which, one or more phosphate groups and a nitrogen-

containing base, are attached. The nucleotides are covalently linked together in a chain through alternating sugars and phosphates. The polarity in a DNA chain is indicated by referring to one end as the 3' end (hydroxyl) and the other as the 5' end (phosphate). In protein-coding regions of the genome, each set of 3 nucleotides (a codon) corresponds to a specific amino acid used in protein synthesis. A mutation refers to a change in an individual's DNA sequence that may affect the product of a gene. Single nucleotide polymorphisms (SNPs) are base-pair differences in the DNA of individuals within a population (variability for a certain allele).

Although it was thought that only 1-1.5% of the human genome had a functional activity (105) this topic has been intensely debated in recent years (106). The Encyclopedia of DNA Elements (ENCODE) project concluded that many sections of DNA have biochemical functions beyond protein encoding. In the 93% of the genomic bases they studied around 80.4% participate in at least one biochemical RNA and/or chromatin associated event in at least one cell type (107).

The definition of gene, as the basic unit of heredity, has been a controversial matter in recent years. A widely accepted version is from the Sequence Ontology Consortium that describes a gene as a 'locatable region of genomic sequence, corresponding to a unit of inheritance, which is associated with regulatory regions, transcribed regions and/or other functional sequence regions'(108). A recent definition proposes a gene to stand for 'a union of genomic sequences encoding a coherent set of potentially overlapping functional products' (109).

Several approaches have been employed to better understand the genetic determinants of human health and common and rare diseases. Common cardiovascular diseases and cardiac phenotypes in general are highly heritable (26, 110, 111). The genetic risk of developing a common cardiac disease is thought to be mostly determined by several common loci (defined

as alleles with a population frequency of ≥ 0.05) (112). Individually these loci cause negligible effects on the phenotype on an individual (113), but when acting in concert their contribution to a given complex trait can be more substantial (114). This is known as the ‘common disease – common variant’ hypothesis. This hypothesis supports the role of genomic research that aims to study all the genes and their cumulative and interactive effects on the organism. In GWAS subjects are genotyped for hundreds of thousands of common variants in an attempt to identify single nucleotide polymorphisms (SNPs) associated with cardiovascular phenotypes. However, common alleles identified so far in GWAS of common conditions such as hypertension and hyperlipidaemia, have only accounted for a small proportion of phenotypic variance – as little as 2% in total in some instances (115, 116). The ‘missing heritability’ might be due to underpowered phenotyping or genotyping. Another possibility is that there might be rare (with minor allele frequency ≤ 0.01), very rare or indeed private variants that cause large phenotypic changes (‘rare variant-common disease’ hypothesis) (117). Furthermore it is possible that several rare variants might collectively cause a significant phenotypic effect.

At the other end of the disease prevalence spectrum, we have those rare conditions that are caused by extremely rare, or indeed private, variants in one or a few genes leading to large phenotypic effects (118). These conditions support the ‘rare disease – rare variant’ hypothesis that has historically been behind candidate gene and linkage studies.

9.7.1 DNA Sequencing Strategies

9.7.1.1 Sanger Sequencing

Since the late 1970's, DNA sequencing has been dominated by an approach first proposed by Frederick Sanger (119, 120). Sanger sequencing, also referred to as chain-termination sequencing or dideoxy sequencing, is based on the use of dideoxynucleotides (ddNTPs) in addition to the normal nucleotides (deoxynucleotides, dNTPs) required for DNA synthesis. When compared to dNTPs, ddNTPs lack the hydroxyl group (OH) at the 3' end. DNA polymerases copy single-stranded DNA templates by adding dNTPs to the 3' end of a primer. dNTPs added are selected by base-pair matching to the template. However, when DNA polymerases incorporate the ddNTPs, chain elongation is selectively terminated at A, C, G, or T. This occurs because a phosphodiester bond cannot form between the ddNTP and the next incoming dNTP, therefore terminating the DNA chain elongation. For high throughput Sanger sequencing, DNA segments need to be copied (or amplified) many times. Each of the four ddNTPs is labelled with a different fluorescent dye which makes automated identification possible. After many iterations of this process all the potential chain-termination molecules are produced. The result is that copies of varying length are generated. By analysing the end nucleotide from all the DNA fragments, the original DNA sequence is discovered. Presently, instead of running a gel and manually reading it, DNA sequencers carry out capillary gel electrophoresis for size separation, detection and recording of dye fluorescence at each position (121). The Sanger method remains the gold standard for sequencing accuracy.

9.7.1.2 Next Generation Sequencing

Since being introduced in 2005 (122), next generation sequencing (NGS) platforms that allow massively parallel DNA sequencing have revolutionised genomic research (123). The phenomenal reduction in costs and sequencing time when compared to the traditional Sanger approach have provided unprecedented opportunities for high-throughput functional genomic research including whole genome sequencing (WGS) and targeted resequencing. While modern high-throughput Sanger sequencing machines, such as the ones used to sequence the first human genome, read around 2 million bases of sequence per day (124, 125), NGS platforms can sequence up to ~50 billion bases per day (126).

NGS sequencing has been dominated by three platforms: Illumina (Genome Analyser and HiSeq), Applied Biosystems (SOLiD) and Roche (454). Each platform uses a different approach to DNA sequencing and the technique varies if you are aiming to carry out WGS or targeting a certain subset of the genome. If targeting a subgenomic section two main methods are used for DNA enrichment: polymerase chain reaction (PCR) enrichment and hybridisation enrichment. In PCR enrichment, primer pairs are designed to bind to DNA areas either side of the target region. These target regions are then amplified by PCR and pooled to form a library ready for NGS sequencing. In hybridisation enrichment, the DNA is first fragmented and then hybridised to baits that are complementary to the regions of interest. The fragments of DNA attached to the baits are kept and all others are washed out. After selection of the regions of the DNA to be sequenced, these sections are attached to platform specific ‘adaptors’ that provide the sequencing start point. The DNA fragments are then either attached to a bead, which eventually is immobilised on a sequencing slide, or alternatively attached directly to a sequencing slide from the start. These segments are then clonally amplified via PCR, creating a spot with many copies of the same read. They are then separated into single strands to be sequenced. In the Illumina platform, DNA polymerases

and fluorescently labelled nucleotides (with a given colour corresponding to a specific nucleotide) are then added and DNA synthesis resumed. Each time a base is added, an image of the slide is taken, recording the fluorescent signal at each read location. The fluorophore 'label' is then cleaved from the recently added nucleotide and the process repeated. The DNA sequence is read by decoding the sequence of fluorophores imaged at each physical position on the sequencing slide. These sequence fragments are computationally aligned with a reference sequence and mismatches identified (126).

Current NGS systems have a typical accuracy rate of over 99.9%. However, to confirm variant calls it is essential either to perform a Sanger sequencing validation, or repeat the deep sequencing method while accepting only those variants that are reproduced.

According to the National Human Genome Research Institute (127), the cost of sequencing a single human genome, using the automated Sanger approaches available in 2001 was US\$1000000000 while by mid-2014 it had fallen to around US\$5000 using NGS methods. With the cost of a multi-gene targeted-sequencing panel estimated to be around US\$2000-10000 it is not surprising that many research and clinical institutions are considering moving towards routine WGS (128).

9.7.2 Study designs used in genetic studies

9.7.2.1 Candidate genes studies

These studies are based on previous knowledge of disease pathology and of the role of a single gene, or relatively small number of genes, in causing a defined phenotype. These genes are then sequenced in well characterised cohorts leading to the identification of variants

present in the disease group and not in controls (129-131). As an example, it was this type of approach that led to the discovery of the alleles that influence the response to clopidogrel (CYP2C19) (132) and identification of the causative action of TTNtv in DCM (101).

9.7.2.2 Linkage studies

Linkage studies rely on linkage disequilibrium, recombination frequencies and genetic maps (133). Loci that are close together on the same chromosome segregate together much more often than do loci on different chromosomes. Indeed the further apart they are the more likely that, during meiosis, recombination occurs between them. The probability of recombination of two loci at meiosis is described as the recombination frequency (134). Two loci are in linkage disequilibrium if, across a given population they are found together on the same haplotype more often than expected. For linkage studies, pre-defined markers, regularly spaced across the genome (linkage maps) are genotyped and their segregation through pedigrees studied. The classic approach for Mendelian diseases looks for co-segregation of a disease phenotype with these genetic marker, indicating that such a marker is linked to a nearby disease allele (129). Once a candidate region is identified, it can be sequenced to identify the causative variant.

9.7.2.3 Genome Wide Association Studies

GWAS have been mostly used to identify common variants responsible for common complex traits (135-137). Using commercially available chips (e.g. Illumina HumanOmniExpress BeadChip) large scale case-control studies are carried out where many hundreds of thousands of SNPs are genotyped. Given the large number of subjects usually required, this approach has only been applied to ICCs in a couple of studies (87, 138). The power of a GWAS to

detect SNPs significantly associated to given phenotypes is directly related to the sample size, detectable phenotypic effect size and mean allele frequency (MAF). One of the major strengths of this approach is that it is unbiased by previous knowledge and can identify completely novel genes or biological pathways involved in the trait under investigation. A significant limitation of these studies is the lack of statistical power to detect significant associations, given the need for multiple testing corrections (139). However recent progress in statistical analysis has enabled us to progress from the traditional ultra-conservative Bonferroni correction for multiple testing. Using this method the level of significance (α) is divided by the number of tests being carried out (n) to identify the family wise level of significance: $p = \alpha / n$. Using this approach all tests are considered independent which is known not to be the case in the genome. Computational intensive permutation testing and approaches that leverage Bayesian methods have shown great promise in enhancing the power of GWAS (140, 141). SNPs identified in GWAS invariably need replication in other populations or experimental validation.

9.7.2.4 Whole genome / whole exome sequencing

WGS and whole exome sequencing (WES) have only become feasible approaches to identify single gene and multigene disorders since the advent of NGS. They combine the benefits of candidate gene studies in detecting known and novel variants in a certain sequence of DNA, with the unbiased nature of GWAS. Bioinformatics capacity to handle and interpret the huge amount of data generated is one of the main drawbacks of these approaches. In WGS all SNPs, coding or noncoding, are sequenced independently of the target capture technology used. Given that only <2% of the human genome is protein-coding, WES is an attractive alternative which significantly reduces the bioinformatics requirements and the burden of multiple testing. In WES only the exons in the genome are captured, enriched and

sequenced. WES is dependent on the efficiency of capture of each exon and it has been reported that up to 20% of exons might not be robustly sequenced (113). A recent study found that although WGS might be slightly better at detecting variants than WES (3% coding variants not detected by WES) the sequencing and bioinformatics cost does not, for now, justify the widespread utilisation of WGS (142).

9.8 Cardiovascular Magnetic Resonance

9.8.1 History, principles and techniques of Magnetic Resonance Imaging

Cardiovascular magnetic resonance has evolved in the last few decades into a sophisticated and robust method for studying the cardiovascular system, in research and clinical practice. It builds however on over a century of scientific achievements in mathematics, physics, chemistry and medicine. This imaging modality represents, like few others, the power of collaborative and iterative work by scientists from diverse backgrounds and disciplines. So far, six Nobel Prizes have been awarded for breakthroughs related to the technique.

In the early 20th century, advances in spectroscopy led to the finding that the wavelength of visible light splits into two wavelengths when a substance is placed in a magnetic field. It was Wolfgang Pauli who first recognised, in 1924, that the splitting of the wavelength was caused by magnetic interactions between subatomic particles and that these interactions could be altered by an external magnetic field (143). During his career, Pauli postulated that atomic nuclei have two quantum mechanical properties: spin and magnetic moment. In nuclei with an odd number of nucleons, such as ^1H or ^{31}P , the spin will be non-zero and there is a magnetic moment (μ). Modern magnetic resonance imaging (MRI) relies mostly on the spin and small magnetic moment of the single proton in the hydrogen nucleus. Hydrogen is used because it is abundant in human tissue, water (H_2O) and lipid (CH_2) molecules.

In 1933, Otto Stern and Walther Gerlach were able to measure the effect of the nuclear spin by deflection of a beam of hydrogen molecules through an inhomogeneous magnetic field. For this breakthrough Stern was awarded the 1943 Nobel Prize in physics. In 1937, Isidor Rabi, a former student of Stern, further developed the molecular beam method for measuring

nuclear magnetic moments and succeeded in detecting and measuring single states of rotation of atoms and molecules. He coined the term Nuclear Magnetic Resonance (NMR) and was awarded the Nobel Prize in physics of 1944. In 1946, Felix Bloch and Edward Purcell, working independently, found that when nuclei were placed in a magnetic field they could absorb radiofrequency (RF) energy at a characteristic frequency, and re-emitted this energy when the nuclei returned to their original state (144). Both men were the Nobel laureates in physics in 1952.

Through the pioneer work of these remarkable scientists, we know that when spins are placed in a magnetic field they precess around the direction of the field. They do not align with or against the direction of the field at first; they simply start precessing at whatever angle to the field they happen to be in. All nuclear magnetic moments cancel out because they point in any and all directions in the three dimensional space (an isotropic distribution). However, in the presence of a strong magnetic field (B_0) spins exhibit a tendency to align either towards or against with B_0 . In the case of hydrogen, a small excess of spins aligns with B_0 giving rise to a net magnetic field normally represented as M_0 . The greater the strength of B_0 the larger this net magnetisation will be (145). At any instant the magnetisation can be split into two components, M_z and M_{xy} . The rotating M_{xy} component generates the detectable signal. At equilibrium, the spins precess around B_0 at the resonant frequency of ω_0 but with a random phase, giving a net transverse magnetisation $M_{xy}=0$ (i.e. no signal).

Another significant development came in 1950, when Erwin Hahn introduced pulsed nuclear magnetic resonance. By this method, a sample is exposed to a pulse of RF utilising a wide range of frequencies. When an RF pulse is applied, M_0 stops being completely aligned with B_0 along the z-axis and makes an angle, known as the flip angle. The maximum detectable signal amplitude after a single RF pulse occurs when M_0 lies entirely in the plane of the X and Y axes as this gives the largest M_{xy} component. This pulse has a 90° flip angle and is

referred to as a 90° RF pulse (146). The precessing net magnetisation generates an oscillating magnetic field which can be measured in appropriately placed signal detection equipment. The amount of time that exists between successive pulse sequences applied to the same slice is called repetition time (TR).

Joseph Larmor (1857-1942) is better known in the field of NMR by the frequency and equations that bear his name. The Larmor or precessional frequency refers to the rate of precession of the nuclear magnetic moment (ω) of the proton around the external magnetic field. This precessional frequency is directly proportional to the product of the magnetic field strength (B_0) and the gyromagnetic ratio (γ) (147): $\omega_0 = \gamma B_0$. The unit of the magnetic field is in tesla (T) while the gyromagnetic ratio is constant for each specific nucleus. For hydrogen, γ is $42.576 \text{ MHz T}^{-1}$. The Larmor equation is instrumental to MRI as it is the frequency of precession that determines the frequency at which the nucleus absorbs energy in a given magnetic field.

After excitation, the spins gradually return to their resting state, resulting in an increase in M_z and a gradual decrease in M_{xy} . The rate at which the spins return to their equilibrium (M_0 parallel with B_0) is described by the constant T_1 . A long T_1 means there is a slow recovery, whereas a fast recovery is described a short T_1 . The gradual disappearance of M_{xy} due to spin-spin interaction is described by the time constant T_2 . T_1 is always longer than T_2 . Measurement of T_1 and T_2 relaxation in itself, is not enough to generate an image as it is not possible to determine where those signals are arising from in the imaged object.

In 1973, Paul Lauterbur and Peter Mansfield, independently established the principles of NMR tomographic imaging and laid the foundations for MRI (148, 149). They described the use of magnetic field gradients for spatial localisation of NMR signals allowing the creation of 2D NMR images. Lauterbur created a 2D image by applying gradients at different angles

to produce 1D-projections. He then used a back-projection reconstruction technique to combine these projections into images. Mansfield devised a method to selectively excite a single slice using gradients which identify where to collect the signal from a 3D object.

In MR, the static field (B_0) is always present but gradients are not. When a gradient is applied, the magnetic field, and therefore also the precessional frequency of the spins, changes. In pulsed sequences, an RF pulse, with a limited bandwidth of frequencies, will excite only the spins with the corresponding resonant frequencies. At the same time a slice-selective gradient is applied which results in only spins within a given slice to be excited (slice encoding). This gradient can be in any XYZ direction or indeed in a combination of those. This enables the creation of slices in any anatomical alignment (sagittal, coronal, transverse, oblique, etc). A second magnetic field gradient, known as phase encoding, is then applied, orthogonal to the slice encoding gradient. This causes the protons to precess at different frequencies according to their relative position along the gradient. Where the gradient increases the magnetic field, the protons acquire a higher frequency, while where the gradient decreases the magnetic field, the protons acquire a lower frequency of precession. Phase encoding is applied for a brief period before the readout and the strength of the gradient is changed incrementally between each RF pulse. When the gradient is switched off, the protons will have changed their relative phase by an amount depending on their position along the gradient. By changing the phase encoding gradient for each RF pulse a full two-dimensional matrix of data values can be obtained. A third and final gradient is then applied at a right angle to the previous gradients which causes the resonant frequencies of the spins to vary spatially (frequency encoding). The position of a given spin is now proportional to its frequency and the measured signal consists of the sum of magnetic moments with different frequencies.

Another pivotal development in MRI occurred in 1966, when Richard Ernst and Weston Anderson introduced the Fourier transformation to NMR spectroscopy (150, 151). Joseph Fourier, in 1822, had developed a general mathematical transformation method for analysis of heat transfer between solid bodies (144). Applied to NMR, the Fourier transform enables the separation of the frequencies which contribute to the signal emitted from the image slice. It also enables the measurement of the amplitude of those waves, which correspond to the signal intensity levels in an image. This mathematical method allows for rapid processing of the phase and frequency signals and the efficient utilisation of the information for image reconstruction. This was a much faster alternative to the back-projection technique. Due to the common mathematical use of the parameter 'K' in Fourier calculations, the raw data space is called the k-space (152). In 1991 Richard Ernest was awarded the Nobel Prize in chemistry, for his work on the Fourier Transform and subsequent development of multi-dimensional NMR techniques (151).

K-space has a central role in MRI (153). MRI scanners collect data on the spatial frequencies of the imaged object. They are stored in a regular grid of values forming a data matrix known as k-space. A two-dimensional Fourier transform of this matrix produces the required image of the object within the slice. Each line point in k-space represents a single spatial frequency's contribution across the whole image. Similarly, every MR voxel signal intensity is influenced by every spatial frequency in k-space. The low spatial frequency information (signal from the object and contrast information) is at the centre of k-space. High spatial frequencies (edges of the object and resolution information) are in the periphery of k-space. The number of points in k-space corresponds to the number of voxels in the image. The voxel size in the image is determined by the dimensions of k-space. Finally, the field of view (FOV) of the image is inversely related to the spacing between data points in k-space.

During image acquisition each voxel will contain a mixture of signal and noise. The MR signal is the electrical voltage induced in the receiver coil by the precession of the transverse component of the net magnetization (M_{xy}) around the longitudinal axis. The noise is due to unwanted random electrical fluctuations from other sources. These exist in all conducting materials, including MR receiver coils and human tissue. The signal to noise ratio (SNR) is calculated via: $SNR = \text{signal} / \text{noise}$.

SNR increases with voxel volume and the number of signal samples (proportional to the number of phase encoding steps) but decreases with increasing receiver bandwidth.

Thanks to advances in electronics, computing, signal summation and the development of high-strength superconducting magnets, the scene was finally set for the application of MRI in clinical practice.

One of the first clinical applications of NMR was proposed by Raymond Damadian in 1971. After a series of experiments looking into the relaxation properties of water in bacteria and other organic tissues, he went on to measure the T_1 and T_2 of normal and cancerous cells in rats and humans. He stated that cancer cells had longer relaxation times than healthy cells and proposed NMR as a means of identifying malignancies in humans (154, 155). His team also carried out the first MRI of the human body in 1977 using a scanner with a field strength of 0.05T (156). Given that the homogenous part of the field was very small, the patient's table had to be moved to collect each voxel and it took around 4 hours to collect a single slice.

Lauterbur and Mansfield were jointly awarded the 2003, Nobel Prize in physiology or medicine for their work leading up to MRI. The fact that Damadian was not also included in this award has caused much controversy in the field over the years (157).

From the mid 1970's, the clinical use of MRI was obvious and development occurred rapidly. The prototype of the first commercial scanner (the 'Neptune' 0.15T superconductor system) was installed in 1981 by GE and Oxford Instruments at Hammersmith Hospital in London (158). By 1982 the first commercial MRI scanner, with a field strength of 1.5T, was being marketed by General Electric. According to the NHS England Imaging and Radiodiagnostic activity report 2012/2013, 2.4 million MRI scans took place in England that year. This number represented a 211% rise over a 10 year period.

A modern magnetic resonance scanner is constituted by three components: magnet coils, gradient coils and an integral radiofrequency transmitter coil (**Figure 9.4**). These components create different magnetic fields:

- The magnet coil generates a strong, constant magnetic field
- The gradient coils generate a gradient magnetic field that can be quickly switched on and off
- The RF transmitter coil generates an RF magnetic field that oscillates at a characteristic frequency

When combined together these three components produce spatially encoded signals that are used to form the MR images.

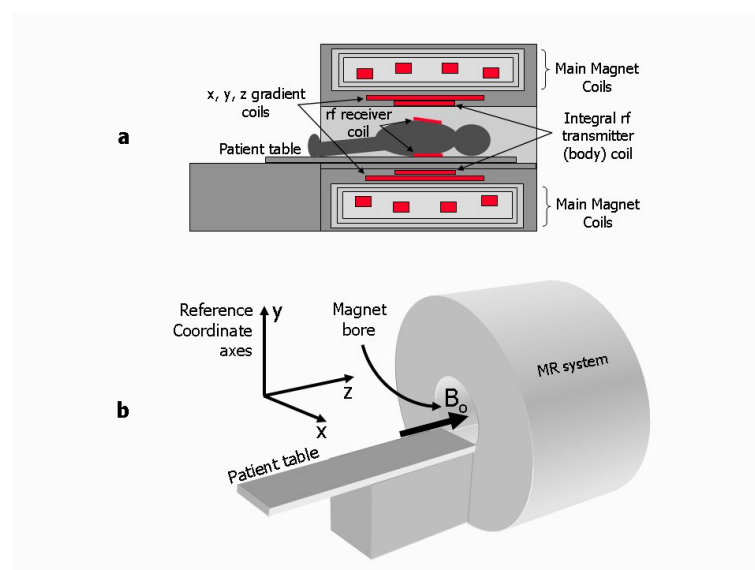


Figure 9.4 – Magnetic Resonance system components. Diagram showing the relative locations of the main magnet coils, x, y, and z gradient coils, integral RF transmitter body

coil and RF receiver coils. b) Typical arrangement for a cylindrical bore MR system showing the magnet bore and the reference coordinate axes with the static B_0 field direction along the horizontal z axis. (Figure from Ridgway JP. Cardiovascular magnetic resonance physics for clinicians: part I. Journal of cardiovascular magnetic resonance. 2010)

9.8.2 Cardiac Magnetic Resonance

Although it is difficult to determine the timing of the first cardiac scan, in 1981, Rob Hawkes and colleagues published a paper dedicated to cardiac NMR (159). They highlighted the issues surrounding respiratory and cardiac motion and went as far as suggesting that the latter could be addressed by an electrocardiogram-linked trigger.

In a 1983 study in canines, Paul Lauterbur's team first described the electrocardiogram-gated CMR (160). Cardiac synchronisation is possible thanks to carbon monitoring electrodes that are attached to the patients' chest wall. There are two types of electrocardiogram (ECG) gating – prospective and retrospective.

In prospectively triggered sequences, software detects the ECG tracing, finds the QRS complex and generates a synchronisation pulse. This initiates the pulse sequence controller so that the pulse sequence is applied at a given time after the R wave. One line of k-space is acquired per each R-R interval. The image acquisition time is proportional to the repetition time (TR) and the number of k-space lines acquired (number of phase encoding steps (N_{PE})): $\text{image acquisition time} = TR \times N_{PE}$. Using this technique, a single image is generated at a single point in the cardiac cycle with the removal of the cardiac motion artefact. High resolution imaging is possible as the image is reconstructed from multiple cardiac cycles. In practice, prospective gating is not performed due to the long periods of time in which no data

is being acquired and because the length of the acquisition cannot be longer than the average R-R interval.

A significantly more efficient approach is to acquire data continuously and then match this to the recorded ECG tracing – retrospective gating (161). During image reconstruction, a retrospective average heart rate is calculated and the image data is mapped onto a pre-determined number of cardiac phases. Using this method all phases are imaged without wasted periods without data acquisition. Artefacts can occur when the differences in the length of the R-R interval are quite significant (e.g. cardiac dysrhythmias). Modern scanners will ignore data when the R–R interval lies outside a predetermined arrhythmia rejection window and continue acquiring phase–encoding steps. This may mean that patients with irregular heart rates have much longer breath–holds to perform. In extreme cases, prospective triggering might be useful in overcoming this challenge.

Respiratory gating can also be used to complement cardiac gating. However, due to the length of the respiratory cycle this method is rarely used. Instead, cardiac acquisitions tend to take place during a period of breath-holding.

There are two main families of sequences used in CMR – spin echo (SE) and gradient echo. Historically, SE was the first sequence to be used and became the benchmark for all subsequent developments, namely in terms of contrast.

In short, SE sequences involve two RF pulses, one at 90° and one at 180° . Echo time (TE) is the time between the 90° RF pulse and the centre of the MR signal sampling window. The sequence starts with a 90° pulse that turns M_0 into M_{xy} . After this pulse, M_{xy} begins to dephase and at around half of the desired TE, a 180° excitation pulse is applied. This pulse rotates the magnetisation by 180° about the axis and results in a rephasing process of the dephased spins. Due to this rephasing process the signal reaches its maximum at TE, the so

called Spin echo. The 180° rephasing pulse compensates for the constant field heterogeneities to obtain an echo that is weighted in T_2 and not in T_2^* (loss of signal strength due to non-homogeneous magnetic field and patient's magnetic susceptibility). The main benefit of the SE sequence is that it is relatively insensitive to magnetic field inhomogeneities and therefore less susceptible to produce artefacts. The major disadvantage is that in order to obtain maximum signal, M_{xy} needs to return to equilibrium before the TR is repeated. If T_1 is long, this can prohibitively lengthen image acquisition. Also, TE needs to be quite long (80 to 140 milliseconds) for improved T_2 contrast. One important issue surrounding SE sequences is the specific absorption rate (SAR) limit (145). When an RF pulse is applied, this energy (measure in watts) is deposited in the patient (per unit of tissue mass). SAR is proportional to the square of B_0 , the square of the flip angle and the duty cycle (percentage of time that a gradient is on). Therefore, SE sequences in which RF pulses are applied to cause flip angles of 90° and 180° are associated with a higher SAR.

Sequences from the gradient-recalled echo (GRE) family represent the majority of those used in CMR due to its speed and versatility. The increased scanning speed is obtained through a reduction in TR (<10 milliseconds). However if the TR is very short there is not enough time for longitudinal recovery and the SNR is severely reduced. GRE pulsed sequences reduce the readout flip angle so that some magnetisation is maintained in M_0 , whilst some is measurable in M_{xy} . In this sequence, a slice-selective gradient is applied to the imaged object while an RF pulse produces a rotation angle that is less than 90° . A low flip angle reduces the T_1 weighting as the overall variation in longitudinal magnetisation is reduced. However, less M_{xy} results in a lower signal. A high flip angle increases T_1 weighting, and if the TR is long enough, increases the signal that is generated. To read the signal, a frequency encoding signal is then applied. Spins will precess at different frequencies along this gradient and the transverse magnetisation will dephase. A second frequency encoding gradient is then applied

which has the same amplitude as the first but a gradient slope in the opposite direction. In practice this second gradient is applied for twice as long as the first so that the spins rephase into a maximum signal amplitude at the centre of the readout gradient (mid TE) and then dephase again generating a symmetrical gradient echo (signal) (146). GRE is limited by a higher susceptibility to magnetic field inhomogeneities.

In practice, the flip angles used in GRE are so small that the TRs are shorter than the relaxation times of blood and myocardium. This means that when the next RF pulse is delivered the signal has not completely dephased. In the early 1980's work was carried out by Rob Hawkes and Bill Moore on a modification of gradient echo imaging that came to be known as steady state free precession (SSFP) (144). SSFP is based on the finding that after several TRs in which an RF pulse is delivered on the altered magnetisation, a steady state of magnetisation is achieved. SSFP was not particularly successful at first due to low image quality when compared with other gradient echo sequences. It was only with the improvements in magnet field homogeneity and fast switching gradients, that SSFP rose to prominence in the last couple of decades (162).

Balanced steady state free precession (b-SSFP) is a special type of SSFP that is currently the mainstay of cine-CMR (163). This sequence is also known as balanced fast field echo (b-FFE), TrueFISP and Fast Imaging Employing Steady-state Acquisition (FIESTA), depending on the manufacturer of the scanner. Due to the low flip angles used in gradient echo it is possible to have such short TR that the transverse magnetisation in the M_{xy} direction has not fully dephased when the next RF pulse is applied. In b-SSFP this remaining magnetisation is maintained using additional rephasing and dephasing gradients.

B-SSFP contrast is related to the tissue's T2/T1 ratio, with fluid and fat in particular appearing brighter than other tissues such as muscle (low T2/T1 ratio). B-SSFP has a high

SNR and the blood inflow enhancement effect, further improves the contrast between blood and the myocardium (**Figure 9.5**) (164). Allied to the fact that it is a relatively fast acquisition, it is well adapted for evaluation of wall motion and volumetric measurement.

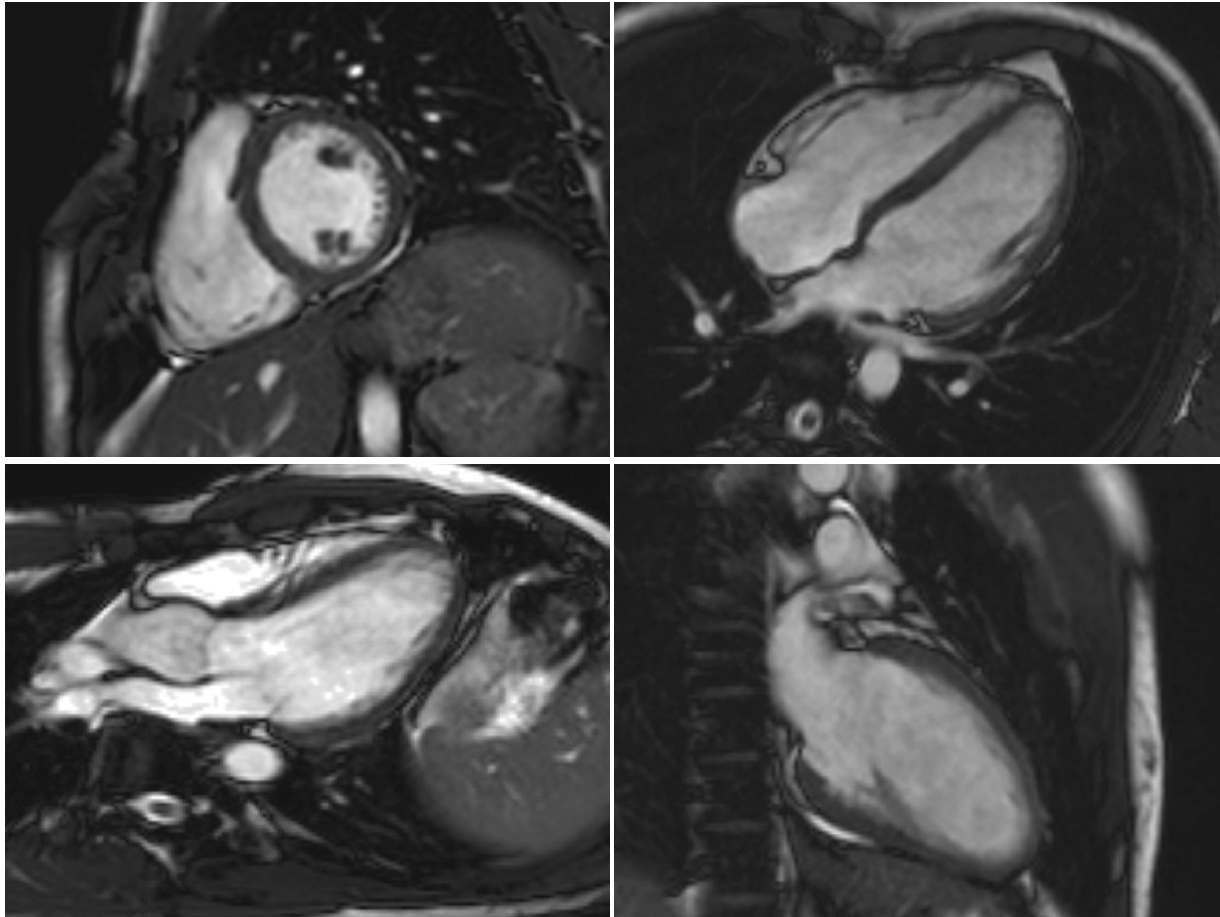


Figure 9.5 – Two-dimensional balanced steady state free precession of the heart. Top left – mid ventricular short axis; top right – 4 chamber view; bottom left – left ventricular outflow; bottom right – left ventricular long axis. $B_0 = 1.5T$, slice thickness = 8mm; spacing between slices = 10 mm; repetition time = 3.0 ms; echo time = 1.5 ms; Flip angle = 60° ; acquired pixel size, 2.0×2.2 mm; reconstructed voxel size, $1.2 \times 1.2 \times 8$ mm; number of sections, 10 – 12; cardiac phases, 30.

SSFP technique is sensitive to areas of magnetic field inhomogeneity as the transverse magnetisation from different excitations can destructively cancel rather than add together in. This makes it prone to dark banding artefacts across the image. This can be addressed by

keeping the TRs short (3-6 ms) or through a patient specific process called dynamic shimming, in which shim coils are used to fine-tune the magnetic field.

Cardiac cine images are short movies that are able to show heart motion in a single slice of the heart, throughout the cardiac cycle. Data are acquired at each phase of the cardiac cycle and assigned a separate k-space. Over several R-R intervals the full k-space is acquired. Cardiac cine imaging requires very short TRs to be used and therefore b-SSFP is used.

Cine-imaging can also be used to quantify flowing blood through a vascular lumen (165). Velocity encoded gradient echo imaging (VENC), also known as phase contrast imaging, uses short-lived bipolar gradients which are equal in magnitude but opposite in direction. In stationary tissues, this results in a net phase of zero near the centre of the echo. However, for moving spins the effects of negative and positive gradients will not exactly cancel each other out and a net phase difference can be detected. This allows each point in the image to be encoded with a phase shift that is directly proportional to the velocity at that point. For analysis three images are necessary: a conventional magnitude image from which the anatomy can be delineated and two phase contrast images acquired at different flow sensitivities (166, 167). Magnetic field inhomogeneities and motion in the non-velocity encoding direction should remain constant for the two acquisitions. Subtraction of the two resulting phase images allows the quantitative assessment of the velocities of the underlying flow or motion (168). To increase the accuracy of measurements from a VENC image, a plane must be selected that is perpendicular to the path of the flowing blood and this is achieved by planning on two orthogonal views (169). The technique creates a velocity encoded image for multiple phases of the heart cycle, thus creating a cine. In the cine produced, stationary tissue appears grey while through-plane flow in the phase-encoding direction appears as white and in the opposite direction as black. The whiter or blacker each voxel is, the faster it is moving. A limitation of VENC arises from the pre-set velocity

encoding parameter (or maximum measurable velocity range). If the actual flow velocity exceeds this value, the image will become aliased in the opposite direction. However, increasing this parameter would result in a loss of sensitivity to slower velocities.

Quantification of blood flow is performed by software that requires the user to outline the vessel of interest for each phase. The software produces time-area, time-velocity and time-flow curves (**Figure 9.6**). This technique is valuable for evaluating valve pathology and flows in the systemic and pulmonary systems. One of the measurable phenotypes using this technique is aortic pulse wave velocity (PWV). PWV is calculated knowing the distance between two points (Δd) and transit time of the velocity wave front between the two sections (Δt): $PWV = \Delta d / \Delta t$. Therefore, if velocity data are measured in the ascending and descending aorta, and the distance between those two sections, inclusive of the aortic arch, is measured then PWV can be calculated (**Figure 9.6**). The temporal resolution of b-SSFP can be further increased by a factor of 2 to 4 by combining it with parallel imaging approaches. These methods make use of coils with different elements (**Figure 9.7**) and considerably enhance the performance of CMR. One of these techniques is known as sensitivity encoding (SENSE) and was first proposed by Klaas Pruessmann in 1999 (171). SENSE enables a significant reduction in imaging time with only a small drop in SNR. When using SENSE, a reference scan is acquired prior to clinical data acquisition to measure coil sensitivity profiles. The full FOV is used but only the central lines of k-space are acquired. As the sensitivity of each separate coil element for a given object is different, this data can be used to reconstruct information without actively having to measure it. Accelerated data acquisition follows in which fewer and more spaced out lines in k-space are acquired. This results in a reduction in the FOV in the image domain. Because k-space is undersampled, an aliased image is produced. Unwrapping of the aliasing is performed in the image-domain (as opposed to on

the k-space data before Fourier transformation) using the sensitivity data from the reference scan to enable the separation of aliased pixels (172).

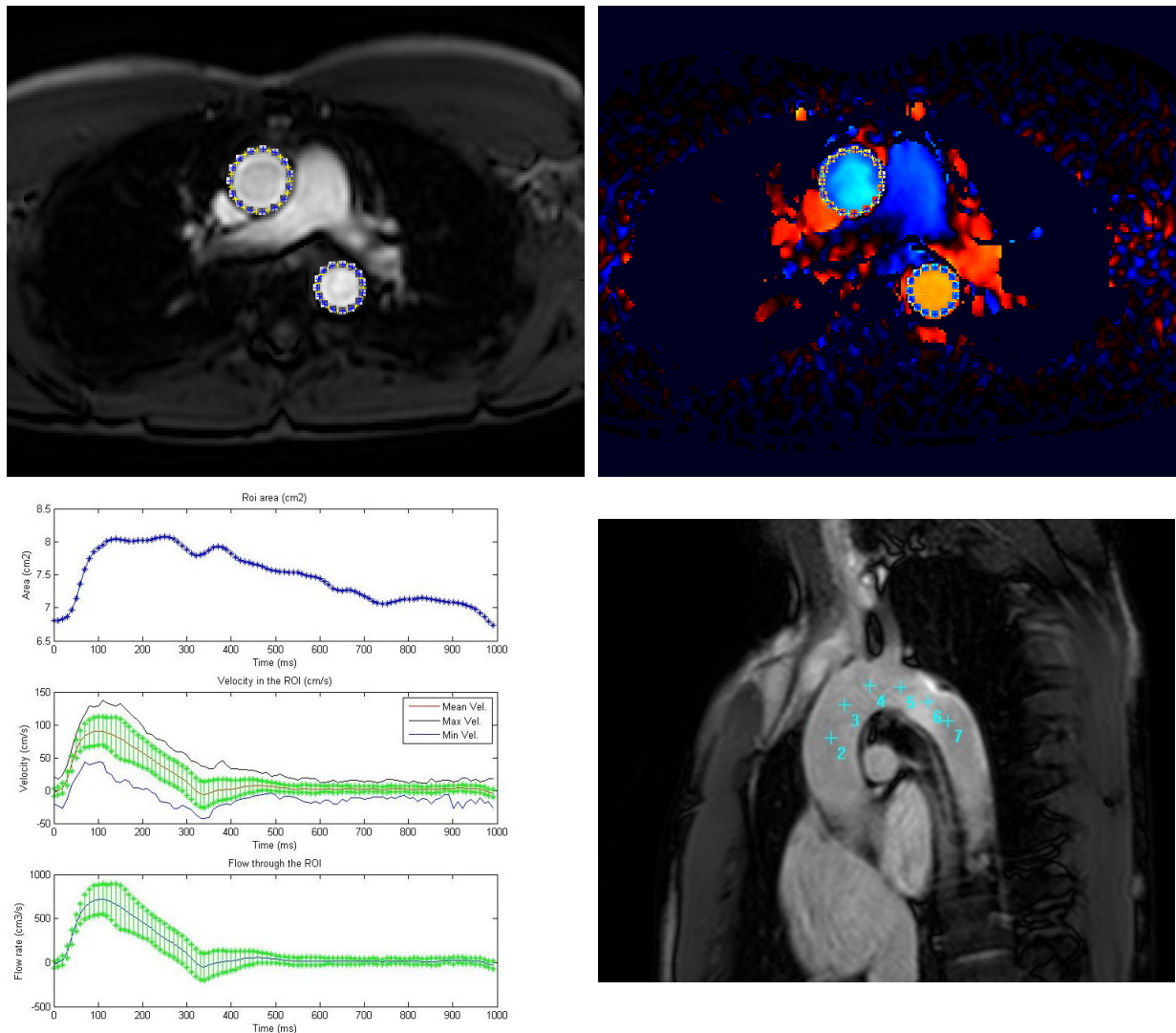


Figure 9.6 – Aortic magnitude and velocity encoded acquisitions and pulse wave velocity measurement. Top left – Magnitude image with the ascending (anterior / top) and descending (posterior / bottom) aorta delineated. Top right – corresponding velocity encoded image. Bottom left – Area, velocity and flow curves in the ascending aorta over a single cardiac cycle. Bottom right - The length of the track along the aortic arch is measured by 3D spline interpolation of points placed along the midline of the aorta on a coronal acquisition (pictured), and the axial image seen in the top left picture. Measurements carried out using ArtFun software (170).

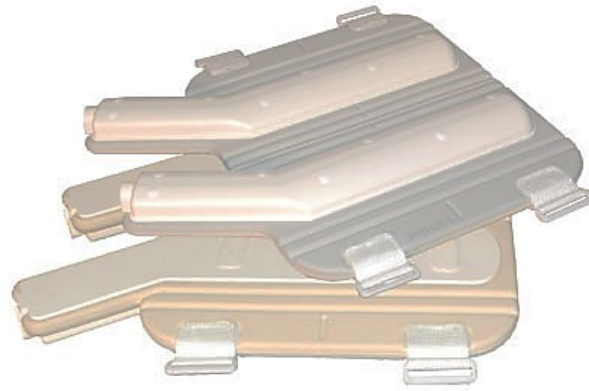


Figure 9.7 – A 32-elements cardiac-coil used to obtain high resolution imaging with high acceleration factors (Philips sensitivity encoding (SENSE) Cardiac coil for Achieva 1.5T). This type of coil enables 3D cine with full left ventricular coverage in a single breath-hold.

Theoretically, the acceleration factor of a parallel-imaging scan is equal to the number of coils used. However, in practice, the degree of acceleration is limited by the change in SNR as calculated by: $\Delta\text{SNR} = 1 / (g\sqrt{R})$. In this context R is the reduction in phase encoding steps (or SENSE factor) and g is the geometry factor which indicates the efficiency of the coil geometry for separating the aliased signals.

Another technique used to reduce scan time is that of half Fourier (or halfscan). Using this approach, slightly more than half of the phase-encoding steps are acquired and the missing data are filled in by the complementary half of k-space. This reduces the scan time by half without affecting the resolution but does result in further SNR reduction (SNR being inversely proportional to the square root of the acceleration factor). This results in the acceleration factor being limited to between 2 and 3. K-space may also be undersampled in the frequency encoding direction (Partial Echo), again benefiting from the fact that k-space halves demonstrate Hermitian symmetry. The shortening in echo time is achieved by only acquiring partial echoes and therefore reducing the readout time.

Conventional CMR has many significant advantages over other forms of cardiac imaging, including the ability to acquire imaging slices in any orientation without moving the patient. However, standard 2D cardiac cine MR images comprise a stack of 8mm sections with 2mm gaps in the LV short axis plane which are acquired over at least five or six breath-holds (173). Variations in the position of the diaphragm with each breath-hold cause shifts in cardiac anatomy, leading to slice misregistration and contributing to analysis error (174). Furthermore, repeated breath-holds can lead to patient fatigue and eventually to poor compliance with breath holding instructions (175). Another limitation of conventional imaging is related to the technical necessity to leave a gap between each acquired slice. In these gaps, tissue is not imaged and therefore localised or regional effects can be missed. This can be addressed by reducing the gaps between slices, although this would cause an unwanted increase in the number of required breath-holds. These challenges can be overcome by using a 3D b-SSFP sequence to acquire, at high-resolution, the whole cardiac volume in a single breath hold.

3D b-SSFP enables the acquisition of very thin slices without gaps. When isotropic resolution is achieved, multiplanar reformatting is also possible, allowing complete freedom to re-slice the 3D volume in any orientation (**Figure 9.8**). This compares with the very blocky appearance that emerges when a 2D image is reformatted in another axis (staircase artefact) (**Figure 9.9**). Until recently, 3D b-SSFP sequences involved long acquisition times and were limited by patients' breath-holding capacity. However, improvements in gradient performance, coil design and parallel imaging sequences have considerably improved image quality and acquisition time, allowing the full sequence to fit into a single breath-hold period (176). 3D b-SSFP, at a comparable spatial resolution to 2D sequences, has been shown to have similar accuracy for manual assessment of LV volumes and mass with favourable scanning times (177-187). 3D suffers however from lower in-plane SNR when compared

with an equivalent 2D b-SSFP sequence as can be seen by comparing **Figure 9.8** with **Figure 9.9**.

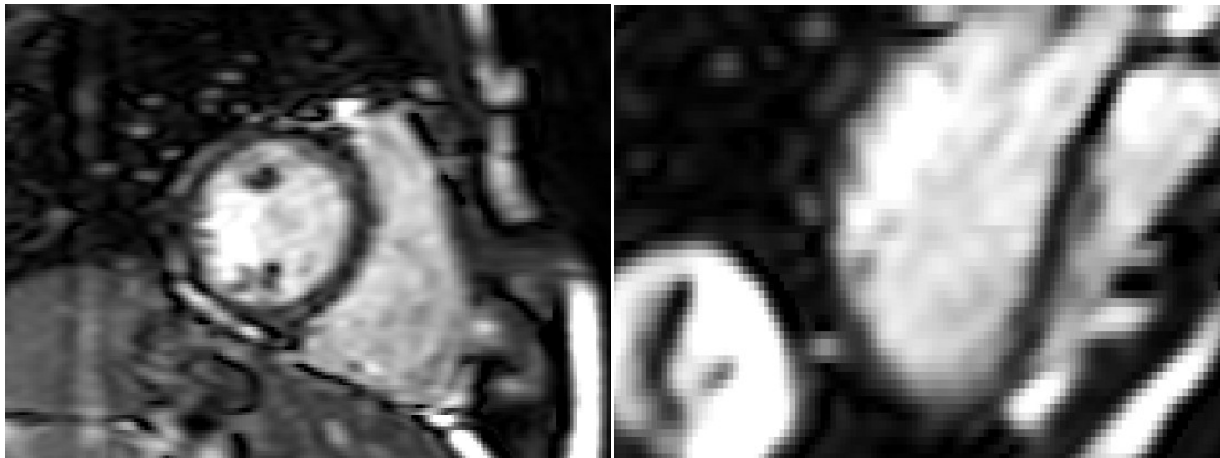


Figure 9.8 – Three-dimensional balanced steady state free precession sequence of the heart. Left – mid ventricular short axis; right – left ventricular long axis reconstruction of short-axis cine; $B_0 = 1.5T$, slice thickness = 2mm, 2 mm overlapping; repetition time = 3.0 ms; echo time = 1.5 ms; Flip angle = 50° ; acquired pixel size, 2.0 x 2.0 mm; reconstructed voxel size, 1.2 x 1.2 x 2mm; number of sections, 50 – 60; cardiac phases, 20; sensitivity encoding (SENSE) factor 2.0 anterior-posterior and 2.0 right-left direction.

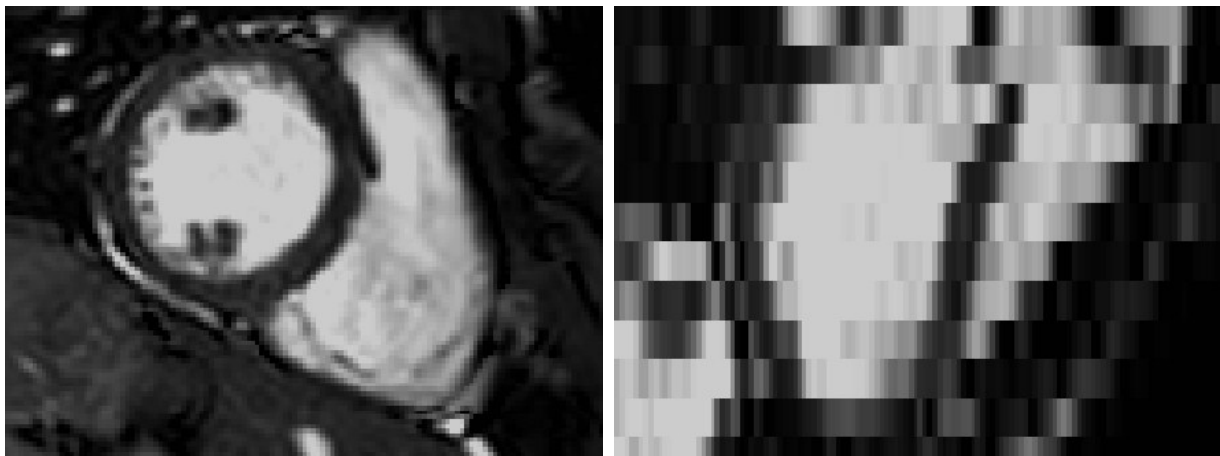


Figure 9.9 – Two-dimensional balanced steady state free precession sequence of the heart. Left – mid ventricular short axis; right – left ventricular long axis reconstruction of short-axis cine. $B_0 = 1.5T$, slice thickness = 8mm; spacing between slices = 10 mm; repetition time = 3.0 ms; echo time = 1.5 ms; Flip angle = 60° ; acquired pixel size, 2.0 x 2.2 mm; reconstructed voxel size, 1.2 x 1.2 x 8mm; number of sections, 10 – 12; cardiac phases, 30.

9.8.3 Cardiac Magnetic Resonance in research

CMR combines excellent spatial and temporal resolution with high contrast between the blood pool and the myocardium and it has established itself as a reliable non-invasive method of assessing cardiac morphology and function. In contrast with echocardiography, CMR is not limited by geometric assumptions in assessing ventricular volumes and image acquisition is less operator-dependent. This allows highly reproducible and accurate measurements to be made of global ventricular function and mass (188-190), making it the ideal modality for assessing differences between small groups (191). The fact that it does not make use of ionising radiation makes it particularly suitable for population and longitudinal studies. Limitations of CMR include claustrophobia, artefacts caused by arrhythmias and motion, metal implants / devices contraindicating CMR and patient's size. CMR is currently considered the 'gold-standard' in cardiac phenotyping and its use in research has increased exponentially in recent years (**Figure 9.10**).

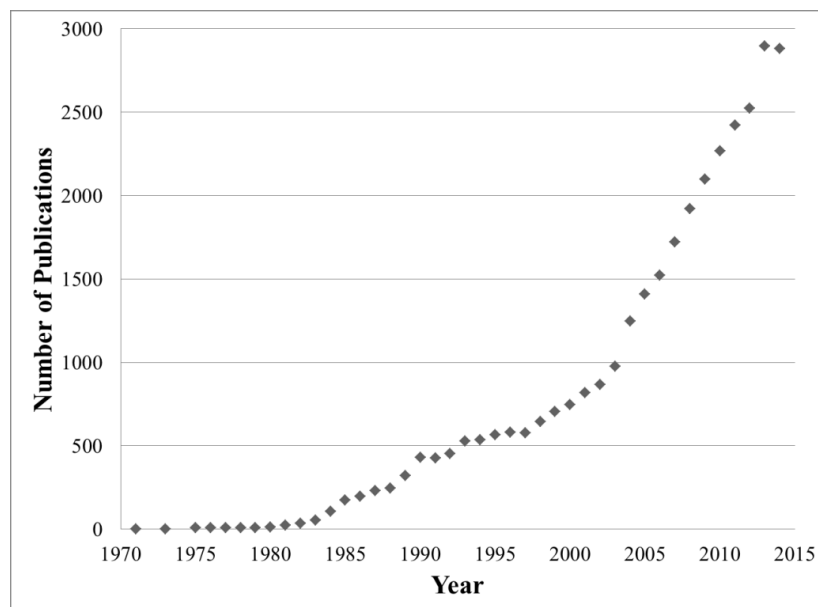


Figure 9.10 – Number of annual publications on cardiac magnetic resonance identified by searching the US National Library of Medicine's PubMed search engine for the terms: NMR and cardiac; NMR and heart; MRI and cardiac; or MRI and heart.

9.8.4 2D-CMR Imaging and Analysis

Standardised Tomographic Imaging and Nomenclature

In accordance with the international guidelines on tomographic imaging (192) a standardised approach to MRI image acquisition and display has been adopted. In CMR, the heart is orientated and displayed using the long axis of the left ventricle. This axis transects the apex of the heart and the centre of the mitral valve plane. Other selected planes are oriented at 90° angles relative to this long axis and are described as short axis, vertical long axis, and horizontal long axis. For analysis the myocardium can be divided into 17-segments (**Figure 9.11**) which are named and localised with reference to both the long axes of the ventricle and the 360° circumferential locations on the short-axis views (193). In relation to their position along the long axis of the heart, segments are described as basal, mid-cavity or apical. To locate the segments in the short axis plane, the basal and mid-cavity slices are divided into 6, 60° sections. The insertion points of the right ventricle onto the left ventricle separate the septum from the LV anterior and inferior wall. The circumferential locations in the basal and mid-cavity are: anterior, anteroseptal, inferoseptal, inferior, inferolateral, and anterolateral. Nearer the apex the LV tapers down so at this level there are only 4 segments: apical anterior, apical septal, apical inferior, and apical lateral. The seventeenth segment is the apex.

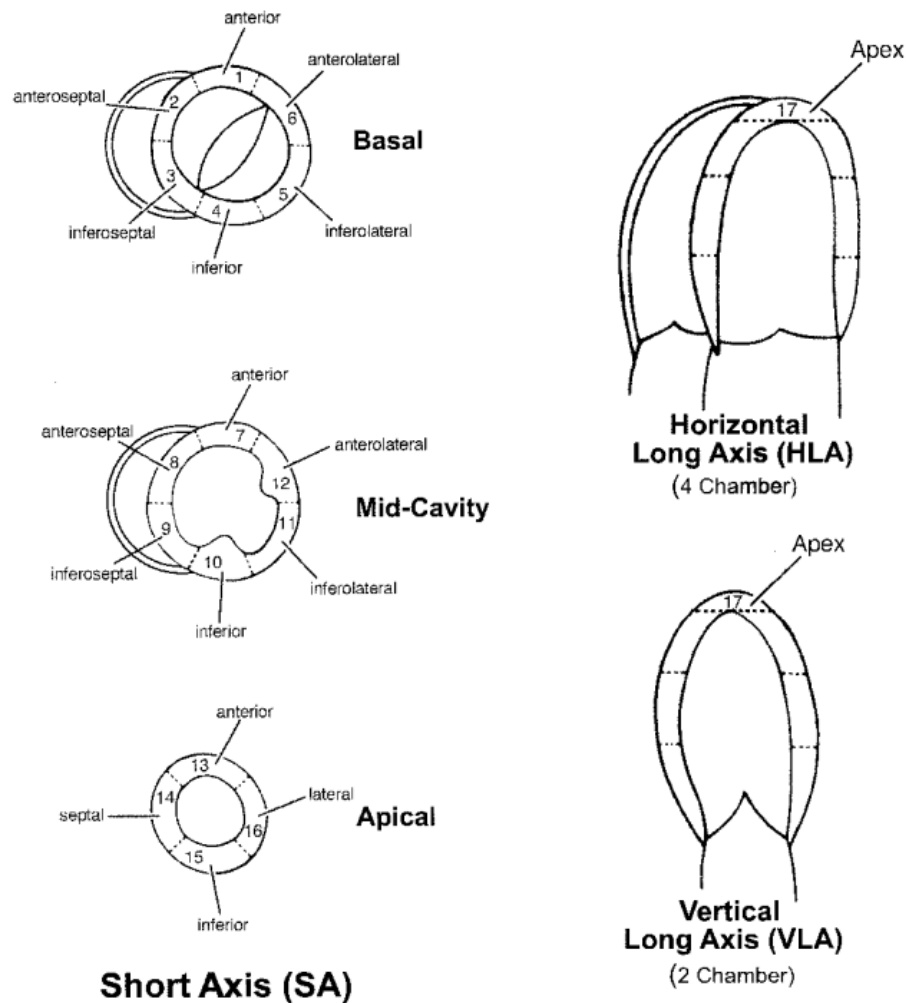


Figure 9.11 – The American Heart Association 17 segment model. Diagram of vertical long-axis, horizontal long-axis, and short-axis (SA) planes showing the name, location, and anatomic landmarks for selection of the basal (tips of the mitral valve leaflets), mid-cavity (papillary muscles), and apical (beyond papillary muscles but before cavity ends) shortaxis slices. (Figure reproduced from Cerqueira MD, et al. Standardized myocardial segmentation and nomenclature for tomographic imaging of the heart. A statement for healthcare professionals from the Cardiac Imaging Committee of the Council on Clinical Cardiology of the American Heart Association. Circulation. 2002).

CMR imaging volumetric analysis

To carry out the volumetric analysis of the heart from a cine image, two frames have to be identified: end-systole and end-diastole. The end-diastolic frame is usually acquired immediately after the R-wave. The end-systolic frame is identified visually as that with the

smallest left and right ventricular cavity. In end-diastole both the epicardial and the endocardial borders need to be delineated. In end-systole only the endocardial border is traced. If only analysing the heart in the short axis plane, care needs to be taken in identifying the basal slice, as this is a potential source of error (194). To increase the accuracy of the measurements, the systolic descent of the mitral valve should be calculated by tracking the valve motion in two long axis cines (195). These data can then be used to correct for the loss of systolic LV volume due to AV ring descent (**Figure 9.12**). The acquisition of contiguous short axis slices allows a volumetric method to be used without the geometric assumptions of the modified Simpson method or other models (196).

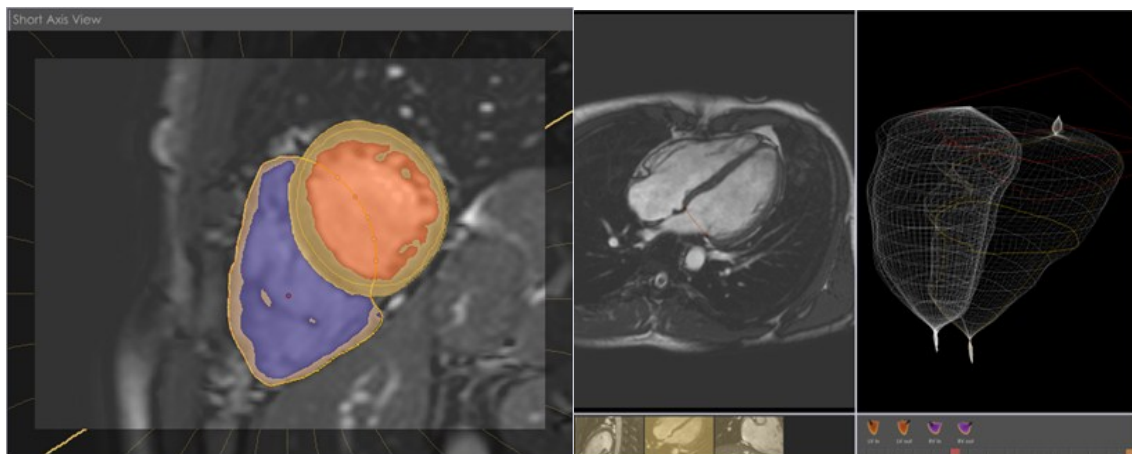


Figure 9.12 – Standard CMR volumetric analysis carried out using CMRtools (Cardiovascular Imaging Solutions, London, UK). Left image - Left ventricular short axis view with manually traced endocardial and epicardial borders. Semi-automated, signal intensity based thresholding technique used to include the papillary muscles in the blood pool. Right image - Mitral valve tracing in a four-chamber view of the heart and corresponding 3 dimensional mesh model.

The inclusion or exclusion of trabeculae may have a significant effect on cardiac volumes and mass (197). Contouring of the endocardial wall, rather than the trabeculae, is a more

reproducible method for manually measuring chamber volumes (198). However, from a physiological viewpoint the trabeculae should be included in the mass measurement and excluded from the cavity volume. The development of semi-automated software for blood pool thresholding (**Figure 9.12**), greatly increased the reproducibility of the delineation of the papillary muscles while enabling gains in the speed of analysis.

For the calculation of the myocardial mass the interventricular septum is included as part of the left ventricle. Myocardial mass is determined by multiplying the tissue volume by 1.05 g/cm^3 (specific density of myocardium).

A technique involving long axis LV base identification, signal threshold-based detailed endocardial contouring, and automated identification of end-systole has higher intra-observer reproducibility than other approaches (195).

To some extent the normal ranges of cardiac volumes are dependent on the CMR sequence used and the post processing software (199-201). The European Society of Cardiology / European Association of Cardiovascular Imaging reference values for adults were published in the *Cardiovascular Magnetic Resonance 2013 Pocket Guide* and can be found in **Table 2** and **Table 3**.

	Males (n=63)		Females (n=45)	
	<35 years (n=31)	≥35 years (n=32)	<35 years (n=23)	≥35 years (n=22)
LVEDV (ml)	173 ± 29 (115 – 231)	149 ± 25 (99 – 199)	137 ± 25 (87 – 187)	128 ± 23 (82 – 174)
LVESV (ml)	57 ± 15 (27 – 87)	43 ± 13 (17 – 69)	43 ± 11 (21 – 65)	40 ± 12 (16 – 64)
LVSV (ml)	118 ± 18 (82 – 154)	106 ± 19 (68 – 144)	96 ± 18 (60 – 132)	89 ± 16 (57 – 121)
LVEF (%)	67 ± 5 (57 – 77)	71 ± 6 (59 – 83)	69 ± 6 (57 – 81)	69 ± 6 (57 – 81)
LVM (g)	131 ± 21 (89 – 173)	120 ± 23 (74 – 166)	92 ± 20 (52 – 132)	92 ± 19 (54 – 130)
LVEDV / BSA (ml/m²)	90 ± 11 (68 – 112)	75 ± 11 (53 – 97)	80 ± 9 (62 – 98)	73 ± 11 (51 – 95)
LVESV / BSA (ml/m²)	30 ± 7 (16 – 44)	22 ± 6 (10 – 34)	25 ± 6 (13 – 37)	23 ± 6 (11 – 35)
LVSV / BSA (ml/m²)	60 ± 8 (44 – 76)	53 ± 8 (37 – 69)	55 ± 6 (43 – 67)	51 ± 8 (35 – 67)
LVM / BSA (g/m²)	67 ± 10 (47 – 87)	60 ± 9 (42 – 78)	53 ± 9 (35 – 71)	52 ± 9 (34 – 70)

Table 2 – Published normal ranges of myocardial mass and function by age and gender. Values are given as mean ± SD; reference ranges in brackets, calculated as ± 2SD of the mean. BSA = body surface area; LVEDV = left ventricular end diastolic volume; LVESV = left ventricular end systolic volume; LVEF = left ventricular ejection fraction; LVM = left ventricular mass. (From Hudsmith LE, et al. Normal human left and right ventricular and left atrial dimensions using steady state free precession magnetic resonance imaging. Journal of cardiovascular magnetic resonance 2005)

	Mean \pm SD (n = 108)	Male (n = 63)	Female (n = 45)
Age (years)	38 \pm 12		
Systolic BP (mmHg)	123 \pm 17		
Diastolic BP (mmHg)	81 \pm 16		
Height (cm)	174 \pm 9		
Weight (kg)	73.4 \pm 12.3		
Body surface area (m ²)	1.88 \pm 0.18		
LVEDV (ml)	150 \pm 31	160 \pm 29 (102 – 218)	135 \pm 26 (83 – 187)
LVESV (ml)	47 \pm 15	50 \pm 16 (18 – 82)	42 \pm 12 (18 – 66)
LVSV (ml)	104 \pm 21	112 \pm 19 (74 – 150)	91 \pm 17 (57 – 125)
LVEF (%)	69 \pm 6	69 \pm 6 (57 – 81)	69 \pm 6 (57 – 81)
LVM (g)	112 \pm 27	123 \pm 21 (81 – 165)	96 \pm 27 (42 – 150)
LVEDV / BSA (ml/m ²)	80 \pm 13	82 \pm 13 (56 – 108)	78 \pm 12 (54 – 102)
LVESV / BSA (ml/m ²)	25 \pm 7	25 \pm 8 (9 – 41)	24 \pm 6 (12 – 36)
LVSV / BSA (ml/m ²)	55 \pm 8	56 \pm 8 (40 – 72)	54 \pm 9 (36 – 72)
LVM / BSA (g/m ²)	59.2 \pm 11	62.5 \pm 9.0 (45 – 81)	54.6 \pm 12 (31 – 79)
Heart Rate (BPM)	65 \pm 10		

Table 3 – Published normal CMR ranges and subject characteristics by gender. Values are given as mean \pm SD; reference ranges in brackets, calculated as \pm 2SD of the mean. BSA = body surface area; BP = blood pressure; LVEDV = left ventricular end diastolic volume; LVESV = left ventricular end systolic volume; LVEF = left ventricular ejection fraction; LVM = left ventricular mass; BPM = beats per minute. (Adapted from Hudsmith LE, et al. Normal human left and right ventricular and left atrial dimensions using steady state free precession magnetic resonance imaging. Journal of cardiovascular magnetic resonance 2005;7:775-82.)

9.8.5 Atlas-Based Segmentation of CMR

Two-dimensional CMR has become the gold-standard for cardiac phenotyping in clinical practice and research. However, a significant limitation of this technique is that it only quantifies global descriptors of LV function and morphology (i.e. ventricular volumes and LVM). It is therefore insensitive to detect regional or asymmetric patterns of change in LV morphology in cohort studies, besides being dependent on visual qualitative assessment to detect subtle deviations from normality in a given individual. This is particularly relevant to large scale genetic studies such as GWAS, where the observable effects of common genetic variants are asymmetric and of small magnitude. Furthermore, in asymptomatic subjects, localised phenotypic changes long precede whole-organ involvement, that is characteristic of advanced disease. In addition, despite having a superior reproducibility when compared to other imaging techniques (188) 2D-CMR still suffers from significant intra- and inter-observer variability (199).

While neuroimaging benefits from automated analysis of high spatial resolution 3D magnetic resonance to detect anatomical variation in brain mapping studies (202-206), the statistical modelling of conventional 2D cardiac cine imaging is constrained by the low spatial resolution of each section and misalignment between breath-holds (207). Despite these limitations, computational approaches to phenotyping have been successfully used in 2D-CMR and potential for epidemiological research in heart disease has been demonstrated (208, 209).

One of the most promising approaches for computational processing of CMR images is through the use of cardiac statistical atlases. These atlases encode anatomical and functional information from a population and provide a spatial framework for the analysis and mapping

of the functional and morphological characteristics of individuals or entire cohorts. These methods enable the alignment of the measured parameters from multiple subjects in a space with a common coordinate system (208). In this way, average physiological and anatomical parameters, and their variability in a population, can be calculated. In addition to the traditional mass and volume analysis, through the use of mathematical modelling, detailed evaluation of regional wall motion and shape characteristics can be carried out. Atlas approaches have been applied to both 2D-CMR (209, 210) and cardiac CT (211). While most studies have included only a small number of subjects, the Cardiac Atlas Project (CAP) makes use of 2D-CMR from over 2500 subjects from the longitudinal Multi-Ethnic Study of Atherosclerosis (MESA) and over 400 patients from the DEfibrillators to REduce Risk by Magnetic Resonance ImagiNg Evaluation (DETERMINE) study (209).

To develop an atlas-based algorithm there is a need for a database of training sets which have to be carefully chosen to avoid bias. This library of images provides the a priori knowledge of the variation in anatomy in a cohort and usually consists of CMR images that have been manually labelled or annotated by experts. This manual annotation is a notoriously laborious, time-consuming undertaking. Although some approaches have been devised for automated atlas creation (212) these are not yet robust enough. In many cases manual landmarks have to be placed at certain anatomical points of a new target image to help define the position of an individual model in the standard coordinate system. Due to the wide anatomical variability most atlas-based approaches use affine transformations (such as scaling, rotation, translation, etc.) during the image processing.

Many different types of atlases have been proposed but commonly they include a template surface mesh, which is used to describe the average shape of the object of interest and a template image, which is the average intensity image from all the subjects aligned to a common space. A probabilistic atlas may also be included, which encodes the anatomical

label information in the template space. Each voxel of the probabilistic atlas stores a vector value, representing the local probability to be a certain structure (e.g. the left ventricle, right ventricle or myocardium) (213). Sometimes, a simple label map is used, which is a manual segmentation of the template image without any probability information (214).

Although many mathematical approaches are used in the processing of atlas data, the statistical shape model (SSM) is the most commonly used method to analyse shape as it provides a robust way in which to define the mean anatomy and its variability. SSM is essentially a point distribution model (PDM), which describes the probability distribution of the vertices of a surface mesh, such as the endocardium or the epicardium. Points which are aligned to match corresponding features in the shape (homologous landmarks) can then be used to derive the variation of cardiac shape using methods such as Principal Component Analysis (215) or Independent Component Analysis (216). More complex approaches include bilinear shape models in which the inter-subject variation and inter-phase variation are encoded separately in two dimensions (211) and a framework for merging multimodality models by spatial normalisation and eigenspace fusion (217).

Atlases have multiple and promising uses in cardiac image analysis. They can provide prior knowledge to guide automated image analysis or segmentation (218), the SSM atlas can provide a common reference space for population-based shape analysis (211) and can be used to generate a personalised patient-specific mesh for biomechanical simulation (219). A four dimensional (space and time) probabilistic atlas was used to describe motion of the myocardium using the variation in shape across a cardiac cycle (215) and a fibre orientation atlas has also been adapted to enable cardiac electromechanical modelling (220). Despite their promise, most of these studies have included very small numbers of subjects in their training sets and their use in health and disease has not yet been demonstrated.

An important step in the automated analysis of CMR images using atlases is the selective labelling of parts of the image based on their different anatomy and location (e.g. myocardium or blood pool). One of the most popular methods of segmentation is based on multi-atlas label fusion (221, 222). The main components of these methods are atlas selection, atlas propagation and label fusion.

In the atlas propagation step, affine or non-rigid registration algorithms are commonly used (223). The registration is frequently based on image intensity similarities and constrained to ensure one-to-one correspondences between the target image and the atlas. This restriction ensures a realistic deformation that preserves the topology of the atlas structures in the target image. However, it also limits the ability of the registration to capture large or local variations in shape. Several solutions have been proposed to relax the method's dependence on accurate registrations including the promising patch-based label fusion methods (224, 225). These approaches compensate registration error by searching for correspondences between the target image and atlas within a limited search window. However, intensity (grey scale) based features, which are often used as patch selection criteria, can have ambiguous matches especially for larger search windows. PatchMatch (226) is a fast algorithm for computing approximate nearest neighbour correspondences between patches of two image regions. However, there is no intrinsic regularisation and the optimal matching patches, in terms of intensity features, may come from different anatomical regions around the heart. A method that could use PatchMatch to search for patch correspondences between the target image and atlases without any restriction of the search window size for the purpose of label fusion, with the robustness of traditional approaches to registration could prove a significant improvement to atlas based segmentation.

Computational, atlas-based quantitative phenotyping of the heart may overcome the issues related to the reproducibility and repeatability of the manual / semi-automated analysis of

2D-CMR. Whole-organ, single-breath hold, high resolution 3D-CMR can encode more anatomical and physiological data than traditional CMR, without being limited by low spatial resolution of each section and misalignment between breath-holds. 3D-CMR coupled with automated analysis techniques might allow the creation of detailed 3D statistical models of the variation in cardiac morphology and function within a population. This could potentially be an efficient, reproducible and highly powered approach for large scale population-studies investigating the environmental, anthropometric and genetic determinants of cardiac morphology and function.

9.9 Phenomics and genomics: towards personalised medicine

After decades of phenomenal developments in DNA sequencing, it is evident that our ability to characterise the cardiac phenotype significantly lags behind our ability to describe the human genotype (227). This mismatch between phenotyping and genotyping is limiting our understanding of the complex genotype-phenotype-environment interactions. In an attempt to overcome the lack of phenotypic power, population-based genetic studies have gradually increased in scale, from a few hundred to several hundreds of thousands of subjects. However, the pursuit of phenomics, an independent discipline dedicated to the development of large scale high-dimensional phenotyping, has been proposed in recent years (227-230). Its supporters believe that a drive to develop comprehensive phenotyping can bring a scientific step change as significant as the Human Genome Project. Initiatives such as the Physiome Project (<http://physiomeproject.org>), the Human Phenotype Ontology project (<http://www.human-phenotype-ontology.org>), the UK Biobank (<http://www.ukbiobank.ac.uk>) or the Cardiac Atlas Project (<https://www.cardiacatlas.org/>) are certainly steps in the right direction.

Along the same lines, in the clinical front, personalised medicine is expected to revolutionise medical practice. Personalised medicine is defined as the tailored approach to patients that offers the most effective therapy to each individual, reduces risks and avoids unnecessary treatments or diagnostic interventions (231). The aim is the integration of molecular markers, genetic variants and structural and functional data to guide an individual's care. Although great progress has been made in genetic diagnosis (e.g. TTN mutations in DCM) and in predicting therapy success (e.g. clopidogrel and genetic variation in the CYP2C19 isozyme), advances in phenotyping have led to less significant breakthroughs in screening, early

diagnosis or assessment of therapy efficacy. The dilemma of genotype positive / phenotype negative cardiomyopathies emphasises the need for detailed, 'deep' phenotypes in assisting clinical decision making (232).

10 Aims of the thesis

1. To determine the feasibility of using 3D-CMR for phenotyping of a large cohort of healthy volunteers
2. To use 3D-CMR to develop a high resolution atlas of the human heart
3. To apply atlas-based computational and quantitative 3D-CMR to examine the population variation in anatomy and physiology and to compare its performance with conventional CMR imaging
4. To use 3D-CMR with computational quantitative analysis to:
 - identify the anthropometric determinants of refined and/or previously unappreciated cardiovascular phenotypes;
 - establish the cardiac effect of rare variants in the titin gene on cardiac form and function in a large healthy population
 - explore the effects of common genetic variations on cardiac form and function in a healthy population

11 Study methods and population characteristics assessed by 2D-CMR

11.1 Introduction

Cardiovascular magnetic resonance imaging (CMR) is the gold standard method for phenotyping cardiac structure and function due to its excellent accuracy and reproducibility (188). In particular, the balanced steady-state free precession (b-SSFP) sequence has been validated in animal models (189) and human cohorts (199, 200). In addition, CMR is free from the geometric assumptions or acoustic window dependencies that greatly limit echocardiographic phenotyping (233). It is a well-tolerated, non-invasive technique without exposure to radiation and with no known side-effects. These characteristics make CMR ideally suited for cardiovascular population-based studies, particularly if longitudinal follow-up is planned. However, even conventional two-dimensional CMR (2D-CMR) is limited by the fact that it incompletely samples the heart and that multiple breath-holds are associated with inter-slice misalignments. Furthermore, 2D-CMR provides limited global metrics and is insensitive to regional or asymmetric changes in left ventricular (LV) morphology. 3D cine sequences have shown promise for imaging the whole heart in a single breath hold (178-187). However, 3D imaging requires a longer breath-hold and whether it is applicable at scale has not been demonstrated.

Left ventricular mass (LVM) is an independent predictor of mortality and adverse cardiovascular events (27, 234, 235). LVM is positively associated with weight, height and systolic blood pressure (33, 34, 236). Body composition has been demonstrated to be a risk factor for hypertrophy (237, 238). The relationship between age and LVM has been the source of debate with some studies reporting increases (239) and others decreases (240).

Although it is a highly heritable trait, genome wide association studies have not significantly enhanced our understanding of the wide variation in LVM (241).

While 93% of the population of the United Kingdom is of European descent, the two other major ethnic subgroups are Black Africans (those from the Caribbean and West Africa) and South Asians (from the Indian Subcontinent). Between these three groups there are marked differences in the prevalence of cardiovascular disease, with Africans having the lowest prevalence of coronary heart disease and South Asians the highest (242). Although socioeconomic variables explain part of the difference, genetic factors certainly play a role. Race has been shown to be associated with differences in LV structure such as higher LVM, ventricular wall thickness and concentricity index (CI) in Africans (236, 243, 244), even when controlling for hemodynamic factors. Compared with other racial or ethnic subgroups, Africans experience a higher prevalence of hypertension and suffer from poorer overall blood pressure (BP) control (245). This translates to an increased risk of adverse, pressure-related consequences of hypertension, particularly premature onset of left ventricular (LV) hypertrophy in Africans. Race has also been shown to be associated with differences in body mass index (BMI), fat mass, fat free mass (244). Metabolic diseases have a higher impact on LV function in South Asians than in Caucasians (246). South Asians have lower LVM, CI and volumes than Caucasians (247).

Although many approaches have been suggested for indexing cardiac parameters to anthropometric variables (e.g. weight, height, body surface area, $\text{height}^{2.7}$ or $\text{height}^{2.13}$), no one method is consistently superior (248, 249). Indexation to body surface area continues to be widely used in both clinical practice and research, using CMR and echocardiography (233, 250).

The aim of the Digital Heart Project was to establish the anthropometric and genetic determinants of cardiovascular phenotypes in a large multi-ethnic cohort of healthy volunteers. To achieve this we used the current gold-standard for cardiac phenotyping, conventional multi-breath hold 2D-CMR, while testing the feasibility and tolerability of 3D cine imaging. In depth analysis of the 3D data is reported in section 12. Given the size of the population recruited we sought to redefine the normal ranges of cardiovascular parameters using b-SSFP for different gender, race and age groups.

11.2 Methods

Study Population

In total 1530 volunteers (54.8% females; 74.8% Caucasian; age range: 18 – 81 years; mean age 41.3 ± 13.0 years) were recruited prospectively via advertisement to the Digital Heart Project at Imperial College London. At screening, participants that had known cardiovascular disease or were being treated for hypertension, diabetes or hypercholesterolemia, were excluded. Subjects taking prescription medicines were also not included in the study although simple analgesics, antihistamines and oral contraceptives were acceptable. Female subjects were excluded if they were pregnant or breastfeeding. Standard published safety contraindications to MR imaging were applied (251) including a weight limit of 120kg. All subjects provided written informed consent for participation in the study, which was approved by the local research ethics committee.

Participant phenotyping

Biophysical assessment

All measurements were performed by specially trained cardiology nurses at the study centre. Height and weight were measured without shoes while wearing scrubs. Total body fat mass was measured with multi-frequency bioelectrical impedance analysis (InBody 230, BioSpace, Los Angeles, CA) (252) and expressed as a percentage of the participant's total body weight. Body mass index (BMI) was calculated as the total weight (kg) divided by the height (m) squared. Body surface area (BSA) was calculated according to the Mosteller formula: $BSA (m^2) = (Height(cm) \times Weight(kg) / 3600)^{1/2}$ (233). Each subject was fasted for 4 hours prior to the visit.

In accordance with European Society of Hypertension guidelines (253), brachial BP measurement was performed following 5 minutes rest using a calibrated oscillometric device (Omron M7, Omron Corporation, Kyoto, Japan) that has been validated in both normal (254) and obese populations (255). The first of three measures was discarded and the second two values were averaged. Mean arterial pressure (MAP) was calculated as $[(2 \times \text{diastolic pressure}) + \text{systolic pressure}] / 3$. An electrocardiogram (ECG) was undertaken during the visit.

Volunteers self-reported their ethnic background as Caucasian, African, South Asians (Indian sub-continent), Chinese, Japanese, mixed or other/ unknown.

Cardiac magnetic resonance imaging

CMR was performed on a 1.5T Philips Achieva system (Best, Netherlands). The maximum gradient strength was 33 mT/m and the maximum slew rate 160 mT/m/ms. A 32 element cardiac phased-array coil was used for signal reception. Scout images were obtained and used

to plan standard 2D cine balanced steady-state free precession (b-SSFP) images in the left ventricular short axis (LVSA) plane from base to apex using the following parameters: field-of-view=370 mm×370 mm, repetition time /echo time = 3.0/1.5msec; flip angle = 60°; bandwidth = 1250 Hz/pixel; acquired pixel size = 2.0 × 2.2 mm; section thickness = 8 mm with a 2 mm gap; reconstructed voxel size = 1.2 × 1.2 × 8 mm; number of sections = 10 – 12; cardiac phases = 30. A single breath hold 3D LVSA b-SSFP sequence was acquired in the same orientation using the following parameters = repetition time /echo time 3.0/1.5msec; flip angle = 50°; bandwidth = 1250 Hz/pixel; pixel size = 2.0 × 2.0 mm; section thickness = 2 mm overlapping; reconstructed voxel size = 1.2 × 1.2 × 2 mm; number of sections = 50 – 60; cardiac phases = 20; sensitivity encoding (SENSE) factor = 2.0 anterior-posterior and 2.0 right-left direction. Phase-contrast sequences were acquired at the level of the pulmonary bifurcation, perpendicular to both the ascending and the descending thoracic aorta, enabling simultaneous study of both vessels. The phase-contrast data were acquired using a retrospectively ECG-gated breath-hold sequence with a through-plane velocity-encoding gradient of 200 cm/s. The sequence parameters were as follows: field-of-view=370 mm×370 mm, repetition time = 2.8 ms, echo time = 1.4 ms, flip angle = 15°, and voxel size =1.65 mm× 1.92 mm × 10 mm, with a temporal resolution of 33ms. For the calculation of aortic length, ECG-gated balanced steady state–free precession images were acquired through the thoracic aorta using the following parameters: field-of-view= 320 mm×320 mm, repetition time = 3.4 ms, echo time = 1.7ms, flip angle = 60°, and voxel size = 1.65 mm×1.92 mm×10 mm. Images were curated on an open-source image database (MRIdb, Imperial College London, UK) (256).

Cardiac magnetic resonance analysis

Analysis of the 2D cine sequences was performed by a trained cardiologist with 3 years of experience in CMR, using commercially available semi-automated software (CMRtools, Cardiovascular Imaging Solutions, London, UK) and using a standard methodology (200). End-systole (ES) and end-diastole (ED) were identified as the smallest and largest ventricular frames at mid-ventricular level. For quantification of left ventricular function and volumes, endocardial and epicardial contours were delineated in all slices, in ED and ES. Measurements from each slice were summed using the method of disks. The LV base was identified using the long-axis images (four chamber and ventricular long axis) where the mitral valve position was traced in ES and ED. The systolic descent and twist of the mitral valve was accounted for by tracking the valve motion on the long axis cines, therefore automatically correcting for loss of systolic LV volume due to atrioventricular (AV) ring descent. The papillary muscles were included in LVM and excluded from the blood pool using the signal-intensity driven, semi-automated threshold function. Thresholding level was manually adjusted until endocardial appearances correlated with visual assessment. LVM was calculated from the total myocardial volume multiplied by the specific gravity of the myocardium (1.05 g/mL). LVM and LV blood volumes were indexed when indicated by dividing the parameter by body surface area (e.g. LVM indexed = LVM / BSA). Cardiac output (CO) was calculated using the measured stroke volume (EDV – ESV) and the subject's heart rate during the scan. Concentricity index (CI) was calculated by dividing LVM by end-diastolic volume (EDV).

Aortic arch PWV ($\Delta d / \Delta t$) was calculated from the time-shift between the flow waveforms in the ascending and descending aorta using sigmoid curves fitted to the systolic up-slope of the normalized flow curves (170). The path length was calculated from spline interpolation using

points manually placed along the midline of the aortic arch in the “candy-cane” aortic view and the axial view taken at the level of the right pulmonary artery.

Reliability

To assess inter-study reproducibility 20 subjects had 2D and 3D LVSA imaging performed on two separate occasions. In each case the subject briefly got off the MR table and the study was then repeated with new pilot images. Inter-observer variability was assessed with a second reader of 10 years cardiac MR experience analysing both sets of 20 images using the same method. Inter-study variability was assessed by averaging the measurements of both observers for scan 1 and comparing it with the average of those parameters for scan 2. Both observers were blinded to the results of their first analyses.

Statistical analysis

Statistical analysis was carried out using RStudio Server version 0.98 (Boston, MA) (257). Continuous variables were expressed as mean \pm standard deviation (SD) and categorical variables as percentages. Ranges were added to CMR derived parameters. The associations between variables and cardiac phenotypes were assessed in separate multiple linear regression models that included age, gender, race, BSA and systolic blood pressure. Race was dummy-coded with the largest group, Caucasian, as the reference. To keep estimations conservative, non-parametric testing were used. When comparing two groups, Mann Whitney U tests were used. When assessing more than two groups a Kruskal-Wallis one-way analysis of variance was carried out. If overall group differences were significant a (Nemenyi) post-hoc pairwise analysis is reported. Test-retest reliability was assessed using an intraclass correlation

coefficient (ICC) with a two-way random model for absolute agreement (258). The coefficient of variability was calculated as the SD of the differences between the two sets of measurements divided by the mean value of the parameter under consideration. P values <0.05 were considered significant.

11.3 Results

All the volunteers included at screening completed the imaging protocol. The 3D sequence was also well tolerated and all datasets were used for analysis (reported in section 12).

Baseline anthropometric and CMR data for the Digital Heart Project cohort, as well as separate values for males and females, are shown in **Table 5**. To facilitate comparison with current accepted normal ranges (found in **Table 2**), in **Table 6**, CMR parameters are shown for groups divided by age and gender. In **Table 7** CMR data is presented in groups divided by Race. Summaries of the regression models using the conventional CMR data are shown in **Table 8** for the whole cohort and separately for men and women in **Table 9**.

Reliability

Inter-observer and intra-study variability were low for ventricular volumes and mass and larger for EF (**Table 4**).

	Inter-observer		Inter-study	
	ICC (95% CI)	CoV	ICC (95% CI)	CoV
LVEDVI (ml/m ²)	0.97 (0.93 - 0.99)	5.4	0.97 (0.93 – 0.99)	5.6
LVESVI (ml/m ²)	0.92 (0.79 – 0.97)	4.4	0.98 (0.96 – 0.99)	6.4
LVSVI (ml/m ²)	0.97 (0.92 – 0.99)	6.6	0.98 (0.95 – 0.99)	4.4
LVEF (%)	0.87 (0.62 – 0.95)	5.5	0.96 (0.89 – 0.98)	3.3
LVM (g/m ²)	0.98 (0.95 – 0.99)	5.81	0.99 (0.98 – 1.00)	3.4

Table 4 – Reproducibility of CMR measurements. CI = confidence interval; CoV = Coefficient of Variability; ICC = Intraclass Correlation; LVEDV = left ventricular end diastolic volume; LVESV = left ventricular end systolic volume; LVEF = left ventricular ejection fraction; LVM = left ventricular mass.

Influence of gender on subject characteristics

There was no difference between males and females in terms of age or ethnic background. Females had significantly lower weight, height, SBP, DBP, PWV and BSA (for all $p < 0.001$). Although the BMI of females was lower than that of males, the fat mass component of weight was significantly higher ($p < 0.001$). Lean mass was higher in males ($p < 0.001$)

	Full Cohort (n = 1530)	Males (n =691)	Females (n =839)	p value
Age (years)	41.3 ± 13.0 (18 – 81)	40.9 ± 12.5 (19 – 81)	41.5 ± 13.4 (18 – 75)	0.56
Race / Ethnicity:				0.89
Caucasian	1144 (74.8%)	518 (75.0%)	626 (74.6%)	
South Asian	194 (12.7%)	97 (14.0%)	97 (11.6%)	
African	104 (6.8%)	39 (5.6%)	65 (7.7%)	
Other	88 (5.8%)	37 (5.4%)	51 (6.1%)	
Systolic BP (mmHg)	118 ± 14	123 ± 13	114 ± 13	<i><0.001</i>
Diastolic BP (mmHg)	78 ± 9	80 ± 9	77 ± 9	<i><0.001</i>
PWV (m/s)	4.67 ± 1.66*	4.86 ± 1.56**	4.53 ± 1.72***	<i><0.001</i>
Height (cm)	170 ± 9	177 ± 7	164 ± 7	<i><0.001</i>
Weight (kg)	71 ± 13	79 ± 12	65.3 ± 11.2	<i><0.001</i>
BSA (m²)	1.8 ± 0.2	2.0 ± 0.2	1.7 ± 0.2	<i><0.001</i>
BMI (kg/m²)	24.7 ± 3.8	25.1 ± 3.3	24.3 ± 4.2	<i><0.001</i>
Fat Mass (kg)	18 ± 8	16 ± 7	20 ± 8	<i><0.001</i>
Lean Mass (kg)	53 ± 11	63 ± 8	45 ± 6	<i><0.001</i>
LVEDV (ml)	145 ± 32 (69 – 256)	165 ± 31 (85 – 256)	129 ± 22 (69 – 198)	<i><0.001</i>
LVESV (ml)	51 ± 16 (17 – 127)	60 ± 16 (24 – 127)	43 ± 11 (17 – 97)	<i><0.001</i>
LVSV (ml)	95 ± 19 (46 – 189)	106 ± 19 (51 – 189)	86 ± 14 (46 – 141)	<i><0.001</i>
LVEF (%)	66 ± 5 (47 – 81)	64 ± 5 (47 – 80)	67 ± 5 (47 – 81)	<i><0.001</i>
LVM (g)	114 ± 34 (40 – 270)	139 ± 31 (68 – 270)	93 ± 19 (40 – 184)	<i><0.001</i>
LVEDV / BSA (ml/m²)	79 ± 13 (44 – 129)	84 ± 14 (46 – 129)	75 ± 11 (44 – 110)	<i><0.001</i>
LVESV / BSA (ml/m²)	28 ± 8 (11 – 66)	30 ± 8 (12 – 66)	25 ± 6 (11 – 57)	<i><0.001</i>
LVSV / BSA (ml/m²)	52 ± 8 (26 – 90)	54 ± 9 (26 – 90)	50 ± 7 (32 – 76)	<i><0.001</i>
LVM / BSA (g/m²)	62 ± 14 (31 – 141)	71 ± 14 (31 – 141)	54 ± 10 (32 – 100)	<i><0.001</i>
CI (g/ml)	0.8 ± 0.2	0.8 ± 0.2	0.7 ± 0.1	<i><0.001</i>
Cardiac Output (L)	6.1 ± 1.4	6.6 ± 1.5	5.6 ± 1.2	<i><0.001</i>
Heart Rate (BPM)	64 ± 10	63 ± 11	66 ± 9.5	<i><0.001</i>

Table 5 – Digital Heart Project subject characteristics and CMR parameters (n=1530). Values are in mean ± SD or percentage. CMR parameters include ranges in brackets. BMI = body

mass index; BP = blood pressure; BPM = beats per minute; BSA = body surface area; CI = concentricity index; LVEDV = left ventricular end diastolic volume; LVESV = left ventricular end systolic volume; LVSV = left ventricular stroke volume; LVEF = left ventricular ejection fraction; LVM = left ventricular mass; PWV = pulse wave velocity. * n= 1196; ** n = 528; *** n= 668

	Males (n=691)			Females (n=839)		
	<35 years (n=261)	≥35 years (n=430)	p	<35 years (n=319)	≥35 years (n=520)	p
LVEDV (ml)	172 ± 30 (108 – 256)	162 ± 31 (85 – 248)	<0.001	132 ± 22 (72 – 198)	127 ± 21 (69 – 186)	0.005
LVESV (ml)	63 ± 16 (24 – 127)	58 ± 16 (24 – 121)	<0.001	46 ± 11 (20 – 97)	41 ± 11 (17 – 83)	<0.001
LVSV (ml)	109 ± 19 (68 – 165)	104 ± 19 (51 – 189)	<0.001	86 ± 15 (46 – 136)	86 ± 14 (49 – 141)	0.83
LVEF (%)	64 ± 5 (50 – 80)	64 ± 5 (47 – 79)	0.03	65 ± 5 (47 – 78)	68 ± 5 (53 – 81)	<0.001
LVM (g)	143 ± 30 (87 – 221)	136 ± 31 (68 – 270)	0.004	93 ± 19 (40 – 165)	93 ± 19 (54 – 184)	0.76
LVEDVI (ml/m²)	88 ± 13 (58 – 126)	82 ± 14 (46 – 129)	<0.001	78 ± 11 (52 – 110)	73 ± 11 (44 – 104)	<0.001
LVESVI (ml/m²)	32 ± 8 (12 – 57)	29 ± 8 (13 – 66)	<0.001	27 ± 6 (13 – 57)	24 ± 6 (11 – 49)	<0.001
LVSVI(ml/m²)	56 ± 8 (36 – 79)	53 ± 9 (26 – 90)	<0.001	51 ± 7 (34 – 76)	49 ± 7 (32 – 75)	<0.001
LVMi (g/m²)	73 ± 13 (44 – 119)	69 ± 14 (31 – 141)	<0.001	55 ± 9 (33 – 87)	53 ± 10 (32 – 100)	<0.001

Table 6 – Digital Heart Project CMR-derived cardiac measurements by age and gender. Values are in mean ± SD or percentage. CMR parameters include ranges in brackets. Volumes and mass indexed to body surface area. LVEDV(I) = (indexed) left ventricular end diastolic volume; LVESV(I) = (indexed) left ventricular end systolic volume; LVSV(I) = (indexed) left ventricular stroke volume; LVEF = left ventricular ejection fraction; LVM(I) = (indexed) left ventricular mass.

	Caucasians (n=1144)	South Asians (n=430)	Africans (n=104)	KW p	Post-hoc Nemenyi p-Value		
					C vs SA	C vs AF	SA vs AF
LVEDV (ml)	150 ± 32 (79 – 252)	126 ± 26 (69 – 220)	141 ± 26 (70 – 208)	<0.001	<0.001	0.141	<0.001
LVESV (ml)	52 ± 16 (17 – 121)	43 ± 13 (19 – 89)	49 ± 14 (21 – 96)	<0.001	<0.001	0.407	<0.001
LVSV (ml)	97 ± 20 (51 – 189)	83 ± 15 (46 – 136)	91 ± 16 (49 – 145)	<0.001	<0.001	0.038	<0.001
LVEF (%)	66 ± 5 (47 – 81)	66 ± 5 (53 – 80)	65 ± 5 (52 – 77)	0.473	-	-	-
LVM (g)	117 ± 34 (56 – 271)	98 ± 26 (40 – 191)	123 ± 36 (57 – 255)	<0.001	<0.001	0.2	<0.001
LVEDVI (ml/m ²)	81 ± 13 (46 – 129)	71 ± 10 (44 – 112)	76 ± 11 (45 – 108)	<0.001	<0.001	<0.001	<0.001
LVESVI (ml/m ²)	28 ± 8 (11 – 66)	24 ± 6 (12 – 43)	26 ± 7 (12 – 43)	<0.001	<0.001	0.088	0.031
LVSVI (ml/m ²)	53 ± 8 (26 – 90)	47 ± 6 (32 – 69)	49 ± 7 (32 – 82)	<0.001	<0.001	<0.001	0.04
LVMi (g/m ²)	63 ± 14 (32 – 141)	55 ± 11 (33 – 90)	65 ± 15 (37 – 101)	<0.001	<0.001	0.25	<0.001

Table 7 – Digital Heart Project CMR-derived cardiac measurements by race. Values are in mean ± SD or percentage. CMR parameters include ranges in brackets. Volumes and mass indexed to body surface area. AF = African; C = Caucasian; KW = Kruskal-Wallis test; LVEDV(l) = (indexed) left ventricular end diastolic volume; LVESV(l) = (indexed) left ventricular end systolic volume; LVSV(l) = (indexed) left ventricular stroke volume; LVEF = left ventricular ejection fraction; LVM(l) = (indexed) left ventricular mass; SA = South Asian.

Summary of linear regression models:

	Standardised β	<i>p</i>
LVEDV		
Gender	0.27	<0.001
Age	-0.26	<0.001
Race: C v AF	-0.07	<0.001
Race: C v SA	-0.21	<0.001
Race: C v Other	-0.04	0.007
Systolic BP	0.06	<0.001
BSA	0.45	<0.001
LVESV		
Gender	0.33	<0.001
Age	-0.26	<0.001
Race: C v AF	-0.04	0.032
Race: C v SA	-0.18	<0.001

Race: C v Other	-0.02	0.238
Systolic BP	-0.01	0.541
BSA	0.30	<0.001
LVS		
Gender	0.17	<0.001
Age	-0.21	<0.001
Race: C v AF	-0.08	<0.001
Race: C v SA	-0.19	<0.001
Race: C v Other	-0.05	0.001
Systolic BP	0.12	<0.001
BSA	0.49	<0.001
LVEF		
Gender	0.05	<0.001
Age	0.05	<0.001
Race: C v AF	0.16	0.459
Race: C v SA	0.01	0.002
Race: C v Other	-0.02	0.812
Systolic BP	0.17	<0.001
BSA	0.06	0.684
LVM		
Gender	0.39	<0.001
Age	-0.18	<0.001
Race: C v AF	0.05	0.002
Race: C v SA	-0.15	<0.001
Race: C v Other	-0.05	0.002
Systolic BP	0.16	<0.001
BSA	0.38	<0.001
Concentricity Index		
Gender	0.31	<0.001
Age	0.05	0.041
Race: C v AF	0.15	<0.001
Race: C v SA	0.01	0.756
Race: C v Other	-0.02	0.4784
Systolic BP	0.17	<0.001
BSA	0.06	0.028
Cardiac Output		
Gender	0.03	0.206
Age	-0.22	<0.001
Race: C v AF	-0.09	<0.001
Race: C v SA	-0.14	<0.001
Race: C v Other	-0.05	0.032
Systolic BP	0.19	<0.001
BSA	0.42	<0.001

Table 8 – Summary of linear regression models for the whole cohort. R² for LVEDV model: 0.5665; R² for LV ESV model: 0.42; R² for LVS: 0.52; R² for LVEF model: 0.13; R² for LVM model: 0.63; R² for concentricity index model: 0.22; R² for Cardiac Output model: 0.34. BP = blood pressure; BSA = body surface area; LVEDV = left ventricular end diastolic volume;

LVESV = left ventricular end systolic volume; LVSV = left ventricular stroke volume; LVEF = left ventricular ejection fraction; LVM = left ventricular mass; Race C = Caucasian; Race AF = African; Race SA = South Asian.

	Males		Females	
	Standardised β	<i>p</i>	Standardised β	<i>p</i>
LVEDV				
Age	-0.31	<0.001	-0.34	<0.001
Race: C v AF	-0.11	<0.001	-0.06	0.029
Race: C v SA	-0.28	<0.001	-0.23	<0.001
Race: C v Other	-0.03	0.251	-0.07	0.010
Systolic BP	0.07	0.023	0.07	0.022
BSA	0.42	<0.001	0.48	<0.001
LVESV				
Age	-0.28	<0.001	-0.34	<0.001
Race: C v AF	-0.08	0.011	-0.00	0.961
Race: C v SA	-0.23	<0.001	-0.19	<0.001
Race: C v Other	-0.02	0.573	-0.03	0.363
Systolic BP	-0.00	0.947	-0.04	0.294
BSA	0.29	<0.001	0.27	<0.001
LVSV				
Age	-0.26	<0.001	-0.24	<0.001
Race: C v AF	-0.10	0.001	-0.09	<0.001
Race: C v SA	-0.26	<0.001	-0.19	<0.001
Race: C v Other	-0.04	0.192	-0.08	0.001
Systolic BP	0.12	<0.001	0.14	<0.001
BSA	0.42	<0.001	0.52	<0.001
LVEF				
Age	0.15	<0.001	0.24	<0.001
Race: C v AF	0.02	0.546	-0.06	0.088
Race: C v SA	0.08	0.033	0.07	0.027
Race: C v Other	0.02	0.685	-0.02	0.469
Systolic BP	0.09	0.012	0.15	<0.001
BSA	-0.01	0.747	0.04	0.299
LVM				
Age	-0.23	<0.001	-0.24	<0.001
Race: C v AF	0.06	0.05	0.09	<0.001
Race: C v SA	-0.26	<0.001	-0.15	<0.001
Race: C v Other	-0.06	0.04	-0.05	0.048
Systolic BP	0.20	<0.001	0.20	<0.001
BSA	0.41	<0.001	0.43	<0.001
Concentricity Index				
Age	0.07	0.062	0.04	0.221
Race: C v AF	0.18	<0.001	0.17	<0.001
Race: C v SA	-0.02	0.546	0.04	0.189

Race: C v Other	-0.04	0.326	0.00	0.945
Systolic BP	0.18	<0.001	0.18	<0.001
BSA	0.07	0.043	0.04	0.228
Cardiac Output				
Age	-0.25	<0.001	-0.22	<0.001
Race: C v AF	-0.09	0.006	-0.11	<0.001
Race: C v SA	-0.17	<0.001	-0.14	<0.001
Race: C v Other	-0.02	0.597	-0.07	0.011
Systolic BP	0.17	<0.001	0.19	<0.001
BSA	0.32	<0.001	0.42	<0.001

Table 9 – Summary of linear regression models split by gender. R^2 for LVEDV model: males - 0.36, females - 0.37; R^2 for LV ESV model: males - 0.21, females - 0.21; R^2 for LVSV: males - 0.34, females - 0.39; R^2 for LVEF: males - 0.03, females - 0.11; R^2 for LV mass model: males - 0.35, females - 0.34; R^2 for concentricity model: males - 0.08, females - 0.07; R^2 for Cardiac Output: males - 0.22, females - 0.27. BP = blood pressure; BSA = body surface area; Race C = Caucasian; Race AF = African; Race SA = South Asian; LVEDV = left ventricular end diastolic volume; LVESV = left ventricular end systolic volume; LVSV = left ventricular stroke volume; LVEF = left ventricular ejection fraction; LVM = left ventricular mass.

Influence of gender on LV parameters

LV end-diastolic, end-systolic and stroke volume as well as LVM were markedly lower in females ($p < 0.001$). However, EF was 3% higher in females ($p < 0.001$). Even after adjusting the CMR derived parameters for BSA, ventricular volumes and mass were still significantly higher in the men ($p < 0.001$). CI was higher in men as was CO (for both $p < 0.001$). The difference in CO was driven by SV as women had a higher heart rate during scanning ($p < 0.001$).

In multiple regression analysis adjusted for BSA, Race, SBP and age, male gender was shown to be strongly associated with a higher LVEDV, LVESV, LVSV, LVM and CI (lowest $\beta = 0.17$ and all $p < 0.001$). The effect size of gender on LVEF is smaller ($\beta = 0.05$, < 0.001). There was no significant association between gender and CO after adjustment for other variables.

Influence of age on LV parameters

When subdividing the genders by an age cut off of 35, in men and women, LVEDV, LVEDVI, LVESV and LVESVI were lower in the older subcohort ($p < 0.001$). This contrasts with EF that rises with age in both males and females ($p = 0.03$ and $p < 0.001$ respectively). Although LVM was lower in males in the older subgroup ($p < 0.001$) there was no difference between age groups in females. If LVM is indexed to BSA, a reduction occurs in this parameter with rising age in both genders.

Age was negatively associated with LVEDV, LVESV, LVSV, LVM and CO in both males and females (for all $p < 0.001$). Age was associated in both genders with an increase in EF. There was a small positive association between CI and age that was borderline significant in the whole cohort ($\beta = 0.05$, $p = 0.04$) but that was not present when analysing the genders separately.

Influence of ethnicity on LV parameters

Race 'Other' includes a heterogeneous ethnic background including Chinese, Japanese, mixed other / unknown which makes interpretation and extrapolation of results difficult. Caucasians had higher absolute and indexed LVEDV, LVESV and LVSV than South Asians (for all $p < 0.001$). Between Caucasians and Africans the only significant differences were a lower LVSV ($p = 0.038$), LVEDVI and LVESVI (for both $p < 0.001$) in Africans. South Asians had smaller absolute and indexed LV volumes and mass than Africans (for all $p < 0.05$). LVMI is lowest in South Asians than in Africans and Caucasians ($p < 0.001$) and no difference was found between the latter two groups when comparing them without adjusting for other

variables. Plotting LVMI against SBP in each ethnic group indicates that there is a greater interaction between these variables in Caucasians and Asians than in Africans (**Figure 11.1**).

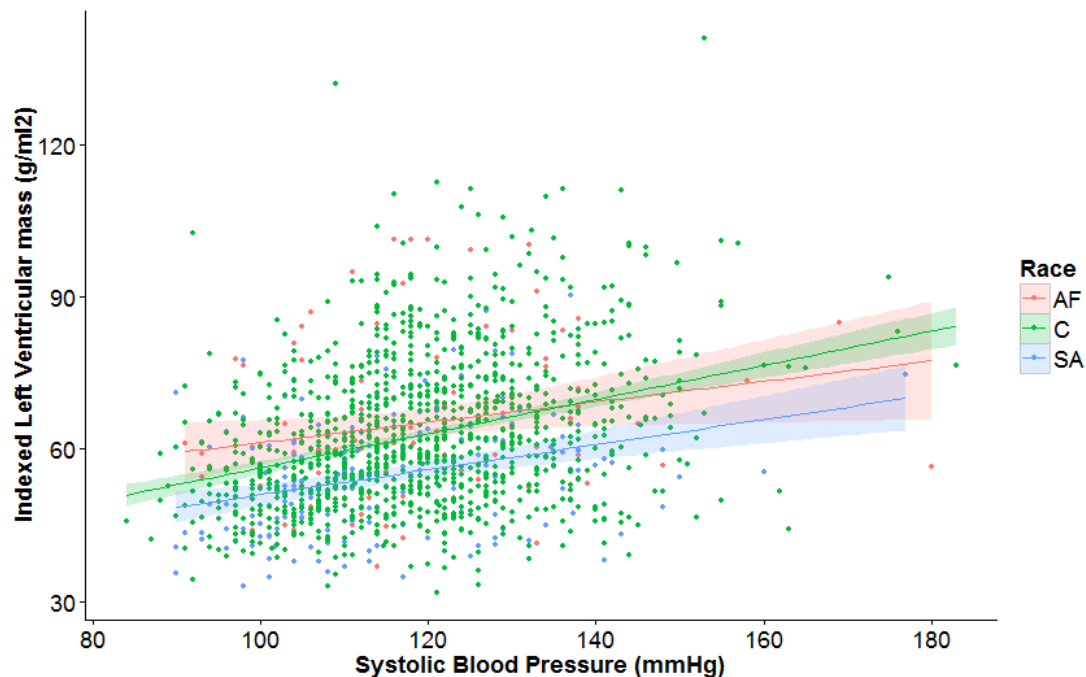


Figure 11.1 – Scatterplot of indexed left ventricular mass against systolic blood pressure by Race. Linear regression fits with 95% confidence intervals are shown for Africans (AF, pink), Caucasians (C, green) and South Asians (SA, blue).

Regression analyses adjusted for other variables showed that when compared to Caucasians, smaller LVEDV, LVSV and CO were associated with African ethnicity in both genders. LVESV was negatively associated with African ethnicity in males but no difference was found in females. African ethnicity has a higher positive association with LVM than Caucasian (males $\beta = 0.06$, $p = 0.05$; females $\beta = 0.09$, $p < 0.001$). There was a strong positive association between being African and higher CI (males $\beta = 0.18$, $p < 0.001$; females $\beta = 0.17$, $p < 0.001$). Volunteers of South Asian descent showed a negative association with LVEDV,

LVESV, LVSV and LVM in both males and females (for all <0.001). CI was not significantly associated with South Asian ethnicity.

Influence of systolic blood pressure on LV parameters

Systolic blood pressure was associated with a higher LVEDV and LVSV in both genders. There was no significant association between LVESV and SBP. In both genders SBP was strongly positively associated with LVM (in both $\beta = 0.20$, $p < 0.001$) and CI (in both $\beta = 0.18$, $p < 0.001$).

Influence of body surface area on LV parameters

BSA was strongly positively associated with LVEDV, LVESV, LVSV, LVM and CO in both genders (for all $p < 0.001$). BSA was not associated with LVEF and only weakly positively associated with CI in men ($\beta = 0.07$, $p = 0.04$) but not in women.

11.4 Discussion

This was one of the largest studies of healthy adults phenotyped by CMR, only comparable in scale to projects such as the Framingham Heart Study (FHS) Offspring cohort (259), the Dallas Heart Study (244) or the Multi-Ethnic Study of Atherosclerosis (260). It was different from these in that the mean age in the cohort was lower (age range from FHS subjects with CMR (n=1547): 60 ± 9 ; age range from MESA (n=800): 45 – 84). Furthermore, in other population-based studies, participants had different degrees of subclinical and clinical cardiovascular disease while our cohort was self-proclaimed free from cardiovascular disease and drug-naïve. This study was the largest of a UK population using CMR.

Our data showed that LV volumes and mass vary with gender, age and ethnic groups and were also significantly influenced by body surface area and systolic blood pressure. When compared with published normal ranges shown in **Table 2** and **Table 3** (199), the values we obtained were similar for LVEDV, LVESV and LVM in females (maximal difference in mean volumes: 5ml; maximal difference in mean mass: 1g). In our cohort females had a lower LVSV in the younger sub-cohort (difference in means: 10ml). The difference in LVSV in the older cohort was smaller (difference in means: 3ml). LVEF was also lower in our cohort of young females (difference in means: 4%). In men, our study found higher LVEDV in the older group (difference in means: 13ml) but equivalent results in the younger group. LVESV was also larger in our cohort than in that studied by Hudsmith and colleagues (difference in means <35 years: 6ml; ≥ 35 years: 15ml). In our cohort, LVM in men was considerably higher (difference in means <35 years: 12g; ≥ 35 years: 16g). After indexing for body surface area the differences followed a very similar trend. Dissimilarities between the studies can be potentially explained by small variations in the imaging analysis approaches.

In our method we defined the mitral valve in the long-axis planes, while Hudsmith and colleagues chose the basal slice when at least fifty percent of the blood volume was surrounded by myocardium (199). Furthermore, our large cohort was multi-ethnic while the racial background of their subjects is unclear.

In terms of inter-observer and inter-study reproducibility, our study is comparable with other projects (188, 199, 260). While in our study, subjects were re-scanned immediately after the first scan, Hudsmith's subjects had their second scan at least one week apart, which might have included physiological changes in their measure of inter-study variability (inter-observer CoV: LVEDVI – 2.7, LVEF – 3.3, LVM – 5.2; inter-study CoV: LVEDVI – 5.5; LVEF – 7.5; LVM – 9.4). The MESA study reported similar inter-observer ICCs (LVEDV: 0.98; LVESV: 0.94, LVM: 0.98, LVEF: 0.81). Grothues and colleagues in their paper on reproducibility of CMR and echocardiography reported results almost identical to ours (inter-study CoV: LVEDVI – 2.9; LVESVI – 6.5; LVSVI – 3.9; LVEF – 2.4%; LVMI – 2.8%). As in these studies the inter-observer ICC was lower for EF than for the other parameters.

In contrast with the MESA cohort (260) and Hudsmith's study we found that all cardiac parameters, indexed or not, were significantly different between men and women. These included LVSV and CI that were not different between genders in the MESA cohort and LVEF, LVEDVI, LVESVI and LVSVI for which Hudsmith et al. found no significant difference between men and women. LVEF was the only cardiac parameter that is higher in females than males. This was probably due to the fact that our subject sample was much larger than in previous studies.

When analysing the effect of age on cardiac phenotypes by comparing gender subgroups dichotomised by age (using 35 years as a cut-off), increase in age past the cut-off point was associated with a reduction in cardiac volumes and mass in males. In females, LVSV and

LVM were not significantly different between the older and younger cohorts. Age was dichotomised to enable comparison with current European Society of Cardiology recommended normal ranges, based on the work of Hudsmith and colleagues (199). However, dichotomising continuous variables leads to a loss of statistical power to detect associations between variables and the outcomes and increases the risk of a positive result being a false positive (261). This was addressed by investigating the effect of age on cardiac phenotypes using regression modelling. Using this approach we found a negative association between age and LVEDV, LVESV, LVSV, LVM and CO in both males and females. LVEF was positively associated with age. Our findings are consistent with the MESA cohort (260) that also found a negative association between both volumes and LVM and age in men. However in their study in women, while LVEDV showed a negative association with age, LVESV showed only a trend towards negative association. They found no significant association between age and LVM in females and supported their finding with an autopsy study that showed a decrease in LV mass with age in men but not in women (262). In contrast with their findings, when we examine the association between LVM and age in females while adjusting for other variables, we found a highly significant negative association ($\beta = -0.2$, $p < 0.001$). The fact that in their study, the effects of variables such as race or BP were not adjusted for, might help explain the differences between our findings.

When directly comparing the ethnic sub-cohorts without adjusting for other variables, we found no difference in LVM between Caucasians and Africans even after indexing to body surface area. However in the regression analysis accounting for age, SBP and BSA a significant positive association between LVM and African ethnicity was found in both genders. This finding was in line with the Dallas Heart Study (CMR) (240) and the Coronary Artery Risk Development in Young Adults (263) study (echocardiography). It contrasts with the North Manhattan Stroke Study (NOMAS) (254) and the Hypertension Optimal Treatment

(HOT) study (255), both using echocardiography, as well as the MESA study using CMR (260) that reported no LVM difference between these two ethnicities. The reason underlying these inconsistencies is unclear. However we note that in the studies that found no association between LVM and African ethnicity, other clinical variables were not accounted for. Furthermore, although we found no difference in non-indexed absolute volumes and mass between Caucasians and Africans, Africans do have smaller LVEDVI and LVESVI. This suggests that our study might have been underpowered to detect absolute differences between Caucasians and Africans without adjustment for other variables. This might be due to the small number of African volunteers (n=104) and the fact that 62.5% of these were females. Regression analysis shows that African ethnicity was associated with lower LV volumes and higher mass and CI. The strong association between CI, SBP and African ethnicity may explain the increase risk of heart failure in Africans of all age groups (264). In Africans, increased prevalence of hypertension, obesity, smoking, alcohol consumption, as well as genetic factors have been proposed as the cause of the increased incidence of heart failure in this population (265, 266).

Our finding that South Asians have smaller LVEDV, LVESV, LVSV and LVM was consistent with 3D echo results from the Left Ventricular Structure in the Southall and Brent Revisited (SABRE) study (247) and the MESA cohort (260). The cause of this is not known, although it has been suggested that it reflects inappropriate allometric indexation for body size. However, it may also represent a pathological process with implications on myocardial wall stress and oxygen demand leading to increased vulnerability to ischaemia and infarction (247).

Although BSA, age, gender, race and systolic blood pressure are strong determinants of cardiovascular phenotypes, the proportion of total variation (R^2) explained by the multiple regression models remains limited (R^2 for LVEDV model: 0.57; R^2 for LVESV model: 0.42;

R^2 for LVSV: 0.52; R^2 for LVEF model: 0.13; R^2 for LVM model: 0.63; R^2 for concentricity model: 0.22; R^2 for Cardiac Output: 0.34). This suggests that other environmental, anthropometric and / or genetic factors contribute to inter-individual variability.

In this study we demonstrated that high resolution imaging of the whole heart in a single breath-hold, using 3D-CMR, is feasible and well tolerated in a healthy population. In depth analysis of these datasets can be found in section 12.

This study, while the largest of its type in the UK, was limited by the small number of participants from African and other ethnic minorities, as well as by a lack of longitudinal outcome data. Metabolic profiling, smoking status and activity levels are also known to influence cardiac structure and were not included in this analysis although will be available in the future. The clear strength of our study is that it studied a large, well characterised healthy population with using gold-standard 2D-CMR.

11.5 Conclusions

LV parameters were determined, in part, by age, systolic blood pressure, gender, ethnic background and body surface area. However, the variance in these cardiac phenotypes that can be explained by regression models including clinical variables thought to be important was moderate, suggesting that other unmeasured anthropometric, environmental and genetic factors, in addition to stochastic effects, also play a major role. Studies that assess the genetic determinants of cardiovascular function and structure may begin to better account for normal variations in cardiac form and function in this population. Furthermore, the power to detect the associations between variables and cardiac phenotypes might be limited by current 2D imaging approaches. These data may have significant clinical and research utility by providing gender, age and ethnicity specific normal ranges of b-SSFP derived CMR parameters in a large healthy population.

11.6 Acknowledgments

The Digital Heart Project was conceived and coordinated by Professor Stuart Cook and Dr. Declan O'Regan. CMR volumetric data collection was carried out with Tim Dawes, under the supervision of Dr. Declan O'Regan and Dr. Niall Keenan. PWV velocity measurements were carried out with Ben Corden, Wareed Alenaini, Marina Quinlan and Katie Francis.

12 3D-CMR cardiac atlas and automated analysis methods

12.1 Introduction

The structure of the human heart is highly heritable (26) and influenced by complex interactions between genetic and environmental factors (32). Although left ventricular (LV) mass (LVM) is an important heritable trait which independently predicts the risk of heart failure, sudden death and all-cause mortality (27), the genes that regulate LVM remain elusive (241). Inherited cardiac conditions typically cause regional or asymmetric changes in LV structure (267, 268) and therefore total mass may be an insensitive indicator for detecting genetic influences. This is supported by the increasing numbers of the so called genotype-positive, phenotype-negative subjects that are being identified through family screening of cardiomyopathy genes (269, 270). Whether this is due to incomplete penetrance or simply due to the fact that subtle phenotypic disease expression is currently undetectable by standard imaging approaches, has not yet been ascertained. Quantitative phenotyping of the heart may help overcome these limitations by creating detailed 3D statistical models of the variation in cardiac morphology and function within a population. These statistical models can be adjusted for known determinants of cardiac functional and structural phenotypes, which could further increase the power to detect genetic factors. Furthermore, automated approaches may also address the significant intra- and inter-observer variability that accompanies manual analysis of 2D cine imaging (199).

A computational approach to phenotyping has been successfully used in brain mapping studies (202-206) and also has potential for epidemiological research in heart disease (208, 209). While neuroimaging benefits from high spatial resolution 3D magnetic resonance (MR)

to detect anatomical variation, the statistical modelling of conventional 2D cardiac cine imaging is constrained by the low spatial resolution of each section and misalignment between breath-holds (207). Standard 2D cardiac cine MR images comprise a stack of 8mm sections with 2mm gaps in the LV short axis plane which are acquired over five or six breath-holds (173). Three-dimensional cardiac magnetic resonance (3D-CMR), at a comparable spatial resolution to 2D sequences, has been shown to have similar accuracy for manual assessment of LV volumes and mass (178-187). Whole heart 3D coverage at greater spatial resolution, in a single breath-hold, is now possible with the use of high acceleration factors.

Automatic approaches that use prior knowledge of inter-subject variability in cardiac anatomy (cardiac atlases) to analyse new target images have been used in cardiovascular research (225). The main components of atlas-based analysis of CMR images are atlas selection, atlas propagation and label fusion. During the atlas propagation step, affine or non-rigid registration methods are used (223, 271). Registration refers to the process through which different images are transformed into one common coordinate system. Image registration algorithms are classified according to the transformation models applied to the images. Linear transformations are global in nature and include translation, rotation, scaling and other affine transforms. They are insensitive to local variations between the images. Nonrigid transformations enable local warping of the target image to align it with the atlas.

In neuroimaging research, algorithms that make use of multiple atlases have been shown to be superior to single atlas approaches (221, 222, 272). Using multiple atlases to inform automated anatomical labelling (segmentation), normally involves the combination of the multiple propagated labels to create consensus segmentation. Increasing the number of atlases results in higher accuracy of segmentation as more of the variability in anatomical shapes is accounted for. Furthermore, having more cardiac atlases enables segmentation errors caused by incorrect labelling driven by a single atlas to be ‘averaged’ out. Another advantage of the

multi-atlas approach is that accuracy can be increased without necessarily increasing the computational cost. This can be achieved by selecting atlases within the pool which are most similar to the target image (273, 274).

Registration between atlas and target has been traditionally constrained to ensure one-to-one correspondences based on intensity similarities. The main advantage of this restriction is that the topological characteristics of the atlas are preserved after deformation. However, a very significant limitation is that it limits the ability to detect local variations in shape in the target image. To reduce the dependency on accurate registration, a patch-based label fusion subtype of multi-atlas segmentation has been proposed (275). This PatchMatch segmentation algorithm divides the target and the atlas images into patches and searches for correspondences between them. Although some versions of PatchMatch limit the search window, it is plausible to assume that if a good match is found between two patches then there is an increased likelihood that neighbouring patches will also be similar. The level of similarity determines the weights for the label fusion process and segmentation (225).

Alignment of a large number of segmentations in a space with a common coordinate system should enable the accurate modelling of cardiac parameters at corresponding points of the LV within a group of subjects.

Having established the tolerability of high spatial resolution 3D-CMR in our population, our primary purpose in this study was to develop a high resolution 3D atlas of the human heart. Secondly, we aimed to evaluate the feasibility and accuracy of an automated analysis technique, which makes use of a large number of 3D-CMR cardiac atlases to guide the segmentation of unseen cardiac images. Finally, we intended to determine if high resolution mapping of ventricular wall thickness enables a reduction in the sample size required for population-based research of myocardial hypertrophy.

12.2 General methods

Study Population

In total 1530 volunteers (54.8% females; age range: 18 – 81 years; mean age: 41.3 years) were recruited prospectively via advertisement to the Digital Heart Project at Imperial College London. Detailed descriptions of the full cohort, eligibility criteria and biophysical assessment methods can be found in section 11.3 above.

A randomly selected sub-cohort of 138 volunteers (56.5% females; age range 18 – 65 years; mean age: 39.9 years) was used in the validation experiments of the cardiac atlas. Of these, twenty subjects were randomly selected to create the first set of cardiac atlases (50% females; age range: 24 – 59 years; mean age: 38 years), and 20 volunteers (45% females, age range: 18 – 54 years; mean age: 36.5 years) were imaged on two separate occasions for assessment of reproducibility. To assess inter-study variability 1 male (age = 40 years) and 1 female (age = 27 years) subjects were scanned on 8 separate occasions over a period of 18 months.

Imaging Protocol

CMR was performed on a 1.5T Philips Achieva system (Best, Netherlands). Full details of the imaging protocol can be found in section 11.3 above. In this study we used the 2D cine balanced steady-state free precession (b-SSFP) images, as well as the single breath-hold 3D left ventricular short axis (LVSA) b-SSFP sequence.

Image quality assessment

Two readers with 10 and 6 years of experience in cardiac MR respectively, who were blinded to the imaging protocol, independently assessed the image quality of the 2D and 3D LVSA images in 20 subjects. The overall image quality of each technique was assessed on a four-point scale (score 1, severe artefact or poor image quality making the myocardium not evaluable; score 2, fair delineation of the myocardium with moderate artefact affecting the heart; score 3, good delineation of the myocardium with mild artefact affecting the heart; and score 4, excellent delineation of the myocardium and no artefacts within the heart).

To account for spatial variation in image noise on the undersampled images the contrast on 2D and 3D cine images was assessed by measuring contrast ratios (276). A contrast ratio (CR) was calculated using the following equation: $CR = \frac{SI_1 - SI_2}{\sqrt{(SD_1^2 + SD_2^2)}}$, where SI_1 and SI_2 are the mean signal intensities of relatively homogeneous areas of the myocardium and blood pool and SD_1 and SD_2 are their respective standard deviations.

Statistical analysis

Data was analysed using RStudio Server version 0.98 (Boston, MA) (257) and SigmaPlot (Systat Software, San Jose, CA). Normally distributed data were reported as mean \pm one standard deviation (SD) or otherwise as median and interquartile range (IQR). Comparison between methods was made using Bland-Altman plots (277). CRs were compared using a two-sided paired t-test and reported with 95% confidence interval (CI) for the difference of the mean. Image quality scores were compared with the Wilcoxon signed-rank test. Test-retest reliability was assessed using an intraclass correlation coefficient (ICC) with a two-way random model for absolute agreement (258). Voxelwise comparisons between the 2D and 3D

techniques were made using the Wilcoxon signed rank test. The sample size required for automated segmentation of 2D and 3D techniques to detect a 1mm difference in wall thickness at each point across the myocardium was calculated from the voxelwise interstudy variances (see appendix) (188). A P value <0.05 was considered significant and Bonferroni correction was made for multiple comparisons in all voxelwise tests.

Reliability

Twenty subjects had 2D and 3D LVSA imaging performed on two separate occasions. In each case the subject briefly got off the MR table and the study was then repeated with new pilot images. An independent reader of 10 years cardiac MR experience manually analysed the 2D LVSA datasets using cardiac analysis software (Extended WorkSpace, Philips, Best, Netherlands). Endocardial and epicardial borders were defined on the left ventricular cine images using a standard methodology to derive LVEDVI and LVMI (200). Trabeculae and papillary muscles were excluded from the mass measurement and included in the cavity volume.

12.3 3D cardiac atlas method

For the creation of the first set of cardiac atlases, the 3D LVSA images from 20 randomly selected subjects had each voxel manually labelled as LV cavity, myocardium or right ventricular blood pool in end-diastole and end-systole (**Figure 12.1**). Manual segmentations were carried out by two readers using freely available software (ITKsnap, National Library of Medicine's Insight Segmentation and Registration Toolkit, <http://www.itk.org>) (278). On average there were ~50000 voxels labelled as LV cavity, ~30000 as myocardium and ~60000 as right ventricular blood pool. The atlases were quality controlled by a reader of 10 years cardiac CMR experience. These atlases provided baseline information about the inter-subject variability in cardiac anatomy within the population (225). Given the large variability in papillary muscle anatomy within the cohort these were not labelled independently and were instead included in the blood pool.

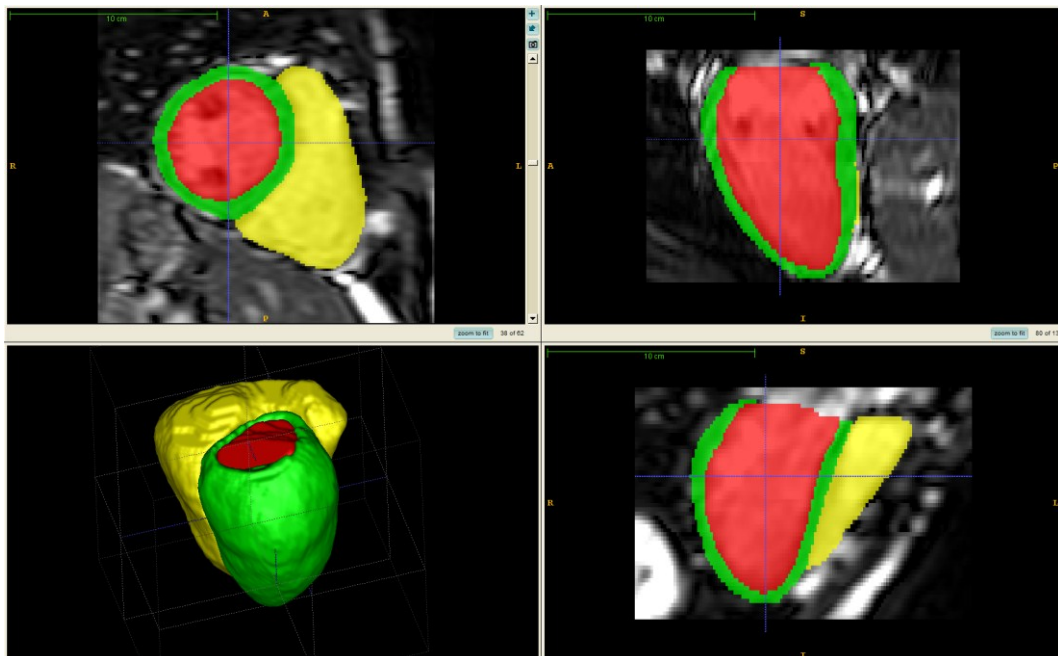


Figure 12.1 – One of the initial 20 cardiac atlases with each voxel from the three-dimensional balanced steady-state free precession LV short axis cine sequence, manually

labelled in end-diastole as LV blood pool (in red), LV myocardium (green) and right ventricular blood pool (yellow). Top left – mid ventricular short axis; top and bottom right – left ventricular long axis reconstructions of the short-axis cine; bottom left – 3D model of the labelled voxels.

12.4 Automated segmentation method

To initiate the atlas-based segmentation algorithm, six manual landmarks were placed in a new target image. This enabled a landmark-based registration between the target image and the atlases images. Subsequently, non-rigid image registration was performed between the target image and the atlas images, following which the atlas segmentations were warped onto the target image space. A multi-atlas PatchMatch algorithm (279) was then used to find correspondences between “patches” of neighbouring voxels ($5 \times 5 \times 5$ mm) within the atlases and target images, without any restriction of the search window size for the purpose of label fusion (**Figure 12.2**).

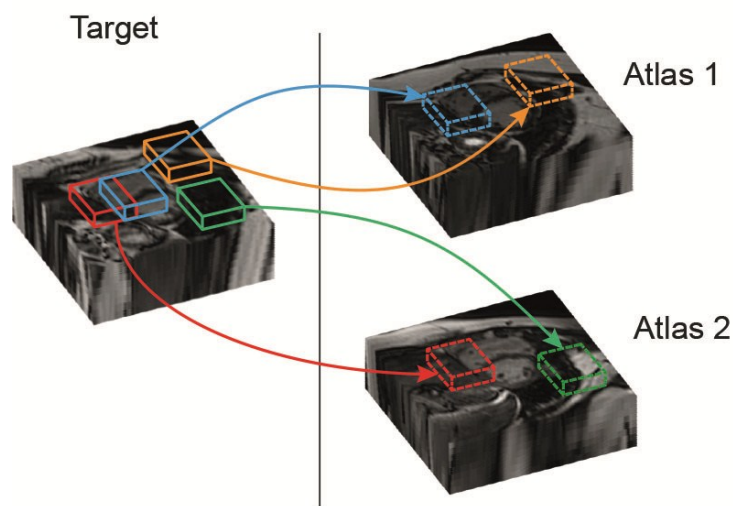


Figure 12.2 – The PatchMatch automated cardiac segmentation method looked for similarities between cubic patches in the pool of atlases and each new target image. It then assigned the labels of the atlas image patches onto the matching target image patches forming the segmentation result

Each selected atlas patch was given a weighting according to its similarity and distance to the target patch. Labels from all the atlas patches were then combined to produce a final segmentation. This segmentation was then registered to the template in the common space ensuring that each spatial coordinate in the 3D model was consistent between all subjects. The registrations were performed using the IRTK software package (280). A probabilistic atlas was computed by averaging all the segmentations. A label map was created by selecting the label with the maximum probability at each voxel. The template image was created by averaging the intensity images after all the subjects were registered to the common reference space. The template image can be regarded as the average heart size, position and orientation. This method is summarised in **Figure 12.3**.

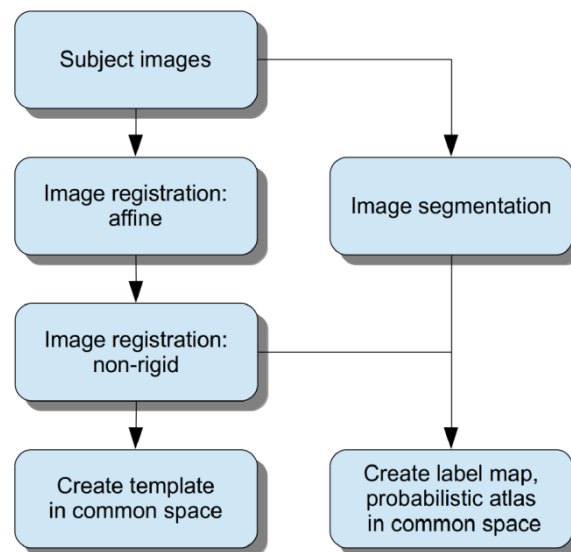


Figure 12.3 – Flow chart for atlas construction.

Through a process of surface rendering, meaningful information can be extracted from segmentation volume data into a surface representation. This was achieved here using a

marching cubes algorithm (281-283). This algorithm enables the generation of high quality images by approximating a surface of interest by a mesh of polygons. It is based on a division of a data volume into elementary cubes, followed by a standard triangulation inside each cube. Each volume cell (or cube) is analysed at a time, hence the term marching cubes. The mesh was smoothed using a Laplacian smoothing filter. The end result of this process was the reconstruction of endocardial and epicardial mesh surfaces with 19185 and 27623 points respectively. All data were represented in a standard coordinate system and visualized on the 3D myocardial template.

Although the segmentation algorithm was automated, it was initialised by manually placing 6 pre-defined landmarks on each target image: LV lateral wall, right ventricular free wall, and right ventricle (RV) insertion points at the level of the papillary muscles (**Figure 12.4**), as well as at the LV apex and mid cavity at the level of the mitral valve. These landmarks enable an initial alignment between atlases and target images.

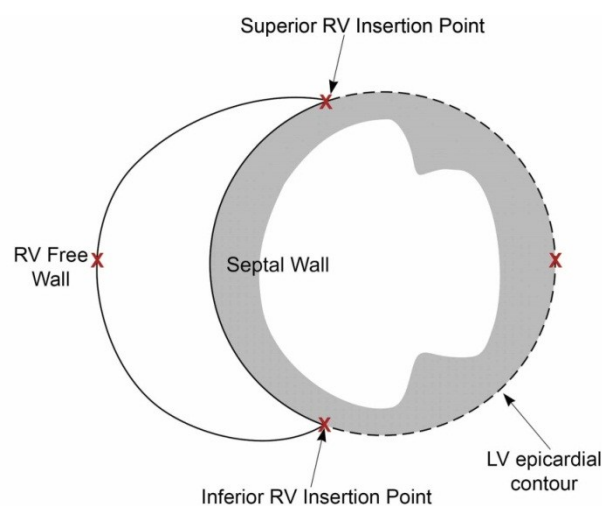


Figure 12.4 – Diagram of a left ventricular short axis image at the level to the papillary muscles. Location of the typical landmarks used to initiate the segmentation algorithm, are represented by the red crosses.

Numerous iterations of the automated segmentation algorithm were tested on the initial 20 cardiac atlases using a leave-one-out approach (using 19 atlases to segment the remaining). Two independent readers assessed the quality of the automated segmentations by comparing them to the manual labels (**Figure 12.5**).

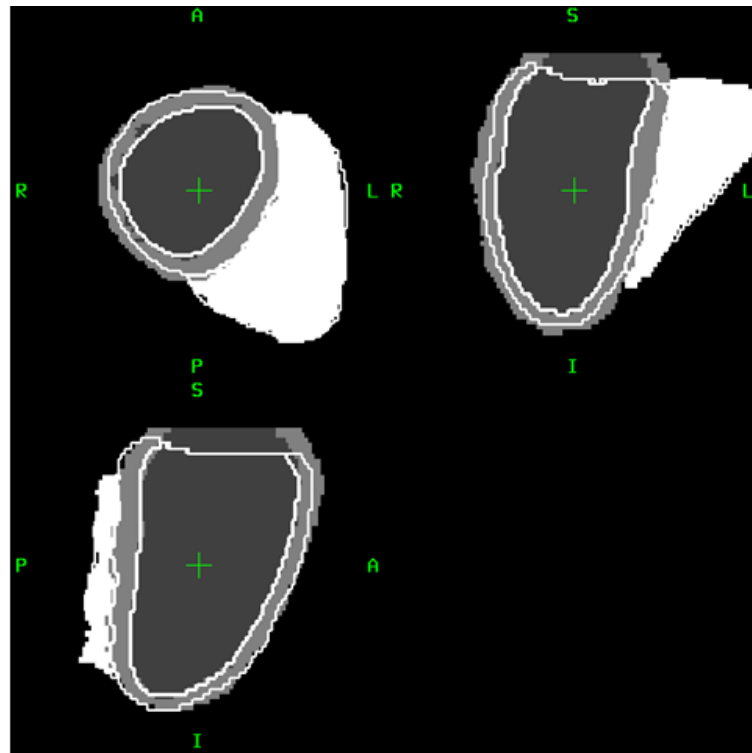


Figure 12.5 – Rendering of the automated segmentation (white contours) and the manual label map used to assess the accuracy of segmentation during the initial stages of development of the PatchMatch algorithm.

Variations in the number and location of manual landmarks were systematically tested including the use of no landmarks, landmarks in the long axis only (apex and mitral valve), landmarks in the short axis only (many iterations with the number of markers varying from 1 in the mid-cavity to >10 at multiple positions in the LV and RV walls) and combinations of long and short axis landmarks. The no-landmarks approach was associated with a high number of failed segmentations (structures outside the heart being labelled as the LV) and

was quickly abandoned (**Figure 12.6**). The absence of long axis markers led to a high incidence of voxels in left atrium and outflow tract being incorrectly labelled as LV blood pool and / or LV myocardium (**Figure 12.7**). In similar fashion, LV only landmarks led to frequent LV / RV incorrect labelling. Increasing the number of landmarks in the short axis above 4 led to significant inter-observer variability in the placement of these markers. This was due to the fact that these points were not associated with easily definable and consistent cardiac anatomy. Overall a number of landmarks above 6 did not contribute to increased accuracy.

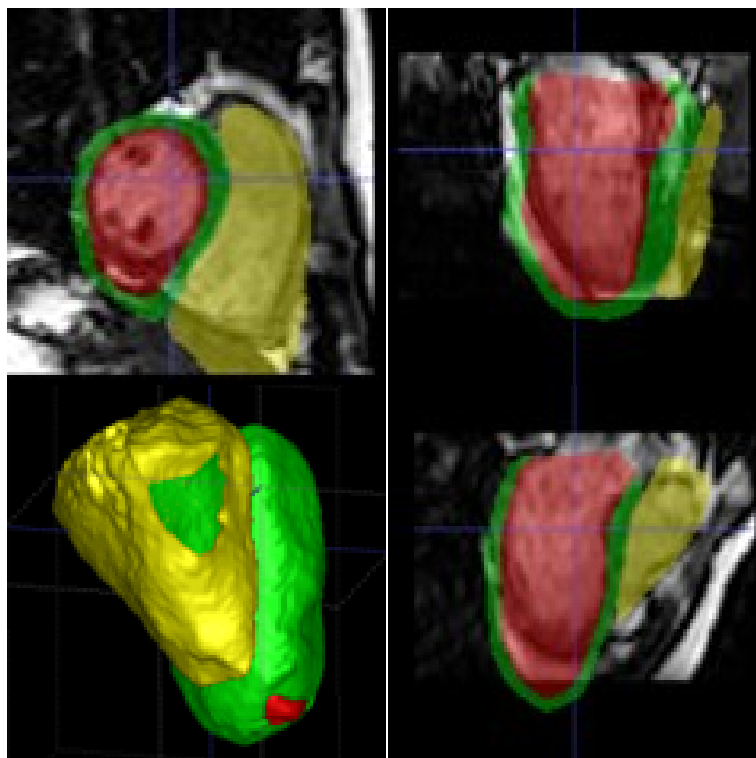


Figure 12.6 – Example of a failed automated segmentation of a 3D left ventricular short axis cine sequence using a no-landmark approach to initiate the algorithm. The mismatch between the automated labels and the target grey-scale image is evident with a high number of voxels outside the heart being attributed cardiac labels.

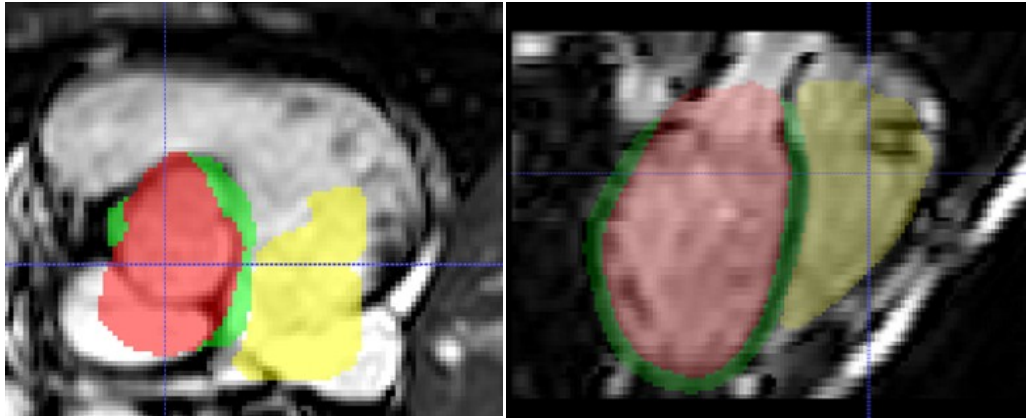


Figure 12.7 - Example of two failed automated segmentations of 3D left ventricular short axis cine sequences using no long axis landmarks. A high number of voxels in the outflow tract were labelled as left ventricular blood and wall.

Once the segmentation algorithm was optimised using the leave-one-out approach, new target images were segmented. The resulting segmentations were then visually inspected against the grey-scale target image (**Figure 12.8**). Failed segmentations remained in the ‘targets’ cohort while accurate segmentations were added to the atlas pool. Those images that were almost correctly labelled were manually adjusted and then added to the atlas library. All additions to the atlas pool were supervised by an experienced reader in CMR. This process was repeated until the atlas pool included 1093 atlases. As the pool of atlases increased, an additional atlas selection step was added in which the 40 atlases most similar to the target image were chosen to guide segmentation.

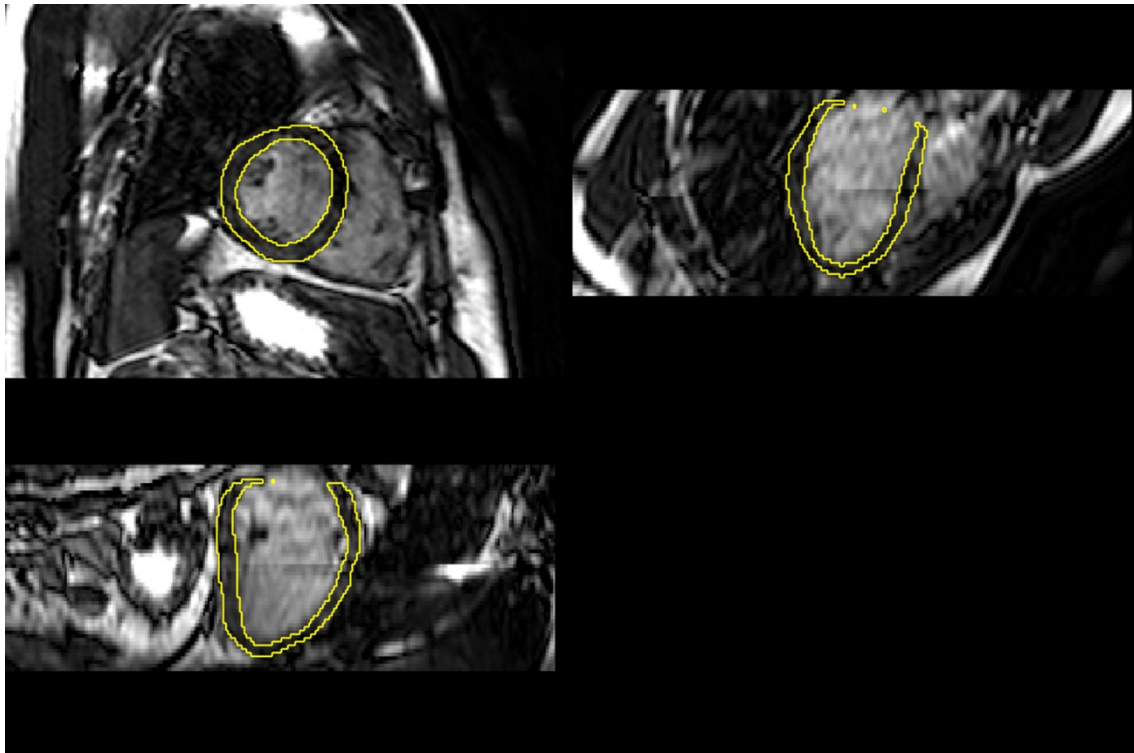


Figure 12.8 – Automated segmentation superimposed on a 3D-CMR image of one of the Digital Heart Project’s volunteers. Yellow contours represent the borders of the myocardial segmentation of the left ventricle (endocardium and epicardium) from which the 3D dimensional models are derived. All images are manually quality controlled by visual inspection of the correspondence between the labels and the greyscale image.

Analysis was performed using numerical computing software (Matlab, Natick, MA). For the atlas construction and initial segmentation experiments a workstation (Xeon quad-core 2.4 GHz with 8GB of random access memory; Intel, Santa Clara, CA) was used. When the segmentation method was applied to the whole cohort (n=1530) a high performance server (Dell, Round Rock, TX) was required.

To enable an unbiased evaluation, the 2D LVSA images were compared to the corresponding manually-labelled atlas down-sampled to the equivalent spatial resolution. For the 3D and 2D LVSA data the distance between each epicardial and endocardial point on the segmentations and its corresponding point on the labelled atlas was measured. The accuracy of segmentation

was also assessed by the proportion of concordant voxels in the target images and the corresponding manually labelled atlas. This agreement was expressed using the Dice similarity coefficient where 0 indicates no overlap and a value of 1 indicates perfect agreement (284).

12.5 3D-CMR derived phenotypes

The following phenotypes can be derived from the each individual segmentation:

LV mass and blood volumes:

The volume of the voxels labelled as left ventricle cavity and myocardium were used to calculate LV end-diastolic volumes and mass which were then indexed to body surface area (LVEDVI and LVMI respectively). Myocardial density was assumed to be 1.05 g/mL (285).

Wall Thickness:

Wall thickness (WT) was measured perpendicular to a midwall plane equidistant to the endocardial and epicardial surfaces (in mm).

3D Relative Wall Thickness:

To adjust the 3D derived cardiac parameters to cardiac size a computational approach was adopted. A registration between the patient specific LV myocardial model and the reference model was performed using a 7 degrees of freedom transformation including translation, rotation and scaling. The translation and rotation transform the model into reference space and scaling does the normalisation.

Fractional wall thickening:

Fractional wall thickening (FWT) was calculated as (end-diastolic WT – end-systolic WT)/end-diastolic WT x 100.

Ventricular geometry:

Variation in the position of the endocardial and epicardial surfaces was assessed by the distance and direction required to translate each point on the heart to the coregistered average cardiac shape.

Wall Stress:

Three-dimensional models of the heart provide an unparalleled opportunity to measure cardiac phenotypes such as LV wall stress at every point in the heart. For wall stress calculations, it is necessary to measure the radius of the ventricle or the local curvature. At any point on a curve, the line that best approximates the curve is the tangent line. In the same way, the best approximating circle that passes through this point and is tangent to the curve, can be identified. The reciprocal of the radius of this circle is the curvature of the curve at this point. As the circle that passes through this point may lie to the left or to the right of the curve, a sign is attributed by convention (286) (**Figure 12.9**). This value can then be used to calculate local wall stress through: $\propto \text{SBP} \times R/\text{WT}$ (287).

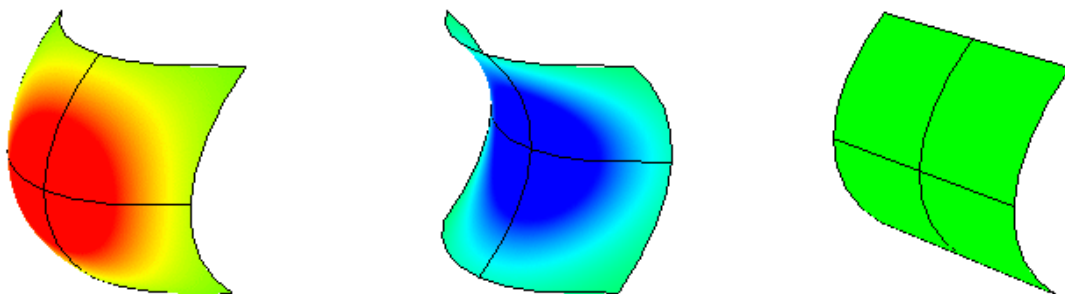


Figure 12.9 – Curvature of a surface. Red is assigned to a positive value of Gaussian curvature, green is assigned to zero Gaussian curvature, and blue to a negative value of

Gaussian curvature. Left - A positive Gaussian curvature value means the surface is bowl-like. Middle - A negative value means the surface is saddle-like. Right - A zero value means the surface is flat in at least one direction. (Planes, cylinders, and cones have zero Gaussian curvature).

12.6 Results

All of the 1530 healthy volunteers successfully completed the imaging protocol. Of these 20 subjects had their 3D LVSA cine images manually labelled and a further 1072 were added to the atlas pool after automated segmentation. Subject characteristics are shown in **Table 5**. The 2D LVSA data acquisition required 5 or 6 breath holds of 12 – 15 secs each while the typical breath hold for the 3D LVSA cine typically lasted 20 – 25 secs depending on heart rate and number of sections acquired.

3D Cardiac Atlas

A high resolution cardiac atlas was created from the 3D-CMR images of 1092 volunteers of the Digital Heart Project. The atlas includes template images, label maps and surface meshes in end-diastole and end-systole (**Figure 12.10**, **Figure 12.11** and **Figure 12.12**).

Image quality

The mean CR between blood pool and myocardium was greater on the 2D images compared to 3D 12.2 ± 2.5 vs 8.7 ± 1.9 (95% CI: 2.2 – 4.9; $P < 0.0001$). The image quality ratings for 2D imaging were slightly higher than for 3D imaging (median 4.0 vs 3.5, $P = 0.002$), but all images were interpretable.

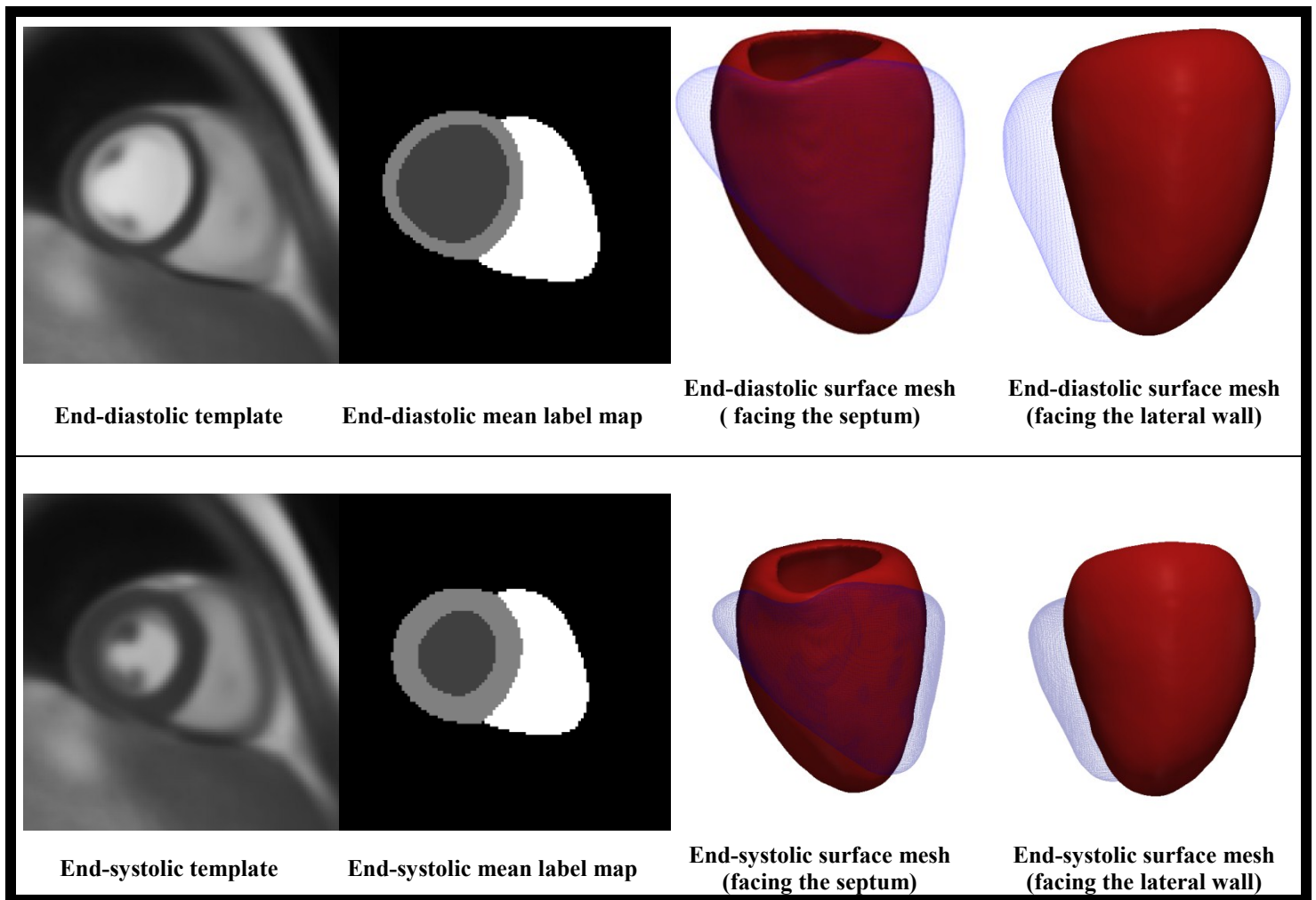


Figure 12.10 – The Digital Heart Project cardiac atlas in end-diastole (top panel) and end-systole (bottom panel).

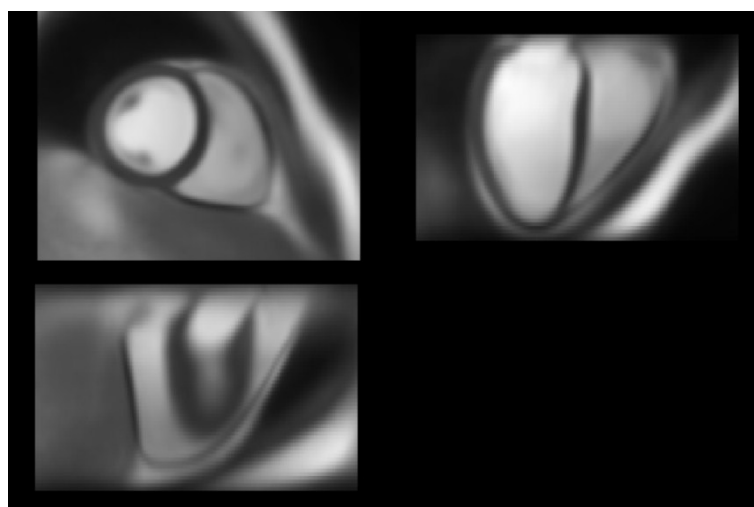


Figure 12.11 – End-diastolic template from 1092 volunteers of the Digital Heart Project.

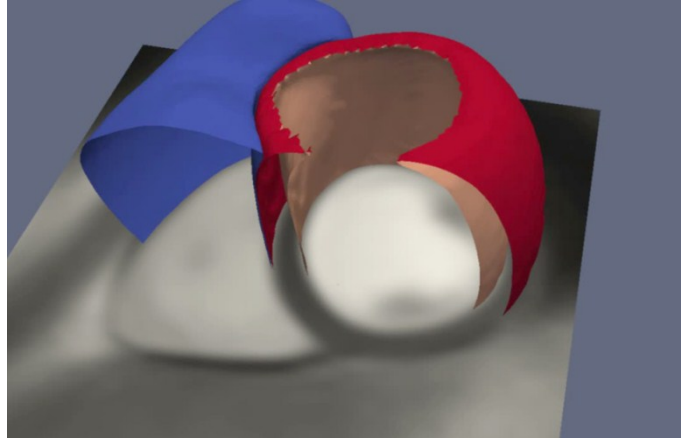


Figure 12.12 – End-diastolic template from 1092 subjects of the Digital Heart Project with the corresponding 3D surface mesh: endocardium (pink), epicardium (red) and the right ventricle (blue)

Accuracy of the automated 3D segmentations

In the initial validation study with 20 manually labelled atlases, the accuracy of automated segmentation progressively improved as the number of cardiac atlases was increased, but there was modest benefit beyond 10 atlases (**Figure 12.13**). There was better segmentation accuracy of the 3D LVSA compared to 2D LVSA for both the endocardium, 0.952 vs 0.927 ($P<0.001$) and epicardium, 0.952 vs 0.928 ($P<0.001$) using the Dice overlap coefficients (**Figure 12.14**).

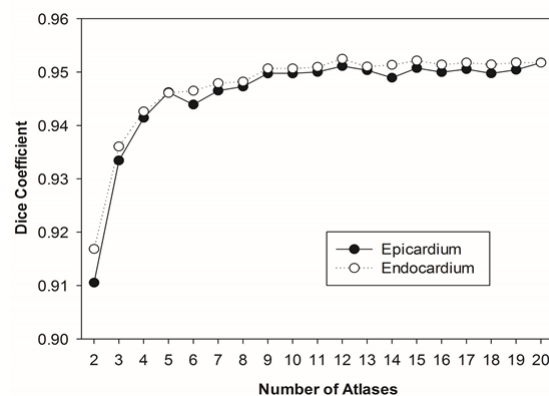


Figure 12.13 – The accuracy of cardiac segmentation measured with the Dice coefficient improved as a larger number of 3D atlases were included in the analysis.

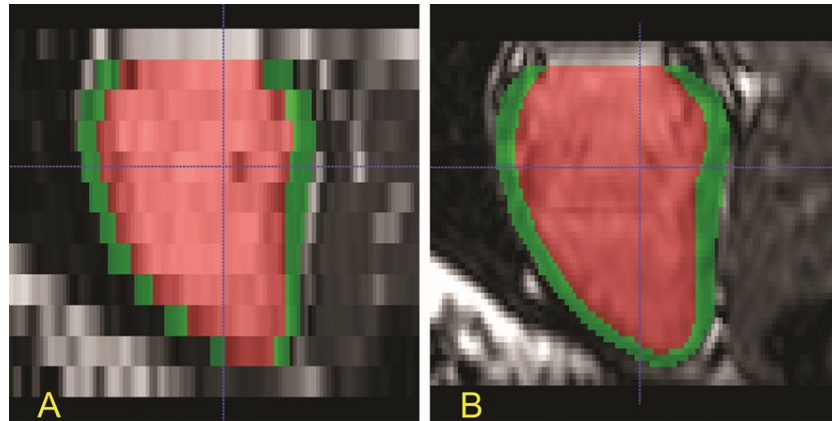


Figure 12.14 – Left ventricular long axis reconstructions of short-axis cine MR images at end-diastole in a healthy volunteer. Automated segmentation of the myocardium is shown in green and the cavity in red. Data from a conventional 2D LVSA is shown in a) compared to a high-spatial resolution 3D LVSA in b).

The mean distance between the surfaces of the segmentation and the manually labelled reference was less for the 3D LVSA compared to the 2D LVSA for both endocardium: $1.09 \text{ mm} \pm 1.07$ vs $2.02 \text{ mm} \pm 1.45$ (95% CI: $0.74 \text{ mm} - 1.12 \text{ mm}$; $P < 0.001$), and epicardium: $1.29 \text{ mm} \pm 1.32$ vs $2.23 \text{ mm} \pm 1.64$ (95% CI: $0.73 - 1.14 \text{ mm}$; $P < 0.001$). An example of wall thickness mapping in one individual using 3D and 2D LVSA images is shown in **Figure 12.15** where the effect of thinner sections using 3D imaging is most apparent at the base and apex of the LV.

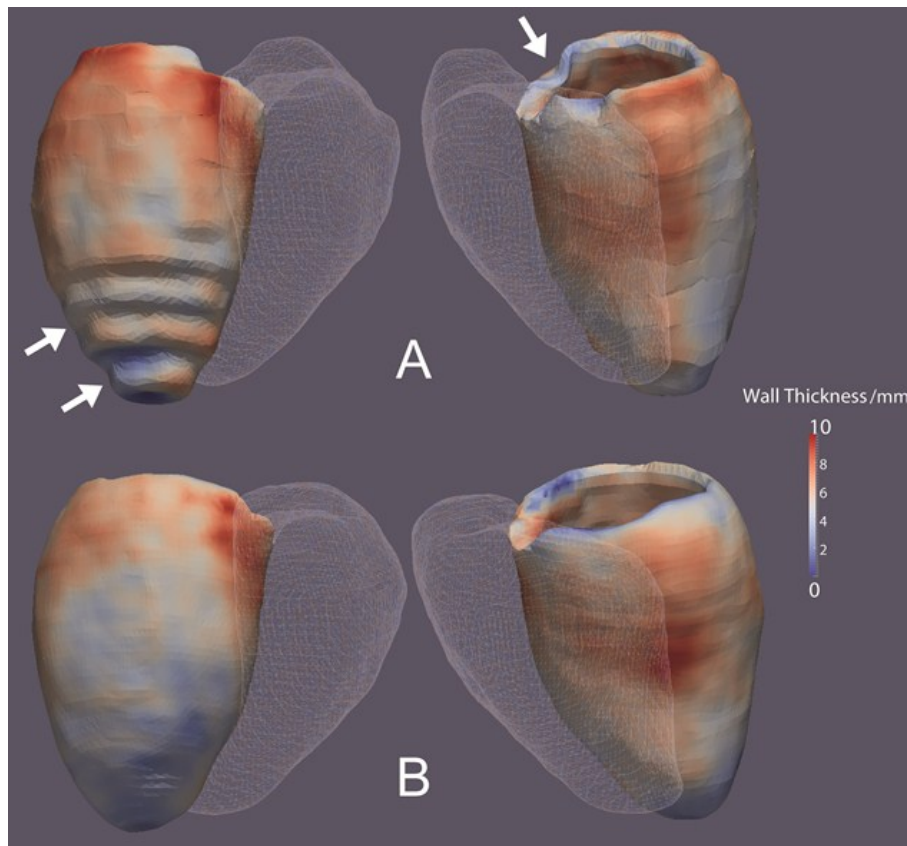


Figure 12.15 – Segmentations of the myocardium in a healthy volunteer with wall thickness shown as a colour-scale. Data from 2D (a) and 3D (b) LVSA cine images are presented with the right ventricle depicted as a mesh. Step artefact due to lower spatial resolution of 2D imaging is visible at the base and apex of the left ventricle (arrows).

Comparison of the 3D LVSA automated segmentations with the respective manually-labelled atlas showed that there was no bias introduced by the segmentation process for calculating LVEDI and LVMI (**Figure 12.16**). Comparison of the automated 3D segmentation with manual volumetry of the corresponding 2D images demonstrated that there was also no bias due to the different imaging techniques for calculating LVEDI and LVMI (**Figure 12.17**).

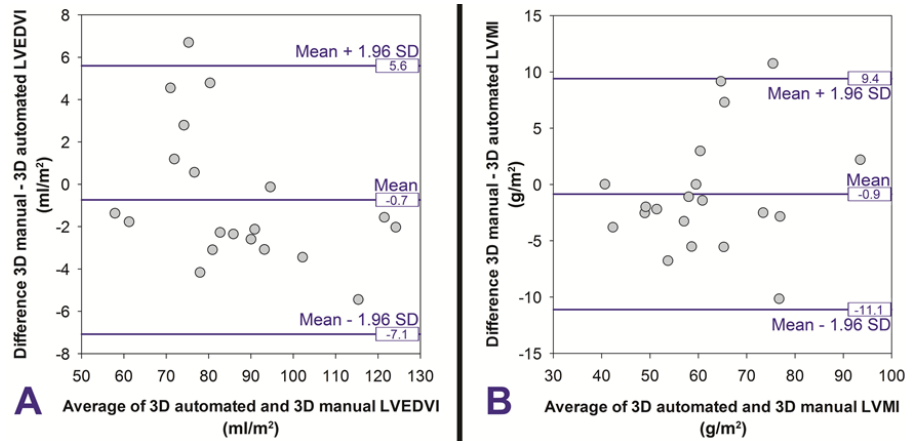


Figure 12.16 – Comparison of automated 3D-LVSA segmentations to their respective manually labelled cardiac atlas in 20 volunteers demonstrating no bias for calculating LVEDI (a) or LVMI (b).

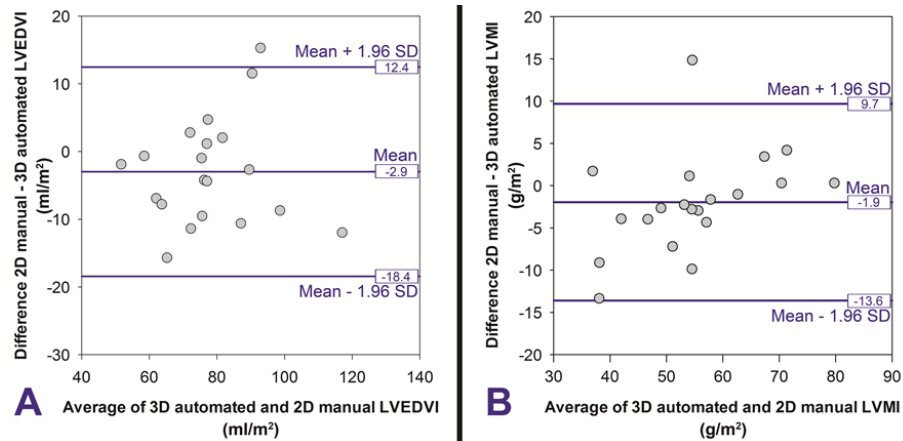


Figure 12.17 - Comparison of automated 3D-LVSA segmentations to manual volumetry of the corresponding 2D LVSA images in 20 volunteers demonstrating no bias for calculating LVEDI (a) or LVMI (b).

The power calculations, performed at each point on the co-registered myocardial surfaces, showed that overall fewer subjects were required for 3D imaging to detect a 1mm difference in wall thickness than 2D imaging (56 IQR: 39 – 78 vs 72 IQR: 49 – 104, $P < 0.001$). The voxelwise reduction in sample size over the surface of the LV is shown in **Figure 12.18**.

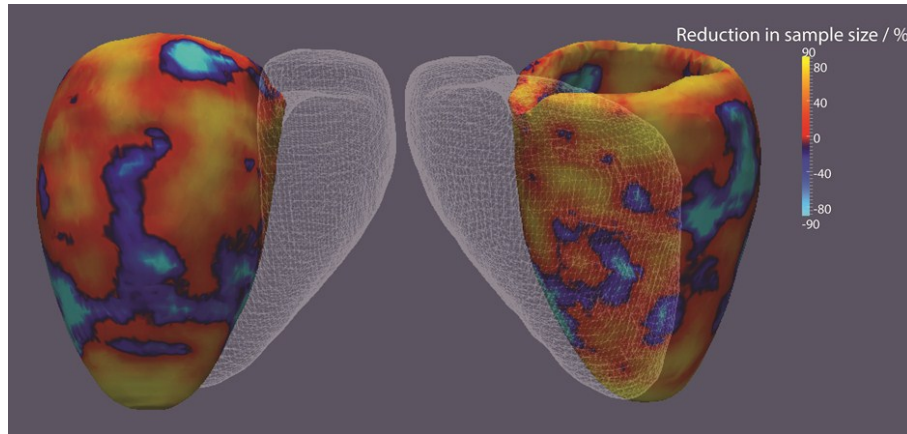


Figure 12.18 – The reduction in sample size required for 3D LVSA segmentations to detect a 1mm difference in left ventricular wall thickness compared to 2D LVSA segmentations is shown using reproducibility data from 20 healthy subjects. The right ventricle is depicted as a mesh. The hot colours show where 3D imaging has the largest effect on reducing sample size which is predominantly at the basal and apical regions. (Values of $\pm 90\%$ are shown).

Reliability

The overall test-retest reliability of both 3D automated analysis and 2D manual analysis for global LV volumes and mass was high. The ICC between 3D LVSA segmentations was 0.97 (95% CI: 0.93 – 0.99, $P < .0001$) for LVEDI and 0.93 (95% CI: 0.82 – 0.97; $P < .0001$) for LVMI. The ICC between manual analyses of 2D LVSA images was 0.98 (95% CI: 0.95 – 0.99; $P < .0001$) for LVEDVI and 0.97 (95% CI: 0.91 – 0.99; $P < .0001$) for LVMI.

The inter-study variability in wall thickness measurements in the 2 subjects scanned on 8 separate occasions was small in both the male (mean standard deviation across the LV = $0.61\text{mm} \pm 0.21$; SD $< 1\text{mm}$ in 95% of the area) and female (subject mean standard deviation across the LV = $0.56\text{mm} \pm 0.26$; SD $< 1\text{mm}$ in 95% of the area) participants (**Figure 12.19**).

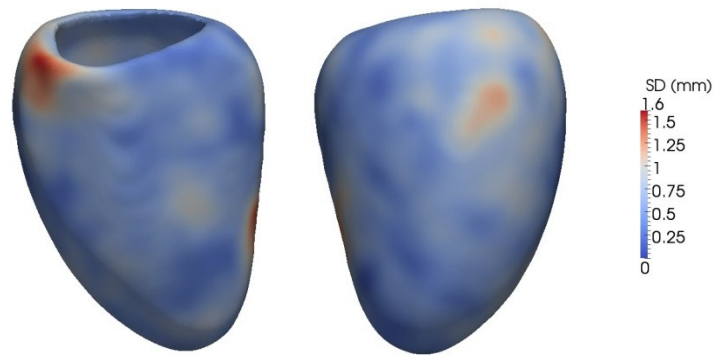


Figure 12.19 – Inter-study variability in wall thickness measurements in a subject scanned on 8 separate occasions over a period of 18 months. In this model standard deviations are plotted (in mm) at each point. SD = standard deviation.

Population mapping of wall thickness

The images of 100 subjects were segmented with a mean unsupervised automated analysis time of 46 minutes per 3D sequence and 12 minutes for 2D. There were no failures of the segmentation algorithm in the cohort. Non-parametric comparison between 2D and 3D LVSA mapping of wall thickness is shown as a significance map in **Figure 12.20**.

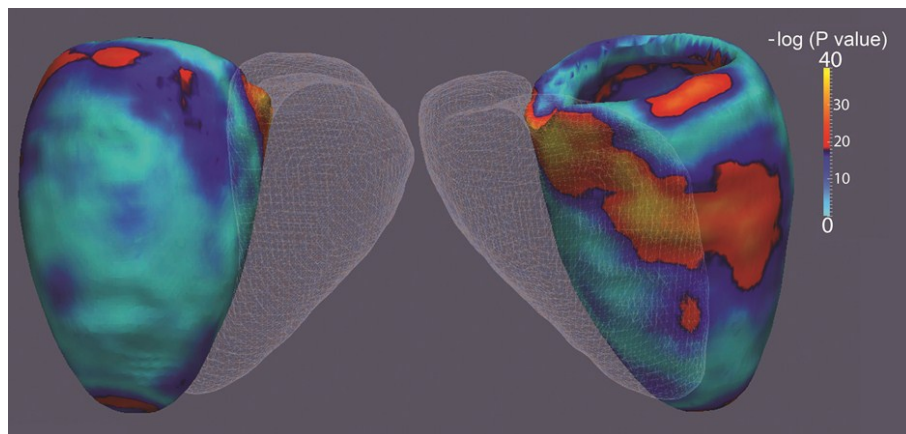


Figure 12.20 – Voxelwise comparisons between LV wall thickness on 2D and 3D LVSA myocardial segmentations in 100 healthy volunteers is shown. The right ventricle is depicted as a mesh. A significance level of 5% corresponds to a value of 12.7 on the scale. Differences in wall thickness between the imaging techniques are apparent at highly curved regions of the base, interventricular septum and apex.

12.7 Discussion

In this study we successfully created a high resolution cardiac atlas using 3D-CMR cine images of 1093 healthy volunteers. This is one of the largest cardiac atlases ever reported. Our cohort is smaller than the number of images available in the Cardiac Atlas Project (CAP) database (approximately $n=2864$ from the MESA study + $n=470$ myocardial infarction patients from the DETERMINE cohort) (288). From these only a sub-cohort of 1991 MESA subjects has been included in an atlas based study (289). Our study is however different from the CAP in that we used high resolution 3D b-SSFP (reconstructed voxel size = $1.2 \times 1.2 \times 2\text{mm}$) whereas the CAP dataset was acquired using a standard 2D cine SSFP sequence (spatial resolution of the images varies from $1.4 \times 1.4 \times 6\text{ mm}$ to $2.5 \times 2.5 \times 6\text{ mm}$) (289). In addition to higher spatial resolution, our single breath hold 3D-CMR is not limited by inter-slice shifts that occur in multi-breath hold sequences. The fact that all are images were acquired in the same scanner, with the same imaging sequence also facilitates consistent analysis.

The results of this study indicate that automated segmentation of high spatial resolution 3D cardiac imaging is a feasible technique for population phenotyping which provides greater accuracy for mapping ventricular wall thickness than conventional 2D cine MR. The greater statistical power to detect changes in wall thickness within the LV promises a significant reduction in sample size for epidemiological and genetic studies into the causes of myocardial hypertrophy and may also have applications in experimental medicine research and interventional trials.

Left ventricular hypertrophy (LVH) is an important cardiac phenotype which is associated with adverse cardiovascular outcomes. In order to explore the genetic and environmental

determinants of LVH large populations are required to reach statistical significance when conventional cardiac MR is used to measure total LV mass (290-292). Although manual assessment of global LV parameters with MR requires a smaller sample size to detect a given change in mass and volume than echocardiography (188), this approach does not extract the regional variations in ventricular wall thickness and function that are characteristic of both hypertrophic and hypertensive cardiomyopathies (293, 294). Cardiac atlases address this problem by creating computational models of phenotypic variation within a population by segmenting and co-registering each subject's MR images (208). Previous studies have relied on conventional 2D cardiac MR but its low through-plane spatial resolution sets intrinsic limitations on evaluating ventricular thickness and cardiac motion especially at the base and apex of the LV (295, 296).

Three dimensional single breath-hold imaging of the LV has shown promise as a method to reduce total acquisition times and avoid section misalignment which provides good agreement for volumes and mass compared to 2D techniques (178-187). These techniques have in general used parallel imaging or exploited temporal correlations in k-space to reduce acquisition time to a single breath hold. In our study we took advantage of the 3D acquisition to use SENSE in two spatial directions simultaneously (183) which significantly reduces geometry-related noise enhancement compared to 1-dimensional parallel imaging (297). This enabled us to acquire high spatial resolution 3D cine images with an acceptable reduction in contrast and image quality compared to 2D imaging. Future studies in patient groups may also benefit from improvement in myocardium to blood pool contrast by using intravenous contrast medium (298).

As 3D imaging generates between 50 to 60 sections per cardiac phase manual analysis of the images is impractical and also does not fully exploit the advantages of whole organ imaging. Many approaches have been used for automated cardiac segmentation (299) and in our study

we developed a multi-atlas technique which uses prior data from a set of manually-labelled high spatial resolution cardiac images. By finding correspondences between anatomical patches in the target images and each of the 20 twenty atlases we were able to achieve an accurate segmentation that was tolerant of lower image contrast and was not biased by any single atlas. We found a good agreement between our segmented data and conventional 2D volumetric quantification. However, the greatest advantage in 3D imaging was shown to be in assessing regional variations in wall thickness where partial volume effects at the base, septum and apex were significantly reduced compared to 2D imaging.

The ability to anatomically co-register each point in the heart throughout a large study population offers a powerful technique for extracting phenotypic data (208). It allows the creation of statistical models of whole-heart physiology and anatomy that can be adjusted for anthropometric or environmental covariates. Neuroimaging studies have modelled the statistical power of 3D imaging (300) and our calculations indicate a significant reduction in sample size is possible over most of the myocardium for detecting differences in wall thickness. The primary application of this technique will be to allow prospective imaging-genetics association studies to be conducted more efficiently and reach statistical significance with fewer patients. Studies such as the enhanced phase of UK Biobank will collect cardiac MR data from large cohorts of unselected participants and these techniques will enable comprehensive, efficient and statistically powerful computational modelling of the biological effects of environment and genetic effects on cardiac structure and function (301). Based on the 1093 segmented datasets so far included in the atlas pool we have computed a statistical shape model that encodes the normal variation in cardiac anatomy. Our healthy atlas model has the potential to be used in studies of disease cohorts and help determine the likelihood that a given phenotype is normal or pathological. The integration of high-resolution imaging with multiparametric “-omics” data may also have a role in “precision medicine” where

diagnostic, prognostic, and therapeutic strategies are specifically tailored to each patient's requirements (302).

As we did not include subjects with known cardiovascular disease we have not tested if the imaging sequence or segmentation methods will be transferable to all patient groups. However, even within our healthy population the phenotypic variability was considerable. Furthermore, we note that despite the wide age range and heterogeneous levels of physical fitness all our participants successfully completed the imaging protocol. Our power calculations were conservative and did not model the more plausible biological effects of concentric or localised asymmetric changes in wall thickness. Translating these approaches to genetic studies will require the development of regression models which address the potential problem of multiple testing within large imaging datasets.

12.8 Conclusions

In this study we have used an automated approach to segment 3D-CMR images and created a high resolution atlas of the human heart. We have demonstrated that automated segmentation of high spatial resolution single breath-hold 3D cine MR imaging was more accurate than conventional 2D imaging for mapping LV anatomy and offered a reduction in the sample size required for epidemiological and genetic studies of heart disease.

12.9 Acknowledgments

The Digital Heart Project was conceived and coordinated by Professor Stuart Cook and Dr. Declan O'Regan. The creation of the original set of 20 cardiac atlases was shared with Tim Dawes, under the supervision of Dr. Declan O'Regan. Wenzhe Shi and Wenjia Bai developed the automated segmentation algorithm with Professor Daniel Rueckert. Christopher Minas contributed to the statistical analysis of the data. Dr. Niall Keenan contributed to the manual data analysis.

12.10 Appendix

For simplicity we consider each of the $P = 46808$ points across the myocardium independently and assume that the difference in wall thickness is normally distributed. This allows us to compute the sample size required to detect a change in wall thickness of δ at point j given a significance level α , power p and variance σ_j^2 as:

$$N_j = \frac{2f(\alpha, p)\sigma_j^2}{\delta^2}$$

where $f(\alpha, p) = (u_\alpha + u_{2(1-p)})^2$ where u_γ is the value of the standard Normal distribution (mean 0 and variance 1) such that the probability of lying between $-u_\gamma$ and u_γ is $1 - \gamma$ (303). Here, α and p can be set accordingly; typical values are $\alpha = 0.05$ and $p \in [0.8, 0.9]$, and here we use $p = 0.9$. In order to conservatively account for the multiple comparisons in considering all P points independently, we use the Bonferroni adjusted significance level of α/P instead of simply α . Then $f(\alpha/P, p) = 38.04$.

Two myocardium images were obtained for each of $N = 20$ control subjects at the two time-points; 2D segmentations denoted $\{x_{ij}^{2D}\}$ and $\{y_{ij}^{2D}\}$, and 3D segmentations denoted $\{x_{ij}^{3D}\}$ and $\{y_{ij}^{3D}\}$ for $i = 1, \dots, N$ and $j = 1, \dots, P$. For the 2D and 3D segmentations, the differences in wall thickness between time-points at each point across the myocardium are given by $\{d_{ij}^{2D}\} = \{x_{ij}^{2D} - y_{ij}^{2D}\}$ and $\{d_{ij}^{3D}\} = \{x_{ij}^{3D} - y_{ij}^{3D}\}$ respectively. We note that for both the 2D and 3D segmentations, the differences do not exhibit non-normal behaviour (Shapiro test p-values are greater than the Bonferroni adjusted 5% significance level of $0.05/46808$). Hence

the assumption of normality of the differences which is required to use the above sample size formula is valid.

The variance of the differences at each of the P points of the 2D and 3D segmentations are computed and denoted $(\sigma^2)_j^{2D}$ and $(\sigma^2)_j^{3D}$. These can then be inserted in place of σ_j^2 in the above sample size formula. In particular, the sample size required to detect a change in wall thickness of $\delta = 1$ at point j with $f(\alpha/P, p) = 38.04$ ($\alpha = 0.05/46808$ and $p = 0.9$) for the 2D and 3D segmentations can then be obtained via

$$N_j^{2D} = 75.99 \times (\sigma^2)_j^{2D} \text{ and } N_j^{3D} = 38.04 \times (\sigma^2)_j^{3D}$$

respectively. The percentage decrease in sample size in using a 3D segmentation over a 2D segmentation can be computed at each point as

$$\left(\frac{N_j^{2D} - N_j^{3D}}{N_j^{2D}} \right) \times 100$$

13 Blood pressure as a determinant of left ventricular morphology and function

13.1 Introduction

At least a quarter of the world's adult population has hypertension and the increasing burden of disease has prompted efforts to search for earlier interventions and more effective therapeutic targets (304). Adverse structural and functional adaptations of the heart are of crucial relevance to the heightened cardiovascular risk associated with systemic hypertension, are frequently already established by the time therapy has been initiated (305-307), and are independent determinants of all-cause mortality (308-310). It remains uncertain what determines the onset and pattern of left ventricular (LV) remodelling but the duration and severity of elevated blood pressure (BP) as well as genetic, metabolic and environmental factors are all likely to be important (311). Although LV remodelling is known to begin at below-hypertensive levels there is little data on how untreated healthy subjects adapt to rising BP, at what stage adverse LV changes are initiated, the true nature of remodelling at high-resolution and what mechanical factors drive hypertrophy (236, 312).

Our knowledge of the natural history of hypertensive heart disease in human populations has been developed from volume and mass measurements derived using conventional 2-dimensional (2D) echocardiography and cardiac magnetic resonance (CMR) imaging. These 2D methods have intrinsic limitations as they incompletely sample the heart, rely on geometric assumptions and are poorly equipped to assess regional variations. Three-dimensional CMR (3D-CMR) combined with computational cardiac-atlas based phenotyping of the heart has advantages over conventional imaging as it enables quantitative whole-heart

assessment of cardiac physiology and non-invasive modelling of the predictors of LV morphology, function and wall stress. Furthermore, we have shown increased accuracy for mapping ventricular wall thickness when compared to conventional 2D cine MR. This provides greater statistical power to detect changes in LV wall thickness making this technique particularly suited for studies in which global phenotypes, typical of advanced disease, are unlikely to be prevalent.

In this study we used an automated algorithm based on the Digital Heart Project's cardiac atlas to analyse 3D-CMRs in a large cohort. Our primary purpose was to define the relationship between SBP and region-specific LV adaptations in a population of healthy adults not taking anti-hypertensive medications.

13.2 Methods

Study population

1530 volunteers (54.8% females; 74.8% Caucasian; age range: 18 – 81 years; mean age 41.3 ± 13.0 years) were recruited prospectively via advertisement to the Digital Heart Project at Imperial College London. Detailed descriptions of the full cohort, eligibility criteria and biophysical assessment methods can be found in section 11.3 above.

Imaging Protocol

CMR was performed on a 1.5T Philips Achieva system (Best, Netherlands). Full details of the imaging protocol can be found in section 11.3 above. In this study we used the 2D cine

balanced steady-state free precession (b-SSFP) images, as well as the single breath-hold 3D left ventricular short axis (LVSA) b-SSFP sequence.

Cardiac magnetic resonance analysis

Volumetric analysis of 2D LV cine images was performed using CMRtools (Cardiovascular Imaging Solutions, London, UK) as described in section 11.2. Cardiac volumes and mass were indexed to body surface area (BSA).

Three dimensional assessment of ventricular structure and function

Atlas-based automated segmentation of the 3D-CMR images was used to extract the myocardial shape and quantify phenotypic parameters as was described in section 12.4 (**Figure 13.1**). Segmentation was implemented using Matlab (Mathworks, Natick, MA) and performed on a high performance server (Dell, Round Rock, TX). Each subject's dataset was co-registered to Digital Heart Project cardiac atlas spatial template ensuring that every point in the statistical model had the same anatomic correspondence throughout the population.

LV wall parameters were calculated at 19185 points in the endocardium and 27623 points in the epicardium. Wall thickness (WT) was measured perpendicular to a midwall plane equidistant to the endocardial and epicardial surfaces. Conventionally relative wall thickness (RWT) is calculated by adjusting for LV end-diastolic volume (LVEDV) or cavity radius. However, taking advantage of whole organ phenotyping, here we applied the computational 3D spatial normalisation approach described in section 12.5 to correct each wall thickness measurement for heart size. Variation in the position of the endocardial and epicardial surfaces was assessed by the distance and direction required to translate each point on the

heart to the coregistered average cardiac shape. Fractional wall thickening (FWT) was calculated as $(\text{end-diastolic WT} - \text{end-systolic WT}) / \text{end-diastolic WT} \times 100$.

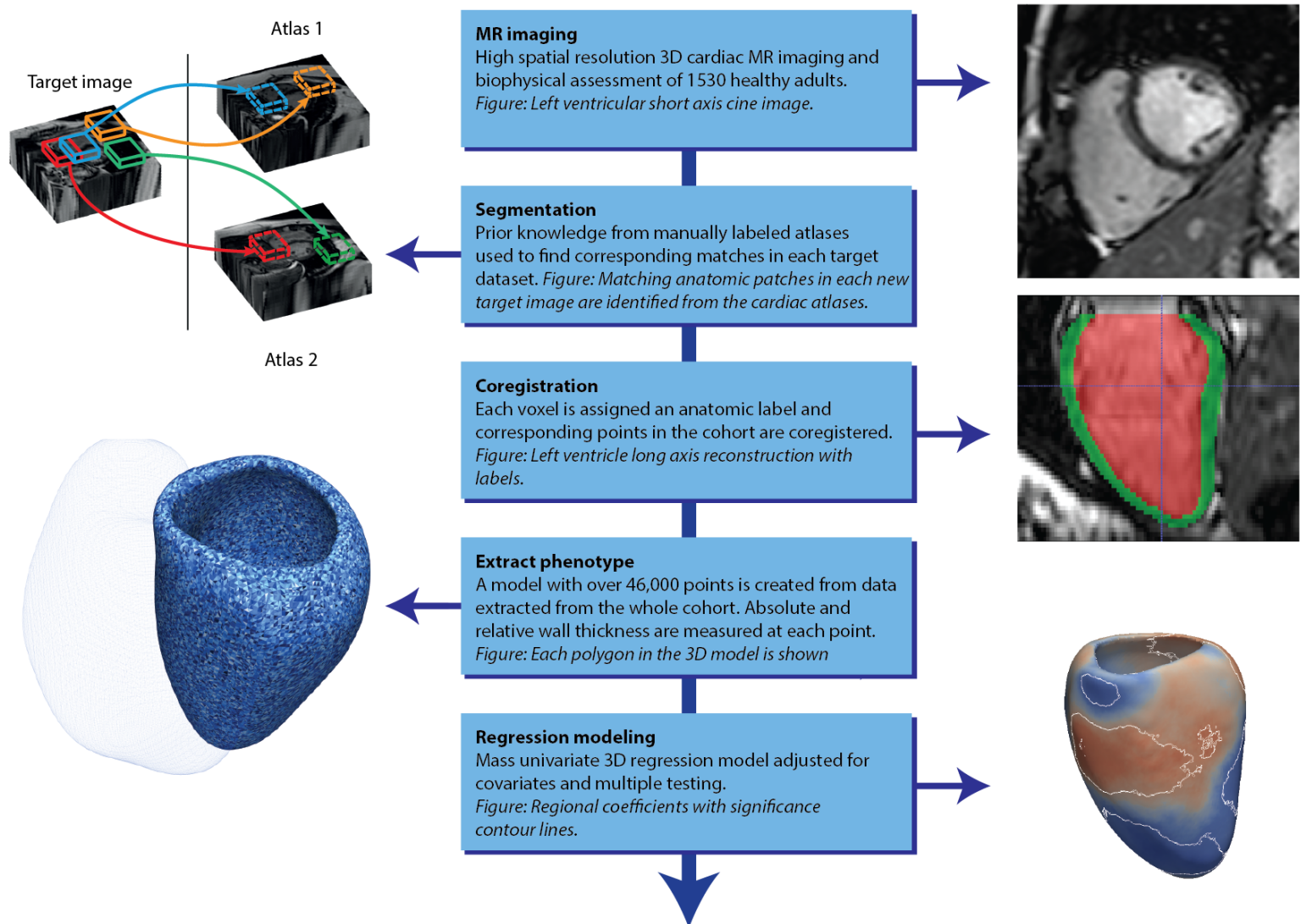


Figure 13.1 – 3D-CMR atlas-based automated method used to build 3D statistical models of how anthropometric, environmental or genetic factors influence left ventricular phenotype. This paradigm allows the adaptations of whole-heart structure and function in response to a stimulus to be explored.

The definitions of LV geometry used in conventional assessment of chamber size were adapted for 3D datasets (313). A regional hypertrophic response by the myocardium was defined as a positive regression coefficient between WT and SBP. A concentric pattern was

present if there was a positive SBP correlation with RWT and a negative correlation with endocardial volume. Conversely, an eccentric pattern was indicated by a positive SBP correlation with endocardial volume and a negative correlation with RWT.

Regional end-systolic wall stress (WS) was determined at each point in the left ventricle from the 3D endocardial radius of curvature (R) on the endocardial surface and myocardial WT and calculated as follows (287):

$$Wall\ stress \propto SBP \times \frac{R}{WT}$$

Statistical analysis

Data were analysed using RStudio Server version 0.98 (Boston, MA). Continuous variables are expressed as mean \pm standard deviation (SD) and categorical variables as percentages. Ranges have been included for CMR derived parameters. Data from more than two groups were analysed using a Kruskal-Wallis one-way analysis of variance test. When significant differences were detected a Nemenyi post-hoc test was applied for pairwise multiple comparisons. The associations between variables and cardiac phenotypes were assessed in separate multiple linear regression models that included age, gender, race, BSA and systolic blood pressure. Race was dummy-coded with the largest group, Caucasian, as the reference. The associations between morphological and functional parameters for each point in the 3D datasets were assessed using a regression model adjusted for age, gender, race and BSA with correction to control the false discovery rate (314). Contiguous regions of the left ventricle where the association between variables was significant ($p < 0.05$) were identified and the relationship with SBP reported as the mean of the standardized β coefficients within that area.

13.3 Results

Study population characteristics

A summary of subject characteristics for the whole cohort and by gender is shown in **Table 5**. In **Table 10** the same data were split by levels of systolic blood pressure (SBP) according to the Seventh Report of the Joint National Committee on Prevention, Detection, Evaluation, and Treatment of High Blood Pressure (JNC-7) criteria (315). Of the 1530 volunteers, 7.1% had stage 1 or 2 systolic hypertension ($SBP \geq 140$ mmHg), 37.1% had systolic pre-hypertension (SBP 120 – 139 mmHg) and 55.8 % had systolic normotension ($SBP < 120$ mmHg) as shown in **Figure 13.2**. Summary of the linear regression models can be found in **Table 8** for the whole cohort and in **Table 9** for males and females separately.

Two dimensional imaging

After adjusting for Age, Race and BSA, SBP was positively associated with LVEDV in males ($\beta=0.07$, $p=0.023$) and females ($\beta=0.07$, $p=0.022$). In both genders there is a positive association between SBP and LV stroke volume (LVSV; women: $\beta=0.12$, $p<0.001$; men: $\beta=0.12$, $p<0.001$). No association was found between SBP and LV end systolic volume (LVESV) in either gender or with LV ejection fraction (LVEF) in males. In females LVEF is positively associated to SBP ($\beta=0.15$, $p<0.001$). SBP is strongly positively associated in both genders with Concentricity index (males and females: $\beta=0.18$, $p<0.001$) and LV mass (males and females: $\beta=0.20$, $p<0.001$). Finally, cardiac output and SBP are positively associated in both males ($\beta=0.17$, $p<0.001$) and females ($\beta=0.17$, $p<0.001$).

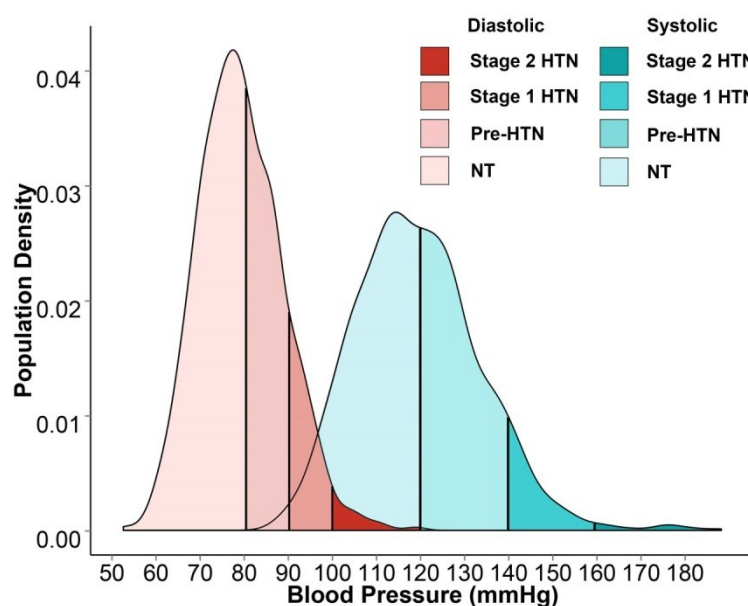


Figure 13.2 – Density plot showing the distribution of blood pressure readings in the cohort. The thresholds applied are those recommended in the Seventh Report of the Joint National Committee on Prevention, Detection, Evaluation, and Treatment of High Blood Pressure (JNC-7) within our cohort (n=1530). HTN = hypertension; Pre-HTN = pre-hypertension; NT = normotension.

There was a significantly higher number of females in the normotensive cohort than in the two other groups which were very similar in gender composition. Indeed, as we can see from **Table 5**, SBP was consistently higher in males than in females (**Figure 13.3**). Hypertensives were significantly older than members of the other cohorts. No difference was found between the groups in terms of racial background. As expected, SBP, Pulse wave velocity and diastolic blood pressure are closely associated and rise in tandem. While there were no differences between pre-hypertensives and hypertensives in terms of height, weight, body surface area (BSA), body mass index (BMI), fat mass and lean mass, subjects from the normotensive group had lower indices of all these variables than the other two groups.

					K-W P-Value	Post-hoc Nemenyi p -Value		
	NT n=854 (55.8%)	Pre-HTN n=567 (37.1%)	HTN n=109 (7.1 %)			NT vs PHTN	NT vs HTN	PHTN vs HTN
Gender					<0.001	<0.001	<0.001	0.94
Males (%)	275 (32.2%)	347 (61.2%)	69 (63.3%)					
Females (%)	579 (67.8%)	220 (38.8%)	40 (36.7%)					
Age (years)	38.3 ± 11.9	43.6 ± 13.1	52 ± 12.2		<0.001	<0.001	<0.001	<0.001
Race / Ethnicity:					0.24	-	-	-
Caucasian	610 (71.4%)	441 (77.8%)	93 (85.3%)					
South Asian	125 (14.6%)	59 (10.4%)	10 (9.2%)					
African	63 (7.4%)	36 (6.3%)	5 (4.6%)					
Other	56 (6.6%)	31 (5.5%)	1 (0.9%)					
Systolic BP (mmHg)	108.4 ± 7.4	127.6 ± 5.3	147.8 ± 9.1					
Diastolic BP (mmHg)	73.2 ± 6.7	83.3 ± 7.3	93.2 ± 8.7		<0.001	<0.001	<0.001	<0.001
PWV (m/s)	4.2 ± 1.2* (* n=682)	5.1 ± 1.7 ** (**n=436)	6.6 ± 2.6*** (*** n=78)		<0.001	<0.001	<0.001	<0.001
Height (cm)	168.4 ± 9.0	171.8 ± 9.2	171.7 ± 10.8		<0.001	<0.001	0.003	0.90
Weight (kg)	67.9 ± 12.4	75.2 ± 12.6	78.0 ± 14.4		<0.001	<0.001	<0.001	0.38
Body Surface Area (m²)	1.8 ± 0.2	1.9 ± 0.2	1.9 ± 0.2		<0.001	<0.001	<0.001	0.59
BMI (kg/m²)	23.9 ± 3.7	25.4 ± 3.8	26.4 ± 4.1		<0.001	<0.001	<0.001	0.10
Fat Mass (kg)	17.8 ± 7.7	18.7 ± 8.8	20.4 ± 9.2		0.03	0.37	0.03	0.17
Lean Mass (kg)	50 ± 10.6	56.5 ± 10.9	57.6 ± 12.7		<0.001	<0.001	<0.001	0.93

LVEDV (ml)	140 ± 30 (69 – 256)	152 ± 32 (79 – 251)	154 ± 37 (82 – 252)	<0.001	<0.001	<0.001	0.99
LVESV (ml)	49 ± 15 (19 – 127)	53 ± 17 (19 – 121)	52 ± 19 (17 – 111)	<0.001	<0.001	0.47	0.53
LVSV (ml)	91 ± 18 (46 – 189)	99 ± 19 (57 – 172)	102 ± 23 (61 – 168)	<0.001	<0.001	<0.001	0.85
LVEF (%)	65 ± 5 (47 – 80)	66 ± 6 (47 – 81)	67 ± 6 (51 – 80)	0.001	0.18	0.001	0.04
LVM (g)	105 ± 30 (40 – 270)	123 ± 33 (56 – 255)	134 ± 41 (68 – 245)	<0.001	<0.001	<0.001	0.18
LVEDVI (ml/m²)	78 ± 12 (44 – 126)	80 ± 14 (48 – 129)	80 ± 14 (48 – 117)	0.04	0.03	0.858	0.715
LVESVI (ml/m²)	27 ± 7 (12 – 57)	28 ± 8 (11 – 66)	27 ± 8 (11 – 49)	0.22	-	-	-
LVSVI (ml/m²)	51 ± 7 (26 – 90)	53 ± 8 (34 – 88)	53 ± 9 (35 – 74)	<0.001	<0.001	0.14	0.99
LVMi (g/m²)	59 ± 13 (33 – 182)	65 ± 14 (31 – 112)	69 ± 18 (38 – 141)	<0.001	<0.001	<0.001	0.16
CI (g/ml)	0.8 ± 0.1	0.8 ± 0.2	0.9 ± 0.2	<0.001	<0.001	<0.001	0.003
Cardiac Output (L)	5.7 ± 1.2	6.4 ± 1.5	6.6 ± 1.7	<0.001	<0.001	<0.001	0.68
Heart rate (BPM)	63.9 ± 9.6	65.1 ± 10.8	65.8 ± 12.0	0.11	-	-	-

Table 10 - Subject characteristics and CMR-derived cardiac measurements by SBP group (n=1530). Values are in mean ± SD or percentage. CMR parameters include ranges. Kruskal-Wallis tests were carried for each variable to determine if difference between groups (NT, PHT and HT) were significant. P-values are for pairwise comparisons. NT = normotension; PHTN = pre-hypertension; HTN = hypertension; BMI = body mass index; BP = blood pressure; BPM = beats per minute; CI = concentricity index; LVEDV(I) = (indexed) left ventricular end diastolic volume; LVESV(I) = (indexed) left ventricular end systolic volume; LVEF = left ventricular ejection fraction; LVM(I) = (indexed) left ventricular mass; PWV = pulse wave velocity

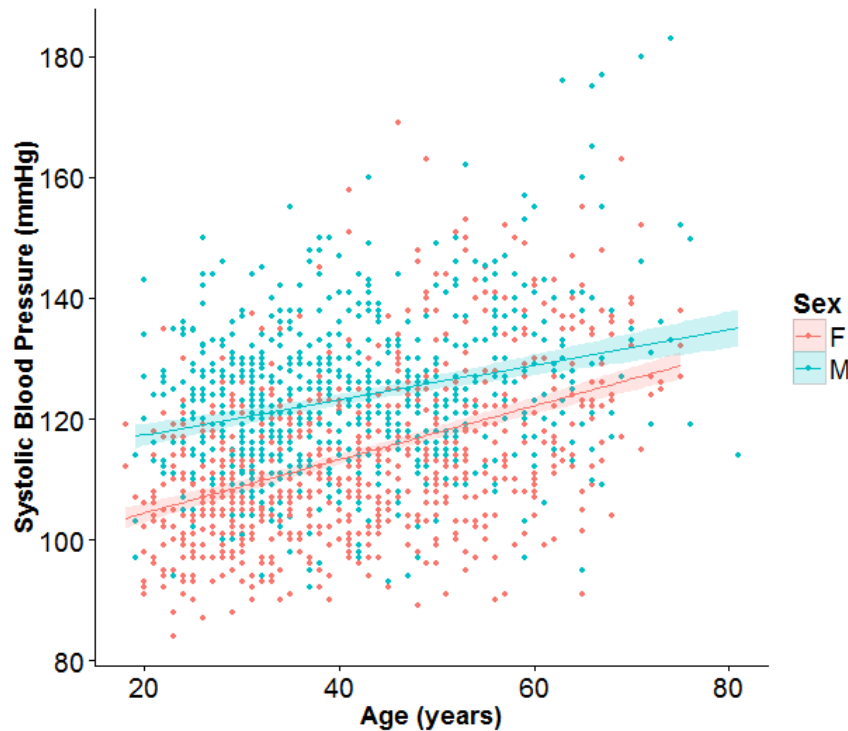


Figure 13.3 – Scatterplot of age against systolic blood pressure by gender with a linear regression fit (with 95% confidence intervals). F = Female; M = Male)

In terms of cardiac parameters normotensives had lower LVEDV, LVESV, LVSV and LVM than in the groups with higher blood pressure. After indexation those with SBP <120mmHg still had the lowest LVEDVI, LVSVI and LVMI. There was no difference between the groups in terms of LVESVI. Concentricity index was progressively higher in subgroups with higher SBP.

Three dimensional LV geometry

The regression model explained more of the variability in WT within the septum and anterior walls than the lateral wall (**Figure 13.4**). The pattern of LV hypertrophy and remodeling observed with respect to each of the phenotypic variables is illustrated in **Figure 13.5**.

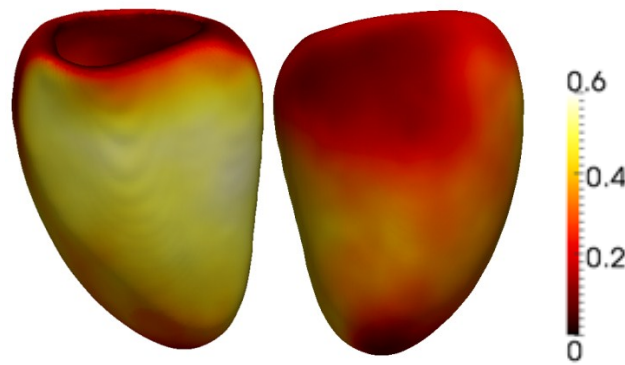


Figure 13.4 – Three dimensional R^2 for the regression model of systolic blood pressure vs wall thickness in the whole cohort. Spatial variation in the R^2 coefficient is shown within the left ventricle for the regression model of systolic blood pressure vs wall thickness adjusted for body surface area, gender, race and age. Left ventricular projections in each panel: Left = facing the septum; Right = facing the lateral wall.

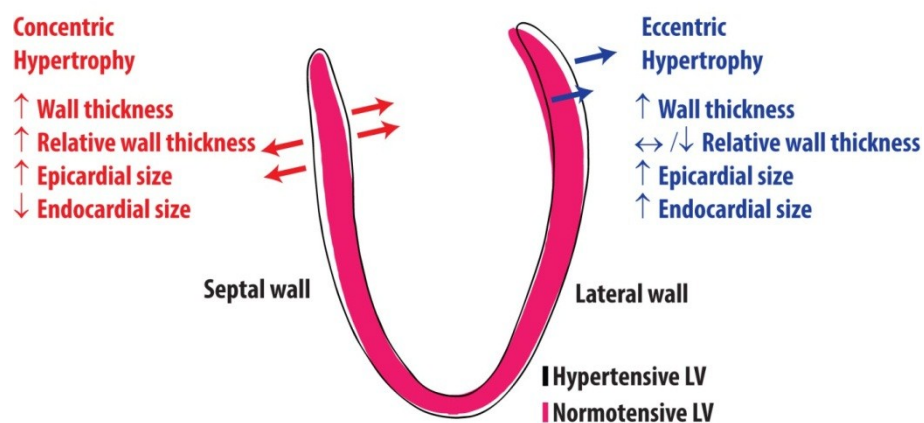


Figure 13.5 – Three dimensional model of the regional changes in left ventricular geometry associated with systolic blood pressure. A long-axis section of the 3D-CMR-derived fitted regression model taken at systolic blood pressures of 100 mmHg (red filled contour) and 180 mmHg (black outline) shows how LV geometry varies between these two blood pressures. Arrows indicates the relationship between each coefficient and systolic blood pressure.

In normotensives the 3D regression models revealed a positive relationship between SBP and WT throughout the left ventricle ($\beta = 0.08$, significant area = 99%) with the strongest effect

observed in the septum and anterior wall. Controlling for ventricular volume, a positive relationship was also found between SBP and RWT that was strongest in the mid-ventricular anterior and septal walls ($\beta = 0.06$, significant area = 32%) but was not observed in basal or lateral walls **Figure 13.6**).

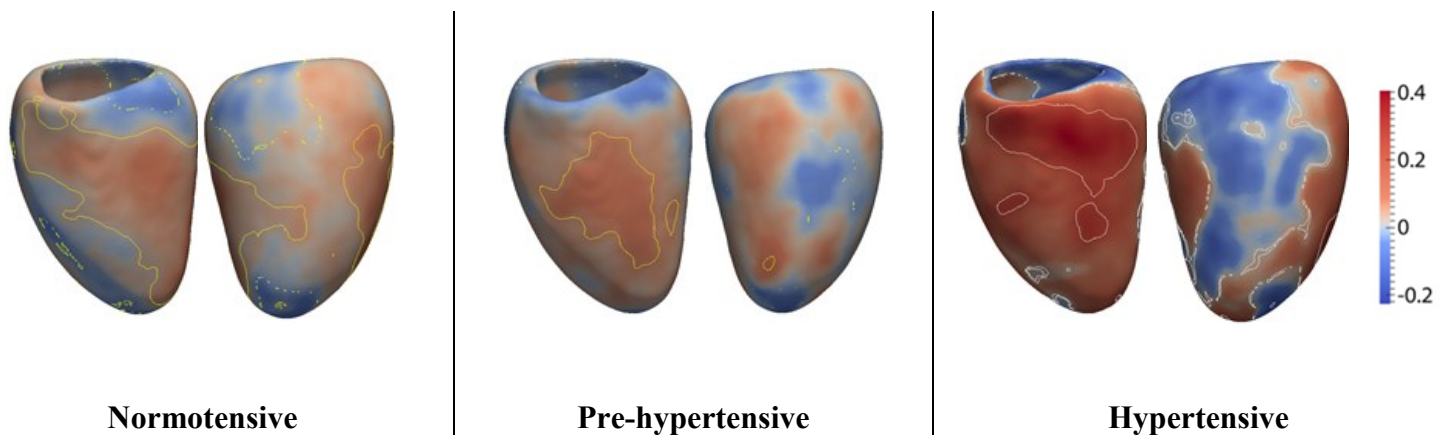


Figure 13.6- Three dimensional regression models of the association between systolic blood pressure and left ventricular relative wall thickness in normotensives, pre-hypertensives and hypertensives. The regression coefficients between systolic blood pressure and left ventricular relative wall thickness are shown for subjects categorized by JNC-7 thresholds. Positive coefficients indicate concentric hypertrophy and negative coefficients eccentric hypertrophy. Contour lines indicate significant regions ($p < 0.05$) before (white border) and after (yellow border) correction for multiple testing respectively. Left ventricular projections in each panel: Left = facing the septum; Right = facing the lateral wall.

In pre-hypertensives, WT was positively related to SBP throughout the septal and anterior walls including the apico-anterior and lateral walls $\beta = 0.11$, significant area = 15%. The greatest hypertrophic response in RWT was observed in the mid-ventricular anterior and septal walls ($\beta = 0.08$, significant area = 8%) with negative coefficients elsewhere.

In hypertensives, there was a strong and asymmetric association between SBP and both WT ($\beta = 0.41$, significant area = 0.7%) and RWT ($\beta = 21.5$, significant area = 14.4%) that was observed in the basal septal and anterior walls, with a negative association in the lateral wall.

To determine the nature of the LV remodeling we examined the effects of SBP on both the epicardial and endocardial surfaces. Overall, there was a global increase in LV epicardial volume associated with SBP ($\beta = 0.09$, significant area = 92%). The majority of the LV endocardial surface also showed an outward expansion in response to ($\beta = 0.06$, significant area = 51%). Taken together, these data show a predominant eccentric hypertrophic pattern in response to SBP. However, in a region from the basal anteroseptal wall to the mid-ventricular anterolateral wall the increase in WT had an inwards component ($\beta = -0.02$, significant area = 4.6%) at the expense of the LV cavity (**Figure 13.7**). Considering the changes in both RWT and endocardial volume, increasing SBP is characterized by a pattern of regional concentric hypertrophy in the septum and anterolateral wall and eccentric hypertrophy elsewhere.

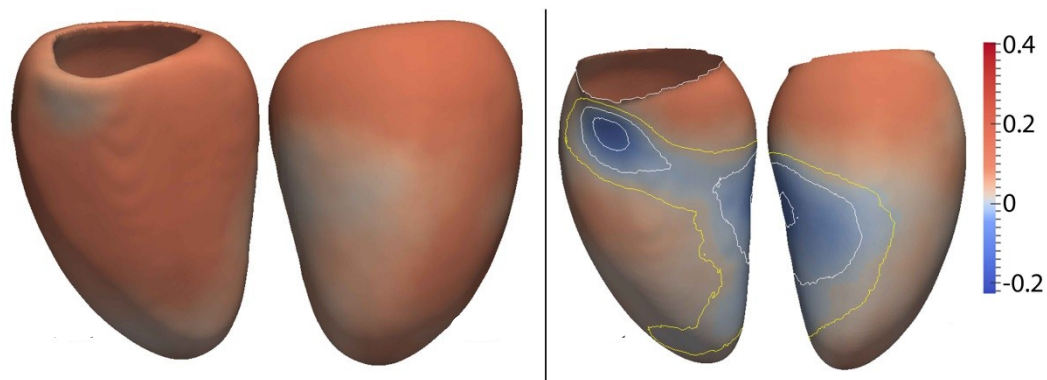


Figure 13.7 - Three dimensional regression models of the association between systolic blood pressure and left ventricular geometry across the cohort. The regression coefficients between systolic blood pressure and left ventricular shape are shown for the epicardial (left panel) and endocardial (right panel) surfaces. A positive coefficient indicates an outward expansion of the surface and a negative coefficient an inward contraction. Contour lines indicate significant regions ($p < 0.05$) before (white border) and after (yellow border) correction for multiple testing. When no lines are visible all points are significant. While the majority of the left ventricle exhibits eccentric hypertrophy, the septum and anterior wall undergo concentric hypertrophy. Left ventricular projections in each panel: Left = facing the septum; Right = facing the lateral wall.

We then assessed the effect of sex and found a significant interaction between gender and the hypertrophic response to SBP with males having larger coefficients at the mid-ventricular anterior and septal walls (interaction $\beta = 0.67$, significant area = 8.5%).

Three dimensional LV function

In normotensives, FWT was positively associated with SBP in the anterior and septal walls and lateral wall ($\beta = 0.10$, significant area = 25.2%) indicating preserved or hyperdynamic radial function across SBP in normotension. In pre-hypertensives the positive relationship between SBP and FWT was limited to the mid-ventricular lateral and inferior walls ($\beta = 0.09$, significant area = 15.7%) with negative coefficients in the basal septum and anterior walls. In hypertensives FWT had stronger negative association with SBP which was localised to the basal and mid-ventricular septum ($\beta = -0.23$, significant area = 3.2%) revealing reduced radial function co-localised to the area of greatest hypertrophic response. When analysing the whole cohort, FWT was positively associated with SBP throughout most of the LV. However in the septum there is either no association or negative association between SBP and FWT. This occurs in the areas where the most significant hypertrophy in response to SBP was observed (**Figure 13.8**).

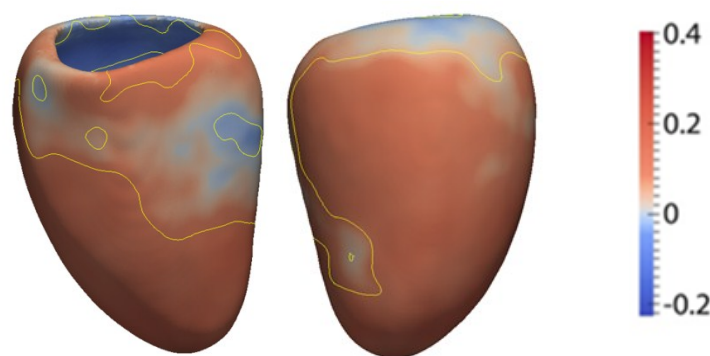


Figure 13.8 - Three dimensional regression models of the association between systolic blood pressure and fractional wall thickening across the cohort. The regression coefficients

between systolic blood pressure and fractional wall thickening are shown in the epicardial surface. Yellow contour lines indicate significant regions ($p < 0.05$) and after correction for multiple testing. While fractional wall thickening is positively associated with SBP in the majority of the left ventricle it is either not associated or negatively associated with SBP in the septum. This occurs in the regions where the most significant hypertrophy occurs. Left ventricular projections in each panel: Left = facing the septum; Right = facing the lateral wall.

Three dimensional wall stress

Across the full cohort WS was strongly positively associated with SBP ($\beta = 0.34$, significant area = 91%) in the majority of LV, demonstrating an uncompensated increase in WS. However, in the basal anteroseptum and mid-ventricular anterior wall there was no significant association between WS and SBP. This demonstrates that only in these regions was the increase in blood-pressure dependent WS compensated for by proportionate concentric hypertrophy (**Figure 13.9**).

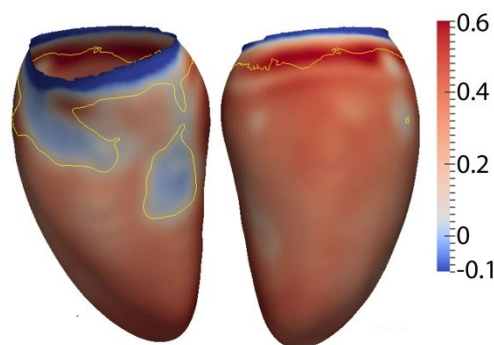


Figure 13.9 - Three dimensional regression models of the association between systolic blood pressure and regional end-systolic wall stress (WS) across the cohort. The regression coefficients are shown in the endocardial surface with positive coefficients indicating increased WS with rising SBP. Yellow contour lines indicate significant regions ($p < 0.05$) after correction for multiple testing. In areas of septal concentric hypertrophy the increase in WS is matched by an increase in WT, however elsewhere there is a significant increase in

WS in response to rising SBP. Left ventricular projections: Left = facing the septum; Right = facing the lateral wall.

13.4 Discussion

This study provides new insights into the effects of SBP on LV morphology and function using advanced cardiovascular phenotyping and computational modelling. This approach provides new opportunities for understanding the regulation of LV hypertrophy in humans and can be applied to large population-level datasets for mechanistic or interventional studies (316, 317). Our findings show that the precursors of the hypertensive heart phenotype can be traced to healthy normotensive adults and that an independent and continuous relationship exists between adverse LV remodelling and SBP in a low-risk population.

The invasive multimodality assessment of cardiac remodelling performed by Grossman et al in 1975 continues to raise unanswered questions about the distinction between adaptive and maladaptive hypertrophy in LV pressure overload (318). This seminal study advanced the hypothesis that pressure overload causes elevated WS, which stimulates a concentric pattern of compensatory hypertrophy that is a central dogma of physiology and medical teaching (319). However, such responses are not purely compensatory as load-induced hypertrophy does not always have adaptive value (320) and an augmented contractile state can occur without hypertrophy (321). Both LV mass (306) and SBP (322) show a continuous and independent relationship to disease risk, but the mechanisms underlying these associations remain elusive.

Biomechanical stress is thought to induce compensatory concentric hypertrophy and this premise underpins well-established experimental models of pressure overload (323).

However, our findings in a large cohort challenge a simplistic Laplacian relationship between WS and hypertrophy in humans (320). In contrast to conventional classifications of remodelling, we have demonstrated that there is a strong and distinct regionality to the homeostatic response of myocardium in the face of rising SBP in which concentric and eccentric adaptations occur concurrently (324-327). We observed that rising SBP is associated with a normalization of WS in the septum where concentric hypertrophy is predominant. However, in the majority of the left ventricle the increase in WS with rising SBP was not balanced by a proportionate increase in RWT. High WS without signs of decompensation has been reported in uncomplicated hypertension due to an increase myocardial contractility in the early stages of disease (328, 329). In keeping with this, we observed preserved or hyperdynamic radial function in normotensives with rising SBP, despite early geometric changes. However, in hypertensives this relationship was reversed and function was most diminished in the regions exhibiting the greatest hypertrophy.

This study may begin to address a key unresolved question by showing BP-induced regional ventricular dilatation can occur in low-risk adults without clinical evidence of myocardial infarction and without a change in LV end-diastolic volume (330-332). The mechanisms underlying this anatomic asymmetry of hypertensive hypertrophy and remodelling is only partly-understood but may reflect the spiral trajectory of subepicardial fibre architecture, the influence of titin isoform expression on myocardial compliance, embryonic origins of myocardial regions and local variations in both mechanoreceptors and mechanical loading (333-335). Histological studies suggest a gradient of fibrosis within the lateral wall of hypertensive hearts that may, in part, be related to the features described in the current study (336).

Prognostically adverse cardiovascular features, including LV hypertrophy and increased vascular stiffness, have been observed in pre-hypertensives with a high prevalence of obesity

and diabetes (337). Our data show that a “hypertensive pattern” of remodelling is also observed in asymptomatic normotensive adults. This suggests that rising SBP may have a much earlier impact on cardiac structure and function than previously recognised and point towards a nuanced relationship between homeostasis and cardiovascular risk. It was notable that with rising SBP the increase in septal RWT is progressively more pronounced. The mechanism for increasing hypertrophic sensitivity in response to rising SBP remains to be determined. However, this observation suggests a positive feedback in the septum between cardiac myocyte hypertrophy and vascular, mechanical and/or neurohormonal factors that contribute to the acceleration in the regional RWT increase as SBP rises (338-340). Longitudinal studies have shown that increased WT is associated with a progression to hypertension and we propose that this may be linked to initiation of an adverse hypertrophic phenotype amongst normotensives with rising SBP (341).

Genetic, epigenetic and environmental factors are influential in determining the pattern of hypertrophic response (342). Our data show that LV remodelling is variable in nature and region-specific thus providing a compelling rationale for using whole-heart techniques in genetic association studies. Despite the strong heritability of LV mass conventional association studies of the heart using 2D data have failed to find strong genetic associations, perhaps in part due to the regional effects shown here (292, 343).

We categorized subjects according to JNC-7 thresholds as more recent guidelines have not addressed the definitions of hypertension or prehypertension (38). We did not assess peak systolic WS as segmentations were performed at end-diastole and end-systole. We did not assess subjects for insulin resistance or sub-clinical diabetes which is thought to influence the pattern of LV remodelling although findings have been inconsistent (331). We controlled for racial group, but did not explore ethnic differences in LV remodelling (244). Voxelwise

significance thresholds were used as a conservative approach and statistical associations may have been underestimated.

13.5 Conclusions

These data define LV remodelling in a drug-naïve population and reveal that SBP is associated with a continuous progression towards the hypertensive cardiac phenotype. Rising SBP is associated with concentric hypertrophy of the septum and eccentric remodelling of the lateral wall, which exhibits elevated WS. These findings challenge conventional models of compensated cardiac hypertrophy in pressure overload.

13.6 Acknowledgements

The Digital Heart Project was conceived and coordinated by Professor Stuart Cook and Dr. Declan O'Regan. Building on previous work with Wenjia Bai, Wenzhe Shi developed the automated segmentation algorithm with Professor Daniel Rueckert. Tim Dawes contributed with advice regarding the statistical analysis of the data.

14 Body composition as a determinant of left ventricular morphology and function

14.1 Introduction

More than a third of US adults are obese and obesity-related conditions are some of the leading causes of preventable death (344). An increased incidence of cardiovascular disease is driven not only by diabetes and hypertension but also by subclinical myocardial injury, left ventricular (LV) hypertrophy and diastolic dysfunction (345, 346). Adiposity is thought to influence these factors via both hemodynamic and metabolic effects (347) with the cumulative exposure to obesity being a major predisposing factor (348). While a distinct cardiomyopathy of obesity is controversial, recent studies have pointed towards a pattern of concentric remodelling or hypertrophy in obese subjects even in the absence of hypertension (349). As LV hypertrophy is independently associated with all-cause morbidity and mortality (350), the interaction between obesity and cardiac geometry is critical for understanding the influence of this modifiable risk factor on cardiovascular health (309, 351).

While research has focussed on those with clinical obesity (body mass index ≥ 30) less is known about how changes in the body composition of healthy adults initiate early adaptations of LV structure and function, and how gender affects prognostically adverse cardiovascular remodelling. Cohort studies have conventionally relied on assessing LV mass-to-volume ratio to determine geometric concentricity and risk stratify cardiac phenotypes. However standard 2D imaging is poorly equipped to understand the complex relationship between body composition and LV structure. We have used computational approaches to cardiac phenotyping to unravel distinct regional variations of hypertrophy and remodelling within the

left ventricle in response to systolic blood pressure. In this study we applied our automated algorithm based on the Digital Heart Project's cardiac atlas, on the 3D-CMR images from our large cohort free from known cardiovascular disease. Our main purpose was to define how the heart adapts to increasing body fat in a healthy adult population and understand how prognostically important gender differences emerge.

14.2 Methods

The prospective cohort of 1530 volunteers (54.8% females; 74.8% Caucasian; age range: 18 – 81 years; mean age 41.3 ± 13.0 years) of the Digital Heart Project at Imperial College London was used in this study. Details of the study population, CMR imaging protocol, as well as imaging analysis methods were described in section 11.2 above. 3D-CMR automated quantitative analysis was carried out as described in sections 12 and 13.2.

In this study, the association between 3D phenotypic parameters and either lean mass or fat mass was assessed using a regression model adjusted for age, gender, race and height with correction to control the false discovery rate. Contiguous regional effects in the left ventricle were identified where the association between variables was significant ($p < 0.05$) and are reported as the mean of the standardized β coefficients within that area. Comparison between groups and regression models was performed using analysis of variance, corrected for covariates

14.3 Results

Summary statistics for the main variables across the cohort as a whole, as well as split by gender are shown in **Table 5**. Summaries of the regression models using the conventional CMR data are shown in **Table 11** for the whole cohort and separately for men and women in **Table 12**.

	Standardised β	p
LVEDV		
Age	-0.20	<0.001
Gender	-0.007	0.95
Race: C v AF	-0.07	<0.001
Race: C v SA	-0.15	<0.001
Race: C v Other	-0.03	0.06
Systolic BP	0.07	<0.001
Height	0.12	<0.001
Lean Mass	0.55	<0.001
Fat Mass	0.09	<0.001
Gender X Lean Mass	0.23	0.11
Gender X Fat Mass	-0.19	<0.001
LVS		
Age	-0.15	<0.001
Gender	0.08	0.52
Race: C v AF	-0.08	<0.001
Race: C v SA	-0.14	<0.001
Race: C v Other	-0.04	0.01
Systolic BP	0.12	<0.001
Height	0.14	<0.001
Lean Mass	0.60	<0.001
Fat Mass	0.13	<0.001
Gender X Lean Mass	0.03	0.86
Gender X Fat Mass	-0.20	<0.001
LVM		
Age	-0.14	<0.001
Gender	-0.05	0.69
Race: C v AF	0.04	0.005
Race: C v SA	-0.11	<0.001
Race: C v Other	-0.04	0.01
Systolic BP	0.15	<0.001
Height	-0.03	0.24
Lean Mass	0.53	<0.001
Fat Mass	0.06	0.003

Gender X Lean Mass	0.37	0.005
Gender X Fat Mass	-0.08	0.02
Concentricity Index		
Age	0.03	0.24
Gender	0.27	0.12
Race: C v AF	0.14	<0.001
Race: C v SA	-0.003	0.90
Race: C v Other	-0.02	0.41
Systolic BP	0.16	<0.001
Height	-0.17	<0.001
Lean Mass	0.23	0.001
Fat Mass	-0.007	0.82
Gender X Lean Mass	-0.09	0.65
Gender X Fat Mass	0.12	0.03
Cardiac Output		
Age	-0.19	<0.001
Gender	0.21	0.20
Race: C v AF	-0.09	<0.001
Race: C v SA	-0.11	<0.001
Race: C v Other	-0.04	0.06
Systolic BP	0.19	<0.001
Height	0.19	<0.001
Lean Mass	0.40	<0.001
Fat Mass	0.17	<0.001
Gender X Lean Mass	-0.25	0.19
Gender X Fat Mass	-0.08	0.09
Heart Rate		
Age	-0.08	0.004
Gender	0.02	0.91
Race: C v AF	-0.03	0.18
Race: C v SA	0.01	0.76
Race: C v Other	-0.01	0.83
Systolic BP	0.13	<0.001
Height	0.07	0.17
Lean Mass	-0.20	0.01
Fat Mass	0.08	0.02
Gender X Lean Mass	-0.16	0.48
Gender X Fat Mass	0.12	0.04

Table 11 – Linear regression models using body composition data. R^2 for LVEDV model: 0.63, R^2 for LVSV model: 0.58, R^2 for LVM model: 0.68; R^2 for concentricity model: 0.24; R^2 for heart rate model: 0.05. BP = blood pressure; Concentricity Index = LVM / LVEDV, LVEDV = left ventricular end diastolic volume; LVSV = left ventricular stroke volume; LVM = left ventricular mass; Race C = Caucasian; Race AF = African; Race SA = South Asian.

	Males		Females	
	Standardised β	p	Standardised β	p
LVEDV				
Age	-0.21	<i><0.001</i>	-0.27	<i><0.001</i>
Race: C v AF	-0.11	<i><0.001</i>	-0.06	<i>0.03</i>
Race: C v SA	-0.20	<i><0.001</i>	-0.15	<i><0.001</i>
Race: C v Other	-0.02	0.55	-0.06	<i>0.03</i>
Systolic BP	0.07	<i>0.01</i>	0.08	<i>0.01</i>
Height	0.07	0.08	0.14	<i><0.001</i>
Lean Mass	0.49	<i><0.001</i>	0.43	<i><0.001</i>
Fat Mass	-0.07	<i>0.02</i>	0.13	<i><0.001</i>
LVSV				
Age	-0.17	<i><0.001</i>	-0.19	<i><0.001</i>
Race: C v AF	-0.10	<i><0.001</i>	-0.10	<i><0.001</i>
Race: C v SA	-0.18	<i><0.001</i>	-0.13	<i><0.001</i>
Race: C v Other	-0.02	0.42	-0.08	<i>0.004</i>
Systolic BP	0.12	<i><0.001</i>	0.14	<i><0.001</i>
Height	0.11	<i>0.01</i>	0.13	<i><0.001</i>
Lean Mass	0.44	<i><0.001</i>	0.46	<i><0.001</i>
Fat Mass	-0.04	0.23	0.17	<i><0.001</i>
LVM				
Age	-0.17	<i><0.001</i>	-0.21	<i><0.001</i>
Race: C v AF	0.05	0.13	0.08	<i>0.004</i>
Race: C v SA	-0.20	<i><0.001</i>	-0.09	<i>0.002</i>
Race: C v Other	-0.05	0.08	-0.05	0.08
Systolic BP	0.19	<i><0.001</i>	0.19	<i><0.001</i>
Height	-0.05	0.27	-0.01	0.70
Lean Mass	0.53	<i><0.001</i>	0.51	<i><0.001</i>
Fat Mass	-0.01	0.82	0.11	<i><0.001</i>
Concentricity Index				
Age	0.04	0.30	0.03	0.50
Race: C v AF	0.17	<i><0.001</i>	0.15	<i><0.001</i>
Race: C v SA	-0.04	0.26	0.05	0.20
Race: C v Other	-0.04	0.25	0.001	0.99
Systolic BP	0.17	<i><0.001</i>	0.16	<i><0.001</i>
Height	-0.11	<i>0.04</i>	-0.16	<i><0.001</i>
Lean Mass	0.11	<i>0.03</i>	0.19	<i><0.001</i>
Fat Mass	0.09	<i>0.03</i>	-0.0004	0.99
Cardiac Output				
Age	-0.22	<i><0.001</i>	-0.19	<i><0.001</i>
Race: C v AF	-0.08	<i>0.01</i>	-0.11	<i><0.001</i>
Race: C v SA	-0.14	<i><0.001</i>	-0.10	<i>0.001</i>
Race: C v Other	-0.01	0.74	-0.07	<i>0.02</i>
Systolic BP	0.18	<i><0.001</i>	0.20	<i><0.001</i>
Height	0.17	<i><0.001</i>	0.13	<i>0.001</i>
Lean Mass	0.18	<i><0.001</i>	0.29	<i><0.001</i>
Fat Mass	0.10	<i>0.006</i>	0.20	<i><0.001</i>
Heart Rate				

Age	-0.11	0.005	-0.06	0.16
Race: C v AF	-0.02	0.64	-0.05	0.17
Race: C v SA	0.004	0.92	0.01	0.80
Race: C v Other	0.009	0.81	-0.02	0.66
Systolic BP	0.11	0.005	0.13	0.001
Height	0.07	0.17	0.03	0.54
Lean Mass	-0.20	<0.001	-0.10	0.04
Fat Mass	0.17	<0.001	0.08	0.04

Table 12 – Linear regression models using body composition data split by gender. R^2 for LV mass models: men = 0.42, women = 0.43. R^2 for LV EDV models: men = 0.47, women = 0.45. R^2 for concentricity models: men = 0.10, women = 0.10. R^2 for stroke volume models: men = 0.42, women = 0.45, R^2 for heart rate models: men = 0.06, women = 0.02, R^2 for cardiac output models: men = 0.24, women = 0.29. BP = blood pressure; Concentricity Index = LVM / LVEDV; LVEDV = left ventricular end diastolic volume; LVSV = left ventricular stroke volume; LVM = left ventricular mass; Race C = Caucasian; Race AF = African; Race SA = South Asian.

Two dimensional imaging

Fat mass was positively associated with LVM in women, but not in men (females $\beta = 0.11$, $p < 0.001$; males $\beta = -0.01$, $p = 0.82$; p for interaction = 0.02). In women, increasing fat mass was associated with increased LVEDV, whereas men showed the opposite relationship – smaller LV cavity volume with increasing fat mass (females $\beta = 0.13$, $p < 0.001$; males $\beta = -0.07$, $p = 0.02$; p for interaction < 0.001). In contrast, men showed increased LV concentricity index (CI, LVM / LVEDV) with increasing adiposity, a relationship absent in women (females $\beta = -0.00$, $p = 0.99$; males $\beta = 0.09$, $p = 0.03$; p for interaction = 0.03).

SV increased with fat mass in women but not in males (females $\beta = 0.17$, $p < 0.001$; males $\beta = -0.04$, $p = 0.23$; p for interaction < 0.0001). In contrast, heart rate increased with adiposity in both sexes but the relationship was significantly stronger in males (females $\beta = 0.08$, $p = .04$; males $\beta = 0.17$, $p = < 0.0001$; p for interaction = 0.04). As a result, cardiac output was positively associated with fat mass in males and females but with a trend towards a stronger

relationship in women (females $\beta = 0.20$, $p < 0.001$; males $\beta = 0.10$, $p = 0.006$; p for interaction = 0.09).

In both genders, lean mass is strongly positively associated with LVEDV, LVSV, LVM, CI and cardiac output (for all $p < 0.03$). Heart rate was negatively associated with lean mass (females $\beta = -0.10$, $p = 0.04$; males $\beta = -0.20$, $p < 0.001$).

Three dimensional LV geometry

Consistent with the global LVEDV results, high resolution analysis using 3D-CMR showed that, in males, fat mass was associated with a decrease in LV cavity volume except for a small area in the basal anterolateral wall ($\beta = -0.22$, significant area = 91%). In females, explaining the rise in LVEDV detected by 2D analysis, the LV cavity expanded across the basal anterior and lateral walls in association with fat mass ($\beta = 0.07$, significant area = 22%). Across the rest of the heart the cavity volume decreased (Figure 14.1). Lean mass was strongly associated, in males and females, with a global pattern of LV cavity expansion that was significant throughout the endocardial surface.

Demonstrating a similar trend to the LVM analysis using 2D, 3D WT was positively associated with fat mass throughout most of the left ventricle apart from the basal lateral wall, with similar findings in both sexes (females $\beta = 0.25$, significant area = 94%, males $\beta = 0.31$, significant area = 95%). Lean mass was also associated with global thickening of the LV in men ($\beta = 0.23$, significant area = 96%) and women ($\beta = 0.21$, significant area = 90%).

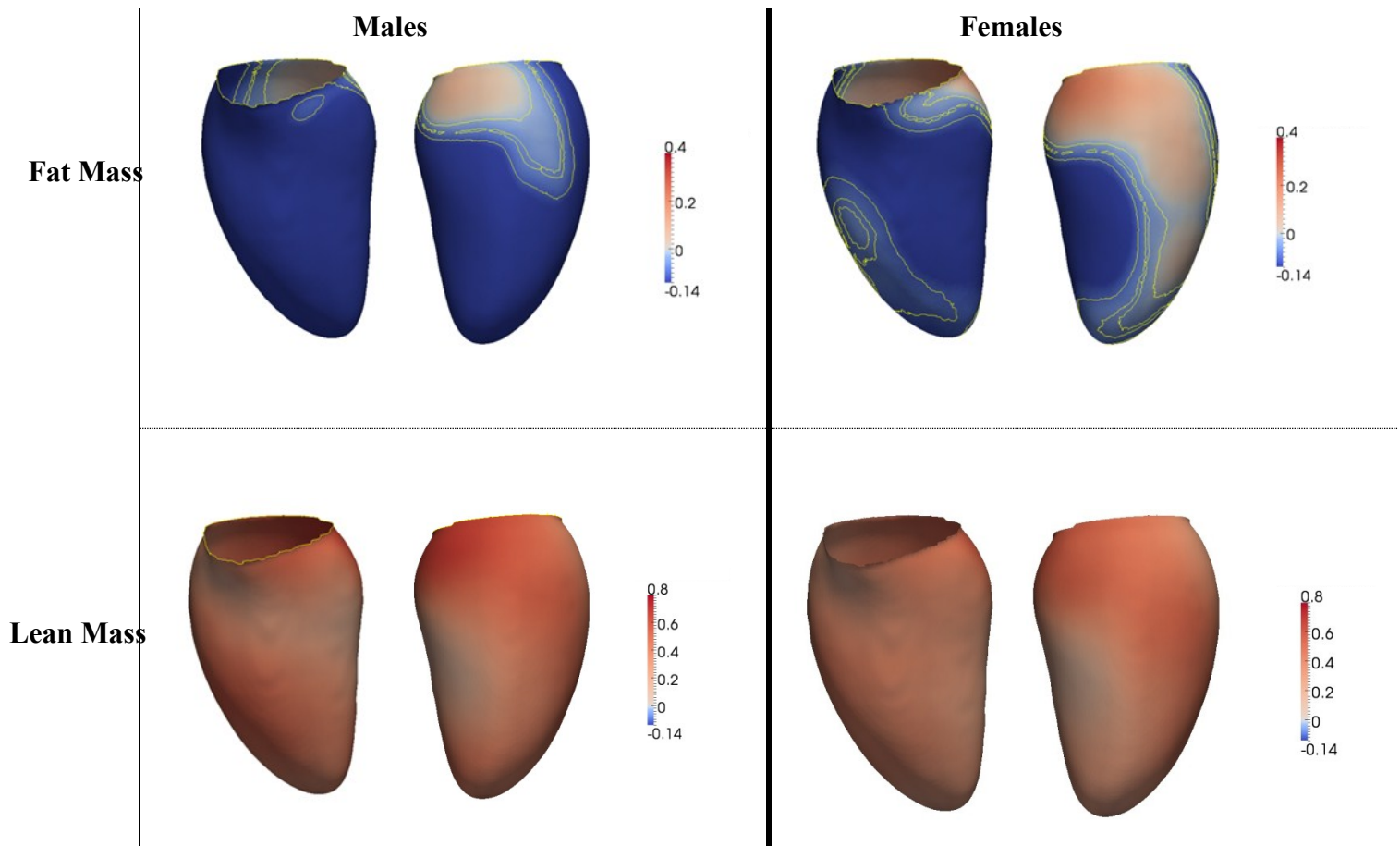


Figure 14.1 – Three dimensional regression models of the association between fat mass and endocardial left ventricular geometry. The regression coefficients between fat mass (upper row) and lean mass (lower row) and endocardial shape are shown for subjects split by gender. A positive coefficient indicates an outward expansion of the surface and a negative coefficient an inward contraction. Contour lines indicate significant regions ($p < 0.05$) before (white border) and after (yellow border) correction for multiple testing respectively. When no lines are visible all points are significant. Left ventricular projections in each panel: Left = facing the septum; Right = facing the lateral wall.

In males, RWT results (**Figure 14.2**) demonstrated that fat mass was strongly associated with concentric remodelling throughout most of the left ventricle ($\beta = 0.36$, significant area = 98%) apart from a small area in the mid lateral wall ($\beta = -0.03$, significant area = 1.7%). In females, overall there was a significant positive relationship between RWT and fat mass but this was weaker than in males and more asymmetric, with a large area of negative association

in the lateral wall (β in lateral wall = -0.11, significant area = 7%; β in rest of the heart = 0.27, significant area = 85%).

The relationship between RWT and lean mass was more complex (**Figure 14.2**). There was increased septal RWT in both genders but the effect was larger and over a bigger area in females (β in septum = 0.11, significant area = 13.4%) than in males (β in septum = 0.10, significant area = 2%). Although there was a reduction in RWT in the basal anterolateral wall associated with lean mass in both genders this was more pronounced in females (females: β in basal anterolateral wall = -0.14, significant area = 9%; males: β in basal anterolateral wall = -0.18, significant area = 0.6%).

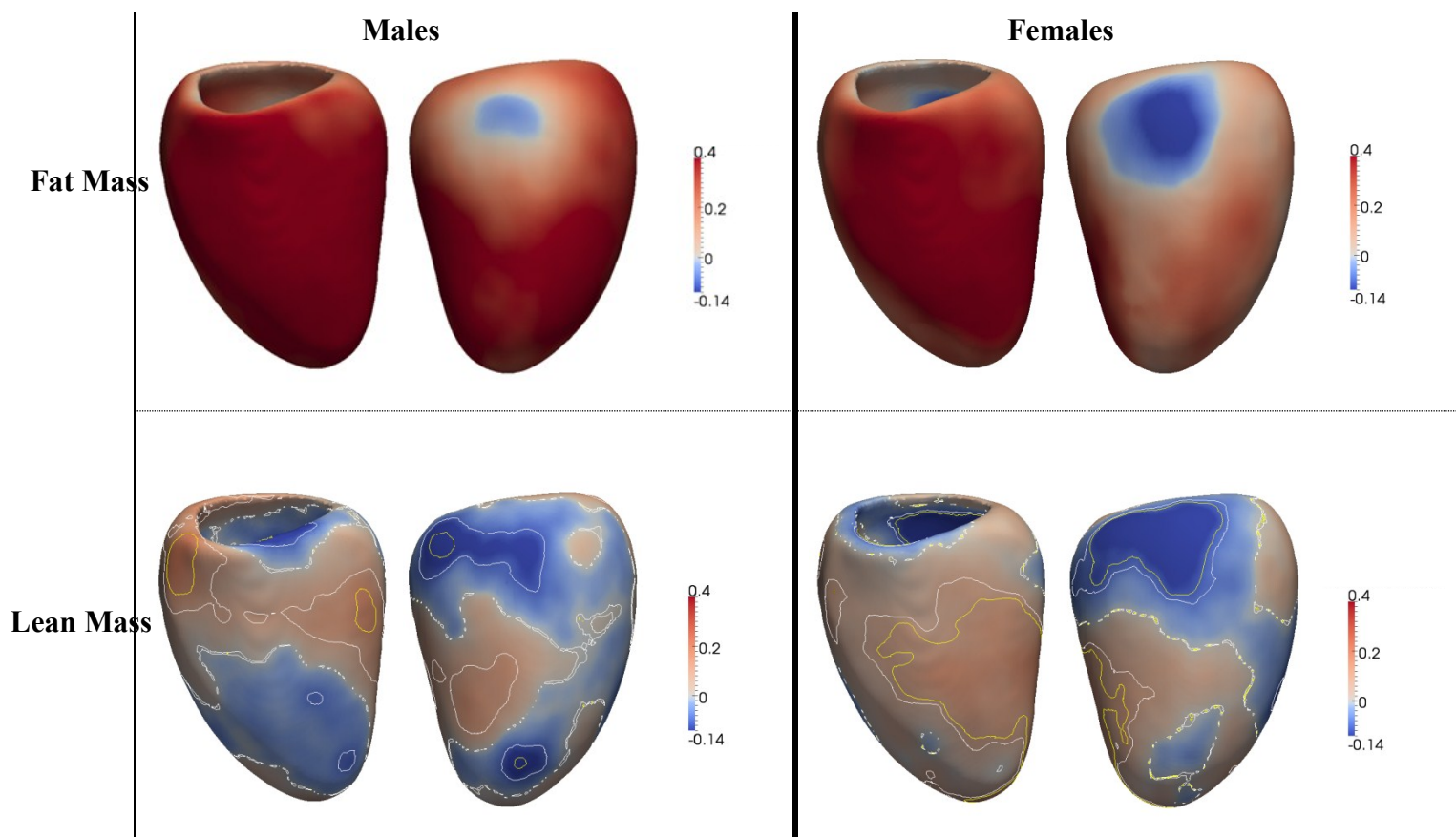


Figure 14.2 - Three dimensional regression models of the association between relative wall thickness and body composition. The regression coefficients between fat mass (upper row) and lean mass (lower row) and left ventricular relative wall thickness are shown for subjects split by gender. Positive coefficients indicate concentric hypertrophy and negative

coefficients eccentric hypertrophy. Contour lines indicate significant regions ($p < 0.05$) before (white border) and after (yellow border) correction for multiple testing respectively. FM = fat mass; LM = lean mass; S2S = surface to surface (i.e. signed distance between template surface and observed surface). Left ventricular projections in each panel: Left = facing the septum; Right = facing the lateral wall.

In summary, 3D-CMR uncovered an asymmetric cavity size change in response to fat mass increases. This explained that the higher LVEDV found by 2D-CMR in females associated with fat mass is due to anterolateral chamber dilatation. While the concentricity index had no association with fat mass in our 2D analysis of women, 3D-CMR demonstrated that this was due to regional opposing effects: concentric hypertrophy across most of septum while in the lateral there was eccentric hypertrophy. In men fat mass was associated with concentric remodelling throughout most of the LV.

14.4 Discussion

Variation in the body composition of healthy adults is associated with distinctive adaptive patterns of LV hypertrophy and remodelling that are revealed with 3D cardiovascular imaging. Fat mass is associated with concentric remodelling throughout most of the left ventricle with the strongest response seen in septum. However, there are gender differences as females show a weaker concentric response to increasing body fat than males with a more asymmetrical geometry. Furthermore, women show a stronger LV dilatatory response to increasing fat mass which is most pronounced in the lateral wall. As concentric hypertrophy has been linked to cardiovascular mortality, these observations may help explain the greater risk of cardiovascular death observed in obese males compared to females (352, 353). Our

data show that fat mass is associated with increased stroke volume, and thus circulating volume, in women but with increased heart rate predominately in males, suggesting that gender-specific hemodynamic responses to increasing adiposity may underpin the observed differences in LV remodelling.

We show that unadjusted wall thickness is increased throughout the LV with increasing fat mass, similarly for both males and females, but that relative wall thickness and LV mass/volume (i.e. measures of concentricity) are significantly more related to fat mass in males. These findings broadly concur with other large studies using CMR. In a multi-ethnic cohort, the MESA group found that BMI was associated with LV mass/volume in males but not females (349). In a smaller cohort of exclusively normotensive subjects, LV mass/volume was associated with BMI and fat mass in both sexes but with a stronger relationship for males (353).

Automated quantitative phenotyping of 3D-CMR uncovered, previously unknown, regional relationships between fat mass and LV geometry. There was a strong concentric remodelling response throughout the majority of the LV in males but a weaker, more asymmetrical response in women. The strongest increases in RWT with fat mass were in the septum and the weakest in the lateral wall. The reasons for this asymmetry are currently unclear but it is interesting that we also found a regional response to blood pressure in our study described in section 13. Causative mechanisms for this asymmetry may include the spiral trajectory of subepicardial fibre architecture, the influence of titin isoform expression on myocardial compliance and local variations in both mechanoreceptors and mechanical loading (333-335). It is possible that gender and body composition may influence these factors, thereby producing the asymmetry in LV remodelling we have observed in this study.

We also found a gender-specific relationship between fat mass and LV cavity dilatation such that fat mass was independently associated with increased LV cavity volume for females but decreased cavity volume for males. Rider et al. found corresponding results in their study of a healthy cohort; BMI was associated with LVEDV for females only (353). In the MESA study, estimated fat mass was positively associated with LV EDV for females; in males there was a trend towards a negative association (349). Our 3D-CMR data confirm these findings and provide novel insights into the regional variation of these changes: males show an essentially symmetrical reduction in volume with increasing fat mass; females demonstrate eccentric remodelling predominately in the lateral wall of the LV.

We found that fat mass was associated with increased SV in females but not males; the association with HR, in contrast, was more pronounced in males. This suggests gender differences in the hemodynamic response to increasing fat mass, which may underpin the differences we observed in LV remodelling.

Adipose tissue is known to increase circulating volume and the resulting increase in SV over time is a plausible stimulus for eccentric remodelling (354). In the Strong Heart Study cohort, fat mass was associated with increased SV in both sexes, but the strength of the association was stronger in females (355). The same is true for the association of BMI with stroke volume in the MESA cohort (349). To date, no studies have looked for gender differences in the augmentation of circulating volume with increasing adiposity - we hypothesise that this response would be proportionally greater in females. A possible mechanism for this differing hemodynamic response may relate to gender differences in the renin-angiotensin-aldosterone (RAAS) system, which is involved in fluid volume homeostasis. Sex differences in RAAS activity are well documented (356, 357) but recent work suggests these gender effects can be modulated by adiposity. For example, intra-renal RAAS activity is higher in obese human

females than males (358) and C57BL/6 mice show tissue-specific modulation of components of the RAAS by gender and adiposity (359).

Increasing adiposity has been linked to changes in the autonomic nervous system (360); in particular sympathetic activity has been shown to be related to BMI in males but not in females (361). The stronger relationship we observed between fat mass and HR in males may therefore reflect an enhanced sympathetic response in males to increasing adiposity. Of note, increased visceral body fat, a pattern of adiposity observed predominately in males (361), has been linked to increased heart rate (362) and muscle sympathetic nerve activity (363, 364). As well as via effects on blood pressure, sympathetic nerve activity has been linked to concentric remodelling through increasing insulin resistance (365), which itself has stronger links to BMI in males than in females (366, 367). Therefore, it is possible that in females adiposity predominately produces increases in circulating volume, whereas in males there is a predominate increase in sympathetic tone, resulting ultimately in gender-differences in LV remodelling.

Males tend to store body fat in a central, visceral pattern, females in a more peripheral distribution (368). These gender differences may partly explain the observed differences in LV remodelling with adiposity. An analysis of the Dallas Heart Study found that visceral fat was associated with higher concentricity and lower LV EDV, whereas lower body fat was associated with the opposite pattern (369). Furthermore, lower body fat was associated with higher cardiac output (369) and other studies show that HR and other markers of sympathetic activation are associated with a central pattern of adiposity (362-364). Of note, central obesity has recently been found to be an independent risk factor for sudden cardiac death (370) – it may be postulated that this is mediated through increased likelihood of concentric LV remodelling.

We note that although measured body composition using bioimpedence is a well validated method of assessing body fat (371), dual energy X-ray absorptiometry and whole body MRI may be more accurate in defining the distribution of fat, the pattern of which may have hemodynamic consequences (369). This study on body composition would have been strengthened by adjustment for the metabolic profile and physical activity levels of the participants, as well as by longitudinal data.

14.5 Conclusions

Fat mass is associated with concentric remodelling of the left ventricle, with the strongest response seen in septal regions and the least strong response seen in the lateral wall. However, there are gender differences, with a predominately concentric remodelling pattern in males but a mixed eccentric and concentric remodelling pattern in females. These gender effects may relate to differences in the hemodynamic response to obesity. As concentric hypertrophy has been linked to cardiovascular mortality, these observations may help explain the greater risk of cardiovascular death observed in obese males compared to females (352).

14.6 Acknowledgements

The Digital Heart Project was conceived and coordinated by Professor Stuart Cook and Dr. Declan O'Regan. Building on previous work with Wenjia Bai, Wenzhe Shi developed the automated segmentation algorithm with Professor Daniel Rueckert. Tim Dawes and Ben Corden contributed with statistical advice for data analysis. Grateful to Ben Corden for helpful discussion in the interpretation of results.

15 Truncating variants in titin as a determinant of cardiac morphology and function in a healthy population

15.1 Introduction

A major objective of human genetic research is the identification of genetic variation underlying phenotypes, in health and in disease. Current imaging techniques, particularly since the introduction of cardiac magnetic resonance (CMR), have aided in the identification of several genes associated with extreme cardiac morphology and function. This is evident in hypertrophic cardiomyopathy (HCM), where mutations in genes encoding sarcomeric proteins were found in 40-70% of HCM patients (71, 73-75), and also in dilated cardiomyopathy (DCM) where more than 60 genes have been associated with the condition (76). Furthermore, enhanced phenotyping with CMR has improved our prognostic ability in disease cohorts (372-374), leading to the inclusion of CMR-derived metrics in recent guidelines for the management of cardiomyopathies (e.g. ejection fraction cut-offs for the insertion of implantable cardioverter defibrillators). However, both echocardiography and 2D-CMR rely on global mass and volumetric assessment to summarise the complexity of cardiac anatomy and physiology. This is a particularly relevant limitation in the study of cardiomyopathies, which are known to cause variable and asymmetric patterns of regional LV remodelling (267, 268). Furthermore, in genetically susceptible individuals, cardiac phenotypes associated with end-stage cardiomyopathies are often either not present or latent using standard imaging. This presents an increasingly common clinical dilemma, as more subjects are being identified through family genetic screening (genotype-positive), which have global phenotypes within the normal ranges (phenotype-negative) (269, 270). The

apparent lack of a phenotype in an affected individual may be due to incomplete penetrance of a given mutation, sub-clinical disease or late-onset disease manifestations but equally may reflect incomplete phenotypic assessment. Overall, our understanding of genotype-phenotype associations in the wider population, and our ability to predict disease progression from a given genotype has been limited by a lack of a comprehensive, accurate, specific and high-resolution approach to cardiac phenotyping (230, 375). Having demonstrated the increased power of quantitative phenotyping using three-dimensional CMR (3D-CMR) to uncover the regionality of effects of anthropometric factors on cardiac phenotypes, this approach might also be superior to standard imaging in population-based genetic studies.

Titin (TTN), the largest protein in the human body, is abundant in the cardiac sarcomere and plays a key role in biomechanical sensing and signalling, as well as in sarcomeric structure and function. Heterozygous truncating variants in TTN (TTNtv) account for approximately 25% of familial and severe DCM (91), while all other DCM genes combined are likely to account for ~20% of cases (92). TTNtv are thought to affect ~2% of the general population but whether the apparent absence of phenotypic differences between TTNtv negative and positive subjects (**Table 1**) is due to low penetrance and / or limited expressivity or caused by underpowered phenotypic approaches has not been fully ascertained. This has hindered our ability to completely understand the mechanisms underlying DCM due to TTNtv (376) and has led to discussion on whether or not TTNtv are disease causing or disease modifying. In our previous work, we integrated DNA, RNA and protein analysis, in large DCM and population cohorts and showed that there is diverse TTN isoform expression in the heart (101). The two major TTN isoforms, N2BA and N2B, span the entire sarcomere and are robustly expressed along with the less abundant, shorter isoforms such as Novex-3. Furthermore, we suggested that the location of TTNtv in the gene is likely to help us predict the pathogenicity of the mutation. Nonsense, frameshift, and canonical splice site TTNtv

affecting highly expressed exons were strongly associated with DCM. In contrast, truncations that occur in exons with low proportion spliced-in (PSI), including novex isoforms, were less likely to be pathological. Finally, TTNtv were located more distally in DCM than in controls with A-band and distal I-band enrichment.

The recent advent of next-generation sequencing (NGS) approaches has enabled high-throughput sequencing at a reduced cost. Targeted sequencing and whole exome sequencing are both efficient approaches for the study of monogenic disorders (377). NGS has been shown to have a very high sensitivity, consistently reported to be at least 99.5% at read depth of 20 or over (378). This approach can be supplemented by Sanger sequencing, to provide robust validation to the genotyping of TTN.

In this preliminary analysis of a subset of the Digital Heart Project cohort, we used NGS approaches to sequence TTN, with the purpose of determining the prevalence of truncating variants in a self-proclaimed healthy population. We added these findings to our previous data on TTN in large DCM and longitudinal cohorts (101) to identify any differences in the distribution of TTNtv between the general population and those with DCM. Finally, we used 2D and 3D-CMR to uncover genotype-phenotype correlations in our population, testing the hypothesis that high-resolution mapping of cardiac phenotypes using 3D-CMR provides greater insights into the biological mechanisms that underpin the earliest stages of DCM.

15.2 Methods

Study Population

The first 928 prospectively recruited volunteers to the Digital Heart Project at Imperial College London were included in this study (54.3% females; 76.7% Caucasian; age range: 20 – 81 years; mean age 42.3 ± 13.2 years). One volunteer was excluded from the genotype-phenotype analyses presented here as for technical reasons his CMR images were lost during upload to the database and the volunteer was lost to follow up. Detailed descriptions of the eligibility criteria and biophysical assessment methods can be found in section 10.3 above.

In the results section, in addition to data from the Digital Heart Project, genetic sequencing results on disease and longitudinal cohorts are shown for comparison. This data has been previously published in our study (101), which includes detailed information on cohort specific phenotyping and genotyping. In brief these cohorts are: 374 unselected DCM patients from the Royal Brompton Hospital (RBH); 155 end-stage non-ischemic DCM patients who were listed for cardiac transplantation and/or LV device implantation between 1993 and 2011 at RBH; 163 DCM patients who were referred to the genetics research program at St Vincent's Hospital and Victor Chang Cardiovascular Institute; 1623 participants of the Framingham Heart Study; 1980 participants of the Jackson Heart Study and 667 participants of the Women's Health Initiative.

Imaging Protocol

CMR was performed on a 1.5T Philips Achieva system (Best, Netherlands). Full details of the imaging protocol can be found in section 11.3. In this study we used the 2D cine balanced

steady-state free precession (b-SSFP) images, as well as the single breath-hold 3D left ventricular short axis (LVSA) b-SSFP sequence.

Statistical analysis

Data was analysed using RStudio Server version 0.98 (Boston, MA) (257). Normally distributed data were reported as mean \pm standard deviation (SD) and categorical variables as percentages. Ranges were added to CMR derived parameters. The associations between anthropometric data and cardiac phenotypes were assessed in separate multiple regression models, with adjustment for age, gender, race, BSA and systolic blood pressure. In addition to the base models, whether a subject had TTNtv was added. These final models were then compared to the base models to assess the significance of the TTNtv term by bootstrapping the coefficients (repetitions = 100000). When comparing two groups, Mann Whitney U tests were used. P values < 0.05 were considered significant.

The associations between morphological and functional parameters for each point in the 3D datasets were assessed using a regression model adjusted for age, gender, race, systolic blood pressure and BSA with correction to control the false discovery rate (314). Contiguous regions of the left ventricle where the association between variables was significant ($p < 0.05$) were identified and the relationship with SBP reported as the mean of the standardized β coefficients within that area.

Two dimensional cardiac magnetic resonance analysis

Analysis of the 2D cine sequences was performed using commercially available semi-automated software (CMRtools, Cardiovascular Imaging Solutions, London, UK) and using a standard methodology (200) as described in section 11.2. Cardiac volumes and mass were indexed to body surface area (BSA).

Three dimensional assessment of ventricular structure and function

Automated segmentation of the 3D-CMR images was carried out using the methods described 12.4 and 13.2 using Matlab (Mathworks, Natick, MA) and performed on a high performance server (Dell, Round Rock, TX).

Genetic sequencing of titin

In total, 409 subjects underwent targeted sequencing of 201 genes associated with inherited cardiac conditions, including TTN, using custom hybridization capture probes. RNA baits were designed using Agilent's eArray platform. Baits targeted all exons of all Ensembl version 54 TTN transcripts, including untranslated regions, with a 100 base pair (bp) extension into adjacent introns, and 1.25 kb of upstream sequence (379). DNA library preparation and target capture were performed according to the manufacturers' protocols before paired-end sequencing on the SOLiD 5500xl (Life Technologies). Reads were demultiplexed and aligned to the human reference genome (hg19) in colour space using LifeScope v2.5.1 "targeted.reseq.pe" pipeline. SOLiD Accuracy Enhancement Tool (SAET) was used to improve colour call accuracy before mapping. All other LifeScope parameters were used as default. Duplicate reads and those mapping with a quality score <8 were removed. Variant calling was performed with diBayes (SNPs) and small indels modules, as well as GATK v1.5-2.7 (380) and SAMtools v0.1.18 (381). Variants called by any of these methods were taken forward for Sanger validation. Alignment and coverage metrics were calculated using Picard v1.40 (<http://picard.sourceforge.net>), BEDTools v2.12 (382), and in-house Perl scripts. GATK CallableLoci Walker was used to identify target genomic regions covered sufficiently for variant calling (minimum depth >4 with base quality >20 and mapping quality >10).

An additional 519 participants underwent WES that was carried out using the Nextera Rapid Capture 37MB Whole Exome kit and sequenced on a HiSeq 2500 (Illumina). Illumina paired-end reads were demultiplexed with HiSeq Control software and reads quality checked using FastQC v.0.10.1 (<http://www.bioinformatics.babraham.ac.uk/projects/fastqc/>). Low quality (<20) reads/bases were trimmed using PrinSeq v0.20.4 (383) and the good quality reads were aligned into hg19 reference using BWA v0.7.9 (384). Marking duplicate reads, local realignment around known indels and base quality score recalibration process were performed in Picard v1.115 (<http://picard.sourceforge.net>) and GATK v3.1-1 (380). Alignment summary metrics, callability and coverage report were calculated using Picard, Samtools v0.1.18, Bedtools v2.11.2 and RBH genetics and genomics laboratory in house Perl scripts. A subset file was created (ontarget), based on reads mapping quality > 8 and use this “ontarget” file to make consistent variant calls in GATK HaplotypeCaller. Bases covered by at least 4 reads with a mapping quality ≥ 10 and base quality ≥ 20 were denoted as “callable” (i.e. adequately covered for variant calling within recommended GATK parameters). Variants were functionally annotated using the Ensembl VEP v75_37 and HGMD Professional version 2014.1 (385) to predict the effect of variant in protein function. Putative TTNtv that passed quality control analysis were taken forward for Sanger validation. To facilitate standardised variant annotation in accordance with international guidelines we report our results using the Locus Reference Genomic (LRG) sequence for TTN developed in collaboration with the European Bioinformatics Institute (386).

15.3 Results

Of the 928 subjects, 29 truncating variants in the gene titin were detected by NGS. Of these 18 were validated through Sanger sequencing and are presented in **Table 13**. **Figure 15.1** provides a schematic of TTN with the sarcomeric regions demarcated, as well as the distribution of TTNtv in our cohort and in DCM and longitudinal populations. In **Table 14**, a summary of subject characteristics is shown with the cohort split by the presence (TTNtv) or absence (TTNtv negative). No difference was found between the cohorts in terms of anthropometric variables.

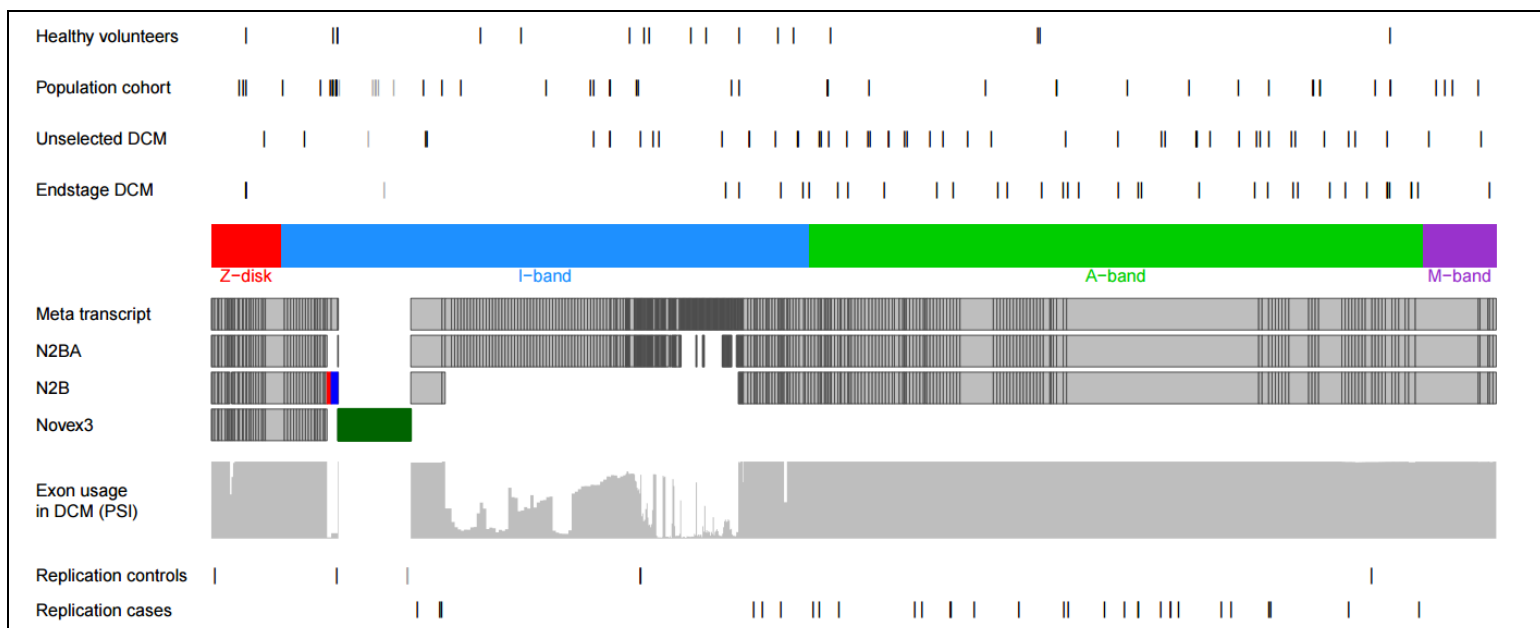


Figure 15.1 – Schematic of the TTN meta-transcript with sarcomeric regions demarcated. Exon usage for the two principal adult cardiac isoforms, N2BA and N2B, is shown, although exon usage in vivo is variable. Exon usage in the human left ventricle is depicted as the proportion spliced-in (PSI) (range, 0 to 1; grey bars): the proportion of transcripts that include a given exon. TTNtv are located more distally in subjects with DCM compared with the Digital Heart Project volunteers (represented as healthy volunteers in the top row). There is A-band enrichment in end-stage (n = 155) and unselected DCM patients (n = 374), and corresponding depletion in the population (n = 3603) and healthy volunteers (n = 927) cohorts.

Sample identification	Hg19 genomic start position	LRG genomic start position	Transcript effect	Protein effect	Exon number	Median exon PSI	Present in N2BA	Present in N2B	Present in Novex-3	Variant type
14AG01422	179647533	52997	c.3100G>A	p.Val1034Met	18	1.00	Y	Y	Y	Splice variant prediction
14SS01830	179621351	79179	c.10852C>T	p.Gln3618X	46	0.07				Nonsense
14AO01372	179620947	79583	c.11254+2T>C		46	0.07				Splice donor variant
14RH01353	179620947	79583	c.11254+2T>C		46	0.07				Splice donor variant
14ZN01340	179595884	104646	c.17508dupA	p.Gly5837ArgfsX9	61	0.41	Y			Frameshift
14JD01896 *	179588844	111686	c.21142C>T	p.Arg7048X	74	0.36	Y			Nonsense
14EC01433	179560998	139532	c.30803-2A>G		115	0.84	Y			Splice acceptor variant
14KN01429	179553775	146755	c.32095+5G>A		126	0.22	Y			Splice variant prediction
14AH01539	179549632	150898	c.32554+1G>C		131	0.17	Y			Splice donor variant
14RM02225	179529171	171359	c.36267_36280+16del TGTACCTGTCAAA GGTACATTCTTAA CTGT		169	0.02				Splice donor variant / Frameshift
14AJ02284	179523083	177447	c.37628-1G>A		186	0.11				Splice acceptor variant
14CB02200	179506963	193567	c.40558+1G>A		220	1.00	Y	Y		Splice donor variant
14HB02599	179495671	204859	c.44015-1G>T		239	1.00	Y	Y		Splice acceptor variant
14MO01427	179486054	214476	c.45391delA	p.Ile15131TyrfsX46	247	1.00	Y	Y		Frameshift
14RS02105	179479631	220899	c.48703C>T	p.Gln16235X	261	1.00	Y	Y		Nonsense
14JM01448	179444855	255675	c.67159delA	p.Ile22387X	319	1.00	Y	Y		Nonsense
14SM01546	179444666	255864	c.67348C>T	p.Gln22450X	319	1.00	Y	Y		Nonsense
14JC01930	179404286	296244	c.98506C>T	p.Arg32836X	353	1.00	Y	Y		Nonsense

Table 13 - Titin truncating variants identified in 18 out of 928 volunteers. LRG = Locus Reference Genomic sequence for TTN; HG19 = human reference genome against which reads were aligned; N2BA, N2B and Novex-3 = titin isoforms; PSI = proportion spliced in. * patient excluded from genotype-phenotype analysis due to loss of imaging dataset.

	TTNtv Negative (n =910)	TTNtv (n =17)	Mann-Whitney U test p-value
Age (years)	42.3 ± 13.2 (20 – 81)	43.0 ± 13.7 (24 – 72)	0.86
Gender			0.38
Males (%)	418 (45.9%)	6 (35.3%)	
Females (%)	492 (54.1%)	11 (64.7%)	
Race / Ethnicity:			0.99
Caucasian	698 (76.7%)	13 (76.5%)	
South Asian	109 (12.0%)	1 (5.9%)	
African	55 (6.0%)	2 (11.8%)	
Other	48 (5.3%)	1 (5.9%)	
Systolic BP (mmHg)	120 ± 14	125 ± 17.9	0.17
Diastolic BP (mmHg)	79 ± 10	83.5 ± 11.1	0.05
PWV (m/s)	4.79 ± 1.73 *	5.31 ± 2.05**	0.43
Height (cm)	170.0 ± 9.5	165.9 ± 6.3	0.07
Weight (kg)	71.7 ± 13.3	69.1 ± 16.2	0.28
Body surface area (m²)	1.8 ± 0.2	1.8 ± 0.2	0.21
BMI (kg/m²)	24.8 ± 3.8	25.0 ± 5.3	0.74
Fat Mass (kg)	18.5 ± 8.3	21.2 ± 10.9	0.45
Lean Mass (kg)	53.0 ± 11.4	48.0 ± 9.7	0.11
LVEDV (ml)	146 ± 32 (70 – 252)	145 ± 22 (103 – 188)	0.84
LVESV (ml)	51 ± 17 (17 – 121)	53 ± 12 (37 – 85)	0.41
LVSV (ml)	95 ± 19 (49 – 168)	92 ± 14 (66 – 117)	0.58
LVEF (%)	65 ± 5 (47 – 81)	64 ± 5 (55 – 72)	0.12
LVM (g)	115 ± 33 (56 – 255)	113 ± 26 (71 – 157)	0.98
LVEDVI(ml/m²)	80 ± 13 (45 – 129)	82 ± 8 (61 – 93)	0.24
LVESVI (ml/m²)	28 ± 8 (11 – 66)	30 ± 6 (21 – 42)	0.14
LVSVI (ml/m²)	52 ± 8 (32 – 81)	52 ± 6 (39 – 62)	0.70
LVMI(g/m²)	62 ± 14 (32 – 141)	64 ± 13 (42 – 84)	0.56
CI (g/ml)	0.8 ± 0.2	0.8 ± 0.1	0.93
Cardiac Output (L)	6.1 ± 1.4	6.2 ± 1.4	0.46
Heart Rate (BPM)	64.8 ± 10.6	67.8 ± 10.6	0.1

Table 14 – Subject characteristics and CMR-derived cardiac measurements split by the presence (TTNtv) or absence (TTNtv negative) of titin truncating variants. P-values are for pairwise comparisons. BMI = body mass index; BP = blood pressure; BPM = beats per

minute; CI = concentricity index; LVEDVI = indexed left ventricular end diastolic volume; LVESVI = indexed left ventricular end systolic volume; LVEF = left ventricular ejection fraction; LVMI = indexed left ventricular mass; PWV = pulse wave velocity. * n=688; ** n=8.

Two dimensional imaging

In absolute terms and after indexing to BSA, there was no statistically significant difference between the TTNtv positive and negative sub-groups (**Table 14, Figure 15.2**). However, when adjusting the effect of TTNtv for other clinical variables we found that the regression model for LVEF with the added TTNtv variable was significantly improved from the one that did not include genotype information. LVEF was negatively associated with the presence of TTNtv ($\beta = -0.06$, $p = 0.02$, **Table 15**).

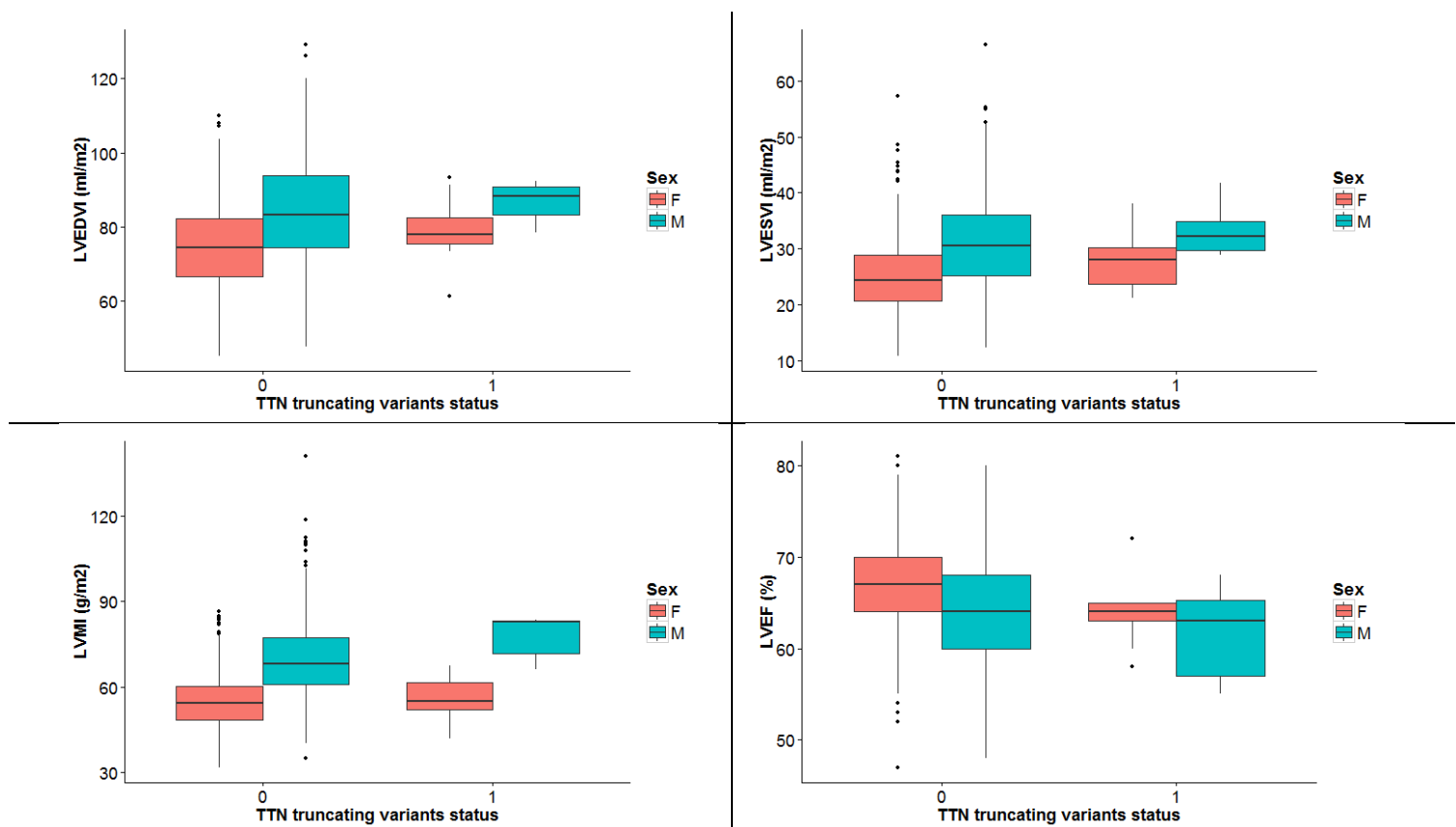


Figure 15.2 – Box plot of cardiac parameters by gender in TTNtv positive and negative sub-cohorts. Differences between groups do not reach significance. 0 = titin truncating variants

negative; 1 = titin truncating variants positive; F = Females; M = Males; LVEDVI = indexed left ventricular end-diastolic volume; LVESVI = indexed left ventricular end-systolic volume; LVMI = indexed left ventricular mass.

Phenotype	Model terms	Adjusted R ²	P value of comparison	Bootstrapped Coefficient of the added covariate
LVEDV	Age, Sex, SBP, Race, BSA	0.52		
	+ TTNtv	0.52	0.37	0.02
LVSEV	Age, Sex, SBP, Race, BSA	0.38		
	+ TTNtv	0.38	0.07	0.04
LVEF	Age, Sex, SBP, Race, BSA	0.14		
	+ TTNtv	0.15	0.02	-0.06
LVM	Age, Sex, SBP, Race, BSA	0.59		
	+ TTNtv	0.59	0.39	0.01

Table 15 – Linear modelling of the relationship between the TTN genotype and cardiac phenotypes. Linear regression models were built to adjust for the contribution of anthropometric variables to morphologic and functional parameters. In addition to the base models, whether a subject had a TTNtv was added. These final models were then compared to the base models to assess the significance of the TTNtv term by bootstrapping the coefficients (100000 repetitions).

Three dimensional imaging

Three dimensional regression models adjust for age, gender, race and systolic blood pressure demonstrated that TTNtv were associated with a small area of mid anterior wall thickening ($\beta = 0.11$, significant area = 1.8%, **Figure 15.3**). When adjusting for ventricular size, 3D relative wall thickness showed a small area of negative association with TTNtv in the anterior basal wall ($\beta = 0.03$, significant area = 4%).

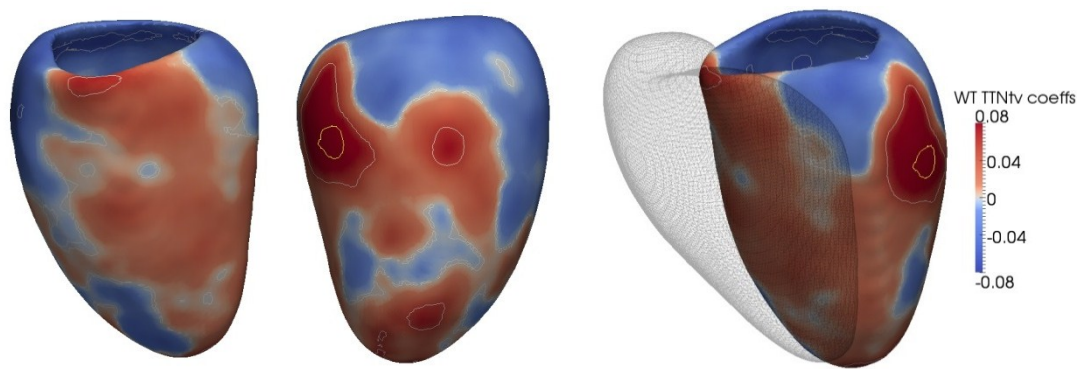


Figure 15.3 – Three dimensional regression models of the association between TTNtv and left ventricular wall thickness. The regression coefficients between wall thickness and the presence of TTNtv are shown. Positive coefficient indicate thickening and negative coefficients indicate thinning. Contour lines indicate significant regions ($p < 0.05$) before (white border) and after (yellow border) correction for multiple testing respectively. Left ventricular projections: Left = facing the septum; Middle = facing the lateral wall, Right = facing the anterior wall with the right ventricle represented by a mesh.

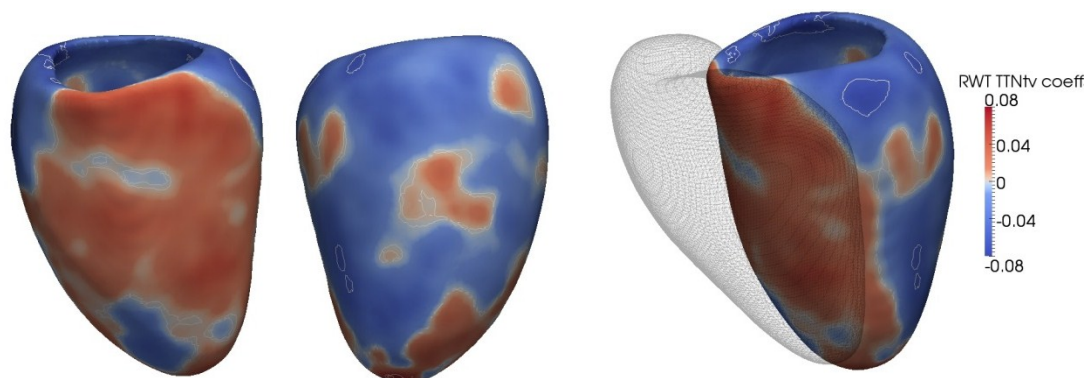


Figure 15.4 – Three dimensional regression models of the association between TTNtv and relative ventricular wall thickness. The regression coefficients between relative wall thickness and the presence of TTNtv are shown. Contour lines indicate significant regions ($p < 0.05$). Left ventricular projections: Left = facing the septum; Middle = facing the lateral wall, Right = facing the anterior wall with the right ventricle represented by a mesh.

When analysing the association between the endocardial and epicardial shape and TTNtv our data shows that in end-diastole, the epicardium expanded in the septum and in the basal lateral wall ($\beta = 0.06$, significant area = 13%) in the presence of truncating variants (**Figure 15.5**). TTNtv was associated with an expansion of the end-diastolic endocardial surface in the

basal lateral wall ($\beta = 0.05$, significant area = 7%). In end-systole the effect was similar with a basal antero-lateral cavity expansion ($\beta = 0.06$, significant area = 11%).

In summary, 3D-CMR analysis showed that the presence of TTNtv was associated with an expansion of the LV cavity in the basal lateral wall in both systole and diastole, and that this was associated with a reduction in RWT in the basal anterior wall. Although the areas reaching significance were small they were surrounded by large contiguous patches that demonstrated similar effect trend.

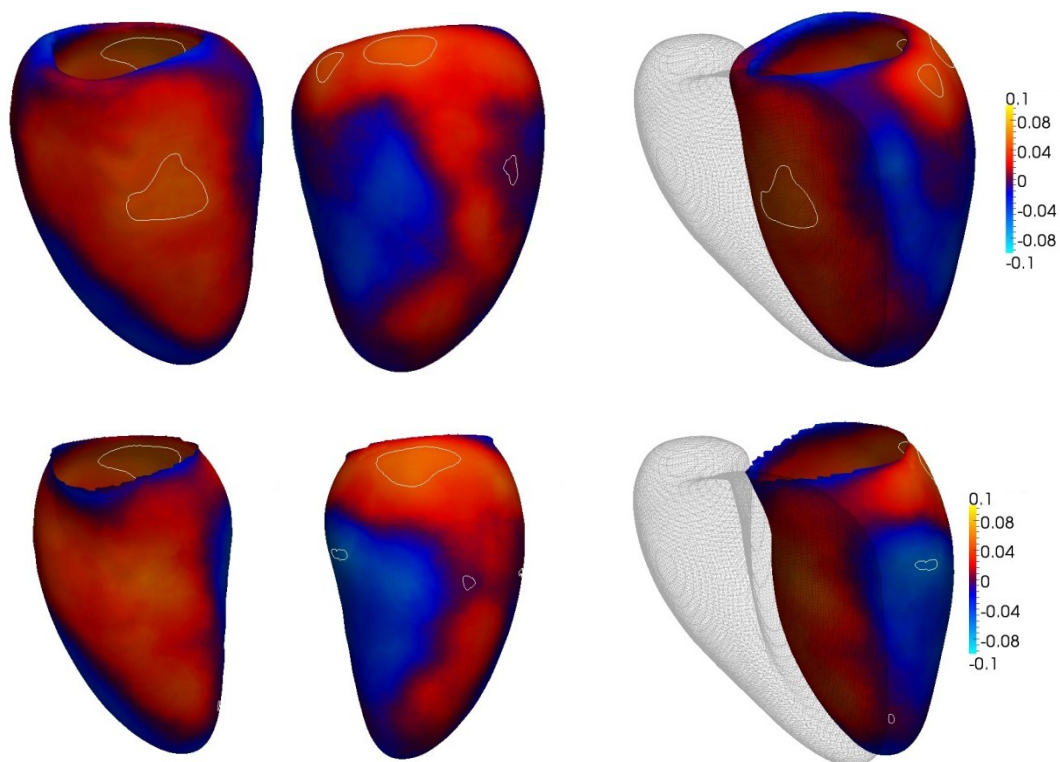


Figure 15.5 – Three dimensional regression models of the association between TTNtv and epicardial and endocardial left ventricular geometry. The regression coefficients between epicardial (upper row) and endocardial (lower row) shape and TTNtv are shown for subjects split by gender. A positive coefficient indicates an outward expansion of the surface and a negative coefficient an inward contraction. Contour lines indicate significant regions ($p < 0.05$). Left ventricular projections: Left = facing the septum; Middle = facing the lateral wall, Right = facing the anterior wall with the right ventricle represented by a mesh.

15.4 Discussion

The prevalence of TTNtv in our cohort was 1.9%, in line with our previous work on population cohorts (101). Compared to our published data, in this study we found a larger number of asymptomatic volunteers with TTNtv in the distal I-band that were located mainly in exons with low PSI. This suggests that enrichment in the A-band alone might be the main driver behind the DCM phenotype. A potential limitation of using PSI data was that this exon usage information was derived from DCM hearts (n=84), and it is plausible to expect different expression profiles between end-stage heart failure patients and those from asymptomatic subjects. Nonetheless, this added information on the frequency of TTNtv in the population will assist in the interpretation of clinical genotypes and in DCM disease stratification.

When analysing the unadjusted 2D-CMR derived parameters, similarly to the Framingham Heart Study (**Table 1**) data, we found no difference in cardiac parameters between the TTNtv negative and positive cohorts. When adjusting the analysis for other clinical covariates we found that LVEF was negatively associated with the presence of TTNtv. The difference in the mean EF between the two subgroups was 1.9%, being lower in TTNtv. 3D-CMR analysis suggests a reduction in basal anterior RWT and expansion of the blood cavity in end diastole and end-systole. Although only very small areas in the model reached significance we can observe that they are surrounded by large, contiguous areas of the LV that followed similar trends. This might indicate that TTNtv are associated with LV cavity dilatation in the septum, basal anterior and lateral wall. RWT appeared to increase in the septum but reduced across the rest of the heart. Again noting that statistical significance was not reached, LVESV demonstrated a tendency to be larger in TTNtv positive subjects ($\beta = 0.04$, $p = 0.07$), when accounting for other variables. We know from case-control studies that DCM subjects have lower LVEF and wall thickness and higher LVEDVI, LVESVI and LVMI. Furthermore

previous studies have found that regional variation in LV function was present in DCM in addition to global reduction in EF and a disproportionate increase in LV cavity in relation to wall thickening (decrease in RWT) (387, 388).

Our statistical approach for the analysis of 3D-CMR was chosen to be robust and conservative during the validation studies of this novel method. At each point in the LV model an effect was considered independently from the all the points that surround it. For each of the 46808 LV points a linear regression model was carried out and the association between a given variable and the cardiac parameter was tested for significance. We then addressed the multiple comparison problem (probability of a type I error increasing with the number of tests), by considering significant only those points whose p-values were under a corrected level of significance. Initially we used the ultra-conservative Bonferroni method ($\alpha = 0.05 / 46808 = 1.06 \times 10^{-6}$) which greatly increased the proportion of false negatives. The Benjamini-Hochberg false discovery rate (FDR) procedure allowed an increase power while maintaining stringent control on multiple testing. Instead of focusing on excluding all points that might be falsely declared significant (like Bonferroni), this method controlled the rate at which declarations of significance were false. This means that when we predefined our tolerance to false discovery to 5%, this method ensured that fewer than 5% of those points deemed significant were incorrectly defined. This takes into consideration the fact that p-values are not equally distributed (by ranking them in order from high to low). FDR then adjusts each p-value taking into consideration their rank: the highest p-value is corrected for the FDR α , while each of the following is corrected for ever decreasing criterion; the lowest p-value is corrected for a Bonferroni α . The FDR approach is well suited to datasets where effects are large and easily detectable. By considering all tests independently, FDR ‘protects’ against positively correlated data. This is a significant limitation of this approach in our dataset, as parameters across the LV are likely to be highly correlated. Given 3D-CMR’s high

sensitivity to detect changes in LV phenotypes, the larger effect sizes associated to variables such as systolic blood pressure or body composition remained significant even after voxelwise correction. However, in this study of a small subcohort (n=17), in which subtler effects of genetic variants on phenotype were being investigated, the voxelwise significance testing was perhaps too conservative and associations may well have been underestimated. In support of this, we note that large numbers of points in contiguous, biologically plausible areas, demonstrated similar direction of effect. It is unlikely that randomly distributed ‘noise’ would follow homogenous patterns over extended areas. Furthermore, although highly correlated, when the different 2D and 3D-CMR acquisitions were analysed using different techniques and they showed similar ‘trends’ in the association between TTNtv and cardiac phenotypes.

Neuroimaging research has encountered similar problems in the analysis of high resolution brain phenotypes, in particular in the field of functional MRI (fMRI) and addressed these challenges through different approaches. 25-30% of fMRI studies reported using arbitrary thresholds such as an uncorrected $p < 0.001$ in 10 or more contiguous voxels (389). Such approaches have been shown to be more sensitive to detect true signal than approaches, such as ours, that use voxelwise thresholds (390). However, these methods are limited by the need to arbitrarily set a threshold that defines cluster-formation (size of effect and or/area of the cluster). The guidelines for threshold-setting are vague, subjective and very dependent on each data-set: “broader signals are best detected by low thresholds and sharp focal signals are best detected by high thresholds” (391). Furthermore, this approach might be flawed as in a study comparing multiple testing correction methods (Gaussian Random Field Theory, Bonferroni, FDR, Šidák and permutation) it was found that in only 8 out of 11 published fMRI and positron emission tomography (PET) studies, were the differences between voxels truly significant (392). In other words, in 3 of these 11 studies false positive voxels were

declared true. Another frequently used method that avoids the need to correct for multiple testing is to perform region of interest (ROI) analysis therefore excluding the need for multiple correction (only one test is carried out) (393-395). This approach is biased to look for differences in specific anatomical segments and might not be adequate in discovery studies, such as ours, in which no physiological or anatomical correlation with a given variable is assumed. Yet another method that has been validated in neuroimaging studies and that makes use of spatial neighbouring information to boost belief in extended areas of signal is Threshold-Free Cluster Enhancement (TFCE) (396, 397). This method is designed to keep the sensitivity of cluster-based thresholding while avoiding the bias described above. Briefly, TFCE automatically enhances voxels that are ‘supported’ by neighbouring voxels which demonstrate similar effect changes and uses permutation testing to control for multiple comparison errors. In studies of fMRI this approach was found to be more sensitive than voxelwise methods in identifying broad, small effects, as well as focal large effects. TFCE might allow us to increase the sensitivity of our method to detect small changes in cardiac phenotypes and therefore confidently interpret some of the ‘trends’ that we can currently observe.

Targeted and whole exome sequences enable the detection of rare and novel variants in candidate genes such as TTN. Exome sequencing is not without limitations. By its very design, it targets only the coding region of the genome and bypasses many other genetic variants that may be important for controlling gene transcriptional regulation or splicing. Whole exome sequence is superior to targeted sequencing in that the large amount of sequencing data produced provides the substrate for an unbiased examination of the exome.

This genetic study was designed to maximise sensitivity in detecting TTNtv. The potential loss in specificity was addressed by Sanger validation of the mutations found. Despite the high sensitivity of the sequencing techniques, certain regions of the TTN exon were not

adequately enriched and / or reads were not mapped uniquely to the genome. Work carried out in our group demonstrated that the assay used in this cohort provides over 97% sequence capture reliability across the TTN gene. Five per cent of the gene's coding sequence was poorly captured. This was most likely due to the fact that TTN has exons with a high degree of homology (or repetitive sequence) which are technically challenging to sequence.

The exact mechanisms of TTNtv driven DCM remain unclear but the position dependent functional effects that we have reported suggest a dominant negative effect. This has been questioned given the high proportion of sporadic cases in which no affected family members have been identified. However, it is plausible that many of these phenotype-negative family members have subclinical disease instead of silent mutations.

At a molecular level, the exact mechanism through which TTNtv cause DCM has not yet been established. This might result from deficits in force generation, force transmission or indeed through other biological mechanisms. This has significant impact on our ability to identify therapeutic targets. Being able to document the earliest pathological changes caused by TTNtv in humans might provide important insights into the molecular and cellular changes that precede overt disease and help guide mechanistic 'bench-side' studies.

Although volunteers in this study did not have self-reported cardiovascular disease, we have not corrected our findings for other clinical variables known to cause DCM, alcohol intake being perhaps one of the most relevant. This preliminary analysis might have been underpowered to detect true genotype-phenotype associations. Sequencing and CMR data will soon be available on the remaining ~900 subjects of the Digital Heart Project, nearly doubling the sample size. In this enlarged cohort, analysing the correlation between wall stress and TTNtv would be relevant given the known pathological progression in DCM from myocyte failure and cytoskeletal uncoupling to chamber dilatation without concomitant

increase in wall thickness. Given the small number of TTNtv subjects, no sub-group analysis was carried out. However the inclusion of 5 volunteers with TTNtv in low PSI exons (29% of the total cohort) might have contributed to a dilution of the phenotypic signal. Future studies would be improved by the inclusion of genotypic data from other DCM associated genes. This would help segregate true controls from early DCM subjects. Longitudinal follow-up would greatly strengthen our ability to extrapolate our findings, in particular our predictions of pathogenicity.

15.5 Conclusions

The prevalence of TTNtv in the general population was confirmed to be ~1.9%. When compared to the DCM cohorts, TTNtv in our asymptomatic volunteers were located more proximally and more often in exons with low PSI. Based on data from disease cohorts, both of these features were associated with better prognosis. However, two dimensional and 3D-CMR imaging data seem to suggest that the presence of TTNtv was associated with larger volumes and decreased function. These differences were however small, making biological interpretation of these findings difficult. It is possible that the voxelwise significance testing used in this study was too conservative and associations may well have been underestimated. The sensitivity of 3D-CMR to detected phenotypic changes may be increased by the use of statistical approaches that reward the spatial correlation of points across the LV model.

15.6 Acknowledgements

The Digital Heart Project was conceived and coordinated by Professor Stuart Cook and Dr. Declan O'Regan. Building on previous work with Wenjia Bai, Wenzhe Shi developed the automated segmentation algorithm with Professor Daniel Rueckert. The plot of exon usage in the heart, distribution of TTNtv, distribution of sites susceptible to truncation, usage of TTN exons across isoforms and cohorts was generated using R code first written by James Ware. Data on longitudinal and disease cohorts was obtained and analysed by James Ware, Angharad Roberts and colleagues under the supervision of Professor Stuart Cook and Christine Seidman (101). Samuel Wilkinson performed Sanger validation. Rachel Buchan and the team at the RBH Genetics and Genomics laboratory extracted DNA, prepared the sequencing libraries and carried out the target sequencing on SOLiD. Whole exome sequencing was carried by the Edinburgh Genomics team. Thanks to James Ware, Roddy Walsh and Francesco Mazzarotto for fruitful discussion and advice.

16 Future work - 3D genome-wide association study

16.1 Introduction

Left ventricular mass (LVM) is, in part, under genetic control with estimates of heritability ranging from 17-59% (28, 30, 398, 399). LVM is a complex trait influenced by variants in multiple genes in interaction with environmental and anthropometric variables. A genome wide association study (GWAS) is a commonly used study design in research into the common genetic variants that underlie complex traits. Typical GWAS examine hundreds of thousands to millions of single nucleotide polymorphisms (SNPs), testing their statistical association with discrete outcomes ('case-control' such as DCM vs. controls) or continuous outcomes (quantitative traits such as LVM or gene expression levels). Its main advantages are that it is unbiased by prior knowledge (or belief) of associations between certain genes and certain phenotypes (as are candidate genes studies) and it is powered to find associations between genome wide common variants and complex traits (unlike linkage studies) (400) . A GWAS is based, at population level, on the principle of linkage disequilibrium (LD) that underpins linkage studies within pedigrees: the association between alleles at different loci is not random and those loci that are closer together in the chromosome are more likely to be segregated together; two loci are in LD if they are found together across a population more often than it would be expected (therefore nearby loci are more likely to be in LD than those further apart). Therefore markers across the genome can be used to identify which genomic regions are associated with a given trait. The main limitation of GWAS stems from the fact that the huge number of statistical tests being performed carries the risk for large number of false positive results (401). In response to this, traditional multiple testing correction approaches have been used, which resulted in a lack of statistical power to detect genotype-phenotype associations (139). This has been addressed by recruiting larger cohorts and by

refining the statistical analysis methods, replacing the traditional Bonferroni correction for Bayesian or permutation-based methods (140, 141). GWAS of LVM have so far failed to uncover more than a handful of common variants associated with this phenotype (241, 292, 402) and none have been replicated. Given the high sensitivity and accuracy of current genotyping techniques it is plausible that the lack of positive findings is, at least partially, due to the lack of high-fidelity, high-resolution comprehensive phenotypes (227-230). The motivation to combine the accurate quantitative phenotyping of 3D-CMR with a GWAS is clear and the potential increase in power quite significant. However, there are many challenges to overcome mainly with regards to the statistical approaches to be used.

Traditional statistics study the relationships between small numbers of predictor variables and single outcomes. Our 3D-CMR data however, is formed by voxelwise phenotypes at 46808 points across the LV. Therefore we have a huge number of phenotypes (p) in a large sample of the population ($n \sim 1800$). This creates a problem described as ‘large p , small n ’ in which the number of variables measured outstrips the number of subjects being studied. Furthermore, testing independent associations between these high resolution phenotypes and millions of SNPs from over 1800 subjects using traditional statistical approaches, would be computationally expensive, prohibitively lengthy and result in a huge loss of power via the required correction for multiple testing. A possible approach to this problem could be to reduce the number of variables before analysis by choosing a subset of features to represent the high-dimensional phenotype. This could be achieved with methods such as principal component analysis (PCA). PCA is a descriptive statistical technique that summarises the variance observed in the dataset via linearly uncorrelated (orthogonal) variables (414). The lower dimensional descriptors (principal components) can then be more efficiently processed and used for subsequent modelling of genetic and environmental effects (413). However, PCA is a linear method for dimensionality reduction that would neglect the spatial correlation

between our 3D-CMR phenotypes. Furthermore, such methods have been criticised as they might lead to the loss of biologically relevant information if certain features are selected or discarded *a priori* (227).

Bayesian latent factor analysis, and in particular the ‘probabilistic estimation of expression residual’ (PEER) algorithm seem, in theory, well suited to our dataset. PEER is a software package that combines a collection of Bayesian approaches to explore genotype-phenotype associations. It was initially designed for the analysis of gene expression as the complex high-dimensional phenotype. Into the model a large number of additional information can be added such as anthropometric, environmental and experimental variables (**Figure 16.1**). PEER also accounts for spatial correlation within the dataset which can be supplied to the model as prior information (403, 404). Our 3D-CMR data replaces gene expression as the phenotype and the variability in our dataset is accounted for by the computed ‘hidden factors’. These lower dimension ‘hidden factors’ are then used as single traits to carry out genotype-phenotype association studies.

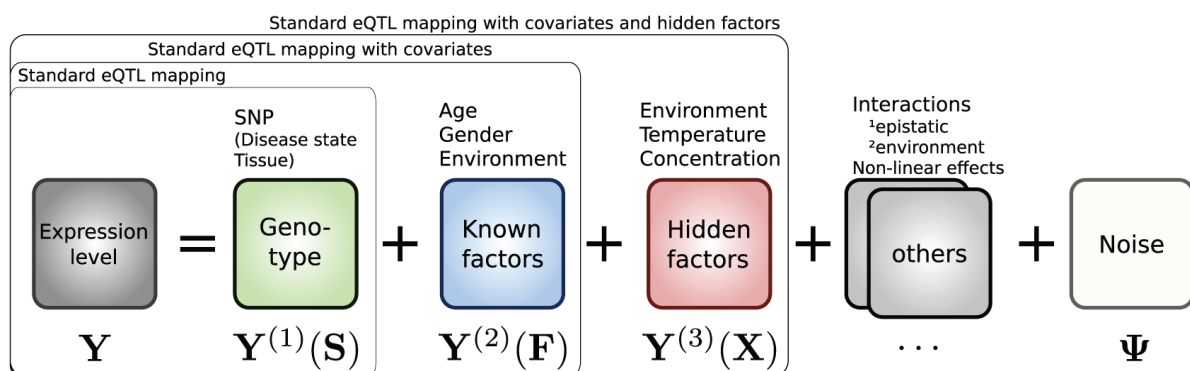


Figure 16.1 – PEER is a Bayesian latent factor analysis framework for understanding sources of variation in high-dimensional data. The expression level (in our case the 3D-CMR derived parameters) can be distilled into an a priori defined number of hidden factors taking into consideration a large set of known anthropometric and environmental factors. (Figure reproduced from Stegle O, et al. A Bayesian framework to account for complex non-genetic factors in gene expression levels greatly increases power in eQTL studies. PLoS computational biology 2010)

In this preliminary study we genotyped common variants in a large healthy population and performed a GWAS using phenotypes derived from 2D and 3D-CMR. The main purpose of this experiment was to test the applicability of PEER to our high dimensional dataset and to explore if this approach of dimensionality reduction shows potential to increase the power of GWAS to detect genotype-phenotype associations.

16.2 Preliminary methods

Genotyping of common variants in 1346 volunteers recruited into the Digital Heart Project was carried out using the Illumina HumanOmniExpress-12v1-1 SNP array (Sanger Institute, Cambridge). SNPs were subsequently called via the GenCall software for clustering, calling and scoring of genotypes (405). The quality of the genotypes was evaluated both on a per-individual and per-marker level following an adapted version of a published quality control (QC) protocol (406). Unless stated otherwise, the PLINK software (407) was used for all QC analyses.

In brief, the per-individual QC included the identification of individuals with discordant sex information, missing SNP rates and outlying heterozygosity rates. Related individuals were excluded from the sample cohort in order to remove bias towards genotypes shared within a family and to accurately represent the allele frequency of the entire population. Relatedness was estimated by the proportion of SNPs shared between two individuals and subsequent calculation of identity by descent. Population substructures arising due to different ethnical origins of samples were examined by comparison of sample genotypes to genotypes of the HapMap Phase III study (408) from four ethnic populations (determined by principal

component analysis; program: EIGENSTRAT/smartpca (409). Cohort samples clustering with HapMap III individuals of Caucasian ancestry were kept for further analyses.

The per-marker QC included filtering of SNPs with a minor allele frequency of less than 1%, SNPs with missing call rate in more than 1% of the samples and SNPs which significantly deviate from Hardy-Weinberg equilibrium ($p > 0.001$). After applying these QC filters and population based filtering (only keeping Caucasians for further analyses), 438 males and 509 females remained in the sample cohort. The total genotyping rate in these individuals was 0.997. After frequency and genotyping pruning, there were 618153 SNPs (99201 excluded).

Phasing and imputation

Phasing, i.e. inferring the samples' haplotypes from their genotypes, and imputation, i.e. prediction of genome-wide SNPs in the samples based on SNP information of a reference dataset, were conducted in two separate steps. The SHAPEIT software (version 2) (410, 411) was used to generate a set of estimated haplotypes based on the combined 1000 Genomes (412) and UK10K (UK10K Project, <http://www.uk10k.org>) reference panel as genetic map. The same reference panel was used for the imputation of the samples' genome-wide SNP genotypes via the IMPUTE2 software (version 2.3.0) (413, 414). SNPs with a certainty score of less than 0.4 were excluded from further analyses. IMPUTE2 yields imputed genotypes encoded in triplets of posterior probabilities for the possible allele combinations (AA, AB, BB). These genotypes were converted into an expected genotype G by the dosage model (415): $G = 0 * p(AA) + 1 * p(AB) + 2 * p(BB)$.

16.3 Preliminary 3D-GWAS experiments

After imputation, 9.45 million common variants from 947 Caucasian individuals (by genotype rather than self-reported as previously in this thesis) were used in these genome-wide association experiments. We used a Bayesian latent factor analysis software (PEER) to reduce the dimensions of our 3D-CMR wall thickness datasets, while preserving the spatial information. The PEER model included gender, age, height and weight. The software returned 100 hidden factors, which accounted for the variability in the dataset, as well as the effect of the factors on each original wall thickness measure (factor weights). These factors were then treated as single traits in a linear mixed model analysis using LIMIX (<https://github.com/PMBio/limix>). Associations were adjusted for multiple testing using the false discovery rate method, and SNPs which passed the genome-wide significance threshold were identified. The genotype of these significant SNPs across the cohort was then fed into a linear regression model that included as dependent variables: ‘hidden factor’ x associated weights at each point and the original wall thickness measurements. The strength of the association of the significant SNPs with these two phenotype measures at each position, was calculated as the goodness of fit (R^2) multiplied by the sign of the effect size (β). The strength of association was then plotted back into the 3D space to further explore the physiological significance of the association (**Figure 16.2**). In this preliminary analysis the number of SNPs that achieved statistical significance was vastly higher than when the data was used explored using the 2D-CMR derived LVM (**Figure 16.3**).

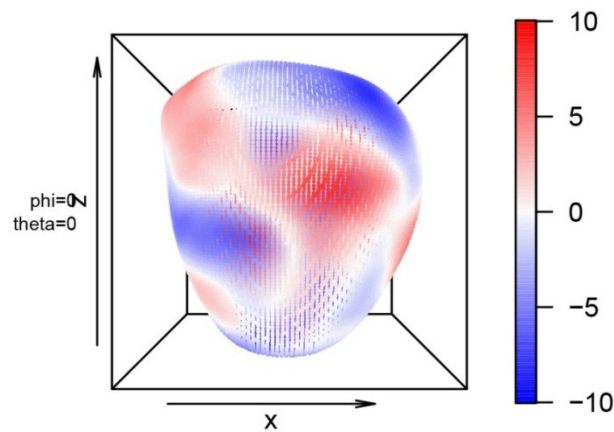


Figure 16.2 – Bayesian factor analysis was used to project the high dimensional wall thickness 3D-CMR data from the whole cohort into a lower dimensional ‘hidden factor’ space after correction for variables such as age, gender, height and weight. These hidden factors account for the variability in the dataset. Each factor is then used as a single trait to model SNP-phenotype effect. This is adjusted for multiple testing to identify SNPs which pass genome-wide significance. In this figure the strength of association between wall thickness and one of these SNPs is plotted.

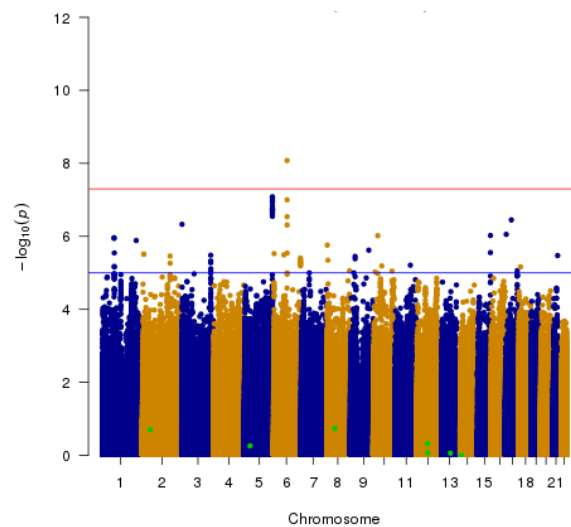


Figure 16.3 – Preliminary data of the Digital Heart Project genome-wide association study for 2D left ventricular mass in 947 Caucasian individuals. Manhattan plot showing the genome-wide $-\log_{10}(p)$ values for the interrogated 9.4 million variants across the 22 autosomal chromosomes for left ventricular mass (LVM). Conventional genome-wide levels of significance ($p < 5 \times 10^{-8}$) is represented by the red line. The blue line is a threshold for “suggestive” association ($p \leq 1 \times 10^{-5}$).

16.4 Conclusions

Bayesian latent factor analysis of 3D-CMR datasets shows great promise in increasing the power of GWAS to detect significant associations between common genetic variants and cardiac phenotypes. If confirmed and replicated in other cohorts, this methodology might provide an invaluable, unbiased discovery process for exploring the common genetic determinants of cardiac structure and function.

16.5 Acknowledgments

The quality control, phasing and imputation of the genotypes were carried out by Hannah Meyer under the supervision Professor Ewan Birney. The exploratory experiments of Bayesian latent factor analysis were carried out in parallel by Hannah Meyer and the PEER team at the Wellcome Trust Sanger Institute and by me under the supervision of Dr. Leonardo Bottolo and Dr. Enrico Pettreto

17 Overview of thesis

Through the work described in this thesis, the feasibility of high-resolution, single breath-hold whole organ 3D-CMR, was established in a large healthy population. The longer breath-holds were well tolerated and the reduction in signal-to-noise, when compared to equivalent 2D b-SSFP, did not hinder the analysis of the 3D datasets. Some of the advantages derived from this technique include the ability to phenotype the whole heart at a much higher resolution, without being limited by inter-slice gaps and inter-slice misalignments characteristic of 2D imaging. While the longer breath holds were well tolerated and our large population included a wide range of ages, cardiac phenotypes and levels of physical fitness, in future studies the applicability of this technique in disease cohorts needs to be investigated. A probable higher prevalence of arrhythmias, metallic implants and intracardiac devices might somewhat limit its use in subjects with severe cardiovascular disease.

Using 3D-CMR images of over 1000 subjects we successfully created the first high resolution atlas of the human heart. Using this atlas we were able to compute a statistical model that encodes the normal variation in anatomy within a multi-ethnic healthy population. The first 20 of these atlases were manually created and used to provide baseline information about the inter-subject variability in cardiac structure. Based on these datasets, we developed a multi-atlas PatchMatch algorithm to automatically segment new target images. Through an iterative process, correctly labelled images were added to the atlas pool, each providing some extra anatomical information and reducing the potential bias from any given atlas. This expanding pool of atlases was used to guide increasingly accurate segmentations. Registering each individual's cardiac phenotype to a template in a common coordinate system, ensured that each point in the 3D model was consistent between all subjects. We measured a series of

cardiac phenotypes at over 46000 points in the cardiac model including wall thickness, wall stress and ventricular geometry.

We went on to demonstrate that there was good agreement between 2D and 3D-CMR volumetric analysis but that the automated atlas-based segmentation of 3D-CMR provided greater accuracy in mapping ventricular wall thickness particularly in the cardiac base and apex. This increased accuracy provided a reduction in the sample size required to detect statistically significant differences in wall thickness.

To explore the association between LV parameters and clinical variables we created linear regression models at each point in the 3D model, correcting for other covariates and for multiple testing. This approach enabled us to identify previously unappreciated associations between anthropometric variables and regional cardiac phenotypes. The use of linear regressions when some of its assumptions (normal distribution of the error; linear relationship between dependent and independent variables; constant variance of the errors) were violated, might have some impact on the precision of the p-values of the tests for some points in the model. However, linear models do help explain most of the differences and trends observed in the data. Furthermore, linear regression is the most commonly used statistical method in biomedical research and applying this simple approach to our otherwise novel method allowed for better comparison with previous studies. Some of the data presented throughout (e.g. pulse wave velocity) could have been transformed to improve statistical analysis. However, using non-transformed data allowed us to keep the focus of our interpretation on the originally measured parameters. In the words of the famous statistician George Box: ‘all models are wrong, but some are useful’(416). In future work, methods such as nonparametric permutation testing and Bayesian procedures should be investigated. These are based on weaker assumptions of the characteristics of the data and might at the same time be helpful in addressing the multiple testing problem.

In this thesis, cardiac parameters were indexed to body surface area (BSA), in line with most published research. However, height, height^{2.7} or height^{2.13} may perhaps account for more of the variance in cardiac phenotypes, as was suggested by comparing the R^2 of the regression models using BSA in our study of blood pressure, with the R^2 using height, lean mass and fat mass in our study of body composition.

In our study of systolic blood pressure (SBP), 3D-CMR supplemented the 2D finding that left ventricular mass and concentricity index are positively associated with SBP, by demonstrating a strong and distinct regionality of response across the LV. Our data showed that in response to rising SBP there is concentric hypertrophy of the septum and eccentric remodelling of the lateral wall. Furthermore, our findings challenged the conventional models of compensated hypertrophy by demonstrating a normalisation of wall stress in the areas of concentric hypertrophy, while detecting elevated wall stress elsewhere in the LV that was not balanced by a proportionate rise in wall thickness.

When we studied the association between different ratios of body composition and LV phenotypes, 3D-CMR was instrumental to reveal gender specific patterns of remodelling. In males, the association between fat mass and concentric remodelling was much stronger than in females and this might help explain the increased cardiovascular risk observed in men. These interesting findings could be strengthened by the addition of metabolic profiling and physical activity levels to our models and this will be done in the near future.

To explore the effects of rare and disruptive variants in titin on cardiac morphology and function within our healthy population, we combined high resolution phenotypes with genotyping data. Using next-generation sequencing approaches we identified and validated titin truncating variants (TTNtv) in 17 subjects within a sub-cohort of 927 volunteers. The rare variants we identified were located more proximally in our asymptomatic population

than in DCM patients, and were more often located in the I-band than in the A-band. Furthermore, a significant proportion of TTNtv were in exons that are expressed at very low levels in the heart. Based on our previous work, this would suggest that these TTNtv are less likely to be pathogenic. However, 2D-CMR analysis indicated a reduction in ejection fraction in the cohort with TTNtv. Using 3D-CMR a pattern of asymmetric LV cavity dilatation and wall thinning was apparent. Although the areas that remain statistically significant after correction for multiple testing are small, it is possible that the observed ‘trends’ would reach significance if a statistical approach that rewards extended areas of signal was used. These methodological improvements and the sequencing of another ~900 subjects might provide additional power to confirm our preliminary findings. If these are confirmed there are potentially significant implications for understanding TTNtv effects and disease pathobiology in addition to patient stratification.

Initial work on a 3D-GWAS has demonstrated the promise of Bayesian approaches to summarise the variability in our highly spatially correlated LV voxelwise phenotypes. Early data indicates that the use of PEER-derived low dimension factors in single trait analysis, greatly increases the power to detect associations between common genetic variants and cardiac phenotypes, when compared to traditional GWAS approaches. The fact that we are able to visualise the location and strength of effect of these associations on the 3D model might provide a clearer biological context for interpreting the downstream functional and morphological effects of genetic variation. However, some of the associations we detected in our preliminary analyses show very complex patterns of wall thickness variation across the LV and the true physiological relevance of these ‘structures’ is currently unclear. We will begin to address this and refine our findings by re-analysing our data once the full cohort is genotyped and phenotyped, as well as by comparing the 3D and 2D GWAS. It is expected that the SNPs associated with the most significant global changes across the LV to also be

detected by 2D imaging when tested at the level of the single, most strongly 3D-parameter associated lead SNP. Any significant variants will be subjected to replication in additional cohorts as standard practice for GWAS. An interesting avenue might be to carry out targeted genotyping of key variants identified in our 3D discovery study, in large 2D-CMR population based-cohorts such as the UK Biobank or the Framingham cohorts.

In summary, the next stage in this work will involve refining the statistical analysis methods and testing the technique's feasibility in disease cohorts. Any significant genotype-phenotype associations will have to be replicated in other populations and validated in 'bench-side' mechanistic studies. As more genotype, phenotype and longitudinal data become available, machine learning approaches might assist in the development of genotype-phenotype specific risk calculators, moving us closer to personalised medicine.

Conclusions

This thesis demonstrates that 3D-CMR combined with computational analysis methods provides high-resolution insight into the earliest stages of heart disease. These methods show promise for population-based studies of the anthropometric, environmental and genetic determinants of LV structure and function in health and disease.

18 References

1. Acierno LJ. The history of cardiology. London ; New York: Parthenon Pub. Group; 1994. ix, 758 p. p.
2. Braunwald E. Cardiology: the past, the present, and the future. Journal of the American College of Cardiology. 2003;42(12):2031-41.
3. Hamburger WW. The earliest known reference to the heart and circulation: The Edwin Smith surgical papyrus, circa 3,000 B.C. American heart journal. 1939;17(3):259-74.
4. Willius FA, Dry TJ. A history of the heart and the circulation. Mansfield Centre, CT: Martino; 2006.
5. Lander ES, Linton LM, Birren B, Nusbaum C, Zody MC, Baldwin J, et al. Initial sequencing and analysis of the human genome. Nature. 2001;409(6822):860-921.
6. Rosner F. Encyclopedia of medicine in the Bible and the Talmud. Northvale, N.J.: Jason Aronson; 2000. xxxiv, 361 p. p.
7. Savona VC, Grech V. Concepts in cardiology - a historical perspective. Images in paediatric cardiology. 1999;1(1):22-31.
8. Harvey W, Willis R, Sydenham Society. The works of William Harvey. London,: Printed for the Sydenham Society; 1847. xcvi, 624 p. p.
9. Ho SY. Anatomy and myoarchitecture of the left ventricular wall in normal and in disease. European journal of echocardiography : the journal of the Working Group on Echocardiography of the European Society of Cardiology. 2009;10(8):iii3-7.
10. Harvey PA, Leinwand LA. The cell biology of disease: cellular mechanisms of cardiomyopathy. The Journal of cell biology. 2011;194(3):355-65.
11. Greenbaum RA, Ho SY, Gibson DG, Becker AE, Anderson RH. Left ventricular fibre architecture in man. Br Heart J. 1981;45(3):248-63.

12. Sanchez-Quintana D, Garcia-Martinez V, Climent V, Hurle JM. Morphological changes in the normal pattern of ventricular myoarchitecture in the developing human heart. *The Anatomical record*. 1995;243(4):483-95.
13. Pearlman ES, Weber KT, Janicki JS. Quantitative histology of the hypertrophied human heart. *Federation proceedings*. 1981;40(7):2042-7.
14. Zou P, Pinotsis N, Lange S, Song YH, Popov A, Mavridis I, et al. Palindromic assembly of the giant muscle protein titin in the sarcomeric Z-disk. *Nature*. 2006;439(7073):229-33.
15. Luther PK. Three-dimensional structure of a vertebrate muscle Z-band: implications for titin and alpha-actinin binding. *Journal of structural biology*. 2000;129(1):1-16.
16. Agarkova I, Perriard JC. The M-band: an elastic web that crosslinks thick filaments in the center of the sarcomere. *Trends in cell biology*. 2005;15(9):477-85.
17. Kostin S, Heling A, Hein S, Scholz D, Klövekorn W-P, Schaper J. The Protein Composition of the Normal and Diseased Cardiac Myocyte. *Heart Fail Rev*. 1998;2(4):245-60.
18. Morita H, Seidman J, Seidman CE. Genetic causes of human heart failure. *The Journal of clinical investigation*. 2005;115(3):518-26.
19. Kuribayashi T, Roberts WC. Myocardial disarray at junction of ventricular septum and left and right ventricular free walls in hypertrophic cardiomyopathy. *Am J Cardiol*. 1992;70(15):1333-40.
20. Tseng WY, Dou J, Reese TG, Wedeen VJ. Imaging myocardial fiber disarray and intramural strain hypokinesis in hypertrophic cardiomyopathy with MRI. *Journal of magnetic resonance imaging : JMRI*. 2006;23(1):1-8.

21. Schaper J, Froede R, Hein S, Buck A, Hashizume H, Speiser B, et al. Impairment of the myocardial ultrastructure and changes of the cytoskeleton in dilated cardiomyopathy. *Circulation*. 1991;83(2):504-14.
22. Bertini M, Sengupta PP, Nucifora G, Delgado V, Ng AC, Marsan NA, et al. Role of left ventricular twist mechanics in the assessment of cardiac dyssynchrony in heart failure. *JACC Cardiovascular imaging*. 2009;2(12):1425-35.
23. Bers DM. Cardiac excitation-contraction coupling. *Nature*. 2002;415(6868):198-205.
24. Thompson BR, Metzger JM. Cell biology of sarcomeric protein engineering: disease modeling and therapeutic potential. *Anatomical record*. 2014;297(9):1663-9.
25. Lorell BH, Carabello BA. Left ventricular hypertrophy: pathogenesis, detection, and prognosis. *Circulation*. 2000;102(4):470-9.
26. Post WS, Larson MG, Myers RH, Galderisi M, Levy D. Heritability of left ventricular mass: the Framingham Heart Study. *Hypertension*. 1997;30(5):1025-8.
27. Lorell BH, Carabello BA. Left ventricular hypertrophy: pathogenesis, detection, and prognosis. *Circulation*. 2000;102(4):470-9.
28. Bella JN, MacCluer JW, Roman MJ, Almasy L, North KE, Best LG, et al. Heritability of left ventricular dimensions and mass in American Indians: The Strong Heart Study. *J Hypertens*. 2004;22(2):281-6.
29. Garner C, Lecomte E, Visvikis S, Abergel E, Lathrop M, Soubrier F. Genetic and environmental influences on left ventricular mass. A family study. *Hypertension*. 2000;36(5):740-6.
30. Sharma P, Middelberg RP, Andrew T, Johnson MR, Christley H, Brown MJ. Heritability of left ventricular mass in a large cohort of twins. *J Hypertens*. 2006;24(2):321-4.

31. Verhaaren HA, Schieken RM, Mosteller M, Hewitt JK, Eaves LJ, Nance WE. Bivariate genetic analysis of left ventricular mass and weight in pubertal twins (the Medical College of Virginia twin study). *Am J Cardiol.* 1991;68(6):661-8.
32. Marian AJ. Genetic determinants of cardiac hypertrophy. *Curr Opin Cardiol.* 2008;23(3):199-205.
33. Savage DD, Levy D, Dannenberg AL, Garrison RJ, Castelli WP. Association of echocardiographic left ventricular mass with body size, blood pressure and physical activity (the Framingham Study). *Am J Cardiol.* 1990;65(5):371-6.
34. Daniels SR, Kimball TR, Morrison JA, Khoury P, Witt S, Meyer RA. Effect of lean body mass, fat mass, blood pressure, and sexual maturation on left ventricular mass in children and adolescents. Statistical, biological, and clinical significance. *Circulation.* 1995;92(11):3249-54.
35. Himeno E, Nishino K, Nakashima Y, Kuroiwa A, Ikeda M. Weight reduction regresses left ventricular mass regardless of blood pressure level in obese subjects. *American heart journal.* 1996;131(2):313-9.
36. Hales S, Innys W, Manby R, Woodward T, Cartwright T, Hales S. Statical essays containing haemastatics, or, An account of some hydraulick and hydrostatical experiments made on the blood and blood-vessels of animals : also an account of some experiments on stones in the kidneys and bladder with an enquiry into the nature of those anomalous concretions : to which is added, an appendix, containing observations and experiments relating to several subjects in the first volume, the greatest part of which were read at several meetings before the Royal Society : with an index to both volumes. Vol. II. London: Printed for W. Innys and R. Manby, at the west-end of St. Paul's, and T. Woodward, at the Half Moon between the Temple-Gates, Fleetstreet; 1733. xxii, 26 , 361, 23 p. p.

37. Shevchenko YL, Tsitlik JE. 90th Anniversary of the Development by Nikolai S. Korotkoff of the Auscultatory Method of Measuring Blood Pressure. *Circulation*. 1996;94(2):116-8.
38. James PA, Oparil S, Carter BL, Cushman WC, Dennison-Himmelfarb C, Handler J, et al. 2014 evidence-based guideline for the management of high blood pressure in adults: report from the panel members appointed to the Eighth Joint National Committee (JNC 8). *Jama*. 2014;311(5):507-20.
39. Chobanian AV, Bakris GL, Black HR, Cushman WC, Green LA, Izzo JL, Jr., et al. The Seventh Report of the Joint National Committee on Prevention, Detection, Evaluation, and Treatment of High Blood Pressure: the JNC 7 report. *Jama*. 2003;289(19):2560-72.
40. Black HR. The paradigm has shifted to systolic blood pressure. *Journal of human hypertension*. 2004;18 Suppl 2:S3-7.
41. Black HR. The paradigm has shifted, to systolic blood pressure. *Hypertension*. 1999;34(3):386-7.
42. Kannel WB, Gordon T, Schwartz MJ. Systolic versus diastolic blood pressure and risk of coronary heart disease. The Framingham study. *Am J Cardiol*. 1971;27(4):335-46.
43. Frohlich ED. Detection, evaluation, and treatment of hypertension: JNC-5 (Joint National Committee on Detection, Evaluation, and Treatment of High Blood Pressure). *Heart disease and stroke : a journal for primary care physicians*. 1993;2(6):459-60.
44. Lewington S, Clarke R, Qizilbash N, Peto R, Collins R, Prospective Studies C. Age-specific relevance of usual blood pressure to vascular mortality: a meta-analysis of individual data for one million adults in 61 prospective studies. *Lancet*. 2002;360(9349):1903-13.
45. Lenfant C, Chobanian AV, Jones DW, Roccella EJ, Joint National Committee on the Prevention DE, Treatment of High Blood P. Seventh report of the Joint National Committee

on the Prevention, Detection, Evaluation, and Treatment of High Blood Pressure (JNC 7): resetting the hypertension sails. *Hypertension*. 2003;41(6):1178-9.

46. Alter P, Rupp H, Stoll F, Adams P, Figiel JH, Klose KJ, et al. Increased end diastolic wall stress precedes left ventricular hypertrophy in dilative heart failure--use of the volume-based wall stress index. *International journal of cardiology*. 2012;157(2):233-8.

47. Vlachopoulos C, Aznaouridis K, Stefanadis C. Aortic stiffness for cardiovascular risk prediction: just measure it, just do it! *Journal of the American College of Cardiology*. 2014;63(7):647-9.

48. Willum-Hansen T, Staessen JA, Torp-Pedersen C, Rasmussen S, Thijs L, Ibsen H, et al. Prognostic value of aortic pulse wave velocity as index of arterial stiffness in the general population. *Circulation*. 2006;113(5):664-70.

49. Van Bortel LM, Laurent S, Boutouyrie P, Chowienczyk P, Cruickshank JK, De Backer T, et al. Expert consensus document on the measurement of aortic stiffness in daily practice using carotid-femoral pulse wave velocity. *J Hypertens*. 2012;30(3):445-8.

50. Ben-Shlomo Y, Spears M, Boustred C, May M, Anderson SG, Benjamin EJ, et al. Aortic pulse wave velocity improves cardiovascular event prediction: an individual participant meta-analysis of prospective observational data from 17,635 subjects. *Journal of the American College of Cardiology*. 2014;63(7):636-46.

51. Sutton-Tyrrell K, Najjar SS, Boudreau RM, Venkitachalam L, Kupelian V, Simonsick EM, et al. Elevated aortic pulse wave velocity, a marker of arterial stiffness, predicts cardiovascular events in well-functioning older adults. *Circulation*. 2005;111(25):3384-90.

52. de Wit A, Vis K, Jeremy RW. Aortic stiffness in heritable aortopathies: relationship to aneurysm growth rate. *Heart, lung & circulation*. 2013;22(1):3-11.

53. Lalande A, Khau Van Kien P, Walker PM, Zhu L, Legrand L, Claustres M, et al. Compliance and pulse wave velocity assessed by MRI detect early aortic impairment in

young patients with mutation of the smooth muscle myosin heavy chain. *Journal of magnetic resonance imaging : JMRI*. 2008;28(5):1180-7.

54. Teixido-Tura G, Redheuil A, Rodriguez-Palomares J, Gutierrez L, Sanchez V, Forteza A, et al. Aortic biomechanics by magnetic resonance: early markers of aortic disease in Marfan syndrome regardless of aortic dilatation? *International journal of cardiology*. 2014;171(1):56-61.

55. Redheuil A, Yu WC, Wu CO, Mousseaux E, de Cesare A, Yan R, et al. Reduced ascending aortic strain and distensibility: earliest manifestations of vascular aging in humans. *Hypertension*. 2010;55(2):319-26.

56. Kaess BM, Rong J, Larson MG, Hamburg NM, Vita JA, Levy D, et al. Aortic stiffness, blood pressure progression, and incident hypertension. *Jama*. 2012;308(9):875-81.

57. Grotenhuis HB, Westenberg JJ, Steendijk P, van der Geest RJ, Ottenkamp J, Bax JJ, et al. Validation and reproducibility of aortic pulse wave velocity as assessed with velocity-encoded MRI. *Journal of magnetic resonance imaging : JMRI*. 2009;30(3):521-6.

58. Bolster BD, Jr., Atalar E, Hardy CJ, McVeigh ER. Accuracy of arterial pulse-wave velocity measurement using MR. *Journal of magnetic resonance imaging : JMRI*. 1998;8(4):878-88.

59. Wentland AL, Grist TM, Wieben O. Review of MRI-based measurements of pulse wave velocity: a biomarker of arterial stiffness. *Cardiovascular diagnosis and therapy*. 2014;4(2):193-206.

60. Tarnoki AD, Tarnoki DL, Stazi MA, Medda E, Cotichini R, Nistico L, et al. Heritability of central blood pressure and arterial stiffness: a twin study. *J Hypertens*. 2012;30(8):1564-71.

61. Medda E, Fagnani C, Schillaci G, Tarnoki AD, Tarnoki DL, Baracchini C, et al. Heritability of arterial stiffness and carotid intima-media thickness: an Italian twin study. *Nutrition, metabolism, and cardiovascular diseases : NMCD*. 2014;24(5):511-7.
62. Mitchell GF, DeStefano AL, Larson MG, Benjamin EJ, Chen MH, Vasan RS, et al. Heritability and a genome-wide linkage scan for arterial stiffness, wave reflection, and mean arterial pressure: the Framingham Heart Study. *Circulation*. 2005;112(2):194-9.
63. Mitchell GF, Verwoert GC, Tarasov KV, Isaacs A, Smith AV, Yasmin, et al. Common genetic variation in the 3'-BCL11B gene desert is associated with carotid-femoral pulse wave velocity and excess cardiovascular disease risk: the AortaGen Consortium. *Circulation Cardiovascular genetics*. 2012;5(1):81-90.
64. Burton H, Alberg C, Stewart A. Heart to Heart: Inherited Cardiovascular Conditions Services - A Needs Assessment and Service Review. PHG Foundation. 2009.
65. Christiaans I, van Engelen K, van Langen IM, Birnie E, Bonsel GJ, Elliott PM, et al. Risk stratification for sudden cardiac death in hypertrophic cardiomyopathy: systematic review of clinical risk markers. *Europace : European pacing, arrhythmias, and cardiac electrophysiology : journal of the working groups on cardiac pacing, arrhythmias, and cardiac cellular electrophysiology of the European Society of Cardiology*. 2010;12(3):313-21.
66. Priori SG, Wilde AA, Horie M, Cho Y, Behr ER, Berul C, et al. HRS/EHRA/APHRS expert consensus statement on the diagnosis and management of patients with inherited primary arrhythmia syndromes: document endorsed by HRS, EHRA, and APHRS in May 2013 and by ACCF, AHA, PACES, and AEPC in June 2013. *Heart rhythm : the official journal of the Heart Rhythm Society*. 2013;10(12):1932-63.
67. Ware JS, Roberts AM, Cook SA. Republished review: Next generation sequencing for clinical diagnostics and personalised medicine: implications for the next generation cardiologist. *Postgrad Med J*. 2012;88(1038):234-9.

68. Report of the WHO/ISFC task force on the definition and classification of cardiomyopathies. *Br Heart J*. 1980;44(6):672-3.
69. Maron BJ, Towbin JA, Thiene G, Antzelevitch C, Corrado D, Arnett D, et al. Contemporary definitions and classification of the cardiomyopathies: an American Heart Association Scientific Statement from the Council on Clinical Cardiology, Heart Failure and Transplantation Committee; Quality of Care and Outcomes Research and Functional Genomics and Translational Biology Interdisciplinary Working Groups; and Council on Epidemiology and Prevention. *Circulation*. 2006;113(14):1807-16.
70. Teare D. Asymmetrical hypertrophy of the heart in young adults. *Br Heart J*. 1958;20(1):1-8.
71. Geisterfer-Lowrance AA, Kass S, Tanigawa G, Vosberg HP, McKenna W, Seidman CE, et al. A molecular basis for familial hypertrophic cardiomyopathy: a beta cardiac myosin heavy chain gene missense mutation. *Cell*. 1990;62(5):999-1006.
72. Gersh BJ, Maron BJ, Bonow RO, Dearani JA, Fifer MA, Link MS, et al. 2011 ACCF/AHA guideline for the diagnosis and treatment of hypertrophic cardiomyopathy: a report of the American College of Cardiology Foundation/American Heart Association Task Force on Practice Guidelines. *Circulation*. 2011;124(24):e783-831.
73. Olivetto I, Girolami F, Ackerman MJ, Nistri S, Bos JM, Zachara E, et al. Myofilament protein gene mutation screening and outcome of patients with hypertrophic cardiomyopathy. *Mayo Clinic proceedings*. 2008;83(6):630-8.
74. Morita H, Rehm HL, Menesses A, McDonough B, Roberts AE, Kucherlapati R, et al. Shared genetic causes of cardiac hypertrophy in children and adults. *N Engl J Med*. 2008;358(18):1899-908.
75. Alcalai R, Seidman JG, Seidman CE. Genetic basis of hypertrophic cardiomyopathy: from bench to the clinics. *Journal of cardiovascular electrophysiology*. 2008;19(1):104-10.

76. McNally EM, Golbus JR, Puckelwartz MJ. Genetic mutations and mechanisms in dilated cardiomyopathy. *The Journal of clinical investigation*. 2013;123(1):19-26.
77. Hershberger RE, Hedges DJ, Morales A. Dilated cardiomyopathy: the complexity of a diverse genetic architecture. *Nature reviews Cardiology*. 2013;10(9):531-47.
78. Elliott P, Andersson B, Arbustini E, Bilinska Z, Cecchi F, Charron P, et al. Classification of the cardiomyopathies: a position statement from the European Society Of Cardiology Working Group on Myocardial and Pericardial Diseases. *European heart journal*. 2008;29(2):270-6.
79. Mestroni L, Maisch B, McKenna WJ, Schwartz K, Charron P, Rocco C, et al. Guidelines for the study of familial dilated cardiomyopathies. Collaborative Research Group of the European Human and Capital Mobility Project on Familial Dilated Cardiomyopathy. *European heart journal*. 1999;20(2):93-102.
80. Parsai C, O'Hanlon R, Prasad SK, Mohiaddin RH. Diagnostic and prognostic value of cardiovascular magnetic resonance in non-ischaemic cardiomyopathies. *Journal of cardiovascular magnetic resonance : official journal of the Society for Cardiovascular Magnetic Resonance*. 2012;14:54.
81. Burkett EL, Hershberger RE. Clinical and genetic issues in familial dilated cardiomyopathy. *Journal of the American College of Cardiology*. 2005;45(7):969-81.
82. Watkins H, Ashrafian H, Redwood C. Inherited cardiomyopathies. *N Engl J Med*. 2011;364(17):1643-56.
83. Bick AG, Flannick J, Ito K, Cheng S, Vasan RS, Parfenov MG, et al. Burden of rare sarcomere gene variants in the Framingham and Jackson Heart Study cohorts. *American journal of human genetics*. 2012;91(3):513-9.
84. Norton N, Li D, Rampersaud E, Morales A, Martin ER, Zuchner S, et al. Exome sequencing and genome-wide linkage analysis in 17 families illustrate the complex

contribution of TTN truncating variants to dilated cardiomyopathy. *Circulation Cardiovascular genetics*. 2013;6(2):144-53.

85. Wells QS, Becker JR, Su YR, Mosley JD, Weeke P, D'Aoust L, et al. Whole exome sequencing identifies a causal RBM20 mutation in a large pedigree with familial dilated cardiomyopathy. *Circulation Cardiovascular genetics*. 2013;6(4):317-26.

86. Theis JL, Zimmermann MT, Larsen BT, Rybakova IN, Long PA, Evans JM, et al. TNNI3K mutation in familial syndrome of conduction system disease, atrial tachyarrhythmia and dilated cardiomyopathy. *Human molecular genetics*. 2014;23(21):5793-804.

87. Villard E, Perret C, Gary F, Proust C, Dilanian G, Hengstenberg C, et al. A genome-wide association study identifies two loci associated with heart failure due to dilated cardiomyopathy. *European heart journal*. 2011;32(9):1065-76.

88. Meder B, Ruhle F, Weis T, Homuth G, Keller A, Franke J, et al. A genome-wide association study identifies 6p21 as novel risk locus for dilated cardiomyopathy. *European heart journal*. 2014;35(16):1069-77.

89. Haas J, Frese KS, Peil B, Kloos W, Keller A, Nietsch R, et al. Atlas of the clinical genetics of human dilated cardiomyopathy. *European heart journal*. 2014.

90. Pugh TJ, Kelly MA, Gowrisankar S, Hynes E, Seidman MA, Baxter SM, et al. The landscape of genetic variation in dilated cardiomyopathy as surveyed by clinical DNA sequencing. *Genetics in medicine : official journal of the American College of Medical Genetics*. 2014;16(8):601-8.

91. Herman DS, Lam L, Taylor MR, Wang L, Teekakirikul P, Christodoulou D, et al. Truncations of titin causing dilated cardiomyopathy. *The New England journal of medicine*. 2012;366(7):619-28.

92. Ackerman MJ, Priori SG, Willems S, Berul C, Brugada R, Calkins H, et al. HRS/EHRA expert consensus statement on the state of genetic testing for the channelopathies

and cardiomyopathies this document was developed as a partnership between the Heart Rhythm Society (HRS) and the European Heart Rhythm Association (EHRA). Heart rhythm : the official journal of the Heart Rhythm Society. 2011;8(8):1308-39.

93. Echols MR, Felker GM, Thomas KL, Pieper KS, Garg J, Cuffe MS, et al. Racial differences in the characteristics of patients admitted for acute decompensated heart failure and their relation to outcomes: results from the OPTIME-CHF trial. Journal of cardiac failure. 2006;12(9):684-8.

94. Coughlin SS, Myers L, Michaels RK. What explains black-white differences in survival in idiopathic dilated cardiomyopathy? The Washington, DC, Dilated Cardiomyopathy Study. Journal of the National Medical Association. 1997;89(4):277-82.

95. Coughlin SS, Gottdiener JS, Baughman KL, Wasserman A, Marx ES, Tefft MC, et al. Black-white differences in mortality in idiopathic dilated cardiomyopathy: the Washington, DC, dilated cardiomyopathy study. Journal of the National Medical Association. 1994;86(8):583-91.

96. Coughlin SS, Labenberg JR, Tefft MC. Black-white differences in idiopathic dilated cardiomyopathy: the Washington DC dilated Cardiomyopathy Study. Epidemiology. 1993;4(2):165-72.

97. Gregorio CC, Trombitas K, Centner T, Kolmerer B, Stier G, Kunke K, et al. The NH2 terminus of titin spans the Z-disc: its interaction with a novel 19-kD ligand (T-cap) is required for sarcomeric integrity. The Journal of cell biology. 1998;143(4):1013-27.

98. Linke WA, Granzier H. A spring tale: new facts on titin elasticity. Biophysical journal. 1998;75(6):2613-4.

99. LeWinter MM, Granzier HL. Titin is a major human disease gene. Circulation. 2013;127(8):938-44.

100. LeWinter MM, Granzier H. Cardiac titin: a multifunctional giant. *Circulation*. 2010;121(19):2137-45.
101. Roberts AM, Ware JS, Herman DS, Schafer S, Baksi J, Bick AG, et al. Integrated allelic, transcriptional, and phenomic dissection of the cardiac effects of titin truncations in health and disease. *Science translational medicine*. 2015;7(270):270ra6.
102. Dahm R. Friedrich Miescher and the discovery of DNA. *Developmental biology*. 2005;278(2):274-88.
103. Avery OT, Macleod CM, McCarty M. Studies on the Chemical Nature of the Substance Inducing Transformation of Pneumococcal Types : Induction of Transformation by a Desoxyribonucleic Acid Fraction Isolated from *Pneumococcus* Type Iii. *The Journal of experimental medicine*. 1944;79(2):137-58.
104. Watson JD, Crick FH. Molecular structure of nucleic acids; a structure for deoxyribose nucleic acid. *Nature*. 1953;171(4356):737-8.
105. Blaxter M. Genetics. Revealing the dark matter of the genome. *Science*. 2010;330(6012):1758-9.
106. Pennisi E. Genomics. ENCODE project writes eulogy for junk DNA. *Science*. 2012;337(6099):1159, 61.
107. Consortium EP. An integrated encyclopedia of DNA elements in the human genome. *Nature*. 2012;489(7414):57-74.
108. Pearson H. Genetics: What is a gene? *Nature*. 2006;441(7092):398-401.
109. Gerstein MB, Bruce C, Rozowsky JS, Zheng D, Du J, Korbel JO, et al. What is a gene, post-ENCODE? History and updated definition. *Genome research*. 2007;17(6):669-81.
110. Marenberg ME, Risch N, Berkman LF, Floderus B, de Faire U. Genetic susceptibility to death from coronary heart disease in a study of twins. *N Engl J Med*. 1994;330(15):1041-6.

111. Adams TD, Yanowitz FG, Fisher AG, Ridges JD, Nelson AG, Hagan AD, et al. Heritability of cardiac size: an echocardiographic and electrocardiographic study of monozygotic and dizygotic twins. *Circulation*. 1985;71(1):39-44.
112. Lifton RP. Molecular genetics of human blood pressure variation. *Science*. 1996;272(5262):676-80.
113. Marian AJ, Belmont J. Strategic approaches to unraveling genetic causes of cardiovascular diseases. *Circ Res*. 2011;108(10):1252-69.
114. Iyengar SK, Elston RC. The genetic basis of complex traits: rare variants or "common gene, common disease"? *Methods in molecular biology*. 2007;376:71-84.
115. Arora P, Newton-Cheh C. Blood pressure and human genetic variation in the general population. *Curr Opin Cardiol*. 2010;25(3):229-37.
116. Kathiresan S, Manning AK, Demissie S, D'Agostino RB, Surti A, Guiducci C, et al. A genome-wide association study for blood lipid phenotypes in the Framingham Heart Study. *BMC medical genetics*. 2007;8 Suppl 1:S17.
117. Schork NJ, Murray SS, Frazer KA, Topol EJ. Common vs. rare allele hypotheses for complex diseases. *Current opinion in genetics & development*. 2009;19(3):212-9.
118. Reich DE, Lander ES. On the allelic spectrum of human disease. *Trends in genetics : TIG*. 2001;17(9):502-10.
119. Sanger F, Coulson AR. A rapid method for determining sequences in DNA by primed synthesis with DNA polymerase. *Journal of molecular biology*. 1975;94(3):441-8.
120. Sanger F, Nicklen S, Coulson AR. DNA sequencing with chain-terminating inhibitors. *Proceedings of the National Academy of Sciences of the United States of America*. 1977;74(12):5463-7.
121. Morozova O, Marra MA. Applications of next-generation sequencing technologies in functional genomics. *Genomics*. 2008;92(5):255-64.

122. Margulies M, Egholm M, Altman WE, Attiya S, Bader JS, Bemben LA, et al. Genome sequencing in microfabricated high-density picolitre reactors. *Nature*. 2005;437(7057):376-80.
123. Metzker ML. Sequencing technologies - the next generation. *Nature reviews Genetics*. 2010;11(1):31-46.
124. McPherson JD, Marra M, Hillier L, Waterston RH, Chinwalla A, Wallis J, et al. A physical map of the human genome. *Nature*. 2001;409(6822):934-41.
125. Venter JC, Adams MD, Myers EW, Li PW, Mural RJ, Sutton GG, et al. The sequence of the human genome. *Science*. 2001;291(5507):1304-51.
126. Ware JS, Roberts AM, Cook SA. Next generation sequencing for clinical diagnostics and personalised medicine: implications for the next generation cardiologist. *Heart*. 2012;98(4):276-81.
127. Wetterstrand K. DNA Sequencing Costs: Data from the NHGRI Genome Sequencing Program (GSP). Available from: www.genome.gov/sequencingcosts.
128. Rehm HL. Disease-targeted sequencing: a cornerstone in the clinic. *Nature reviews Genetics*. 2013;14(4):295-300.
129. Altshuler D, Daly MJ, Lander ES. Genetic mapping in human disease. *Science*. 2008;322(5903):881-8.
130. Moulik M, Vatta M, Witt SH, Arola AM, Murphy RT, McKenna WJ, et al. ANKRD1, the gene encoding cardiac ankyrin repeat protein, is a novel dilated cardiomyopathy gene. *Journal of the American College of Cardiology*. 2009;54(4):325-33.
131. Seidman JG, Seidman C. The genetic basis for cardiomyopathy: from mutation identification to mechanistic paradigms. *Cell*. 2001;104(4):557-67.

132. Simon T, Verstuyft C, Mary-Krause M, Quteineh L, Drouet E, Meneveau N, et al. Genetic determinants of response to clopidogrel and cardiovascular events. *N Engl J Med*. 2009;360(4):363-75.
133. Neale BM. Introduction to linkage disequilibrium, the HapMap, and imputation. *Cold Spring Harbor protocols*. 2010;2010(3):pdb top74.
134. Dawn Teare M, Barrett JH. Genetic linkage studies. *Lancet*. 2005;366(9490):1036-44.
135. Consortium CAD, Deloukas P, Kanoni S, Willenborg C, Farrall M, Assimes TL, et al. Large-scale association analysis identifies new risk loci for coronary artery disease. *Nature genetics*. 2013;45(1):25-33.
136. Gudbjartsson DF, Arnar DO, Helgadóttir A, Gretarsdóttir S, Holm H, Sigurdsson A, et al. Variants conferring risk of atrial fibrillation on chromosome 4q25. *Nature*. 2007;448(7151):353-7.
137. Ellinor PT, Lunetta KL, Albert CM, Glazer NL, Ritchie MD, Smith AV, et al. Meta-analysis identifies six new susceptibility loci for atrial fibrillation. *Nature genetics*. 2012;44(6):670-5.
138. Norton N, Li D, Rieder MJ, Siegfried JD, Rampsaud E, Zuchner S, et al. Genome-wide studies of copy number variation and exome sequencing identify rare variants in BAG3 as a cause of dilated cardiomyopathy. *American journal of human genetics*. 2011;88(3):273-82.
139. Sham PC, Purcell SM. Statistical power and significance testing in large-scale genetic studies. *Nature reviews Genetics*. 2014;15(5):335-46.
140. Lopez de Maturana E, Ibanez-Escriche N, Gonzalez-Recio O, Marenne G, Mehrban H, Chanock SJ, et al. Next generation modeling in GWAS: comparing different genetic architectures. *Human genetics*. 2014;133(10):1235-53.

141. McCarthy MI, Abecasis GR, Cardon LR, Goldstein DB, Little J, Ioannidis JP, et al. Genome-wide association studies for complex traits: consensus, uncertainty and challenges. *Nature reviews Genetics*. 2008;9(5):356-69.
142. Belkadi A, Bolze A, Itan Y, Cobat A, Vincent QB, Antipenko A, et al. Whole-genome sequencing is more powerful than whole-exome sequencing for detecting exome variants. *Proceedings of the National Academy of Sciences*. 2015.
143. Morgan CJ, Hendee WR. *Introduction to magnetic resonance imaging*. 1st ed. Denver, Colo.: Multi-Media Pub.; 1984. xii, 215 p. p.
144. Geva T. Magnetic resonance imaging: historical perspective. *Journal of cardiovascular magnetic resonance : official journal of the Society for Cardiovascular Magnetic Resonance*. 2006;8(4):573-80.
145. McRobbie DW. *MRI from picture to proton*. 2nd ed. Cambridge, UK ; New York: Cambridge University Press; 2007. xii, 394 p. p.
146. Ridgway JP. Cardiovascular magnetic resonance physics for clinicians: part I. *Journal of cardiovascular magnetic resonance : official journal of the Society for Cardiovascular Magnetic Resonance*. 2010;12:71.
147. McRobbie DW. *MRI from picture to proton*. 2nd ed. ed. Cambridge: Cambridge University Press; 2007.
148. Mansfield P, Grannell PK. NMR 'diffraction' in solids? *Journal of Physics C: Solid State Physics*. 1973;6(22):L422.
149. Lauterbur PC. Image Formation by Induced Local Interactions: Examples Employing Nuclear Magnetic Resonance. *Nature*. 1973;242(5394):190-1.
150. Kumar A, Welte D, Ernst RR. NMR Fourier zeugmatography. 1975. *Journal of magnetic resonance*. 2011;213(2):495-509.

151. Ernst RR. Nobel Lecture. Nuclear magnetic resonance Fourier transform spectroscopy. *Bioscience reports*. 1992;12(3):143-87.
152. Petersson JS, Christoffersson JO, Golman K. MRI simulation using the k-space formalism. *Magnetic resonance imaging*. 1993;11(4):557-68.
153. Mezrich R. A perspective on K-space. *Radiology*. 1995;195(2):297-315.
154. Damadian R. Tumor detection by nuclear magnetic resonance. *Science*. 1971;171(3976):1151-3.
155. Damadian R, Zaner K, Hor D, DiMaio T, Minkoff L, Goldsmith M. Nuclear magnetic resonance as a new tool in cancer research: human tumors by NMR. *Annals of the New York Academy of Sciences*. 1973;222:1048-76.
156. Damadian R, Goldsmith M, Minkoff L. NMR in cancer: XVI. FONAR image of the live human body. *Physiological chemistry and physics*. 1977;9(1):97-100, 8.
157. Dreizen P. The Nobel prize for MRI: a wonderful discovery and a sad controversy. *Lancet*. 2004;363(9402):78.
158. Reynolds LA, Tansey EM, Wellcome Trust Centre for the History of Medicine at UCL. *Making the Human Body Transparent: The impact of Nuclear Magnetic Resonance and Magnetic Resonance Imaging*. London: Wellcome Trust Centre for the History of Medicine at UCL; 1998. viii, 93 p. p.
159. Hawkes RC, Holland GN, Moore WS, Roebuck EJ, Worthington BS. Nuclear magnetic resonance (NMR) tomography of the normal heart. *Journal of computer assisted tomography*. 1981;5(5):605-12.
160. Heidelberg E, Petersen SB, Lauterbur PC. Aspects of cardiac diagnosis using synchronized NMR imaging. *European journal of radiology*. 1983;3 Suppl 1:281-5.
161. Lenz GW, Haacke EM, White RD. Retrospective cardiac gating: a review of technical aspects and future directions. *Magnetic resonance imaging*. 1989;7(5):445-55.

162. Barkhausen J, Ruehm SG, Goyen M, Buck T, Laub G, Debatin JF. MR evaluation of ventricular function: true fast imaging with steady-state precession versus fast low-angle shot cine MR imaging: feasibility study. *Radiology*. 2001;219(1):264-9.
163. Scheffler K, Lehnhardt S. Principles and applications of balanced SSFP techniques. *European radiology*. 2003;13(11):2409-18.
164. Thiele H, Nagel E, Paetsch I, Schnackenburg B, Bornstedt A, Kouwenhoven M, et al. Functional cardiac MR imaging with steady-state free precession (SSFP) significantly improves endocardial border delineation without contrast agents. *Journal of magnetic resonance imaging : JMRI*. 2001;14(4):362-7.
165. Underwood SR, Firmin DN, Rees RS, Longmore DB. Magnetic resonance velocity mapping. *Clinical physics and physiological measurement : an official journal of the Hospital Physicists' Association, Deutsche Gesellschaft fur Medizinische Physik and the European Federation of Organisations for Medical Physics*. 1990;11 Suppl A:37-43.
166. Biglands JD, Radjenovic A, Ridgway JP. Cardiovascular magnetic resonance physics for clinicians: Part II. *Journal of cardiovascular magnetic resonance : official journal of the Society for Cardiovascular Magnetic Resonance*. 2012;14:66.
167. Pelc NJ, Herfkens RJ, Shimakawa A, Enzmann DR. Phase contrast cine magnetic resonance imaging. *Magnetic resonance quarterly*. 1991;7(4):229-54.
168. Nayler GL, Firmin DN, Longmore DB. Blood flow imaging by cine magnetic resonance. *Journal of computer assisted tomography*. 1986;10(5):715-22.
169. Lotz J, Meier C, Leppert A, Galanski M. Cardiovascular flow measurement with phase-contrast MR imaging: basic facts and implementation. *Radiographics*. 2002;22(3):651-71.
170. Dogui A, Redheuil A, Lefort M, DeCesare A, Kachenoura N, Herment A, et al. Measurement of aortic arch pulse wave velocity in cardiovascular MR: comparison of transit

time estimators and description of a new approach. *Journal of magnetic resonance imaging* : JMRI. 2011;33(6):1321-9.

171. Pruessmann KP, Weiger M, Scheidegger MB, Boesiger P. SENSE: sensitivity encoding for fast MRI. *Magnetic resonance in medicine : official journal of the Society of Magnetic Resonance in Medicine / Society of Magnetic Resonance in Medicine*. 1999;42(5):952-62.

172. van den Brink JS, Watanabe Y, Kuhl CK, Chung T, Muthupillai R, Van Cauteren M, et al. Implications of SENSE MR in routine clinical practice. *European journal of radiology*. 2003;46(1):3-27.

173. Kramer CM, Barkhausen J, Flamm SD, Kim RJ, Nagel E. Standardized cardiovascular magnetic resonance imaging (CMR) protocols, society for cardiovascular magnetic resonance: board of trustees task force on standardized protocols. *Journal of cardiovascular magnetic resonance : official journal of the Society for Cardiovascular Magnetic Resonance*. 2008;10:35.

174. Pattynama PM, Lamb HJ, van der Velde EA, van der Wall EE, de Roos A. Left ventricular measurements with cine and spin-echo MR imaging: a study of reproducibility with variance component analysis. *Radiology*. 1993;187(1):261-8.

175. Gay SB, Sistrom CL, Holder CA, Suratt PM. Breath-holding capability of adults. Implications for spiral computed tomography, fast-acquisition magnetic resonance imaging, and angiography. *Investigative radiology*. 1994;29(9):848-51.

176. Razavi RS, Hill DL, Muthurangu V, Miquel ME, Taylor AM, Kozerke S, et al. Three-dimensional magnetic resonance imaging of congenital cardiac anomalies. *Cardiology in the young*. 2003;13(5):461-5.

177. Barkauskas KJ, Rajiah P, Ashwath R, Hamilton JI, Chen Y, Ma D, et al. Quantification of left ventricular functional parameter values using 3D spiral bSSFP and

through-time Non-Cartesian GRAPPA. *Journal of cardiovascular magnetic resonance* : official journal of the Society for Cardiovascular Magnetic Resonance. 2014;16(1):65.

178. Mascarenhas NB, Muthupillai R, Cheong B, Pereyra M, Flamm SD. Fast 3D cine steady-state free precession imaging with sensitivity encoding for assessment of left ventricular function in a single breath-hold. *AJR Am J Roentgenol*. 2006;187(5):1235-9.

179. Rochitte CE, Azevedo CF, Rosario MA, Siqueira MH, Monsao V, Saranathan M, et al. Single-Breathhold Four-Dimensional Assessment of Left Ventricular Morphological and Functional Parameters by Magnetic Resonance Imaging Using the VAST Technique. *Open Cardiovasc Med J*. 2011;5:90-8.

180. Hamdan A, Kelle S, Schnackenburg B, Wellnhofer E, Fleck E, Nagel E. Single-breathhold four-dimensional assessment of left ventricular volumes and function using k-t BLAST after application of extracellular contrast agent at 3 Tesla. *Journal of magnetic resonance imaging : JMRI*. 2008;27(5):1028-36.

181. Sievers B, Schrader S, Rehwald W, Hunold P, Barkhausen J, Erbel R. Left ventricular function assessment using a fast 3D gradient echo pulse sequence: comparison to standard multi-breath hold 2D steady state free precession imaging and accounting for papillary muscles and trabeculations. *Acta Cardiol*. 2011;66(3):349-57.

182. Parish V, Hussain T, Beerbaum P, Greil G, Nagel E, Razavi R, et al. Single breath-hold assessment of ventricular volumes using 32-channel coil technology and an extracellular contrast agent. *Journal of magnetic resonance imaging : JMRI*. 2010;31(4):838-44.

183. Davarpanah AH, Chen YP, Kino A, Farrelly CT, Keeling AN, Sheehan JJ, et al. Accelerated two- and three-dimensional cine MR imaging of the heart by using a 32-channel coil. *Radiology*. 2010;254(1):98-108.

184. Kozerke S, Tsao J, Razavi R, Boesiger P. Accelerating cardiac cine 3D imaging using k-t BLAST. *Magnetic resonance in medicine : official journal of the Society of Magnetic Resonance in Medicine / Society of Magnetic Resonance in Medicine*. 2004;52(1):19 - 26.
185. Peters DC, Ennis DB, Rohatgi P, Syed MA, McVeigh ER, Arai AE. 3D breath-held cardiac function with projection reconstruction in steady state free precession validated using 2D cine MRI. *Journal of magnetic resonance imaging : JMRI*. 2004;20(3):411-6.
186. Jahnke C, Nagel E, Gebker R, Bornstedt A, Schnackenburg B, Kozerke S, et al. Four-dimensional single breathhold magnetic resonance imaging using kt-BLAST enables reliable assessment of left- and right-ventricular volumes and mass. *Journal of magnetic resonance imaging : JMRI*. 2007;25(4):737-42.
187. Greil GF, Boettger T, Germann S, Klumpp B, Baltes C, Kozerke S, et al. Quantitative assessment of ventricular function using three-dimensional SSFP magnetic resonance angiography. *Journal of magnetic resonance imaging : JMRI*. 2007;26(2):288-95.
188. Grothues F, Smith GC, Moon JC, Bellenger NG, Collins P, Klein HU, et al. Comparison of interstudy reproducibility of cardiovascular magnetic resonance with two-dimensional echocardiography in normal subjects and in patients with heart failure or left ventricular hypertrophy. *The American journal of cardiology*. 2002;90(1):29-34.
189. Fieno DS, Jaffe WC, Simonetti OP, Judd RM, Finn JP. TrueFISP: assessment of accuracy for measurement of left ventricular mass in an animal model. *Journal of magnetic resonance imaging : JMRI*. 2002;15(5):526-31.
190. Beygui F, Furber A, Delepine S, Helft G, Metzger JP, Geslin P, et al. Routine breath-hold gradient echo MRI-derived right ventricular mass, volumes and function: accuracy, reproducibility and coherence study. *The international journal of cardiovascular imaging*. 2004;20(6):509-16.

191. Bellenger NG, Davies LC, Francis JM, Coats AJ, Pennell DJ. Reduction in sample size for studies of remodeling in heart failure by the use of cardiovascular magnetic resonance. *Journal of cardiovascular magnetic resonance : official journal of the Society for Cardiovascular Magnetic Resonance*. 2000;2(4):271-8.
192. Standardization of cardiac tomographic imaging. From the Committee on Advanced Cardiac Imaging and Technology, Council on Clinical Cardiology, American Heart Association; Cardiovascular Imaging Committee, American College of Cardiology; and Board of Directors, Cardiovascular Council, Society of Nuclear Medicine. *Circulation*. 1992;86(1):338-9.
193. Cerqueira MD, Weissman NJ, Dilsizian V, Jacobs AK, Kaul S, Laskey WK, et al. Standardized myocardial segmentation and nomenclature for tomographic imaging of the heart. A statement for healthcare professionals from the Cardiac Imaging Committee of the Council on Clinical Cardiology of the American Heart Association. *Circulation*. 2002;105(4):539-42.
194. Marcus JT, Gotte MJ, DeWaal LK, Stam MR, Van der Geest RJ, Heethaar RM, et al. The influence of through-plane motion on left ventricular volumes measured by magnetic resonance imaging: implications for image acquisition and analysis. *Journal of cardiovascular magnetic resonance : official journal of the Society for Cardiovascular Magnetic Resonance*. 1999;1(1):1-6.
195. Miller CA, Jordan P, Borg A, Argyle R, Clark D, Pearce K, et al. Quantification of left ventricular indices from SSFP cine imaging: impact of real-world variability in analysis methodology and utility of geometric modeling. *Journal of magnetic resonance imaging : JMRI*. 2013;37(5):1213-22.

196. Dulce MC, Mostbeck GH, Friesse KK, Caputo GR, Higgins CB. Quantification of the left ventricular volumes and function with cine MR imaging: comparison of geometric models with three-dimensional data. *Radiology*. 1993;188(2):371-6.
197. Weinsaft JW, Cham MD, Janik M, Min JK, Henschke CI, Yankelevitz DF, et al. Left ventricular papillary muscles and trabeculae are significant determinants of cardiac MRI volumetric measurements: effects on clinical standards in patients with advanced systolic dysfunction. *International journal of cardiology*. 2008;126(3):359-65.
198. Papavassiliu T, Kuhl HP, Schroder M, Suselbeck T, Bondarenko O, Bohm CK, et al. Effect of endocardial trabeculae on left ventricular measurements and measurement reproducibility at cardiovascular MR imaging. *Radiology*. 2005;236(1):57-64.
199. Hudsmith LE, Petersen SE, Francis JM, Robson MD, Neubauer S. Normal human left and right ventricular and left atrial dimensions using steady state free precession magnetic resonance imaging. *Journal of cardiovascular magnetic resonance : official journal of the Society for Cardiovascular Magnetic Resonance*. 2005;7(5):775-82.
200. Alfakih K, Plein S, Thiele H, Jones T, Ridgway JP, Sivananthan MU. Normal human left and right ventricular dimensions for MRI as assessed by turbo gradient echo and steady-state free precession imaging sequences. *Journal of magnetic resonance imaging : JMRI*. 2003;17(3):323-9.
201. Maceira AM, Prasad SK, Khan M, Pennell DJ. Normalized left ventricular systolic and diastolic function by steady state free precession cardiovascular magnetic resonance. *Journal of cardiovascular magnetic resonance : official journal of the Society for Cardiovascular Magnetic Resonance*. 2006;8(3):417-26.
202. Stein JL, Hua X, Lee S, Ho AJ, Leow AD, Toga AW, et al. Voxelwise genome-wide association study (vGWAS). *Neuroimage*. 2010;53(3):1160-74.

203. Hua X, Lee S, Yanovsky I, Leow AD, Chou YY, Ho AJ, et al. Optimizing power to track brain degeneration in Alzheimer's disease and mild cognitive impairment with tensor-based morphometry: an ADNI study of 515 subjects. *Neuroimage*. 2009;48(4):668-81.
204. Vounou M, Nichols TE, Montana G. Discovering genetic associations with high-dimensional neuroimaging phenotypes: A sparse reduced-rank regression approach. *Neuroimage*. 2010;53(3):1147-59.
205. Vounou M, Janousova E, Wolz R, Stein JL, Thompson PM, Rueckert D, et al. Sparse reduced-rank regression detects genetic associations with voxel-wise longitudinal phenotypes in Alzheimer's disease. *Neuroimage*. 2012;60(1):700-16.
206. Shen L, Kim S, Risacher SL, Nho K, Swaminathan S, West JD, et al. Whole genome association study of brain-wide imaging phenotypes for identifying quantitative trait loci in MCI and AD: A study of the ADNI cohort. *Neuroimage*. 2010;53(3):1051-63.
207. Petitjean C, Dacher J-N. A review of segmentation methods in short axis cardiac MR images. *Med Image Anal*. 2011;15(2):169-84.
208. Young AA, Frangi AF. Computational cardiac atlases: from patient to population and back. *Exp Physiol*. 2009;94(5):578-96.
209. Fonseca CG, Backhaus M, Bluemke DA, Britten RD, Chung JD, Cowan BR, et al. The Cardiac Atlas Project-an imaging database for computational modeling and statistical atlases of the heart. *Bioinformatics*. 2011;27(16):2288-95.
210. Frangi AF, Rueckert D, Schnabel JA, Niessen WJ. Automatic construction of multiple-object three-dimensional statistical shape models: application to cardiac modeling. *IEEE Trans Med Imaging*. 2002;21(9):1151-66.
211. Hoogendoorn C, Duchateau N, Sanchez-Quintana D, Whitmarsh T, Sukno FM, De Craene M, et al. A high-resolution atlas and statistical model of the human heart from multislice CT. *IEEE Trans Med Imaging*. 2013;32(1):28-44.

212. Lorenz C, von Berg J. A comprehensive shape model of the heart. *Med Image Anal.* 2006;10(4):657-70.
213. Lorenzo-Valdes M, Sanchez-Ortiz GI, Elkington AG, Mohiaddin RH, Rueckert D. Segmentation of 4D cardiac MR images using a probabilistic atlas and the EM algorithm. *Med Image Anal.* 2004;8(3):255-65.
214. Zhuang X, Rhode KS, Razavi RS, Hawkes DJ, Ourselin S. A registration-based propagation framework for automatic whole heart segmentation of cardiac MRI. *IEEE Trans Med Imaging.* 2010;29(9):1612-25.
215. Perperidis D, Mohiaddin R, Rueckert D. Construction of a 4D statistical atlas of the cardiac anatomy and its use in classification. *Medical image computing and computer-assisted intervention : MICCAI International Conference on Medical Image Computing and Computer-Assisted Intervention.* 2005;8(Pt 2):402-10.
216. Suinesiaputra A, Frangi AF, Kaandorp TA, Lamb HJ, Bax JJ, Reiber JH, et al. Automated detection of regional wall motion abnormalities based on a statistical model applied to multislice short-axis cardiac MR images. *IEEE Trans Med Imaging.* 2009;28(4):595-607.
217. Pereanez M, Lekadir K, Butakoff C, Hoogendoorn C, Frangi AF. A framework for the merging of pre-existing and correspondenceless 3D statistical shape models. *Med Image Anal.* 2014;18(7):1044-58.
218. Heimann T, Meinzer HP. Statistical shape models for 3D medical image segmentation: a review. *Med Image Anal.* 2009;13(4):543-63.
219. Lamata P, Niederer S, Nordsletten D, Barber DC, Roy I, Hose DR, et al. An accurate, fast and robust method to generate patient-specific cubic Hermite meshes. *Med Image Anal.* 2011;15(6):801-13.

220. Marchesseau S, Delingette H, Sermesant M, Cabrera-Lozoya R, Tobon-Gomez C, Moireau P, et al. Personalization of a cardiac electromechanical model using reduced order unscented Kalman filtering from regional volumes. *Med Image Anal.* 2013;17(7):816-29.
221. Heckemann RA, Hajnal JV, Aljabar P, Rueckert D, Hammers A. Automatic anatomical brain MRI segmentation combining label propagation and decision fusion. *Neuroimage.* 2006;33(1):115-26.
222. Rohlfing T, Brandt R, Menzel R, Maurer CR, Jr. Evaluation of atlas selection strategies for atlas-based image segmentation with application to confocal microscopy images of bee brains. *Neuroimage.* 2004;21(4):1428-42.
223. Rueckert D, Sonoda LI, Hayes C, Hill DL, Leach MO, Hawkes DJ. Nonrigid registration using free-form deformations: application to breast MR images. *IEEE Trans Med Imaging.* 1999;18(8):712-21.
224. Coupe P, Manjon JV, Fonov V, Pruessner J, Robles M, Collins DL. Patch-based segmentation using expert priors: application to hippocampus and ventricle segmentation. *Neuroimage.* 2011;54(2):940-54.
225. Bai W, Shi W, O'Regan DP, Tong T, Wang H, Jamil-Copley S, et al. A probabilistic patch-based label fusion model for multi-atlas segmentation with registration refinement: application to cardiac MR images. *IEEE Trans Med Imaging.* 2013;32(7):1302-15.
226. Barnes C, Shechtman E, Goldman D, Finkelstein A. The Generalized PatchMatch Correspondence Algorithm. In: Daniilidis K, Maragos P, Paragios N, editors. *Computer Vision – ECCV 2010. Lecture Notes in Computer Science.* 6313: Springer Berlin Heidelberg; 2010. p. 29-43.
227. Houle D, Govindaraju DR, Omholt S. Phenomics: the next challenge. *Nature reviews Genetics.* 2010;11(12):855-66.

228. Bilder RM, Sabb FW, Cannon TD, London ED, Jentsch JD, Parker DS, et al. Phenomics: the systematic study of phenotypes on a genome-wide scale. *Neuroscience*. 2009;164(1):30-42.
229. Schork NJ. Genetics of complex disease: approaches, problems, and solutions. *American journal of respiratory and critical care medicine*. 1997;156(4 Pt 2):S103-9.
230. Freimer N, Sabatti C. The human phenome project. *Nature genetics*. 2003;34(1):15-21.
231. Kirchhof P, Sipido KR, Cowie MR, Eschenhagen T, Fox KA, Katus H, et al. The continuum of personalized cardiovascular medicine: a position paper of the European Society of Cardiology. *European heart journal*. 2014;35(46):3250-7.
232. Robinson PN. Deep phenotyping for precision medicine. *Human mutation*. 2012;33(5):777-80.
233. Armstrong AC, Gidding S, Gjesdal O, Wu C, Bluemke DA, Lima JA. LV mass assessed by echocardiography and CMR, cardiovascular outcomes, and medical practice. *JACC Cardiovascular imaging*. 2012;5(8):837-48.
234. Fried LP, Kronmal RA, Newman AB, Bild DE, Mittelmark MB, Polak JF, et al. Risk factors for 5-year mortality in older adults: the Cardiovascular Health Study. *Jama*. 1998;279(8):585-92.
235. Gidding SS. Controversies in the assessment of left ventricular mass. *Hypertension*. 2010;56(1):26-8.
236. Lorber R, Gidding SS, Daviglius ML, Colangelo LA, Liu K, Gardin JM. Influence of systolic blood pressure and body mass index on left ventricular structure in healthy African-American and white young adults: the CARDIA study. *Journal of the American College of Cardiology*. 2003;41(6):955-60.

237. de Simone G, Palmieri V, Bella JN, Celentano A, Hong Y, Oberman A, et al. Association of left ventricular hypertrophy with metabolic risk factors: the HyperGEN study. *J Hypertens*. 2002;20(2):323-31.
238. Gottdiener JS, Reda DJ, Materson BJ, Massie BM, Notargiacomo A, Hamburger RJ, et al. Importance of obesity, race and age to the cardiac structural and functional effects of hypertension. The Department of Veterans Affairs Cooperative Study Group on Antihypertensive Agents. *Journal of the American College of Cardiology*. 1994;24(6):1492-8.
239. Gardin JM, Siscovick D, Anton-Culver H, Lynch JC, Smith VE, Klopfenstein HS, et al. Sex, age, and disease affect echocardiographic left ventricular mass and systolic function in the free-living elderly. The Cardiovascular Health Study. *Circulation*. 1995;91(6):1739-48.
240. Cain PA, Ahl R, Hedstrom E, Ugander M, Allansdotter-Johnsson A, Friberg P, et al. Age and gender specific normal values of left ventricular mass, volume and function for gradient echo magnetic resonance imaging: a cross sectional study. *BMC medical imaging*. 2009;9:2.
241. Vasan RS, Glazer NL, Felix JF, Lieb W, Wild PS, Felix SB, et al. Genetic variants associated with cardiac structure and function: a meta-analysis and replication of genome-wide association data. *Jama*. 2009;302(2):168-78.
242. Chaturvedi N. Ethnic differences in cardiovascular disease. *Heart*. 2003;89(6):681-6.
243. Kizer JR, Arnett DK, Bella JN, Paranicas M, Rao DC, Province MA, et al. Differences in left ventricular structure between black and white hypertensive adults: the Hypertension Genetic Epidemiology Network study. *Hypertension*. 2004;43(6):1182-8.
244. Drazner MH, Dries DL, Peshock RM, Cooper RS, Klassen C, Kazi F, et al. Left ventricular hypertrophy is more prevalent in blacks than whites in the general population: the Dallas Heart Study. *Hypertension*. 2005;46(1):124-9.

245. Roger VL, Go AS, Lloyd-Jones DM, Benjamin EJ, Berry JD, Borden WB, et al. Heart disease and stroke statistics--2012 update: a report from the American Heart Association. *Circulation*. 2012;125(1):e2-e220.
246. Park CM, Tillin T, March K, Ghosh AK, Jones S, Wright A, et al. Hyperglycemia Has a Greater Impact on Left Ventricle Function in South Asians Than in Europeans. *Diabetes care*. 2014;37(4):1124-31.
247. Park CM, March K, Ghosh AK, Jones S, Coady E, Tuson C, et al. Left-ventricular structure in the Southall And Brent REvisited (SABRE) study: explaining ethnic differences. *Hypertension*. 2013;61(5):1014-20.
248. Chirinos JA, Segers P, De Buyzere ML, Kronmal RA, Raja MW, De Bacquer D, et al. Left ventricular mass: allometric scaling, normative values, effect of obesity, and prognostic performance. *Hypertension*. 2010;56(1):91-8.
249. Liao Y, Cooper RS, Durazo-Arvizu R, Mensah GA, Ghali JK. Prediction of mortality risk by different methods of indexation for left ventricular mass. *Journal of the American College of Cardiology*. 1997;29(3):641-7.
250. Lang RM, Badano LP, Mor-Avi V, Afilalo J, Armstrong A, Ernande L, et al. Recommendations for cardiac chamber quantification by echocardiography in adults: an update from the American Society of Echocardiography and the European Association of Cardiovascular Imaging. *European heart journal cardiovascular Imaging*. 2015;16(3):233-70.
251. Shellock FG. Reference manual for magnetic resonance safety. 2003 ed. ed. Salt Lake City, Utah: Amirsys; 2003.
252. Jensky-Squires NE, Dieli-Conwright CM, Rossuello A, Erceg DN, McCauley S, Schroeder ET. Validity and reliability of body composition analysers in children and adults. *Br J Nutr*. 2008;100(4):859-65.

253. O'Brien E, European Society of Hypertension Working Group on Blood Pressure M. The Working Group on Blood Pressure Monitoring of the European Society of Hypertension. *Blood Press Monit.* 2003;8(1):17-8.
254. Coleman A, Steel S, Freeman P, de Greeff A, Shennan A. Validation of the Omron M7 (HEM-780-E) oscillometric blood pressure monitoring device according to the British Hypertension Society protocol. *Blood Press Monit.* 2008;13(1):49-54.
255. El Feghali RN, Topouchian JA, Pannier BM, El Assaad HA, Asmar RG, Hypertension ESo. Validation of the OMRON M7 (HEM-780-E) blood pressure measuring device in a population requiring large cuff use according to the International Protocol of the European Society of Hypertension. *Blood Press Monit.* 2007;12(3):173-8.
256. Woodbridge M, Fagiolo G, O'Regan DP. MRIdb: medical image management for biobank research. *Journal of digital imaging.* 2013;26(5):886-90.
257. R Core Team. R: A language and environment for statistical computing. Vienna, Austria: R Foundation for Statistical Computing; 2014.
258. Bland JM, Altman DG. Measurement error and correlation coefficients. *BMJ.* 1996;313(7048):41-2.
259. Hong SN, Gona P, Fontes JD, Oyama N, Chan RH, Kenchaiah S, et al. Atherosclerotic biomarkers and aortic atherosclerosis by cardiovascular magnetic resonance imaging in the Framingham Heart Study. *Journal of the American Heart Association.* 2013;2(6):e000307.
260. Natori S, Lai S, Finn JP, Gomes AS, Hundley WG, Jerosch-Herold M, et al. Cardiovascular function in multi-ethnic study of atherosclerosis: normal values by age, sex, and ethnicity. *AJR Am J Roentgenol.* 2006;186(6 Suppl 2):S357-65.
261. Altman DG, Royston P. The cost of dichotomising continuous variables2006 2006-05-04 21:59:05. 1080 p.

262. Olivetti G, Giordano G, Corradi D, Melissari M, Lagrasta C, Gambert SR, et al. Gender differences and aging: effects on the human heart. *Journal of the American College of Cardiology*. 1995;26(4):1068-79.
263. Gardin JM, Wagenknecht LE, Anton-Culver H, Flack J, Gidding S, Kurosaki T, et al. Relationship of cardiovascular risk factors to echocardiographic left ventricular mass in healthy young black and white adult men and women. The CARDIA study. *Coronary Artery Risk Development in Young Adults*. *Circulation*. 1995;92(3):380-7.
264. Bibbins-Domingo K, Pletcher MJ, Lin F, Vittinghoff E, Gardin JM, Arynchyn A, et al. Racial differences in incident heart failure among young adults. *N Engl J Med*. 2009;360(12):1179-90.
265. Hunt SA, Abraham WT, Chin MH, Feldman AM, Francis GS, Ganiats TG, et al. ACC/AHA 2005 Guideline Update for the Diagnosis and Management of Chronic Heart Failure in the Adult: a report of the American College of Cardiology/American Heart Association Task Force on Practice Guidelines (Writing Committee to Update the 2001 Guidelines for the Evaluation and Management of Heart Failure): developed in collaboration with the American College of Chest Physicians and the International Society for Heart and Lung Transplantation: endorsed by the Heart Rhythm Society. *Circulation*. 2005;112(12):e154-235.
266. Yancy CW. Heart failure in African Americans. *Am J Cardiol*. 2005;96(7B):3i-12i.
267. Hughes SE. The pathology of hypertrophic cardiomyopathy. *Histopathology*. 2004;44(5):412-27.
268. Florian A, Masci PG, De Buck S, Aquaro GD, Claus P, Todiere G, et al. Geometric Assessment of Asymmetric Septal Hypertrophic Cardiomyopathy by CMR. *JACC: Cardiovascular Imaging*. 2012;5(7):702-11.

269. Maron BJ, McKenna WJ, Danielson GK, Kappenberger LJ, Kuhn HJ, Seidman CE, et al. American College of Cardiology/European Society of Cardiology Clinical Expert Consensus Document on Hypertrophic Cardiomyopathy: a report of the American College of Cardiology Foundation Task Force on Clinical Expert Consensus Documents and the European Society of Cardiology Committee for Practice Guidelines. *Journal of the American College of Cardiology*. 2003;42(9):1687-713.
270. Tardiff JC. It's never too early to look: subclinical disease in sarcomeric dilated cardiomyopathy. *Circulation Cardiovascular genetics*. 2012;5(5):483-6.
271. Thirion JP. Image matching as a diffusion process: an analogy with Maxwell's demons. *Med Image Anal*. 1998;2(3):243-60.
272. Svarer C, Madsen K, Hasselbalch SG, Pinborg LH, Haugbol S, Frokjaer VG, et al. MR-based automatic delineation of volumes of interest in human brain PET images using probability maps. *Neuroimage*. 2005;24(4):969-79.
273. Aljabar P, Heckemann RA, Hammers A, Hajnal JV, Rueckert D. Multi-atlas based segmentation of brain images: atlas selection and its effect on accuracy. *Neuroimage*. 2009;46(3):726-38.
274. van Rikxoort EM, Isgum I, Arzhaeva Y, Staring M, Klein S, Viergever MA, et al. Adaptive local multi-atlas segmentation: application to the heart and the caudate nucleus. *Med Image Anal*. 2010;14(1):39-49.
275. Coupe P, Manjon JV, Fonov V, Pruessner J, Robles M, Collins DL. Nonlocal patch-based label fusion for hippocampus segmentation. *Medical image computing and computer-assisted intervention : MICCAI International Conference on Medical Image Computing and Computer-Assisted Intervention*. 2010;13(Pt 3):129-36.
276. Malamateniou C, McGuinness AK, Allsop JM, O'Regan DP, Rutherford MA, Hajnal JV. Snapshot Inversion Recovery: An Optimized Single-Shot T1-weighted Inversion-

Recovery Sequence for Improved Fetal Brain Anatomic Delineation. *Radiology*. 2011;258(1):229-35.

277. Bland JM, Altman DG. Statistical methods for assessing agreement between two methods of clinical measurement. *Lancet*. 1986;1(8476):307-10.

278. Yushkevich PA, Piven J, Hazlett HC, Smith RG, Ho S, Gee JC, et al. User-guided 3D active contour segmentation of anatomical structures: Significantly improved efficiency and reliability. *Neuroimage*. 2006;31(3):1116-28.

279. Shi W, Caballero J, Ledig C, Zhuang X, Bai W, Bhatia K, et al. Cardiac Image Super-Resolution with Global Correspondence Using Multi-Atlas PatchMatch. In: Mori K, Sakuma I, Sato Y, Barillot C, Navab N, editors. *Medical Image Computing and Computer-Assisted Intervention – MICCAI 2013*. Lecture Notes in Computer Science. 8151: Springer Berlin Heidelberg; 2013. p. 9-16.

280. Rueckert D, Frangi AF, Schnabel JA. Automatic Construction of 3D Statistical Deformation Models Using Non-rigid Registration. In: Niessen W, Viergever M, editors. *Medical Image Computing and Computer-Assisted Intervention – MICCAI 2001*. Lecture Notes in Computer Science. 2208: Springer Berlin Heidelberg; 2001. p. 77-84.

281. Cline HE, Dumoulin CL, Hart HR, Jr., Lorensen WE, Ludke S. 3D reconstruction of the brain from magnetic resonance images using a connectivity algorithm. *Magnetic resonance imaging*. 1987;5(5):345-52.

282. Grevera GJ, Udupa JK. Shape-based interpolation of multidimensional grey-level images. *IEEE Trans Med Imaging*. 1996;15(6):881-92.

283. Lorensen WE, Cline HE. Marching cubes: A high resolution 3D surface construction algorithm. [Abstract]. *Computer graphics*. 1987;21(4):163-9.

284. Dice LR. Measures of the Amount of Ecologic Association Between Species. *Ecology*. 1945;26(3):297-302.

285. Salton CJ, Chuang ML, O'Donnell CJ, Kupka MJ, Larson MG, Kissinger KV, et al. Gender differences and normal left ventricular anatomy in an adult population free of hypertension. A cardiovascular magnetic resonance study of the Framingham Heart Study Offspring cohort. *Journal of the American College of Cardiology*. 2002;39(6):1055-60.
286. Trott M. *The Mathematica guidebook for programming*. New York: Telos-Springer; 2004. xxxvii, 1028 p. p.
287. Zhong L, Su Y, Yeo SY, Tan RS, Ghista DN, Kassab G. Left ventricular regional wall curvedness and wall stress in patients with ischemic dilated cardiomyopathy. *American journal of physiology Heart and circulatory physiology*. 2009;296(3):H573-84.
288. Fonseca CG, Backhaus M, Bluemke DA, Britten RD, Chung JD, Cowan BR, et al. The Cardiac Atlas Project--an imaging database for computational modeling and statistical atlases of the heart. *Bioinformatics*. 2011;27(16):2288-95.
289. Medrano-Gracia P, Cowan BR, Ambale-Venkatesh B, Bluemke DA, Eng J, Finn JP, et al. Left ventricular shape variation in asymptomatic populations: the Multi-Ethnic Study of Atherosclerosis. *Journal of cardiovascular magnetic resonance : official journal of the Society for Cardiovascular Magnetic Resonance*. 2014;16:56.
290. Rodriguez CJ, Diez-Roux AV, Moran A, Jin Z, Kronmal RA, Lima J, et al. Left ventricular mass and ventricular remodeling among Hispanic subgroups compared with non-Hispanic blacks and whites: MESA (Multi-ethnic Study of Atherosclerosis). *Journal of the American College of Cardiology*. 2010;55(3):234-42.
291. Gupta S, Berry JD, Ayers CR, Peshock RM, Khera A, de Lemos JA, et al. Left ventricular hypertrophy, aortic wall thickness, and lifetime predicted risk of cardiovascular disease:the Dallas Heart Study. *JACC Cardiovascular imaging*. 2010;3(6):605-13.
292. Fox ER, Musani SK, Barbalic M, Lin H, Yu B, Ogunyankin KO, et al. Genome-wide association study of cardiac structure and systolic function in African Americans: the

Candidate Gene Association Resource (CARE) study. *Circulation Cardiovascular genetics*. 2013;6(1):37-46.

293. Chun EJ, Choi SI, Jin KN, Kwag HJ, Kim YJ, Choi BW, et al. Hypertrophic Cardiomyopathy: Assessment with MR Imaging and Multidetector CT1. *Radiographics*. 2010;30(5):1309-28.

294. Ganau A, Devereux RB, Roman MJ, de Simone G, Pickering TG, Saba PS, et al. Patterns of left ventricular hypertrophy and geometric remodeling in essential hypertension. *Journal of the American College of Cardiology*. 1992;19(7):1550-8.

295. Pattynama PM, Doornbos J, Hermans J, van der Wall EE, de Roos A. Magnetic resonance evaluation of regional left ventricular function. Effect of through-plane motion. *Investigative radiology*. 1992;27(9):681-5.

296. Bloomer TN, Plein S, Radjenovic A, Higgins DM, Jones TR, Ridgway JP, et al. Cine MRI using steady state free precession in the radial long axis orientation is a fast accurate method for obtaining volumetric data of the left ventricle. *Journal of magnetic resonance imaging : JMRI*. 2001;14(6):685-92.

297. Weiger M, Pruessmann KP, Boesiger P. 2D SENSE for faster 3D MRI. *Magnetic Resonance Materials in Physics, Biology and Medicine*. 2002;14(1):10-9.

298. Makowski MR, Wiethoff AJ, Jansen CH, Uribe S, Parish V, Schuster A, et al. Single breath-hold assessment of cardiac function using an accelerated 3D single breath-hold acquisition technique--comparison of an intravascular and extravascular contrast agent. *Journal of cardiovascular magnetic resonance : official journal of the Society for Cardiovascular Magnetic Resonance*. 2012;14:53.

299. Petitjean C, Dacher J-N. A review of segmentation methods in short axis cardiac MR images. *Medical Image Analysis*. 2011;15(2):169-84.

300. Mumford JA. A power calculation guide for fMRI studies. *Social cognitive and affective neuroscience*. 2012;7(6):738-42.
301. Petersen SE, Matthews PM, Bamberg F, Bluemke DA, Francis JM, Friedrich MG, et al. Imaging in population science: cardiovascular magnetic resonance in 100,000 participants of UK Biobank - rationale, challenges and approaches. *Journal of cardiovascular magnetic resonance : official journal of the Society for Cardiovascular Magnetic Resonance*. 2013;15:46.
302. Mirnezami R, Nicholson J, Darzi A. Preparing for precision medicine. *N Engl J Med*. 2012;366(6):489-91.
303. Bland M. *An introduction to medical statistics*. 3rd ed. Oxford ; New York: Oxford University Press; 2000. xvi, 405 p. p.
304. Kearney PM, Whelton M, Reynolds K, Muntner P, Whelton PK, He J. Global burden of hypertension: analysis of worldwide data. *Lancet*. 2005;365(9455):217-23.
305. Lewington S, Clarke R, Qizilbash N, Peto R, Collins R. Age-specific relevance of usual blood pressure to vascular mortality: a meta-analysis of individual data for one million adults in 61 prospective studies. *Lancet*. 2002;360(9349):1903-13.
306. Schillaci G, Verdecchia P, Porcellati C, Cuccurullo O, Cosco C, Perticone F. Continuous Relation Between Left Ventricular Mass and Cardiovascular Risk in Essential Hypertension. *Hypertension*. 2000;35(2):580-6.
307. Levy D, Garrison RJ, Savage DD, Kannel WB, Castelli WP. Prognostic Implications of Echocardiographically Determined Left Ventricular Mass in the Framingham Heart Study. *New England Journal of Medicine*. 1990;322(22):1561-6.
308. Koren MJ, Devereux RB, Casale PN, Savage DD, Laragh JH. Relation of left ventricular mass and geometry to morbidity and mortality in uncomplicated essential hypertension. *Annals of internal medicine*. 1991;114(5):345-52.

309. Krumholz HM, Larson M, Levy D. Prognosis of left ventricular geometric patterns in the Framingham Heart Study. *Journal of the American College of Cardiology*. 1995;25(4):879-84.
310. Verdecchia P, Schillaci G, Borgioni C, Ciucci A, Battistelli M, Bartoccini C, et al. Adverse prognostic significance of concentric remodeling of the left ventricle in hypertensive patients with normal left ventricular mass. *Journal of the American College of Cardiology*. 1995;25(4):871-8.
311. Diez J, Frohlich ED. A translational approach to hypertensive heart disease. *Hypertension*. 2010;55(1):1-8.
312. Dogru MT, Tireli E, Guneri M, Iyisoy A, Celik T. Differences in left ventricular structure, functions and elastance in the patients with normotensive blood pressure. *Anadolu kardiyoloji dergisi : AKD = the Anatolian journal of cardiology*. 2008;8(6):413-21.
313. Lang RM, Bierig M, Devereux RB, Flachskampf FA, Foster E, Pellikka PA, et al. Recommendations for Chamber Quantification: A Report from the American Society of Echocardiography's Guidelines and Standards Committee and the Chamber Quantification Writing Group, Developed in Conjunction with the European Association of Echocardiography, a Branch of the European Society of Cardiology. *Journal of the American Society of Echocardiography*. 2005;18(12):1440-63.
314. Benjamini Y, Krieger AM, Yekutieli D. Adaptive linear step-up procedures that control the false discovery rate. *Biometrika*. 2006;93(3):491-507.
315. Chobanian AV, Bakris GL, Black HR, Cushman WC, Green LA, Izzo JL, Jr., et al. Seventh report of the Joint National Committee on Prevention, Detection, Evaluation, and Treatment of High Blood Pressure. *Hypertension*. 2003;42(6):1206-52.
316. de Marvao A, Dawes TJ, Shi W, Minas C, Keenan NG, Diamond T, et al. Population-based studies of myocardial hypertrophy: high resolution cardiovascular magnetic resonance

atlases improve statistical power. *Journal of cardiovascular magnetic resonance : official journal of the Society for Cardiovascular Magnetic Resonance*. 2014;16(1):16.

317. Medrano-Gracia P, Cowan BR, Ambale-Venkatesh B, Bluemke DA, Eng J, Finn J, et al. Left ventricular shape variation in asymptomatic populations: the multi-ethnic study of atherosclerosis. *Journal of cardiovascular magnetic resonance : official journal of the Society for Cardiovascular Magnetic Resonance*. 2014;16(1):56.

318. Grossman W, Paulus WJ. Myocardial stress and hypertrophy: a complex interface between biophysics and cardiac remodeling. *The Journal of clinical investigation*. 2013;123(9):3701-3.

319. Grossman W, Jones D, McLaurin LP. Wall stress and patterns of hypertrophy in the human left ventricle. *The Journal of clinical investigation*. 1975;56(1):56-64.

320. Sano M, Schneider MD. Still stressed out but doing fine: normalization of wall stress is superfluous to maintaining cardiac function in chronic pressure overload. *Circulation*. 2002;105(1):8-10.

321. Hill JA, Karimi M, Kutschke W, Davisson RL, Zimmerman K, Wang Z, et al. Cardiac hypertrophy is not a required compensatory response to short-term pressure overload. *Circulation*. 2000;101(24):2863-9.

322. Heckbert SR, Post W, Pearson GD, Arnett DK, Gomes AS, Jerosch-Herold M, et al. Traditional cardiovascular risk factors in relation to left ventricular mass, volume, and systolic function by cardiac magnetic resonance imaging: the Multiethnic Study of Atherosclerosis. *Journal of the American College of Cardiology*. 2006;48(11):2285-92.

323. Dorn GW, Robbins J, Sugden PH. Phenotyping Hypertrophy: Eschew Obfuscation. *Circulation Research*. 2003;92(11):1171-5.

324. Knoll R, Iaccarino G, Tarone G, Hilfiker-Kleiner D, Bauersachs J, Leite-Moreira AF, et al. Towards a re-definition of 'cardiac hypertrophy' through a rational characterization of

left ventricular phenotypes: a position paper of the Working Group 'Myocardial Function' of the ESC. *European journal of heart failure*. 2011;13(8):811-9.

325. Khouri MG, Peshock RM, Ayers CR, de Lemos JA, Drazner MH. A 4-tiered classification of left ventricular hypertrophy based on left ventricular geometry: the Dallas heart study. *Circulation Cardiovascular imaging*. 2010;3(2):164-71.

326. Gaasch WH, Zile MR. Left Ventricular Structural Remodeling in Health and Disease With Special Emphasis on Volume, Mass, and Geometry. *Journal of the American College of Cardiology*. 2011;58(17):1733-40.

327. Esposito G, Rapacciuolo A, Naga Prasad SV, Takaoka H, Thomas SA, Koch WJ, et al. Genetic alterations that inhibit in vivo pressure-overload hypertrophy prevent cardiac dysfunction despite increased wall stress. *Circulation*. 2002;105(1):85-92.

328. Hartford M, Wikstrand JC, Wallentin I, Ljungman SM, Berglund GL. Left ventricular wall stress and systolic function in untreated primary hypertension. *Hypertension*. 1985;7(1):97-104.

329. Zile MR, Gaasch WH, Patel K, Aban IB, Ahmed A. Adverse left ventricular remodeling in community-dwelling older adults predicts incident heart failure and mortality. *JACC Heart failure*. 2014;2(5):512-22.

330. Frohlich ED, Susic D. Pressure Overload. *Heart Failure Clinics*. 2012;8(1):21-32.

331. Drazner MH. The progression of hypertensive heart disease. *Circulation*. 2011;123(3):327-34.

332. Levy D, Garrison RJ, Savage DD, Kannel WB, Castelli WP. Left ventricular mass and incidence of coronary heart disease in an elderly cohort. The Framingham Heart Study. *Annals of internal medicine*. 1989;110(2):101-7.

333. Baltabaeva A, Marciniak M, Bijmens B, Moggridge J, He FJ, Antonios TF, et al. Regional left ventricular deformation and geometry analysis provides insights in myocardial

remodelling in mild to moderate hypertension. *European journal of echocardiography : the journal of the Working Group on Echocardiography of the European Society of Cardiology*. 2008;9(4):501-8.

334. Florian A, Masci PG, De Buck S, Aquaro GD, Claus P, Todiere G, et al. Geometric assessment of asymmetric septal hypertrophic cardiomyopathy by CMR. *JACC Cardiovascular imaging*. 2012;5(7):702-11.

335. Nagueh SF, Shah G, Wu Y, Torre-Amione G, King NM, Lahmers S, et al. Altered titin expression, myocardial stiffness, and left ventricular function in patients with dilated cardiomyopathy. *Circulation*. 2004;110(2):155-62.

336. Tanaka M, Fujiwara H, Onodera T, Wu DJ, Hamashima Y, Kawai C. Quantitative analysis of myocardial fibrosis in normals, hypertensive hearts, and hypertrophic cardiomyopathy. *British Heart Journal*. 1986;55(6):575-81.

337. Drukteinis JS, Roman MJ, Fabsitz RR, Lee ET, Best LG, Russell M, et al. Cardiac and systemic hemodynamic characteristics of hypertension and prehypertension in adolescents and young adults: the Strong Heart Study. *Circulation*. 2007;115(2):221-7.

338. Franklin SS. Arterial Stiffness and Hypertension: A Two-Way Street? *Hypertension*. 2005;45(3):349-51.

339. Mukherjee D. Atherogenic vascular stiffness and hypertension: cause or effect? *Jama*. 2012;308(9):919-20.

340. Crowley SD, Gurley SB, Herrera MJ, Ruiz P, Griffiths R, Kumar AP, et al. Angiotensin II causes hypertension and cardiac hypertrophy through its receptors in the kidney. *Proceedings of the National Academy of Sciences of the United States of America*. 2006;103(47):17985-90.

341. Post WS, Larson MG, Levy D. Impact of left ventricular structure on the incidence of hypertension. The Framingham Heart Study. *Circulation*. 1994;90(1):179-85.

342. Shah AM, Pfeffer MA. Left ventricular size, mass, and shape: is the sum greater than the parts? *JACC Heart failure*. 2014;2(5):523-5.
343. Piran S, Liu P, Morales A, Hershberger RE. Where genome meets phenome: rationale for integrating genetic and protein biomarkers in the diagnosis and management of dilated cardiomyopathy and heart failure. *Journal of the American College of Cardiology*. 2012;60(4):283-9.
344. Ogden CL, Carroll MD, Kit BK, Flegal KM. PRevalence of childhood and adult obesity in the united states, 2011-2012. *JAMA*. 2014;311(8):806-14.
345. Ndumele CE, Coresh J, Lazo M, Hoogeveen RC, Blumenthal RS, Folsom AR, et al. Obesity, Subclinical Myocardial Injury, and Incident Heart Failure. *JACC: Heart Failure*. 2014;2(6):600-7.
346. Lavie CJ, Alpert MA, Arena R, Mehra MR, Milani RV, Ventura HO. Impact of Obesity and the Obesity Paradox on Prevalence and Prognosis in Heart Failure. *JACC: Heart Failure*. 2013;1(2):93-102.
347. de Simone G, Izzo R, De Luca N, Gerds E. Left ventricular geometry in obesity: is it what we expect? *Nutr Metab Cardiovasc Dis*. 2013;23(10):905-12.
348. Alpert MA, Lambert CR, Panayiotou H, Terry BE, Cohen MV, Massey CV, et al. Relation of duration of morbid obesity to left ventricular mass, systolic function, and diastolic filling, and effect of weight loss. *The American journal of cardiology*. 1995;76(16):1194-7.
349. Turkbey EB, McClelland RL, Kronmal RA, Burke GL, Bild DE, Tracy RP, et al. The impact of obesity on the left ventricle: the Multi-Ethnic Study of Atherosclerosis (MESA). *JACC Cardiovasc Imaging*. 2010;3(3):266-74.
350. Levy D, Garrison RJ, Savage DD, Kannel WB, Castelli WP. Prognostic implications of echocardiographically determined left ventricular mass in the Framingham Heart Study. *N Engl J Med*. 1990;322(22):1561-6.

351. Gerds E, Cramariuc D, de Simone G, Wachtell K, Dahlöf B, Devereux RB. Impact of left ventricular geometry on prognosis in hypertensive patients with left ventricular hypertrophy (the LIFE study). *Eur J Echocardiogr*. 2008;9(6):809-15.
352. Berrington de Gonzalez A, Hartge P, Cerhan JR, Flint AJ, Hannan L, MacInnis RJ, et al. Body-mass index and mortality among 1.46 million white adults. *N Engl J Med*. 2010;363(23):2211-9.
353. Rider OJ, Lewandowski A, Nethononda R, Petersen SE, Francis JM, Pitcher A, et al. Gender-specific differences in left ventricular remodelling in obesity: insights from cardiovascular magnetic resonance imaging. *Eur Heart J*. 2013;34(4):292-9.
354. Alexander JK, Dennis EW, Smith WG, Amad KH, Duncan WC, Austin RC. Blood volume, cardiac output, and distribution of systemic blood flow in extreme obesity. *Cardiovasc Res Cent Bull*. 1962;1:39-44.
355. Collis T, Devereux RB, Roman MJ, de Simone G, Yeh J, Howard BV, et al. Relations of stroke volume and cardiac output to body composition: the strong heart study. *Circulation*. 2001;103(6):820-5.
356. Fischer M, Baessler A, Schunkert H. Renin angiotensin system and gender differences in the cardiovascular system. *Cardiovasc Res*. 2002;53(3):672-7.
357. Komukai K, Mochizuki S, Yoshimura M. Gender and the renin-angiotensin-aldosterone system. *Fundam Clin Pharmacol*. 2010;24(6):687-98.
358. Thethi T, Kamiyama M, Kobori H. The link between the renin-angiotensin-aldosterone system and renal injury in obesity and the metabolic syndrome. *Curr Hypertens Rep*. 2012;14(2):160-9.
359. Gupte M, Thatcher SE, Boustany-Kari CM, Shoemaker R, Yiannikouris F, Zhang X, et al. Angiotensin converting enzyme 2 contributes to sex differences in the development of obesity hypertension in C57BL/6 mice. *Arterioscler Thromb Vasc Biol*. 2012;32(6):1392-9.

360. Poehlman ET, Gardner AW, Goran MI, Arciero PJ, Toth MJ, Ades PA, et al. Sympathetic nervous system activity, body fatness, and body fat distribution in younger and older males. *J Appl Physiol* (1985). 1995;78(3):802-6.
361. Lambert E, Straznicky N, Eikelis N, Esler M, Dawood T, Masuo K, et al. Gender differences in sympathetic nervous activity: influence of body mass and blood pressure. *J Hypertens*. 2007;25(7):1411-9.
362. Hillebrand S, de Mutsert R, Christen T, Maan AC, Jukema JW, Lamb HJ, et al. Body fat, especially visceral fat, is associated with electrocardiographic measures of sympathetic activation. *Obesity (Silver Spring)*. 2014;22(6):1553-9.
363. Jones PP, Snitker S, Skinner JS, Ravussin E. Gender differences in muscle sympathetic nerve activity: effect of body fat distribution. *Am J Physiol*. 1996;270(2 Pt 1):E363-6.
364. Grassi G, Dell'Oro R, Facchini A, Quarti Trevano F, Bolla GB, Mancia G. Effect of central and peripheral body fat distribution on sympathetic and baroreflex function in obese normotensives. *J Hypertens*. 2004;22(12):2363-9.
365. Sundström J, Lind L, Nyström N, Zethelius B, Andrén B, Hales CN, et al. Left ventricular concentric remodeling rather than left ventricular hypertrophy is related to the insulin resistance syndrome in elderly men. *Circulation*. 2000;101(22):2595-600.
366. Logue J, Walker JJ, Colhoun HM, Leese GP, Lindsay RS, McKnight JA, et al. Do men develop type 2 diabetes at lower body mass indices than women? *Diabetologia*. 2011;54(12):3003-6.
367. Lichnovská R, Gwozdziewiczová S, Hřebíček J. Gender differences in factors influencing insulin resistance in elderly hyperlipemic non-diabetic subjects. *Cardiovasc Diabetol*. 2002;1:4.

368. Geer EB, Shen W. Gender differences in insulin resistance, body composition, and energy balance. *Gend Med*. 2009;6 Suppl 1:60-75.
369. Neeland IJ, Gupta S, Ayers CR, Turer AT, Rame JE, Das SR, et al. Relation of regional fat distribution to left ventricular structure and function. *Circ Cardiovasc Imaging*. 2013;6(5):800-7.
370. Adabag S, Huxley RR, Lopez FL, Chen LY, Sotoodehnia N, Siscovick D, et al. Obesity related risk of sudden cardiac death in the atherosclerosis risk in communities study. *Heart*. 2015;101(3):215-21.
371. Kyle UG, Piccoli A, Pichard C. Body composition measurements: interpretation finally made easy for clinical use. *Curr Opin Clin Nutr Metab Care*. 2003;6(4):387-93.
372. Gulati A, Ismail TF, Jabbour A, Ismail NA, Morarji K, Ali A, et al. Clinical utility and prognostic value of left atrial volume assessment by cardiovascular magnetic resonance in non-ischaemic dilated cardiomyopathy. *European journal of heart failure*. 2013;15(6):660-70.
373. Gulati A, Jabbour A, Ismail TF, Guha K, Khwaja J, Raza S, et al. Association of fibrosis with mortality and sudden cardiac death in patients with nonischemic dilated cardiomyopathy. *Jama*. 2013;309(9):896-908.
374. Wu KC, Weiss RG, Thiemann DR, Kitagawa K, Schmidt A, Dalal D, et al. Late gadolinium enhancement by cardiovascular magnetic resonance heralds an adverse prognosis in nonischemic cardiomyopathy. *Journal of the American College of Cardiology*. 2008;51(25):2414-21.
375. Lanktree MB, Hassell RG, Lahiry P, Hegele RA. Phenomics: expanding the role of clinical evaluation in genomic studies. *Journal of investigative medicine : the official publication of the American Federation for Clinical Research*. 2010;58(5):700-6.

376. McNally EM. Genetics: broken giant linked to heart failure. *Nature*. 2012;483(7389):281-2.
377. Ng SB, Turner EH, Robertson PD, Flygare SD, Bigham AW, Lee C, et al. Targeted capture and massively parallel sequencing of 12 human exomes. *Nature*. 2009;461(7261):272-6.
378. Bamshad MJ, Ng SB, Bigham AW, Tabor HK, Emond MJ, Nickerson DA, et al. Exome sequencing as a tool for Mendelian disease gene discovery. *Nature reviews Genetics*. 2011;12(11):745-55.
379. McLaren W, Pritchard B, Rios D, Chen Y, Flicek P, Cunningham F. Deriving the consequences of genomic variants with the Ensembl API and SNP Effect Predictor. *Bioinformatics*. 2010;26(16):2069-70.
380. McKenna A, Hanna M, Banks E, Sivachenko A, Cibulskis K, Kernysky A, et al. The Genome Analysis Toolkit: a MapReduce framework for analyzing next-generation DNA sequencing data. *Genome research*. 2010;20(9):1297-303.
381. Sakib MN, Tang J, Zheng WJ, Huang CT. Improving transmission efficiency of large sequence alignment/map (SAM) files. *PLoS One*. 2011;6(12):e28251.
382. Quinlan AR, Hall IM. BEDTools: a flexible suite of utilities for comparing genomic features. *Bioinformatics*. 2010;26(6):841-2.
383. Schmieder R, Edwards R. Quality control and preprocessing of metagenomic datasets. *Bioinformatics*. 2011;27(6):863-4.
384. Li H, Durbin R. Fast and accurate short read alignment with Burrows-Wheeler transform. *Bioinformatics*. 2009;25(14):1754-60.
385. Stenson PD, Mort M, Ball EV, Shaw K, Phillips A, Cooper DN. The Human Gene Mutation Database: building a comprehensive mutation repository for clinical and molecular

genetics, diagnostic testing and personalized genomic medicine. *Human genetics*. 2014;133(1):1-9.

386. Dagleish R, Flicek P, Cunningham F, Astashyn A, Tully RE, Proctor G, et al. Locus Reference Genomic sequences: an improved basis for describing human DNA variants. *Genome medicine*. 2010;2(4):24.

387. Hayashida W, Kumada T, Nohara R, Tanio H, Kambayashi M, Ishikawa N, et al. Left ventricular regional wall stress in dilated cardiomyopathy. *Circulation*. 1990;82(6):2075-83.

388. Dec GW, Fuster V. Idiopathic dilated cardiomyopathy. *N Engl J Med*. 1994;331(23):1564-75.

389. Bennett CM, Wolford GL, Miller MB. The principled control of false positives in neuroimaging. *Social cognitive and affective neuroscience*. 2009;4(4):417-22.

390. Friston KJ, Holmes A, Poline JB, Price CJ, Frith CD. Detecting activations in PET and fMRI: levels of inference and power. *Neuroimage*. 1996;4(3 Pt 1):223-35.

391. Friston KJ, Worsley KJ, Frackowiak RS, Mazziotta JC, Evans AC. Assessing the significance of focal activations using their spatial extent. *Human brain mapping*. 1994;1(3):210-20.

392. Nichols T, Hayasaka S. Controlling the familywise error rate in functional neuroimaging: a comparative review. *Statistical methods in medical research*. 2003;12(5):419-46.

393. Hutchison JL, Hubbard NA, Brigante RM, Turner M, Sandoval TI, Hillis GA, et al. The efficiency of fMRI region of interest analysis methods for detecting group differences. *Journal of neuroscience methods*. 2014;226:57-65.

394. Wang XF, Jiang Z, Daly JJ, Yue GH. A generalized regression model for region of interest analysis of fMRI data. *Neuroimage*. 2012;59(1):502-10.

395. Poldrack RA. Region of interest analysis for fMRI. *Social cognitive and affective neuroscience*. 2007;2(1):67-70.
396. Mensen A, Khatami R. Advanced EEG analysis using threshold-free cluster-enhancement and non-parametric statistics. *Neuroimage*. 2013;67:111-8.
397. Smith SM, Nichols TE. Threshold-free cluster enhancement: addressing problems of smoothing, threshold dependence and localisation in cluster inference. *Neuroimage*. 2009;44(1):83-98.
398. Arnett DK, Hong Y, Bella JN, Oberman A, Kitzman DW, Hopkins PN, et al. Sibling correlation of left ventricular mass and geometry in hypertensive African Americans and whites: the HyperGEN study. *Hypertension Genetic Epidemiology Network. American journal of hypertension*. 2001;14(12):1226-30.
399. Post WS, Larson MG, Myers RH, Galderisi M, Levy D. Heritability of left ventricular mass: the Framingham Heart Study. *Hypertension*. 1997;30(5):1025-8.
400. Risch N, Merikangas K. The future of genetic studies of complex human diseases. *Science*. 1996;273(5281):1516-7.
401. Pearson TA, Manolio TA. How to interpret a genome-wide association study. *Jama*. 2008;299(11):1335-44.
402. Arnett DK, Li N, Tang W, Rao DC, Devereux RB, Claas SA, et al. Genome-wide association study identifies single-nucleotide polymorphism in KCNB1 associated with left ventricular mass in humans: the HyperGEN Study. *BMC medical genetics*. 2009;10:43.
403. Stegle O, Parts L, Durbin R, Winn J. A Bayesian framework to account for complex non-genetic factors in gene expression levels greatly increases power in eQTL studies. *PLoS computational biology*. 2010;6(5):e1000770.

404. Stegle O, Parts L, Piipari M, Winn J, Durbin R. Using probabilistic estimation of expression residuals (PEER) to obtain increased power and interpretability of gene expression analyses. *Nature protocols*. 2012;7(3):500-7.
405. Teo YY, Inouye M, Small KS, Gwilliam R, Deloukas P, Kwiatkowski DP, et al. A genotype calling algorithm for the Illumina BeadArray platform. *Bioinformatics*. 2007;23(20):2741-6.
406. Anderson CA, Pettersson FH, Clarke GM, Cardon LR, Morris AP, Zondervan KT. Data quality control in genetic case-control association studies. *Nature protocols*. 2010;5(9):1564-73.
407. Purcell S, Neale B, Todd-Brown K, Thomas L, Ferreira MA, Bender D, et al. PLINK: a tool set for whole-genome association and population-based linkage analyses. *American journal of human genetics*. 2007;81(3):559-75.
408. International HapMap C. A haplotype map of the human genome. *Nature*. 2005;437(7063):1299-320.
409. Price AL, Patterson NJ, Plenge RM, Weinblatt ME, Shadick NA, Reich D. Principal components analysis corrects for stratification in genome-wide association studies. *Nature genetics*. 2006;38(8):904-9.
410. Delaneau O, Marchini J, Zagury JF. A linear complexity phasing method for thousands of genomes. *Nature methods*. 2012;9(2):179-81.
411. Delaneau O, Zagury JF, Marchini J. Improved whole-chromosome phasing for disease and population genetic studies. *Nature methods*. 2013;10(1):5-6.
412. Genomes Project C, Abecasis GR, Auton A, Brooks LD, DePristo MA, Durbin RM, et al. An integrated map of genetic variation from 1,092 human genomes. *Nature*. 2012;491(7422):56-65.

413. Marchini J, Howie B, Myers S, McVean G, Donnelly P. A new multipoint method for genome-wide association studies by imputation of genotypes. *Nature genetics*. 2007;39(7):906-13.
414. Howie BN, Donnelly P, Marchini J. A flexible and accurate genotype imputation method for the next generation of genome-wide association studies. *PLoS genetics*. 2009;5(6):e1000529.
415. Howie B, Marchini J, Stephens M. Genotype imputation with thousands of genomes. *G3*. 2011;1(6):457-70.
416. Box GEP, Draper NR. *Empirical model-building and response surfaces*. New York: Wiley; 1987. xiv, 669 p. p.